

# Biology beyond biochemistry: the mechanics of life

Thesis by

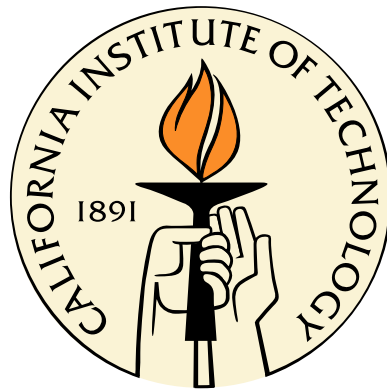
Paul A. Wiggins

Advisor: Rob Phillips

In Partial Fulfillment of the Requirements

for the Degree of

Doctor of Philosophy



California Institute of Technology

Pasadena, California

2005

(Submitted June 2, 2005)

© 2005

Paul A. Wiggins

Advisor: Rob Phillips

All Rights Reserved

# Abstract

In the last half century, biologists have made great strides towards understanding the intricate structure of the cell and the relation between this structure and cellular function. Single-molecule techniques and advances in microscopy have also significantly changed the way in which biologists ask and answer questions. As biological measurements and techniques have become increasingly quantitative, they have allowed biologists to ask ever more quantitative questions: How do the molecular machines, which comprise the cell function microscopically? Can we understand the design principles that govern the structure and function of biological systems on a microscopic scale? One outcome of this new generation of quantitative biological questions is the need to greet quantitative experiments with models at a higher level of abstraction than the traditional cartoons of molecular biology. In this thesis, I present two such quantitative models.

In the first half of this thesis, I present a physical model for mechanotransduction. Mechanosensitive channels are the central agents employed by cells to transduce mechanical stimuli. Our senses of hearing and touch are both examples of this functional motif. The Mechanosensitive Channel of Large conductance (MscL) is arguably the simplest and best studied mechanosensitive channel. I present analytic estimates for the forces and free energy generated by bilayer deformation which reveal a compelling and intuitive model for the function of the MscL channel, analogous to the nucleation of a second phase. The competition between hydrophobic mismatch of the protein with the surrounding membrane and tension results in a surprisingly rich story, which can provide both a quantitative comparison to measurements of the opening tension for MscL when reconstituted in bilayers of different thickness and qualitative insights into the function of the MscL channel and other transmembrane proteins.

In the second half of this thesis, I examine models for the mechanics of DNA. DNA bending, on length scales shorter than a persistence length, plays a central role in the translation of genetic information from DNA to cellular function. Quantitative experimental studies of these biological systems have led to a renewed interest in the short-contour-length polymer statistics relevant for describing the conformational free energy of DNA bending induced by protein-DNA complexes. The recent DNA cyclization studies of Cloutier and Widom have questioned the applicability of the canonical semiflexible polymer theory, the wormlike chain model, to DNA bending on biological

length scales. We describe a new class of polymer models that can resolve the proposed discrepancy between short and long-contour-length bending. These models explain the spectacular success of the wormlike chain model in describing many traditional DNA mechanics experiments, as well as its failure to describe the short-contour-length mechanics of DNA. In particular, I present two toy models for DNA bending which capture the short-contour-length behavior observed by Cloutier and Widom. These toy models make quantitative predictions for chain statistics of DNA, observable in DNA mechanics experiments and of central importance to the qualitative description of cellular function, from chromosomal DNA packaging to transcription and gene regulation to viral packaging.

# Acknowledgements

Let me begin by quickly thanking my committee (**Michael Cross, Grant Jensen, Rob Phillips, David Politzer, and Zhen-Gang Wang**) whose arduous job it is to read these two hundred pages. It has been a very exciting ride for me and I hope that I have conveyed a small part of that excitement in this thesis. Thanks!

It has been an exciting three years and a great privilege to work with my advisor, **Rob Phillips**. Although I admittedly know very little of the hardships of grad school, I have heard enough to truly appreciate what Rob gave me. He was truly generous; intellectually with his ideas and his support for mine, with his trust, his friendship, and his financial support. Perhaps above all, Rob was open minded—he heard us all out. Although I was often far from campus: Northwestern, Delft, Aspen, Villar de Lans, Boston, there was never a place that had quite the same energy and excitement as hanging out with Rob. Boston will be my next home, but a little piece of me will still be at Caltech.

Of course the group would not have been so amazing without my friends and fellow students and postdocs: **Laurent Dupuy, Hernan Garcia, Paul Grayson, Mandar Inamdar, Lin Han, Corinne Ladous, Bertrand Lui, Eric Peterson, Prashant Purohit, Darren Segall, Effrosyni (Frosso) Seitaridou, Tristan Ursell, and Dave Wu**. **Bill Gelbart**’s sabbatical at Caltech has given us all a chance to really get to know him. It has been a real pleasure having him here at Caltech.

Interact with **Jonathon Widom** (Biochemistry, Northwestern) and you will have to acknowledge his sharp, lucid reasoning, his systematic approach to problems, and the experimental knowhow and drive to answer any biological problem. I would especially like to acknowledge Jon for teaching me that research does not always progress in smooth and persistent steps. Sometimes it progresses in fits and starts.

**Phil Nelson** (Physics, U. Penn.) has a history like my own; we both came to biophysics by way of String Theory. Phil and I had been working on an exciting, short paper on on DNA when the floor fell out beneath our feet in the shape of *revised* experimental data. We were on “Skype” at the time and Phil said, “Makes me want to go back to String Theory. There you are never inconvenienced with experimental data.” I replied, “It makes me want to be an experimentalist. At least problems with the experiments would be my own fault.” Working with Phil on DNA mechanics was a joy.

He was very actively involved in the project in a way that Rob could not have been and Phil was an expert in the field. What a ride it was...

**Dong Lai** (Astronomy, Cornell) was the first person who taught me the value of order-of-magnitude calculations. How can one ever forget to thank the person who taught you the most valuable tool in physics?

The Delft biophysics group were great hosts when I visited. I truly enjoyed hanging out with **Cees Dekker, Thijn van der Heijden, and Fernando Moreno**. Thanks for teaching me about AFM!

I thank **Doug Rees** for his encouragement to think about ion channels. He also read our work with an open mind and made many useful comments.

For help on the membrane force project, I would like to thank **Grant Jensen** and his group for teaching me about electron microscopy. I would particularly like to thank **Bill Tivol** for all his help in collecting data and not seeming to care too much when I broke things.

On the theory side of the membrane force project, I would like to thank **Eric Peterson** and **Bill Klug** for helping me with the theory and the numerics! My only regret is that this work was not done in time to appear in my thesis.

I would like to thank **Mandar Inamdar** for not letting me play too fast and loose with physics. He is systematic and careful in a way I may never be.

I would like to thank **Prashant Purohit** for his support, advice, and insight into many problems. Also for putting me up in Philadelphia.

**Steve Quake** I thank for his frank advice and for letting me hang out in his lab occasionally. And, for recommending that I work for Rob four years ago. (Good advice!) His group was a real resource. Especially **Heun Jin Lee** who tirelessly helped me with my actin experiments.

Both **Andy Spakowitz** and **Zhen-Gang Wang** taught me a lot about polymer physics. Both these guys were an amazing resource and an inspiration.

I acknowledge **John Schwarz** for giving me a chance to work on string theory and teaching me that my few talents would be better appreciated elsewhere.

**Todd Squires** and **Mike Diehl** provided the sage advice of seasoned postdocs. Todd's advice about fellowships was extremely useful and Mike's energy is really inspiring.

# Contents

<b>Abstract</b>	<b>iii</b>
<b>Acknowledgements</b>	<b>v</b>
<b>1 The mechanics of life: an introduction</b>	<b>1</b>
1.1 Mechanics and structure . . . . .	2
1.2 Mechanotransduction and MscL . . . . .	3
1.2.1 Road map for the MscL Chapters . . . . .	4
1.3 The high-curvature mechanics of DNA . . . . .	5
1.3.1 Road map for the DNA mechanics chapters . . . . .	5
Bibliography . . . . .	8
<b>2 Mechanotransduction and MscL</b>	<b>10</b>
2.1 Introduction to mechanotransduction . . . . .	10
2.1.1 Biological membranes . . . . .	11
2.1.2 Mechanosensation and mechanosensitive channels . . . . .	12
2.2 Mechanosensation in prokaryotic cells . . . . .	13
2.2.1 MscL is tension gated . . . . .	14
2.3 Patch clamp experiments . . . . .	15
2.4 The MscL crystal structure . . . . .	19
2.5 The importance of membrane-protein interactions . . . . .	19
2.5.1 An analogy to nucleation . . . . .	20
2.6 Summary of MscL Chapters . . . . .	22
Bibliography . . . . .	23
<b>3 Analytic models for mechanotransduction: gating a mechanosensitive channel</b>	<b>25</b>
3.1 Introduction . . . . .	25
3.2 The energy landscape of the bilayer . . . . .	27
3.3 Results . . . . .	31

3.4	Discussion . . . . .	35
	Bibliography . . . . .	38
3.5	Acknowledgments . . . . .	40
3.6	Appendix: Lipids . . . . .	40
3.7	Supporting Methods . . . . .	41
3.7.1	Lipids . . . . .	41
3.7.2	Line Tension . . . . .	41
<b>4</b>	<b>The membrane-protein interactions of mechanosensitive channels</b>	<b>44</b>
4.1	Introduction . . . . .	44
4.2	Free Energy of the Bilayer-Inclusion System . . . . .	46
4.2.1	The Calculation of the Bilayer Free Energy . . . . .	47
4.2.2	Connection between $H'_{\pm}$ and Channel Geometry . . . . .	50
4.2.3	Forces, Torques, and Tensions . . . . .	52
4.2.4	Relation between pressure gradients and generalized forces . . . . .	53
4.3	Free Energy Estimates and Physical Interpretation . . . . .	54
4.3.1	Areal Deformation . . . . .	55
4.3.2	Gaussian Curvature . . . . .	56
4.3.3	Spontaneous Curvature . . . . .	57
4.3.4	Bilayer Interface Energy . . . . .	60
4.3.5	Mid-Plane Deformation . . . . .	61
4.3.6	Thickness Deformation . . . . .	63
4.3.7	Saturation of Thickness Deformation . . . . .	67
4.4	Application to MscL Gating . . . . .	68
4.4.1	Opening Probabilities for Two State System . . . . .	70
4.4.2	Mismatch and Gating . . . . .	72
4.4.3	Spontaneous Curvature and Gating . . . . .	78
4.5	Conclusion . . . . .	79
4.6	Acknowledgments . . . . .	80
4.7	Appendix . . . . .	85
4.7.1	Units and Conversions . . . . .	85
4.7.2	Bilayer Parameter Model . . . . .	86
4.7.3	Effective free energy density . . . . .	88
4.7.4	Equilibrium equations and solutions . . . . .	88
4.7.5	Calculation of Free Energy . . . . .	90
4.7.6	Saturation of Thickness Deformation . . . . .	94

4.7.7	Details of the Perozo vs Powl comparison . . . . .	94
<b>5</b>	<b>All about DNA mechanics</b>	<b>96</b>
5.1	Translating genetic code into biological function . . . . .	97
5.1.1	DNA packaging . . . . .	98
5.1.2	Transcriptional regulation . . . . .	100
5.2	DNA chain statistics and the wormlike chain model . . . . .	102
5.2.1	The random walk model . . . . .	103
5.2.2	The wormlike chain model . . . . .	104
5.2.3	The mechanical limit . . . . .	105
5.2.4	Chain Statistics . . . . .	106
5.2.5	The equivalence of the WLC model to a free quantum particle . . . . .	106
5.2.6	What is the persistence length? . . . . .	109
5.3	Effective concentration . . . . .	110
5.3.1	Chain statistics and the $J$ Factor . . . . .	111
5.3.2	Ligation, kinetics, and the cyclization assay . . . . .	114
5.4	A startling discovery? . . . . .	116
5.5	What's wrong with the wormlike chain model . . . . .	118
	Bibliography . . . . .	119
<b>6</b>	<b>Exact theory of kinkable elastic polymers</b>	<b>123</b>
6.1	Introduction . . . . .	123
6.2	Kinkable Wormlike Chain Model . . . . .	125
6.3	Partition functions . . . . .	127
6.4	Tangent partition function and propagator . . . . .	129
6.4.1	Moment-Bend & kink number . . . . .	134
6.4.2	Persistence length . . . . .	137
6.5	Tangent-spatial and spatial propagators . . . . .	138
6.5.1	Wave number limits . . . . .	141
6.5.2	Partition function in an external field and force-extension characteristic . . . . .	141
6.5.3	Structure factor . . . . .	143
6.6	Cyclized chains and the $J$ factor . . . . .	145
6.6.1	The looping $J$ factor . . . . .	146
6.6.2	The cyclization $J$ factor . . . . .	148
6.6.3	Topologically induced kinking . . . . .	150
6.7	Discussion . . . . .	152
6.8	Acknowledgments . . . . .	153

Bibliography . . . . .	154
6.9 Fourier & Laplace Transforms & convolution theorems . . . . .	157
6.9.1 Circular convolutions . . . . .	158
6.9.2 Numerical inverse transforms . . . . .	159
6.9.3 $J$ factor computation . . . . .	159
6.10 Kinkable rigid rod . . . . .	160
6.11 Gaussian limit . . . . .	162
6.12 Summary of notation . . . . .	163
<b>7 On the experimental front</b>	<b>164</b>
7.1 Does DNA kink? . . . . .	164
7.1.1 The kinking of macroscopic rods . . . . .	165
7.2 Beyond kinking . . . . .	166
7.2.1 AFM measurements of the bending energy of DNA . . . . .	167
7.3 On the experimental front... . . . .	169
7.3.1 Trip to Delft . . . . .	170
7.3.2 Surprising results from Vologodskii . . . . .	172
7.3.3 New data from Jon Widom . . . . .	172
7.3.4 What have we learned? . . . . .	173
7.3.5 General models for stiff polymers . . . . .	174
Bibliography . . . . .	175
<b>8 A generalized theory of stiff polymers</b>	<b>178</b>
8.1 Introduction . . . . .	178
8.1.1 Confronting two world views . . . . .	179
8.1.2 Summary . . . . .	180
8.2 Defining discrete link theories . . . . .	181
8.2.1 Statistical mechanics . . . . .	182
8.2.2 Sub-Elastic Chain Model: A toy model . . . . .	184
8.2.3 The propagator and composition . . . . .	185
8.2.4 Symmetry considerations . . . . .	187
8.2.5 Contour length continuation . . . . .	189
8.2.6 The meaning of persistence length . . . . .	189
8.2.7 Stiff polymer limit . . . . .	190
8.3 The spatial distribution . . . . .	192
8.3.1 The spatial distribution function . . . . .	193
8.3.2 Force-extension . . . . .	195

8.3.3	Structure factor . . . . .	196
8.3.4	Cyclization . . . . .	198
8.4	Discussion . . . . .	200
8.4.1	Unfinished business . . . . .	202
8.5	Conclusion . . . . .	202
	Bibliography . . . . .	204
8.6	Appendix . . . . .	206
8.6.1	Explicit expressions for $g_l$ . . . . .	206
8.6.2	Stiff polymer limit . . . . .	207
8.6.3	The transformed spatial propagator . . . . .	209
8.6.4	Matrix elements of the spatial propagator . . . . .	210
8.6.5	The computation of spatial distributions . . . . .	212
<b>A</b>	<b>Appendix</b> . . . . .	<b>214</b>
A.1	AFM Tracing Code . . . . .	214

# List of Figures

1.1	Channel gating and nucleation . . . . .	4
1.2	Does the Wormlike Chain model fail? . . . . .	6
2.1	Biological membranes . . . . .	11
2.2	Lipid molecules . . . . .	12
2.3	Schematic mechanism for mechanosensation . . . . .	13
2.4	Bacteria are protected from osmotic shock by several mechonsensitive channels . . . . .	14
2.5	Does MscL protein open like the valve of a pressure cooker . . . . .	15
2.6	Electrophysiology: the patch clamp . . . . .	16
2.7	The patch clamp recording from a single MscL channel . . . . .	17
2.8	The free energy difference between the open and closed states as a function of the membrane tension . . . . .	18
2.9	The MscL channel crystal structure . . . . .	20
2.10	The MscL gating tension depends on the thickness of the lipid bilayer . . . . .	21
3.1	The bilayer-inclusion model . . . . .	27
3.2	The bilayer deformation energy landscape . . . . .	30
3.3	The total free energy . . . . .	32
3.4	Free energy difference between open and closed states vs lipid acyl chain length . . . . .	33
4.1	A schematic picture of the bilayer-inclusion model . . . . .	49
4.2	MscL crystal structure . . . . .	51
4.3	A cartoon of areal deformation . . . . .	55
4.4	Areal deformation free energy . . . . .	56
4.5	A schematic depiction of molecular shapes which influence spontaneous curvature . . . . .	57
4.6	A schematic depiction of spontaneous curvature induced by several species of lipids in the bilayer . . . . .	58
4.7	The spontaneous curvature free energy . . . . .	60
4.8	Mid-Plane deformations . . . . .	62
4.9	The mid-plane deformation energy is illustrated above as a function of tension . . . . .	63

4.10	Bilayer thickness deformation . . . . .	64
4.11	Bilayer thickness deformation saturation . . . . .	67
4.12	Interface and thickness deformation energy of the closed state compared to experimental data from Powl . . . . .	69
4.13	The theoretical free energy difference compared to the experimental data of Perozo . . . . .	73
4.14	The theoretical line tension for MscL compared with the line tension estimated from the measurements of East, Lee and coworkers . . . . .	74
4.15	Accuracy of lipid model . . . . .	86
4.16	Validity of asymptotic approximation for dimensionless thickness deformation free energy . . . . .	91
4.17	Validity of asymptotic approximation for dimensionless mid-plane deformation free energy . . . . .	92
5.1	The bending of DNA is ubiquitous in the cellular processes associated with genome management. . . . .	97
5.2	DNA packaging in eukaryotic cells . . . . .	98
5.3	DNA bacteriophages are protein capsids tightly packed with DNA . . . . .	99
5.4	DNA looping is a common functional motif in eukaryotic gene regulation . . . . .	101
5.5	Transcriptional regulation and chain statistics . . . . .	101
5.6	Gene expression depends sensitively on the inter-operator spacing . . . . .	103
5.7	DNA configurations in two dimensions . . . . .	104
5.8	The bending of elastic rods . . . . .	106
5.9	The equivalence of the WLC model to a free quantum particle on a unit sphere . . . . .	107
5.10	The cyclization assay . . . . .	110
5.11	A schematic picture of a DNA operator binding to a protein binding site . . . . .	112
5.12	The results of a cyclization assay for DNA sequences of 116 bp and 94 bp . . . . .	114
5.13	A schematic picture of the DNA cyclization assay . . . . .	115
5.14	Histone affinity is DNA elasticity . . . . .	117
5.15	DNA cyclization data. . . . .	117
6.1	Chain schematic diagram . . . . .	126
6.2	Diagrammatic representation of the kink expansion for the tangent partition function . . . . .	129
6.3	The tangent propagator and the tangent free energy . . . . .	133
6.4	The bending moment $\tau$ and average kink number $\langle m \rangle$ . . . . .	134
6.5	Force-extension characteristic for KWLC compared to WLC and Rigid Rod . . . . .	142
6.6	KWLC force-extension compared with experiment . . . . .	143
6.7	The structure factor . . . . .	144
6.8	The diagrammatic representation of the kink number expansion for cyclized polymers . . . . .	145
6.9	The KWLC looping $J$ factor . . . . .	147

6.10	The KWLC cyclization $J$ factor as a function of contour length $L$ . . . . .	148
6.11	The kink-number distribution compared for cyclized chains . . . . .	150
6.12	A schematic diagram of the coordinate transformation exploited to compute the circular convolution . . . . .	158
7.1	Non-convex bending energy densities induce kinking . . . . .	165
7.2	Kinking: the localization of curvature . . . . .	166
7.3	The bending energy of DNA on short length scales? . . . . .	168
7.4	The new bending energy measurements of Dekker and coworkers . . . . .	170
7.5	Traced DNA conformations . . . . .	171
7.6	The bending energy of DNA revisited . . . . .	171
8.1	Link and vertex numbering . . . . .	182
8.2	The bending energy of DNA on short length scales . . . . .	186
8.3	The evolution of the tangent distribution function . . . . .	188
8.4	The eigen-spectrum of $\mathcal{H}$ for the SEC and WLC models . . . . .	192
8.5	The spatial distribution for the WLC and SEC theories . . . . .	195
8.6	Force-extension . . . . .	197
8.7	The structure factor for the SEC and WLC models . . . . .	197
8.8	The cyclization $J$ factor: probing the high-curvature chain statistics . . . . .	199
8.9	Diagramatic rules for the propagator . . . . .	210
8.10	General matrix elements . . . . .	212

# List of Tables

4.1	Summary of results for inclusion-induced bilayer free energies . . . . .	54
4.2	Summary of the free energy differences measured by Perozo and Powl . . . . .	77
4.3	Lipid bilayer parameters . . . . .	87
4.4	Details of the computation for the comparison between the data of Perozo and Powl. . . . .	94
6.1	Values for the numerically computed integral $I_m$ for the first few $m$ . . . . .	162



## Chapter 1

# The mechanics of life: an introduction

Open a biochemistry text book and you will be presented with intricate diagrams of the biochemical reactions that drive the essential processes of life [1]. From cellular respiration to the transcription of DNA, the cell is portrayed as biology's chemical reactor, containing a rich mix of biological molecules. Is the study of biology anything more than determining the concentrations of the components of the cell and tabulating the rate constants for all reactions? The most compelling evidence against such a simplistic picture is provided by the complex and organized structure of the cell itself.

Over the last fifty years, electron microscopy has revealed the intricate structure of cellular organelles and protein complexes on the nanometer length scale [2]. For example, it was discovered that the mitochondrion, the power plant of the cell, was composed of an inner and outer membrane [3, 4]. The inner compartment (the matrix) is interdigitated by intricately-shaped membrane compartments called cristae [3]. The structure, or shape, of these cristae appears to be actively regulated by the cell and intimately related to function [5].

The interplay between structure and function, illustrated by the mitochondrion, is generic in the cell. Even for individual proteins, function is also intimately linked to structure. Proteins are inactive unless folded into the correct conformation [4] and their function is accompanied and, in many cases, driven by conformational changes. But to discuss the function in terms of individual proteins again oversimplifies the subtlety of biological processes and the importance of structure! Proteins rarely work alone. Most processes in the cell involve complexes of ten or more proteins [6]. Often these processes also involve additional components: nucleic acids or the cell membrane. In fact, I shall discuss examples of both in this thesis! These complexes perform highly organized and coordinated activities. Although the existence of this coordination was long recognized, it is now directly observable. Single-molecule techniques allow biologists to watch reactions unfold by directly observing the conformational changes of individual protein and complexes. For instance, one can observe the rotary motion of the enzyme F1F0 ATP synthase [7].

These ordered movements, which would otherwise violate the second law of thermodynamics, are possible only by the hydrolysis of ATP to ADP. At physiological concentrations, this reaction is essentially irreversible and therefore these ATP driven processes typically proceed in only one direction [8]. This repetitive, machine-like motif of function was beautifully illustrated by a recent study of the mobility of the molecular motor Myosin V. These experiments directly observed the processive, “hand-over-hand” motion of the motor along actin filaments [9].

The chemical reactor analogy of the cell is misleading precisely because it fails to account for the importance of cellular structure and the structural organization and coordination of the vast majority of cellular processes. In fact on the microscopic scale, the cell more closely resembles a factory, whose interconnected assembly lines are ordered and organized [6]. The machines on this assembly line are protein complexes, each consisting of many protein subunits, that function processively due to the hydrolysis of ATP.

## 1.1 Mechanics and structure

In biology, function is determined by structure, but structure is determined by both chemistry and mechanics. From the intricate and dynamic structures of organelles like the mitochondria [5] to the conformational changes of proteins, mechanics and statistical mechanics describe the dynamic structure of the cell. Many protein machines actively convert chemical energy to mechanical work to remodel this structure. A short list of these processes might include DNA replication, transcription, translation, organelle transport, cellular mobility and adhesion, and protein folding [10].

The role of mechanics is not limited to these active processes alone. For example, the mechanics of DNA plays an integral role in gene regulation, the process by which the cell regulates the synthesis of proteins. In a common regulatory motif, rare, thermally-driven configurations, in which DNA is tightly bent, are captured by gene regulatory proteins to create DNA loops [11, 12]. Regulatory DNA looping depends sensitively on the mechanics of DNA [13, 14, 15, 16]. Although this looping motif can be described in the language of biochemistry, the looping equilibrium constant depends both on chemistry (the affinity of DNA for the binding site) and on mechanics (the free energy of bending DNA). The predominance of structure in cellular pathways and processes implies that function is subject to the mechanics of the molecular machines that comprise the cell.

The work described in this thesis describes two examples of the rich interplay between biological function, structure, and mechanics. The first half of this thesis presents a simple model for an example of the biological phenomena of mechanotransduction, the cellular transduction of mechanical stimuli. The second half of the thesis is a reexamination of DNA mechanics applied to biological systems.

Although the atomic structures of the subjects of our study are known, we have not concerned

ourselves with the atomic details of these processes. Instead, we have described these systems with coarse-grained models that significantly reduce the number of degrees of freedom. The advantages of such models over direct simulation are well known. All atom simulations, although much in vogue in biology today, cannot even approach the time scales required to describe most biologically relevant processes. A long simulation of a relatively modest biological system can probe the nanosecond time regime, whereas the relevant time scale for many of the processes we shall describe here is milliseconds and beyond. Furthermore, theoretical models offer a level of insight into processes that is difficult to achieve via simulation alone. Good theoretical models give researchers more than a list of atomic coordinates; they build a framework in which to understand experimental results and make quantitative predictions. They build intuition for the function of biological processes.

On the other hand, the simple coarse-grained techniques employed in this thesis are limited in scope and applicability. As we have discussed above, many of the most important processes in the cell are complicated structurally. We have chosen to study processes that are inherently simple. As the hydrogen atom has served as the proving ground for the ideas in quantum mechanics, we hope that the detailed study of simple biological systems will result in insight into more complicated processes which are not directly tractable by theoretical techniques.

## 1.2 Mechanotransduction and MscL

The cellular phenomena of the detection or transduction of mechanical stimuli is called mechanotransduction. Examples of mechanotransduction are as varied as our own senses of hearing, touch, and pain, to blood pressure, cell volume, and turgor control [17]. Underlying all these phenomena is a common and important functional motif, the mechanosensitive channel. Membrane channels are an essential component of the cellular transport system across membranes. They are ion selective pores in the membrane that undergo a gating transition between open and closed states. Mechanosensitive channels are mechanically gated.

In Chapters 2-4, we investigate the gating mechanism of one of the best characterized mechanosensitive channels: the Mechanosensitive Channel of Large conductance (MscL). The MscL channel is believed to function as an osmo-regulator or emergency relief valve for membrane pressure in bacteria. In Chapters 3 and 4, we present analytic estimates for the forces and free energy generated by membrane-protein interactions. We argue that these calculations reveal a compelling and intuitive model for MscL channel gating analogous to the nucleation of a second phase. This simple model results in a surprisingly rich story, which can provide both a quantitative comparison to measurements of opening tension for MscL when reconstituted in bilayers of different thickness and qualitative insights into the function of the MscL channel and other transmembrane proteins.

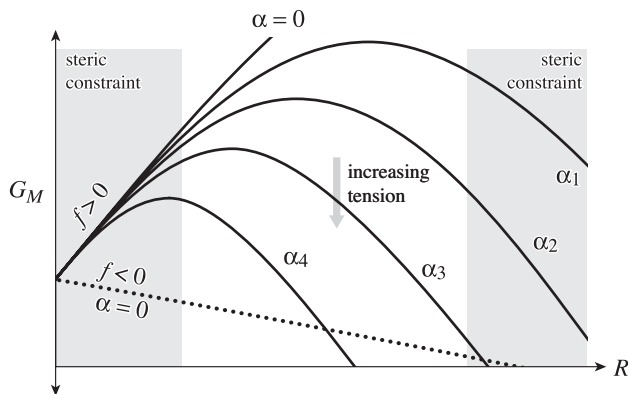


Figure 1.1: Channel gating and nucleation. The MscL channel is a protein pore in the membrane with two conductance states: open and closed. When the channel is gated by membrane tension, it undergoes a conformation change which nearly doubles the radius of the channel and opens an internal pore. The membrane-protein interaction energy ( $G_M$ ) is an important part of the free energy budget of the channel.  $G_M$  consists of a line tension ( $f$ ) induced by the deformation of the membrane at its boundary with the channel, and a contribution from the membrane tension ( $\alpha$ ). These two contributions lead to the classic nucleation free energy plotted as a function of channel radius ( $R$ ) above. At a critical radius ( $R = \alpha/f$ ), the channel becomes unstable to opening. This remarkably simple model describes many features of channel function.

### 1.2.1 Road map for the MscL Chapters

Chapter 2 introduces the concepts of mechanotransduction and mechanosensation and briefly outlines the role of the mechanosensitive channel in these phenomena. This chapter also contains a brief introduction to biological membranes, channels, and the experimental techniques used to study mechanosensitive channels.

Chapter 3 is a short chapter that develops the analogy between the gating of mechanosensitive channels and nucleation, culminating in the results shown in Fig. 1.2.1. This chapter summarizes the most exciting results from an extensive framework developed for studying membrane-protein interactions, which is present in detail in the following chapter. We show that this simple nucleation model makes both qualitative and quantitative predictions that agree with experimental measurements of MscL channel gating. Finally, we discuss the general implication of membrane-protein interactions to channel gating.

Chapter 4 is a detailed development of the framework for studying membrane-protein interactions that was applied in the previous chapter. This model is an effective elastic theory for membrane mechanics, built upon the work of many other authors. To investigate mechanotransduction and the function of the MscL channel, it was necessary to improve and extend the existing models. We make extensive estimates of the various contributions to the membrane-protein interaction energy and apply these results to describing the gating of the MscL channel as a function of the membrane

characteristics. The gating model provides a systematic method for understanding a new series of MscL experiments that study the significance of membrane-protein interactions experimentally. The membrane-protein-interaction framework developed in this chapter can also be applied to studies of the function of other transmembrane proteins.

## 1.3 The high-curvature mechanics of DNA

Simply stated, DNA mechanics is of central importance to both biology and physics. From a biological perspective, DNA bending is ubiquitous in the cellular processes involved in the translation of genetic information from DNA to cellular function. DNA bending figures prominently in processes from chromosomal DNA packaging, to transcription, and gene regulation, to viral packaging. From a biophysical perspective, DNA bending is one of the few problems which is tractable from both a theoretical and experimental perspective. One of the crowning achievements of biophysics is the description of the statistical mechanics of double stranded DNA by the Wormlike Chain model [18], and the agreement between this theory and experimental measurements of the extension of single DNA molecules under an external force [19].

Despite these notable theoretical and experimental successes, recent DNA cyclization studies have revealed that for bending on the short length scales actually relevant for most biological processes, the accepted theories of DNA mechanics may fail dramatically. Cloutier and Widom [20] have reported that there is at least a three-order-of-magnitude ( $10^3$ ) discrepancy between the predictions of theory and experimental measurements! (See Fig. 1.3.) These measurements suggest that highly-curved DNA configurations may be orders-of-magnitude more probable than predicted by the accepted theory of DNA statistics and have the potential to completely change our understanding of DNA bending in a biological setting.

In Chapters 5-8, we reexamine the accepted theoretical model for DNA statistical mechanics: the Wormlike Chain model. This model is equivalent to a theory of fluctuating linear-elastic rods. We demonstrate that the success of the Wormlike Chain model in describing many DNA mechanics experiments does not rule out the possibility that the WLC model fails dramatically to account for the short-contour-length cyclization of DNA sequences as proposed by the experiments of Cloutier and Widom [20]. Thermal fluctuations disguise the underlying mechanics of the polymer. The universal long-contour-length chain statistics of stiff polymers is predicted by the WLC model. (See Fig. 1.3.)

### 1.3.1 Road map for the DNA mechanics chapters

Chapter 5 is an introduction to DNA mechanics. We first outline a number of biological processes in which DNA bending plays an integral role. We then introduce the accepted model of DNA

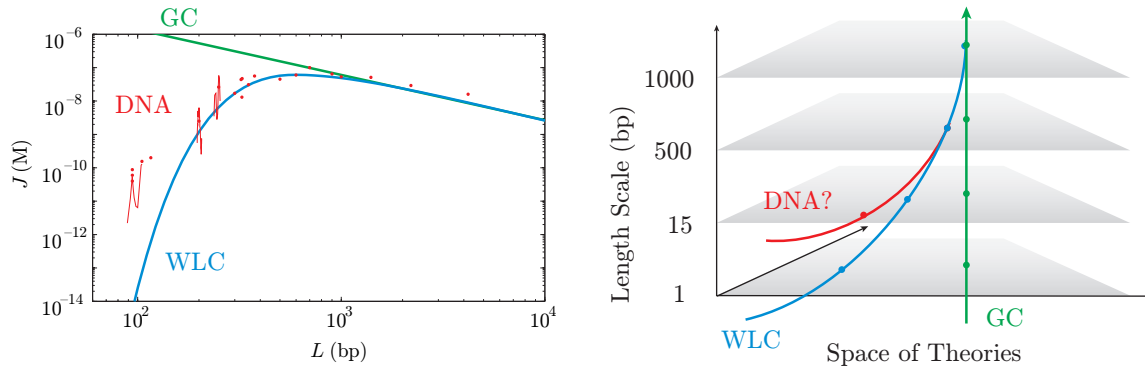


Figure 1.2: Does the Wormlike Chain model fail? The cyclization  $J$  factor measured by Cloutier and Widom [20] (red) is compared to theoretical prediction of the Wormlike Chain model (blue) in the left-hand panel. The  $J$  factor, defined in chapter 5, is the propensity of DNA to spontaneously cyclize. The measurements of Cloutier and Widom posit that the propensity of 94 base pair DNA sequences to cyclize is more than three-orders-of-magnitude higher than predicted by the WLC model! For long-contour-length sequences, the WLC model fits experimental measurements. In Chapter 8, we show that the WLC model predicts the generic long-contour-length behavior of stiff polymers. For short-contour-length chains, the statistics are model dependent. The length scale dependence of polymer theories is illustrated schematically in the right-hand panel. Although the chain statistics of DNA and the WLC model may be dramatically different for short-contour-length chains, as the length scales probed by experiment grow, the chain statistics of DNA becomes indistinguishable from the WLC model. At sufficiently long contour length, both models converge with the predictions of the Gaussian chain model (green).

mechanics, the Wormlike Chain model. Finally, we introduce the concepts of effective concentration and the  $J$  factor and explain the DNA cyclization assay that figures prominently in our discussions of DNA mechanics.

In Chapter 6, we introduce an exact analytic theory of the chain statistics of linear-elastic polymers that undergo a kinking transition at high curvature. We show that the resulting theory, the kinkable Wormlike Chain model, reproduces both the low-curvature linear-elastic behavior which is already well described by the Wormlike Chain model, as well as the high-curvature softening observed in the experiments of Cloutier and Widom [20]. Finally, we discuss possible microscopic realizations of kink formation for DNA bending.

The kinkable Wormlike Chain model is the simplest example of a class of generalized theories we shall introduce in chapter 8. Chapter 7 outlines the limitations of the kinkable Wormlike Chain model described in the previous section. Although high-curvature conformations of DNA are observed, DNA kinking does not seem to be generic at high curvature as implied by the kinkable Wormlike Chain model. We then present some atomic force microscopy (AFM) measurements of the bending energy of DNA, which motivate a less dramatic elastic breakdown. Finally, we briefly outline several recent conflicting experimental studies.

In Chapter 8, we present a near-exact theory of a class of generalized polymer models. The linear-elastic bending energy density is replaced by a bending energy density which is an arbitrary function of curvature. This class of generalized theories includes the kinkable Wormlike Chain model presented in chapter 6. We show that the Wormlike Chain model describes the generic long-length-scale behavior of stiff polymers, implying that there are many polymer models with dramatically different short-length-scale chain statistics, that are identical at long-contour-length. We discuss this behavior as an application of the renormalization group. In particular, we show that generalized theories are nearly indistinguishable from the Wormlike Chain model in force-extension and long-contour-length cyclization measurements. At sufficiently short contour lengths, the Wormlike Chain model fails to describe the chain statistics of the general models. Short-contour-length cyclization experiments, like those performed by Cloutier and Widom [20], may access this regime. Finally we discuss the significance of these results in the context of the current, muddled experimental picture.

# Bibliography

- [1] Gerhard Michal, editor. *Biochemical Pathways: An Atlas of Biochemistry and Molecular Biology*. Wiley-Spektrum, 1998. [1](#)
- [2] Donald W. Fawcett. *The Cell: An Atlas of Fine Structure*. W.B. Saunders, 10th edition, 1981. [1](#)
- [3] G. Palade. The fine structure of mitochondria. *Anat. Rec.*, 114:427—451, 1952. [1](#)
- [4] Bruce Alberts, Dennis Bray, Julian Lewis, Martin Raff, Keith Roberts, and James D. Watson. *Molecular Biology of the Cell*. Garland Publishing, New York, NY, 3rd edition, 1994. [1](#), [11](#), [12](#), [13](#), [16](#), [97](#), [98](#), [100](#), [101](#), [116](#), [167](#), [179](#)
- [5] T. G. Frey and C. A. Mannella. The internal structure of mitochondria. *Trends Biochem Sci*, 25(7):319–24, 2000. [1](#), [2](#)
- [6] Bruce Alberts. The cell as a collection of protein machines: Preparing the next generation of molecular biologists. *Cell*, 92(3):291–294, 1998. [1](#), [2](#), [98](#)
- [7] H. Noji, R. Yasuda, M. Yoshida, and K. Jr Kinosita. Direct observation of the rotation of F1-ATPase. *Nature*, 386(6622):299–302, 1997. [1](#)
- [8] Jonathon Howard. *Mechanics of Motor Proteins and the Cytoskeleton*. Sinauer, 2001. [2](#), [12](#)
- [9] Ahmet Yildiz, Joseph N. Forkey, Sean A. McKinney, Taekjip Ha, Yale E. Goldman, and Paul R. Selvin. Myosin V walks hand-over-hand: Single fluorophore imaging with 1.5-nm localization. *Science*, 300(5628):2061–5, 2003. [2](#)
- [10] Carlos Bustamante, Yann R. Chemla, Nancy R. Forde, and David Izhaky. Mechanical processes in biochemistry. *Annu Rev Biochem*, 73(0066-4154):705–48, 2004. [2](#)
- [11] K. Martin, L. Huo, and R. F. Schleif. The DNA loop model for ara repression: AraC protein occupies the proposed loop sites in vivo and repression-negative mutations lie in these same sites. *Proc Natl Acad Sci USA*, 83(11):3654–8, 1986. [2](#), [165](#)
- [12] R. F. Schleif. Gene regulation: why should DNA loop? *Nature*, 327(6121):369–70, 1987. [2](#)

- [13] Karsten Rippe, Peter R. von Hippel, and Jörg Langowski. Action at a distance: DNA-looping and initiation of transcription. *Trends Biochem. Sci.*, 20(12):500–506, 1995. [2](#), [102](#), [110](#), [114](#), [118](#), [124](#), [152](#), [179](#)
- [14] J. Muller, S. Oehler, and B. Muller-Hill. Repression of lac promoter as a function of distance, phase and quality of an auxiliary lac operator. *J. Mol. Biol.*, 257:21–29, 1996. [2](#), [102](#), [103](#), [118](#), [124](#), [152](#), [202](#)
- [15] J. Muller, A. Barker, S. Oehler, and B. Muller-Hill. Dimeric lac repressors exhibit phasedependent co-operativity. *J. Mol. Biol.*, 284:851–857, 1998. [2](#), [102](#), [103](#), [118](#), [124](#), [152](#)
- [16] Karsten Rippe. Making contacts on a nucleic acid polymer. *Trends Biochem. Sci.*, 26(12):733–740, 2001. [2](#), [102](#), [110](#), [114](#), [118](#), [124](#), [152](#)
- [17] Owen P. Hamill and Boris Martinac. Molecular basis of mechanotransduction in living cells. *Physiol. Rev.*, 81(2):685–740, 2001. [3](#), [10](#), [13](#), [15](#)
- [18] H. Yamakawa. *Helical Wormlike Chains in Polymer Solutions*. Springer, Berlin, 1997. [5](#), [104](#), [108](#), [109](#), [113](#), [123](#), [125](#), [137](#), [146](#), [160](#), [164](#), [192](#), [199](#), [202](#)
- [19] C. Bustamante, J. F. Marko, E. D. Siggia, and S. Smith. Entropic elasticity of lambda phage DNA. *Science*, 265:1599–1600, 1994. [5](#), [96](#), [195](#)
- [20] T. E. Cloutier and J. Widom. Spontaneous sharp bending of double-stranded DNA. *Molecular Cell*, 14(3):355–362, 2004. [5](#), [6](#), [7](#), [96](#), [97](#), [110](#), [114](#), [116](#), [117](#), [118](#), [124](#), [145](#), [148](#), [152](#), [164](#), [169](#), [172](#), [173](#), [174](#), [179](#), [181](#), [185](#), [198](#), [199](#), [200](#), [203](#)

## Chapter 2

# Mechanotransduction and MscL

### 2.1 Introduction to mechanotransduction

Even the smallest, simplest bacteria must sense mechanical stimuli to survive! The cellular phenomena of the detection or transduction of mechanical stimuli is called mechanotransduction. Examples of mechanotransduction are as varied as our own senses of hearing, touch, and pain, to blood pressure, cell volume, and turgor control [1]. Underlying all these phenomena is a common and important functional motif: the mechanosensitive channel. In the next two chapters, I will present a simple, analytic theory that describes the function of one of the most extensively studied mechanosensitive channels: the Mechanosensitive channel of Large Conductance (MscL).

In this chapter, I will first briefly describe how mechanosensitive channels give rise to the phenomena of mechanotransduction. In Sect. 2.1.1, I begin by reminding the reader about the functional role of membranes and channels in the cell. Sect. 2.1.2 explains the role of mechanosensitive channels in the phenomena of mechanosensation in multicellular organisms. Our senses of touch and hearing are examples of mechanosensation. Sect. 2.2 introduces an example of mechanotransduction in prokaryotic cells: the osmo-regulating Mechanosensitive channel of Large Conductance (MscL).

The MscL channel is thought to function as an emergency relief valve for bacteria [2]. If the pressure across the bacterial membrane becomes dangerously high, the MscL channel opens and relieves the pressure. In chapters 3 and 4, the MscL channel will serve as a case study for simple analytic models of mechanosensitive channels. Sect. 2.2.1 explains why osmo-regulating channels like MscL are controlled by membrane tension rather than the pressure difference over the membrane. Sect. 2.3 briefly describes how membrane channels are studied experimentally and what are the experimental observables. Sect. 2.5 introduces membrane-protein interactions and shows experimental evidence for the importance of these interactions to channel function. Sect. 2.5.1 introduces an analogy between nucleation and channel gating that will be developed in the next two chapters. We close this chapter with a road map of the next two chapters.

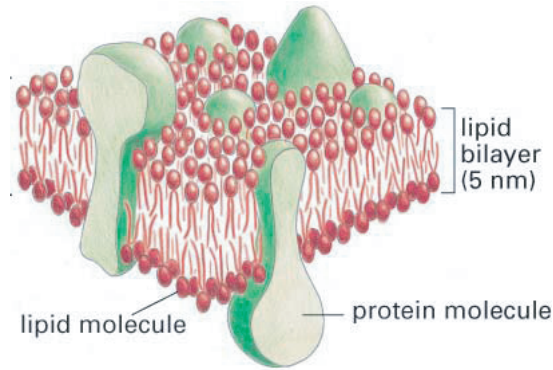


Figure 2.1: Biological membranes. Above is a schematic drawing of the membrane structure. The membrane is composed of a lipid bilayer punctured by many transmembrane proteins. These proteins perform many essential functions; in particular there are carrier and channel proteins which promote the transport of molecules across the membrane. (Figure from Ref. [4]).

### 2.1.1 Biological membranes

The cell membrane essentially forms the barrier between the cell (cytoplasm) and the outside world (periplasm) or the intercellular space in multicellular organisms. In eukaryotic cells, the cellular organelles are also membrane bound. Although this biological membrane is sometimes referred to as a lipid bilayer membrane, this is a misnomer since biological membranes have a very large number of constituent proteins in addition to lipid molecules. Indeed, the ratio by mass of protein to lipid in some prokaryotic membranes can be four to one! In our own cells, the mass ratio of proteins to lipids is typically one to two [3]. Fig. 2.1.1 shows a schematic illustration of a biological membrane with constituent proteins.

In the test tube, lipid bilayer membranes can self-assemble in polar solutions due to the hydrophobic interaction of the tail groups of the lipid molecules, which aggregate into bilayers, exposing their polar head groups.<sup>1</sup> (See Fig. 4.3.3.) Some constituent proteins can also be *reconstituted* into the artificial membrane.

The membrane provides a barrier for large and polar molecules. The impermeability of membrane to charged ions is of particular importance biologically since membrane potentials, the voltage drop over the membrane, have many uses in biology including energy storage and signal transduction.

The cell must constantly exchange molecules across the membrane barrier. Although many of these processes are active, requiring energy, many transport processes are diffusively driven through membrane channels. These channels are simply membrane proteins that form pores in the membrane. Although transport through the channel is passive, they are typically ion-selective and have open and closed conformations [4, 6].

The conformational change of a channel protein between conductance states is called gating.

<sup>1</sup> Other non-lamellar phases are possible, but these are typically not of great biological interest [5].

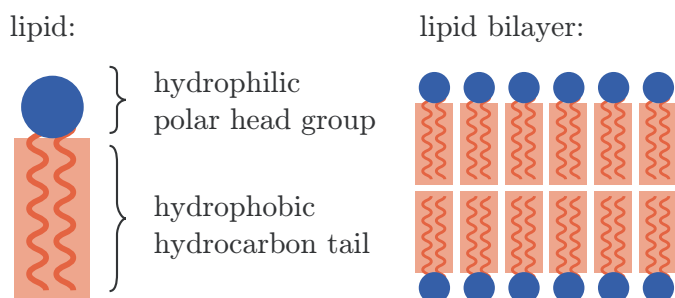


Figure 2.2: Lipids molecules. Lipid molecules are composed of a polar head group and hydrophobic hydrocarbon tails. The lipid molecules can self-assemble into bilayers in polar solutions like water. The tails aggregate to expel the polar solvent.

Channel gating can be triggered in a number of ways. The most common triggers are ligand binding, membrane voltage, and mechanical gating.

### 2.1.2 Mechanosensation and mechanosensitive channels

Mechanosensation derives from mechanosensitive channels, which are typically force-gated. It is worth noting that such a picture is very natural biologically. The force is transduced by coupling it to the gating of a mechanosensitive ion channel [7]. When the channel opens, it depolarizes the membrane by permitting a large number of ions to flow across the membrane. This electro-chemical signal can then be propagated and amplified by voltage sensitive channels [4, 7, 6].

In many eukaryotic force transducers, the mechanosensitive channel is coupled to both an extracellular anchor and the cytoskeleton of the cell [7]. The cytoskeleton is internal protein scaffolding which gives many eukaryotic cells their structure [4, 8, 9]. Fig. 2.1.2 shows a schematic drawing of these linkages.

One of the important biological model systems for mechanosensation is *C. elegans*, a small worm. *C. elegans* is a convenient model system since it has a small, sequenced genome (100 Mbp), it consists of less than one thousand cells, and has a three day life cycle [10]. A genetic screen, testing the response of the worms to the touch of an eyelash, determined a set of mutants with defective mechanosensation (*mec* mutants) [7]. Most of these gene products are believed to constitute the mechanotransduction complex. For instance, the protein responsible for the extracellular anchor, linkers, and mechanosensitive channel have all been identified and match the general outlined discussed above [7]. Although the story in many higher organisms is less complete, it is worth noting that the mechanosensitive channel responsible for our own sense of hearing has recently been identified [11].

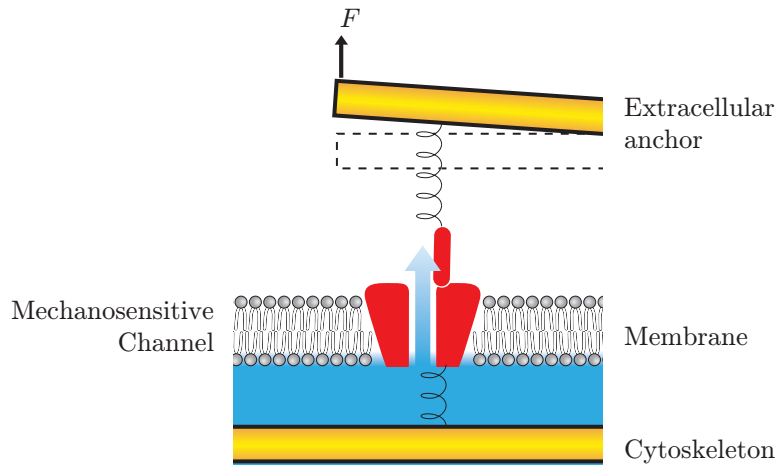


Figure 2.3: Schematic mechanism for mechanosensation. Mechanosensitive channels drive the phenomena of mechanosensation. These channels are force gated. The channel is coupled mechanically to both the cytoskeleton of the cell as well as an extracellular anchor. Mechanical stimuli deflect the extracellular anchor with respect to the cytoskeleton [7]. Once the mechanosensitive channel opens, ions pass through the channel generating an electrochemical signal, which is then amplified and transmitted by other voltage-gated channels [4, 6]. (Figure after Ref. [7].)

## 2.2 Mechanosensation in prokaryotic cells

Despite the comparative simplicity of the mechanoreceptor of *C. elegans*, it is still far too complicated to assemble *in vitro*. In particular, it is necessary to assemble the many different components after reconstituting the mechanosensitive channel in the membrane. Furthermore, although many of the protein components of the mechanoreceptor have been identified, there is comparatively little structural information about them [7]. Quantitative studies of the microscopic mechanism of mechanosensation have therefore focussed on still more simple systems, prokaryotic cells.

Although prokaryotic cells are significantly simpler than even single-celled eukaryotes, they still exhibit mechanosensitive behavior. One of the best studied of the mechanosensitive channels is the MscL channel in *E. coli*. Homologues of this channel are found in many other prokaryotes [2, 1]. MscL is an acronym for MechanoSensitive Channel of Large conductance (2-3 nS) [2].

The MscL channel is believed to function as an osmo-regulator, an emergency relief valve for membrane pressure [2]. If the *E. coli* bacterium experiences a sudden osmotic down shock, for instance if it is suddenly moved from growth media to water, the osmotic pressure over the membrane dramatically increases. As the internal pressure increases, so does the membrane tension. If the bacterium is unable to relieve the membrane tension, the membrane will lyse or burst. (This lysis tension is on order 10 dyne/cm [12].) *E. coli* has several lines of defense against such a scenario, but MscL, with its large 2 to 3 nS conductance can relieve this pressure more quickly than several

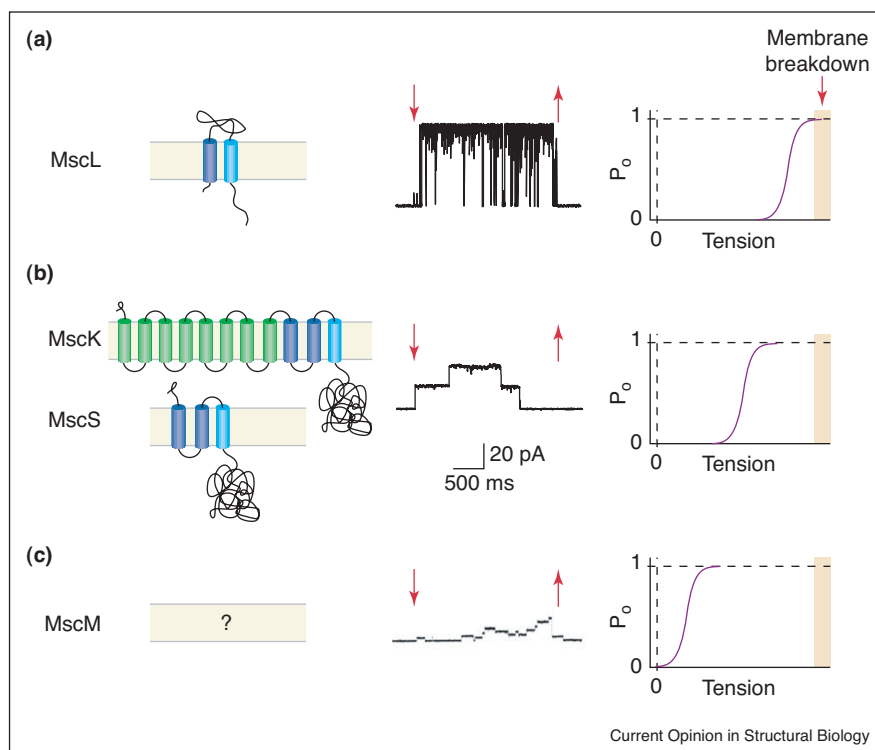


Figure 2.4: Bacteria are protected from osmotic shock by several mechanosensitive channels. The diagram above summarizes the differences between channels: channel topology, channel current, and open-state probability as a function of membrane tension. MscL, the MechanoSensitive Channel of Large conductance, has the largest open-channel conductance (3.5 nS), but is activated at the highest tension, very close to the critical lysis tension. MscS, the MechanoSensitive Channel of Small conductance, has a 1 nS conductance but is activated at a lower tension than MscL. (MscK is similar to MscS.) Note that the current trace shows the response of two channels. MscM, the MechanoSensitive Channel of Mini conductance, has a conductance of just 100-200 nS, but is gated at the lowest tension. Again the trace shows the response of several channels. (Figure from Ref. [13].)

other mechanosensitive proteins present in *E. coli* but with smaller open channel conductance [2]. (See Fig. 2.2.)

### 2.2.1 MscL is tension gated

How does MscL sense the building membrane pressure? There are at least two possibilities<sup>2</sup>: the channel gating can either couple to the pressure difference itself or the resulting membrane tension. A simple calculation reveals that the channel is most likely tension gated.

For the long-length-scale bending that gives rise to gross shape of the *E. coli* bacterium, the forces due to membrane bending elasticity are irrelevant and force balance is achieved by Laplace's

<sup>2</sup>One might imagine that MscL could also couple to structural components of the bacterium, like the bacterial cell wall, and be force gated. But experiments conclusively show that MscL functions in the absence of the bacterial cell wall [2].

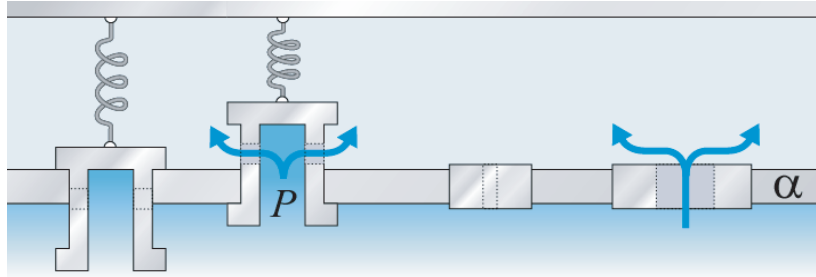


Figure 2.5: Does MscL protein open like the valve of a pressure cooker? Above are two schematic pictures for the function of MscL. Is the channel gated by pressure as depicted on the left or by the membrane tension as depicted on the right. In the text we explain that unlike a pressure cooker valve, MscL is opened by membrane tension.

law of soap bubbles relating the tension and pressure,

$$P = \frac{2\alpha}{R}, \quad (2.1)$$

where we denote the tension  $\alpha$ , the pressure  $P$ , and  $R$  is the radius of curvature of the bacterial membrane, which is on order a micron. The free energy associated with conformational changes of the channel with respect to the pressure are of order

$$\Delta G_P = \ell^3 P, \quad (2.2)$$

where  $\ell$  is the length scale of the channel, which is on order nanometers. The free energy change due to tension are of order

$$\Delta G_\alpha = \ell^2 \alpha. \quad (2.3)$$

The ratio of the free energy due to tension to that due to pressure is [1]

$$\frac{\Delta G_\alpha}{\Delta G_P} = \frac{R}{2\ell} \sim 1000. \quad (2.4)$$

Since the radius of curvature is so large compared with the size of the channel, free energies associated with membrane area changes give rise to free energy orders-of-magnitude larger than conformational changes driven directly by pressure.

### 2.3 Patch clamp experiments

Remarkably, electrophysiologists have long been able to directly observe the behavior of single ion channels [6]. Indeed, despite the great interest currently swirling around single-molecule biophysics, electrophysiologists have been doing single-molecule experiments on ion channels for decades. These

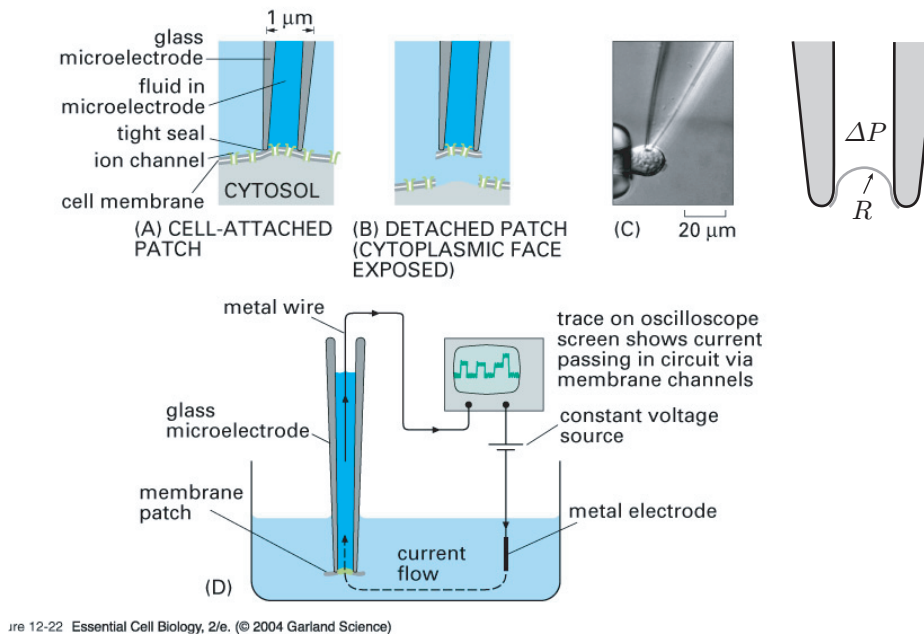


Figure 2.6: Electrophysiology: the patch clamp. Above is a schematic diagram of the patch clamp experiment used to measure channel currents. A membrane patch is created from a cell or vesicle by positioning a micro-pipette next to the membrane and applying suction on the micro-pipette. The glass pipette forms an extremely tight seal with the membrane allowing current to pass through the membrane channels only. The electrical current, generated by the passage of ions through the channel, is then measured. For MscL, the current is measured as a function of the applied pressure difference over the membrane. The radius of curvature of the membrane is observable. The Laplace law relates the radius of curvature and pressure difference to the membrane tension. (Figure from Ref. [4].)

experiments exploit an experimental technique called patch clamp recording [6]. In this technique, a micro-pipette is pressed against the cell (or vesicle) membrane to form a tight seal. (See Fig. 2.3.) This seal is to a good approximation impermeable [6]. The electric current through the membrane patch, corresponding to the passage of ions through the channels, can then be measured as a function of the voltage drop over the membrane.

To study mechanosensitive channels like MscL, the ion current is measured as a function of the pressure difference over the membrane. The radius of curvature of the membrane patch is observable under a microscope. The tension can then be computed using the Laplace law:

$$\alpha = \frac{1}{2}PR, \quad (2.5)$$

where  $P$  is the pressure difference,  $\alpha$  is the tension, and  $R$  is the radius of curvature of the membrane patch.

A patch clamp recording for a single MscL channel is shown in Fig. 7.3.1. In this experiment,

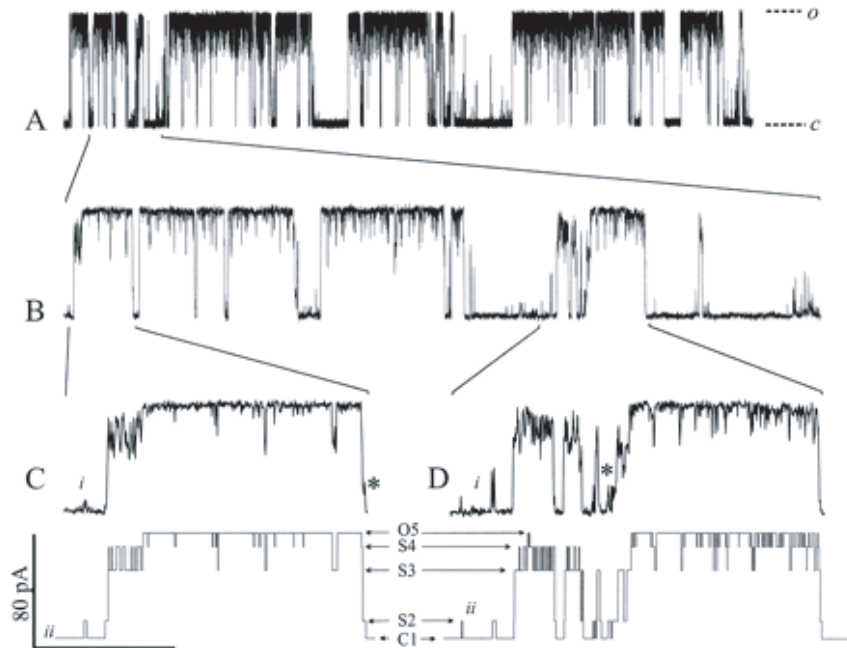


Figure 2.7: The patch clamp recording from a single MscL channel. The channel gating of the MscL channel is stochastic, fluctuating between states. Panel A shows low time resolution data where the time scale bar is 800 ms. Panel B shows an enlarged interval where the time scale bar is 80 ms. Panels C and D show smaller intervals still where the time scale bar is respectively 15 and 20 ms. To analyze the data, it is binned into states based on conductance. Histograms of the data appear to implicate a five state system, but the channel stays predominantly in the open (O) and closed states (C). In this recording, the membrane tension is 12.3 dyn/cm and the probability of the open state is 0.67. (Figure from Ref. [14].)

MscL has been reconstituted into a PC lipid bilayer at low enough MscL concentration that single channels are observed in a typical membrane patch [14]. One important feature to note from the current trace is that the channel inhabits states of well defined conductance. Typically these states can be picked out from a histogram of the channel current. (States correspond to peaks.) Even if the channel were described by two, very well defined conductance states, these peaks would be smeared out by the practical resolution limits of patch clamp experiments. Even in an idealized experiment, there are still fluctuations in the current due to the electrical resistance of the channel (Johnson noise). The fluctuation-dissipation theorem predicts the dependence of Johnson noise on the resistance and bandwidth of the experiment.

For the most part the channel is either in a closed state with negligible conductance or an open state with a fixed conductance. Three additional short-lived sub-states have also been identified with intermediate conductance [14]. We shall assume that these well defined conductance states correspond to well defined channel conformations.

The second important feature of the patch recording is that the channel behavior is stochastic; it fluctuates between conductance states as one would expect for a molecular scale channel undergoing

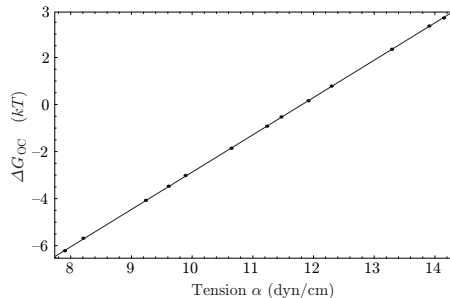


Figure 2.8: The free energy difference between the open and closed states as a function of the membrane tension. The linear dependence on tension suggests that the area difference between the two states is constant. See the discussion in Chapter 4. Data from Ref. [14].

thermally-induced transitions. Clearly the language of statistical mechanics will be important to describing the function of the channel. In order to interpret the channel recordings quantitatively, the records are idealized by assigning a channel state as a function of time based upon the instantaneous conductance. (See Fig. 7.3.1.) It is typically assumed that the transitions are Markovian (without memory) and are described by a set of first-order rate equations. Channels appear to be well described by this model. The rate constants are then fit to the experimental data. For MscL, the typical transition rates vary from hertz to tens of kilohertz [14].

The relative free energies of the states can be computed from their respective probabilities using the Boltzmann distribution:

$$\Delta G_{ij} = -kT \log \frac{\mathcal{P}_i}{\mathcal{P}_j}, \quad (2.6)$$

where  $\mathcal{P}_i$  is the probability of state  $i$  and  $\Delta G_{ij}$  is the free energy difference between states  $i$  and  $j$ . The free energy difference between the open and closed states as a function of membrane tension is plotted in Fig. 2.3.

We shall discuss this free energy in great detail in the next two chapters. For the moment, let us look at the general behavior of the channel. The opening tension (the tension at which the open and closed probabilities are equal) is 11.8 dynes/cm [14]. Experiments show that the lysis tension for membranes is on order 10 dynes/cm [12]. (This opening tension will depend on the properties of the lipid bilayer.) This high gating tension is one of the motivations for the biological explanation of MscL as an emergency pressure relief valve. Note that the channel is also very sensitive to the pressure. For each dyne/cm drop in the membrane tension, the ratio of the open to the closed probabilities decreases by almost a factor of four. For an emergency relief valve, this tension sensitivity is incredibly important. When the MscL channel opens, the pore is on order thirty angstrom in diameter, implying that many small molecules can escape from the bacteria. Clearly the MscL channel must open only in emergencies.

The most striking feature of the free energy difference between the open and closed state is that

it depends linearly on the membrane tension. (See Fig. 2.3.) This is exactly the tension dependence one would naïvely expect for a two state system if each state had a fixed area under external tension. The free energy difference between states would then be

$$\Delta G_{OC} = \Delta G_0 - \alpha \Delta A_{OC}, \quad (2.7)$$

where  $\Delta G_0$  is constant with respect to the tension and  $\Delta A_{OC}$  is the area difference between states the open and closed states. Clearly high tension stabilizes the open state with its larger radius. The sensitivity of the channel, the slope of the free energy with respect to tension, is the area difference between states  $\Delta A_{OC} = 6.5 \text{ nm}^2$ . This measurement of the area change is large for a channel protein.<sup>3</sup> This large area change is a consequence of opening a 3 nm pore in channel core and must correspond to a very significant conformational change in the protein.

## 2.4 The MscL crystal structure

The crystal structures of the MscL and MscS channels were recently solved by Doug Rees' group at Caltech [17, 18].<sup>4</sup> The MscL channel structure shows that the channel is a homopentamer with two transmembrane alpha helices per subunit. (The structure is shown in Fig. 2.4.) The crystal structure appears to be that of the closed conformation of the channel since the inner pore is tightly constricted by the transmembrane alpha helices. (This is not obvious from Fig. 2.4 since the side groups of the amino acids are not drawn in the cartoon.)

The crystal structure of the MscL channel provides many valuable insights into its function [19, 20, 16, 15, 13]. For instance, the structure of the closed state has provided the basis for building atomic scale models of the open-state structure aided by computational techniques [20, 16]. These open-state models can then be tested using a number of different techniques: cross-linking [20, 15], electron paramagnetic resonance spectroscopy, and site-directed spin labeling [16]. These techniques have lead to very detailed, atomic-level models of channel gating.

## 2.5 The importance of membrane-protein interactions

A common perception in the structural biology community is that protein conformation is everything. Rob and I had likewise initially been very interested in the protein structure of MscL. In fact, it was the crystal structure of the closed state that interested us in the channel in the first place. But, as we began estimating the free energies associated with the interaction of the protein with the

---

<sup>3</sup> In fact, it is thought that this measurement significantly underestimates the area change base on structural arguments [15, 16].

<sup>4</sup>This was no mean feat as the crystallization of membrane proteins is particularly difficult since the presence of the membrane is structurally important.



Figure 2.9: The MscL channel crystal structure. The channel is a homopentamer with two transmembrane helices per subunit. In the figure above, each subunit, although identical, is colored differently to distinguish the individual protein subunits. The transmembrane helices are labeled TM1 and TM2. There is a third cytoplasmic alpha helix which protrudes into the cell interior. This five helix complex is thought to function as a filter [13]. Figure from Ref. [17].

membrane, we were struck by how large these interaction energies were for the MscL channel; they were on order the gating free energy. The importance of these interactions was soon demonstrated experimentally by Perozo and coworkers [21] who showed that the gating tension depends sensitively on the membrane characteristics. Fig. 4.4.2 shows the channel opening probability as a function of the applied pressure for the MscL protein reconstituted into several different lipid membranes. The thickness of the lipid membrane is roughly proportional to the number of carbons in the tail group (acyl chain length) [22]. Perozo and coworkers demonstrated that the gating tension rises dramatically with the thickness of the bilayer.

### 2.5.1 An analogy to nucleation

Motivated by the sensitivity of the channel function to the membrane characteristics demonstrated by the experiments of Perozo and coworkers [21] and by our own estimates of the membrane-protein interaction energy, we proposed a very simple model for the gating of mechanosensitive channels. This model harnessed the membrane-protein interaction energy as the spring that opposes tension and keeps the channel from opening spontaneously.

High sensitivity to membrane tension implies that the area change between the open and closed states ( $\Delta A$ ) is large. This large expansion during channel gating implies a significant restructuring of the membrane, since the interface with the protein has also significantly grown with the areal expansion of the channel. As we mentioned above, since the membrane must typically be deformed to accommodate the channel, these membrane-protein interactions act to stabilize the closed state of the channel. This interface energy is proportional to the length of the membrane-protein interface.

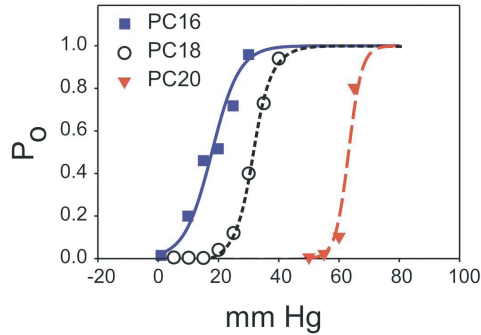


Figure 2.10: The MscL gating tension depends on the thickness of the lipid bilayer. In the plot above, the open-state probability of the channel is plotted as a function of the applied pressure difference over the bilayer for three different bilayers. The bilayer lipids are phosphatidylcholine with acyl chain lengths of 16, 18, and 20. It is assumed that the radius of curvature of the membrane patch, though unobserved, is constant and identical in each of these experiments. Under these assumptions the tension is proportional to the pressure difference over the membrane. This data therefore shows a dramatic rise in the gating tension (the tension at which  $\mathcal{P}_O = 0.5$ ) as a function of the bilayer thickness (acyl chain length). Figure from Ref. [21].

Energy contributions with this scale are generically called line tensions. To summarize, the channel experiences a competition between the tensile forces from membrane tension and compressive forces due to the line-tension induced by membrane-protein interaction.

An analogous competition occurs in the canonical nucleation problem. (When a small region of the nucleating phase forms, for example a precipitate in solution, there is a competition between a surface tension, which in turn scales as the area of the interface with solution ( $R^2$ ) that favors the decay of the precipitate, and a bulk term which scales like the volume ( $R^3$ ) that favors the growth of the precipitate.) Due to the difference in the radial dependence of these two competing energetic contributions, there is an energetic barrier to nucleation. Below a critical radius, the interface energy dominates and the radius of precipitate is unstable to decay. But once the precipitate reaches this critical radius, the bulk term dominates and the precipitate is unstable to further growth.

A similar competition exists for channel gating. The energetic contribution from the line tension scales as the interface size ( $R$ ) and the contribution due to the tension scales as the area ( $R^2$ ) of the channel. In the next chapter we will show that this nucleation picture can both describe many qualitative features of the channel function, for instance the short lifetime of the sub-states, as well as making quantitative predictions about the size of the opening tension and its dependence on the properties of the lipid bilayer, in agreement with recent experiments [21]. These calculations highlight the importance of membrane-protein interaction in describing the function of transmembrane proteins and in particular mechanosensitive proteins.

## 2.6 Summary of MscL Chapters

The next two chapters investigate the analogy between nucleation and channel gating, the membrane-protein interactions, and the function of the MscL protein. Chapter 3 is a short paper that focuses on results directly applied to the MscL protein. This chapter summarizes the most exciting results from an extensive framework developed for studying membrane-protein interactions. This framework, an effective elastic theory for membrane mechanics, builds upon the work of many other authors. To investigate mechanotransduction and the function of the MscL protein, we improved upon the existing models and summarized these general results applied to the MscL protein in a second paper which is reproduced in chapter 4. This Chapter is quite long and contains many detailed calculations, but also the analysis of some new experimental data.

# Bibliography

- [1] Owen P. Hamill and Boris Martinac. Molecular basis of mechanotransduction in living cells. *Physiol. Rev.*, 81(2):685–740, 2001. [3](#), [10](#), [13](#), [15](#)
- [2] Paul Blount and Paul C. Moe. Bacterial mechanosensitive channels: Integrating physiology, structure and function. *Trends in Microbiology*, 7(10):420–424, 1999. [10](#), [13](#), [14](#)
- [3] Derek Marsh. *CRC handbook of lipid bilayers*. CRC Press, Boca Raton, Fla., 1990. [11](#)
- [4] Bruce Alberts, Dennis Bray, Julian Lewis, Martin Raff, Keith Roberts, and James D. Watson. *Molecular Biology of the Cell*. Garland Publishing, New York, NY, 3rd edition, 1994. [1](#), [11](#), [12](#), [13](#), [16](#), [97](#), [98](#), [100](#), [101](#), [116](#), [167](#), [179](#)
- [5] Sol M. Gruner. Stability of lyotropic phases with curved interfaces. *J. Phys. Chem.*, 93:7562–7570, May 1989. [11](#)
- [6] Bertil Hill. *Ion Channels of Excitable Membranes*. Sinauer Associates, Inc., Sunderland, MA, 3rd edition, 2001. [11](#), [12](#), [13](#), [15](#), [16](#)
- [7] Peter G. Gillespie and Richard G. Walker. Molecular basis of mechanosensory transduction. *Nature*, 413(13):194–202, 2001. [12](#), [13](#)
- [8] David Boal. *Mechanics of the cell*. Cambridge University Press, Cambridge, UK, 2002. [12](#)
- [9] Jonathon Howard. *Mechanics of Motor Proteins and the Cytoskeleton*. Sinauer, 2001. [2](#), [12](#)
- [10] <http://www.wormbase.org/>. [12](#)
- [11] David P. Corey, Jaime Garcia-Anoveros, Jeffrey R Holt, Kelvin Y Kwan, Shuh-Yow Lin, Melissa A Vollrath, Andrea Amalfitano, Eunice L-M Cheung, Bruce H Derfler, Anne Duggan, Gwenaelle S G Geleoc, Paul A Gray, Matthew P Hoffman, Heidi L. Rehm, Daniel Tamasauskas, and Duan-Sun Zhang. TRPA1 is a candidate for the mechanosensitive transduction channel of vertebrate hair cells. *Nature*, 432(7018):723–30, 2004. [12](#)
- [12] K. Olbrich, W. Rawicz, D. Needham, and E. A. Evans. Water permeability and mechanical strength of polyunsaturated lipid bilayers. *Biophys J*, 79(1):321–7, 2000. [13](#), [18](#)

- [13] Eduardo Perozo and Douglas C. Rees. Structure and mechanism in prokaryotic mechanosensitive channels. *Curr Opin Struct Biol*, 13(4):432–42, 2003. [14](#), [19](#), [20](#)
- [14] S. I. Sukharev, W. J. Sigurdson, C. Kung, and F. Sachs. Energetic and spatial parameters for gating of the bacterial large conductance mechanosensitive channel, MscL. *J Gen Physiol*, 113(4):525–40, 1999. [17](#), [18](#)
- [15] Monica Betanzos, Chien-Sung Chiang, H. Robert Guy, and Sergei Sukharev. A large iris-like expansion of a mechanosensitive channel protein induced by membrane tension. *Nat Struct Biol*, 9(9):704–10, 2002. [19](#)
- [16] Eduardo Perozo, D. Marien Cortes, Pornthep Sompornpisut, Anna Kloda, and Boris Martinac. Open channel structure of MscL and the gating mechanism of mechanosensitive channels. *Nature*, 418(6901):942–8, 2002. [19](#)
- [17] G. Chang, R. H. Spencer, A. T. Lee, M T Barclay, and D. C. Rees. Structure of the MscL homolog from mycobacterium tuberculosis: A gated mechanosensitive ion channel. *Science*, 282(5397):2220–6, 1998. [19](#), [20](#)
- [18] Randal B. Bass, Pavel Strop, Margaret Barclay, and Douglas C. Rees. Crystal structure of escherichia coli MscS, a voltage-modulated and mechanosensitive channel. *Science*, 298(5598):1582–7, 2002. [19](#)
- [19] S. Sukharev, M. Betanzos, C. S. Chiang, and H. Robert Guy. The gating mechanism of the large mechanosensitive channel MscL. *Nature*, 409(6821):720–4, 2001. [19](#)
- [20] S. Sukharev, S. R. Durell, and H. Robert Guy. Structural models of the MscL gating mechanism. *Biophys J*, 81(2):917–36, 2001. [19](#)
- [21] Eduardo Perozo, Anna Kloda, D. Marien Cortes, and Boris Martinac. Physical principles underlying the transduction of bilayer deformation forces during mechanosensitive channel gating. *Nat Struct Biol*, 9(9):696–703, 2002. [20](#), [21](#)
- [22] W. Rawicz, K. C. Olbrich, T. McIntosh, D. Needham, and E. A. Evans. Effect of chain length and unsaturation on elasticity of lipid bilayers. *Biophys J*, 79(1):328–39, 2000. [20](#)

## Chapter 3

# Analytic models for mechanotransduction: gating a mechanosensitive channel

*This chapter is a reproduction of Ref. [1].*

Analytic estimates for the forces and free energy generated by bilayer deformation reveal a compelling and intuitive model for MscL channel gating analogous to the nucleation of a second phase. We argue that the competition between hydrophobic mismatch and tension results in a surprisingly rich story, which can provide both a quantitative comparison to measurements of opening tension for MscL when reconstituted in bilayers of different thickness and qualitative insights into the function of the MscL channel and other transmembrane proteins.

### 3.1 Introduction

The mechanosensitive channel (MscL) is a compelling example of the interaction between a protein and the surrounding bilayer membrane. The channel is gated mechanically by applied tension and is believed to function as an emergency relief valve in bacteria [2]. MscL is a member of a growing class of proteins that have been determined to be mechanosensitive [3], [4]. The dependence of the conductance on applied tension has been studied extensively in patch clamp experiments [5], [6], [7]. In terms of the observed conductance, these studies have revealed that the channel is very nearly a two state system. MscL spends the vast majority of its life in either a closed state (C) or an open state (O) characterized by a discrete conductance. When the bilayer tension is small, the protein is exclusively in the closed configuration. As the tension grows, the open state becomes ever more prevalent, until it dominates at high tension. The simplest structural interpretation of this conductance data is to assume that each discrete conductance corresponds to a well defined channel conformation. This assumption seems to be compatible with the conductance data. Patch clamp experiments have also revealed that there are at least three additional discrete, intermediate

conductance levels [5] suggesting three additional short lived substates (S1-S3). Rees and coworkers [8] have solved the structure for one conformation that appears to be the open state [7], [8] using X-ray crystallography. MscL has also been trapped in the open state [9],[7]. Betanzos *et al.* [9] have probed the open-state structure using disulfide crosslinking while Perozo *et al.* [7] have used electron paramagnetic resonance spectroscopy (EPR) and site-directed spin labeling (SDSL) to deduce its geometry. Sukharev *et al.* [10] have also proposed an open state conformation based on structural considerations.

The conformational landscape of the MscL channel is extremely complex, depending on a huge number of microscopic degrees of freedom which are analytically intractable. Even from the standpoint of numerical calculations, this number is still very large [11]. As an alternative to a detailed microscopic picture of MscL, we consider a simplified free energy function where we divide the free energy of the system into two contributions, namely,

$$G = G_P + G_{\mathcal{M}}, \tag{3.1}$$

where  $G_P$  is the free energy associated with the conformation of the protein and  $G_{\mathcal{M}}$  is the deformation free energy from the bulk of the bilayer [12]. In general, these two terms are coupled. The conformation of the protein depends on the forces applied by the bilayer. The bilayer deformation is induced by the external geometry of the protein. We denote this external geometry with a state vector,  $X$ , which captures the radius of the channel as well as its orientation relative to the surrounding bilayer as described in more detail below. We calculate the induced bilayer deformation energy,  $G_{\mathcal{M}}(X)$ , by minimizing the free energy of the bilayer and solving the resulting boundary value problem using an analytic model developed for the study of bilayer mechanics [13] and protein-bilayer interactions [12], [14], [15], [16]. We then apply asymptotic approximations to the exact solutions of this model for cylindrically symmetric inclusions, permitting all of the results to be expressed, estimated, and understood with simple scaling relations. The advantage of this model is that it permits us to characterize the protein-bilayer system in a way that is at once analytically tractable and predictive. There is a wealth of useful, physical intuition to be gleaned from this model relating to both the function of MscL and more generally that of mechanosensitive transmembrane proteins. In a forthcoming paper, we will show that the mechanics of the bilayer must play an integral role in mechanotransduction and channel function. Specifically, we will present detailed analytic estimates of the free energy generated by bilayer deformation induced by the channel and show that these free energies are of the same order as the free energy differences measured by Sukharev *et al.* [5]. These analytic calculations reveal a compelling and intuitive model for the gating of the MscL channel which is the subject of this current paper. The competition between hydrophobic mismatch and applied tension, in the presence of radial constraints, generates a bistable system that is implicitly a

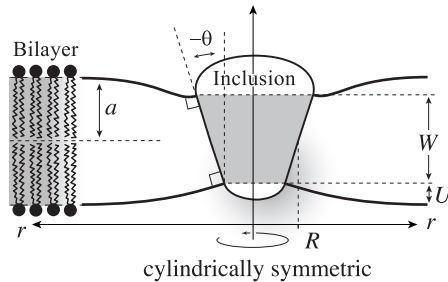


Figure 3.1: The bilayer-inclusion model. The geometry of the inclusion is described by three parameters: the radius,  $R$ , the hydrophobic thickness,  $W$ , and the radial mid-plane slope,  $H'$ . The hydrophobic mismatch,  $2U$ , is the difference between the hydrophobic protein thickness,  $W$ , and the bilayer equilibrium thickness,  $2a$ . We assume the surfaces of the bilayer are locally normal to the interface of the inclusion, as depicted above, implying that the mid-plane slope is related to the interface angle:  $H' = \tan \theta$ .

mechanosensitive channel. Furthermore, this simple model provides a picture, which is both qualitatively and quantitatively consonant with the measured dependence of the free energy on acyl chain length as observed by Perozo *et al.* [6]. In addition, these results may also explain the stabilization of the open state by spontaneous-curvature-inducing lysophospholipids observed by Perozo *et al.* [6], although more experiments are required to check the consistency of this proposal.

## 3.2 The energy landscape of the bilayer

In the calculations considered here, the geometry of the protein, characterized by the conformational state vector  $X$ , is described by three geometrical parameters  $X = (R, W, H')$ , where  $R$  is the radius of the channel,  $W$  is the hydrophobic thickness, and  $H'$  is the mid-plane slope. See Fig. 4.2.1 for details. Although we have parameterized the conformation space of the protein with these three parameters, in this paper, we will focus on the radial dependence alone, claiming that even in this reduced description, the model provides a rich variety of predictions that are compatible with previous observation and suggest new experiments. The radial dependence of the bilayer deformation energy is particularly important for MscL since the radius undergoes a very large change between the open and closed states [10]. The bilayer deformation energy<sup>1</sup> can be written explicitly in terms of the channel radius as

$$G_{\mathcal{M}} = G_0 + f \cdot 2\pi R - \alpha \cdot \pi R^2, \quad (3.2)$$

where  $G_0$  and  $f$  do not explicitly depend on  $R$  and  $\alpha$  is the applied tension which triggers channel gating.  $G_0$  is a radially-independent contribution to the deformation energy which is a function of the other geometrical parameters of the protein. Its importance in gating the channel is most likely

<sup>1</sup>This energy is derived in the Appendix.

secondary since it is independent of  $R$  and it will be ignored in the remainder of the discussion. The dependence of bilayer deformation energy on applied tension can be explained intuitively [4]. The free energy contribution for a small change in the channel area due to the applied tension can be written  $-\alpha dA$ , which is the two dimensional analogue of the  $-PdV$  term for a gas in three dimensions. At high enough applied tension, the state with the largest inclusion area will have the lowest free energy.

The line tension,  $f$ , contributes an energy proportional to the circumference and is a natural consequence of the interface between two different materials. The radial dependence of line tension is linear since the size of this interface is proportional to the circumference. In what follows, we will discuss the two dominant contributions to this line tension: thickness deformation [12], [14], [15] and spontaneous curvature [16]. Though we note that we have treated a wide variety of other contributions to be discussed elsewhere. The thickness deformation free energy is induced by the mismatch between the the equilibrium thickness of the bilayer and the hydrophobic thickness of the protein. The importance of this hydrophobic mismatch in the function of transmembrane proteins has already been established [17]. The bilayer deforms locally to reduce the mismatch with the protein as shown in Fig. 4.2.1. Symbolically, the thickness deformation energy is [12],

$$G_U = f_U \cdot 2\pi R = \frac{1}{2}\mathcal{K}U^2 \cdot 2\pi R, \quad (3.3)$$

where  $\mathcal{K} = 2 \times 10^{-2} kT \text{ \AA}^{-3}$  is an effective elastic modulus defined in the on-line supporting material and is roughly independent of acyl chain length and  $U$  is half the hydrophobic mismatch as defined in Fig. 4.2.1. Naturally the energetic penalty for this deformation is proportional to the mismatch squared since the minimum energy state corresponds to zero mismatch. The area of that part of the bilayer which is deformed is roughly equal to the circumference of the channel times an elastic decay length. As a result, the contribution of thickness deformation to the total free energy budget scales with the radial dimension of the channel. We also note that the thickness deformation free energy is always positive.

In contrast, the free energy induced by spontaneous curvature can be either negative or positive. Physically, this free energy comes from locally relieving or increasing the curvature stress generated by lipids or surfactants that induce spontaneous curvature [16], [18], [19]. Again the radial dependence of this free energy will be linear since the effect is localized around the interface. Since the leaflets of the bilayer can be doped independently [6], the spontaneous curvatures of the top and bottom leaflets,  $C_{\pm}$ , can be different. It is convenient to work in terms of the composite spontaneous curvature of the bilayer,  $C \equiv \frac{1}{2}(C_+ - C_-)$ . The contribution to the deformation energy arising from

spontaneous curvature is given by [16]

$$G_C = f_C \cdot 2\pi R = K_B C H' \cdot 2\pi R, \quad (3.4)$$

where  $H'$  is the mid-plane slope and  $K_B = 20(a/20 \text{ \AA})^3 kT$ , is the bending modulus, which roughly scales as the third power of the bilayer thickness. We will discuss these results in more detail elsewhere. Notice that if  $C$  and  $H'$  have opposite signs, the deformation energy and the corresponding line tension,  $f_C$ , will be negative. We note that the elastic theory of membrane deformations associated with proteins like MscL permit other terms (such as mid-plane deformation, for example), that can be treated within the same framework and which give rise to the same radial dependence as that described here. However, for the purpose of characterizing the energetics of MscL, these other terms are less important than the two considered here.

Typically, in the absence of large spontaneous curvature, the line tension,  $f$ , will be dominated by the mismatch and will be positive. A potential of the form described by equation 3.2 is depicted schematically in Fig. 3.2. In this figure, we have implied that there are steric constraints for the range of radii accessible to the protein. Assuming that there is a lower bound on the radius of the inclusion is very natural. It can be understood as the radius below which the residues begin to overlap. This steric constraint will generate a hard wall in the protein conformation energy, forbidding lower radii. Similar, but slightly more elaborate arguments can be made for an upper bound. The bilayer deformation energy generates a barrier between small radius and large radius states. The location of the peak of this barrier is the turning point  $R_* \equiv f/\alpha$ . At small tension, the turning point is very large and is irrelevant since it occurs at a radius not attainable by the channel due to the steric constraints, but as the tension increases the position of the turning point decreases. This behavior is reminiscent of the competition between surface tension and energy density for nucleation processes which give rise to a similar barrier (*e.g.*, [20]).

Although the conformational landscape of the MscL channel is certainly very complicated, there is an intriguing possibility that the channel harnesses the elastic properties of the bilayer, which quite naturally provide the properties we desire in a mechanosensitive channel: a stable closed state at low tension and a stable open state at high tension. In effect, we will treat the bilayer deformation energy as an external potential with respect to the conformational energy landscape of the protein. The physical effects of the radial dependence of the bilayer deformation energy on the inclusion conformation can be recast in a more intuitive form by appealing to the induced tension, which accounts not only for the applied far field tension, but also for *induced* tension terms due to bilayer deformation. The applied tension is not the whole story! The generalized forces are obtained by differentiating the bilayer deformation energy with respect to bilayer excursions. The net tension

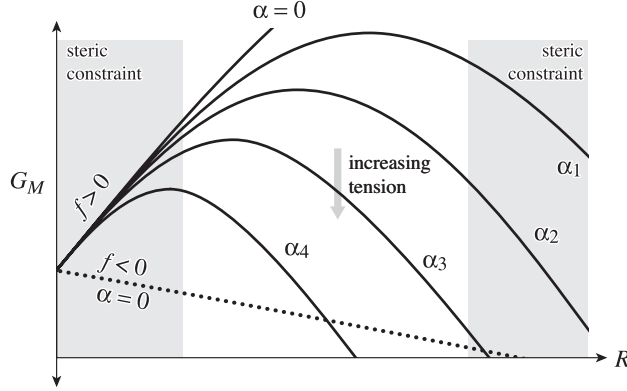


Figure 3.2: The bilayer deformation energy landscape. The bilayer deformation energy is plotted as a function of the radius for different values of applied tension. The solid curves represent the bilayer deformation energy with a positive line tension,  $f$ , for various different tensions ( $0 < \alpha_1 < \alpha_2 < \alpha_3 < \alpha_4$ ). The competition between interface energy and applied tension naturally gives rise to a bistable potential when the radial domain is limited by steric constraints. The gray regions represent radii inaccessible to the channel due to steric constraints. These constraints are briefly motivated in Sect. 3.2. If the line tension is negative, depicted by the dotted curve, the potential is never bistable.

induced by the bilayer on the inclusion interface is

$$\alpha_\Sigma = \alpha - \frac{f}{R}, \quad (3.5)$$

where we have denoted the net tension  $\alpha_\Sigma$  since we have already used  $\alpha$  to denote the applied tension. For radii smaller than the turning point,  $R_*$ , the bilayer deformation energy is an increasing function of radius and therefore the net tension is negative and acts to compress the channel. For radii larger than that at the turning point, the bilayer deformation energy is a decreasing function of radius and the net tension is positive and acts to expand the channel. The combination of these constraints and the bilayer deformation energy lead to a bistable system where the closed and open states correspond to the constraint-induced radial minimum and maximum, respectively. Recall that the net tension on the closed state will be compressive as long as its radius is smaller than that at the turning point, namely,  $R_C < R_*$ . This inequality defines the range of applied tension over which the closed state is stabilized by the bilayer deformation energy. The net tension on the open state will be expansive as long as its radius is greater than that at the turning point:  $R_O > R_*$ . This inequality defines the range of applied tension over which the open state is stabilized by the bilayer deformation energy. There is an intermediate range of tensions for which both states are stabilized by the bilayer,  $f/R_O < \alpha < f/R_C$ . The bilayer deformation energy naturally destabilizes the open state for applied tension below this range while stabilizing the closed state for applied tensions up to

the limit of this range. Both effects help to prevent the channel from leaking at low applied tension. This bistability is precisely the desirable behavior for a mechanosensitive channel designed to relieve internal pressure and yet surprisingly little is required from the protein conformational landscape,  $G_P$ , except for steric constraints which arise very naturally. In Fig. 3.2, we have depicted the way in which MscL mimics this mechanical analogue by using the sum of a schematic protein energy and the bilayer deformation energy to form energy minima corresponding to the open and closed states.

Our discussion of the role of the bilayer enables us to make some rather general observations about the nature of the substates. In order to generate a substate, we assume that there is more than one gating transition in the protein conformational energy. One gating transition would correspond to a closed to open transition. An additional gating transition allows three conductance states. We will assume that these transitions are themselves bistable in nature since the conductance data would seem to imply the lifetimes of the transition states are very short compared to the conductance states [5]. In other words, the conformational gating transition occurs near a local maximum in the conformational free energy. If we add two such transitions to  $G_P$ , we generate a substate of intermediate radius between these two transition state radii. A schematic example of this is illustrated in Fig. 3.2. Sukharev *et al.* [5] have shown that all the substates are short lived and have estimated the areas of each state based on the tension dependence of their free energies.<sup>2</sup> Specifically, they have shown that the radii of the substates lie between the open and closed state radii. If the bilayer deformation dominates the free energy of the states, the ephemeral nature of the substates is a natural consequence of their intermediate radii. The compressive tension due to the mismatch stabilizes the state of lowest radius at low applied tension. At high applied tension the bilayer stabilizes the state with highest radius. All the states with intermediate radii are never stabilized by the bilayer and are therefore short lived. Our deceptively simple mismatch model quite naturally leads to short lived substates at intermediate radii.

### 3.3 Results

The patch clamp experiments of Perozo *et al.* [6] go beyond the earlier work of Sukharev *et al.* [5] by providing experimental values for the free energy difference between the open and closed states for bilayers of several thicknesses. These results can be compared with our predictions. In order to apply our model, we must determine the geometrical parameters of the state vector  $X$  for the open and closed states and in particular the open and closed radii. The radius of the closed state is known from X-ray crystallography [8]:  $R_C \sim 23 \text{ \AA}$ . Structural studies [10] and EPR and SDSL [7] experiments have suggested an open state radius of roughly  $R_O \sim 35 \text{ \AA}$ . In order to estimate the line tension and free energy generated by hydrophobic mismatch, we must determine

---

<sup>2</sup>There is now evidence for additional substates [21].

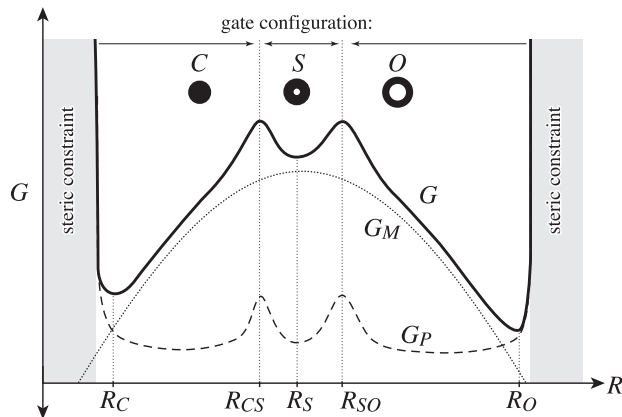


Figure 3.3: The total free energy. The total free energy,  $G$ , of the protein and bilayer are plotted schematically as a function of channel radius. The bilayer deformation energy,  $G_M$ , is represented by the dotted curve. A schematic protein conformational energy is represented by the dashed curve. Their sum gives the total free energy  $G$ . The protein energy has been chosen to contain a single substate,  $S$ . There is a conformational energy barrier corresponding to changing the gate conformation of the channel. These transitions occur at  $R_{CS}$  and  $R_{SO}$ .  $G_P$  also contains steep barriers corresponding to steric constraints. The radii of the conductance states are defined by the free energy minima of  $G$ .

the hydrophobic thickness  $W$ . (We ignore the difference in hydrophobic thickness between the open and closed states.) In principle, one might have thought this could be deduced from the atomic-level structure of MscL, but in practice, real structures are complicated, often lacking a clear transition from hydrophobic to hydrophilic residues on the interface. However, this width may be deduced from the EPR and SDSL data of Perozo *et al.* [6]. EPR and SDSL experiments measure inter-subunit proximity and spin-label mobility, respectively [6]. Compressive tension in the bilayer suppresses the fluctuations of the protein, increasing the subunit proximity and reducing the spin label mobility. In the experiments of Perozo *et al.* [6], the applied tension is low implying that the net tension is dominated by the line tension, induced by thickness deformation ( $\alpha_\Sigma \sim -\mathcal{K}U^2/2R$ ), in the absence of spontaneous curvature. This tension is compressive and proportional to the mismatch squared. Therefore, when the mismatch is zero, the tension reaches a minimum, implying that mobility and subunit separation should reach a maximum. The EPR and SDSL data of Perozo *et al.* [6] may turn over for PC12 bilayers, implying that the mismatch is zero, which would imply in turn that  $W \sim 2a_{n=12}$ . But due to the quadratic dependence on  $U$ , the slope in the vicinity of the turnover is small. Since PC lipids with acyl chain length shorter than  $n = 10$  do not form stable bilayers [6], it is difficult to extensively check the quadratic dependence on  $U$ . The predicted turnover would be more pronounced for PC bilayers with  $n < 10$ . We shall see that this deduced hydrophobic mismatch is compatible with the patch clamp measurements of Perozo *et al.* [6]. However, the interpretation of this EPR data becomes more complicated when the thickness of the channel changes between the

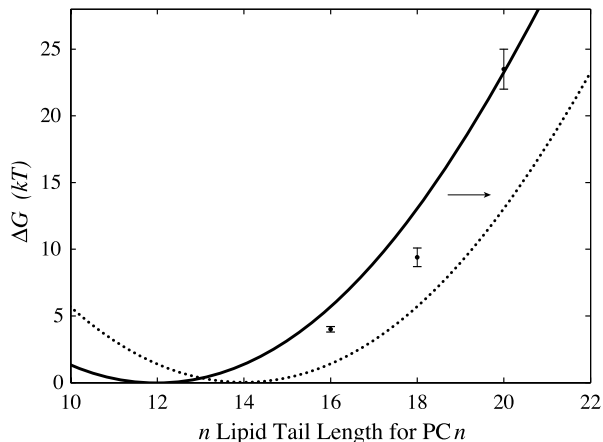


Figure 3.4: Free energy difference between open and closed states vs lipid acyl chain length. The experimental data of Perozo *et al.* [6] for the free energy difference between the open and closed states at zero tension,  $\Delta G_0$ , is plotted with black circles and error bars. The solid curve represents the theoretical values for the bilayer deformation energy generated by a simple thickness deformation model at zero tension,  $\Delta G_{0,\mathcal{M}}$ . The dotted curve represents the translated  $\Delta G_{0,\mathcal{M}}$  for an engineered MscL channel with a hydrophobic thickness matching a PC14 bilayer.

open and the closed state as discussed in section 3.4.

Perozo *et al.* [6] have measured  $\Delta G_0$ , the free energy difference between the open and closed state at zero tension<sup>3</sup> for three acyl chain lengths. Using the value we have deduced for  $W$ , we can now calculate the free energy difference between the open and closed states due to bilayer deformation at zero tension,  $\Delta G_{0,\mathcal{M}}$ , which is given by the line tension contribution alone as  $\Delta G_{0,\mathcal{M}} = f2\pi\Delta R \rightarrow f_U2\pi\Delta R$ , where  $\Delta R$  is the difference between the open and closed radii. The theoretical result,  $\Delta G_{0,\mathcal{M}}$ , is plotted with the experimental measurements of  $\Delta G_0$  in Fig. 3.3. The agreement between experiment and theory is embarrassingly good given the simple fashion in which we have chosen the geometrical parameters and that we have neglected the protein conformational energy,  $G_P$ , entirely. There is a very important point to be made about these results. Perozo *et al.* [6] have measured three data points and our model is quadratic, implying that we could have chosen the parameters of our model to fit the data points perfectly since any three points lie on a parabola, but our parameters have in fact been deduced independently rather than fit, which is why this correspondence with the data is remarkable. This model corresponds to a channel where the free energy difference between the open and closed states is dominated by the bilayer deformation rather than protein conformation. Our model implies that  $\Delta G_0$  for PC10, PC12, and PC14 should be very small. Unfortunately, these bilayers have proved too weak for patch-clamp measurements of  $\Delta G_0$  [6]. Certainly none of these bilayers trap the channel in the open state [6].

<sup>3</sup>The free energy measured by Perozo *et al.* [6] is equivalent to the free energy at zero tension modulo several assumptions [4].

The opening tension is defined as the tension at which the open and closed state probabilities are equal or, analogously, the tension at which the free energies of the open and closed states are equal. The opening tension is

$$\alpha_{1/2} = \frac{f}{\bar{R}} + \frac{\Delta G_P}{\Delta A}, \quad (3.6)$$

where  $\bar{R} \equiv \frac{1}{2}(R_C + R_O)$  is the mean radius,  $\Delta G_P$  is the difference in the open and closed state protein conformation energy, and  $\Delta A$  is the difference in open and closed state area. When the bilayer deformation energy dominates, the opening tension is determined by the first term alone. Changing the sensitivity of the channel is straightforward from this perspective. Changes in the length of the hydrophobic region of the protein can increase or decrease the opening tension of the channel. For example, MscL channels might be engineered with an expanded hydrophobic region which matches PC14 bilayers. Our mismatch based theory would predict that the free energy versus acyl chain length curve would simply be translated to higher  $n$  so that the minimum  $\Delta G_{0,\mathcal{M}}$  is realized for a PC14 bilayer. This shift should be measurable, reducing  $\Delta G_0$  for PC16, PC18, and PC20 bilayers. The reduction in mismatch may also allow MscL to be reconstituted into PC22 bilayers, allowing an additional data point. The proposed shift should also be measurable in EPR and SDSL measurements of residue proximity and mobility. The maximum mobility and separation should now be centered around  $n = 14$ , perhaps permitting a clear measurement of the rise in induced tension for a PC10 bilayer predicted by the quadratic dependence of the line tension on the mismatch.

Perozo *et al.* [6] have proposed that asymmetric bilayer stresses play a central role in MscL gating. They have proposed this model based on patch clamp, EPR, and SDSL experiments showing that spontaneous curvature can induce MscL channel opening. Specifically, they find that MscL reconstituted into PC vesicles with high enough concentrations of asymmetrically incorporated LPC stabilizes the open state of the channel, while MscL reconstituted into PC vesicles with symmetrically incorporated LPC, does not stabilize the open state. Unlike Keller *et al.* [22], Perozo *et al.* have measured neither the spontaneous curvature for the mixed bilayer nor the free energy difference between open and closed states as a function of LPC concentration. In the absence of these quantitative experimental results, it is difficult to make concrete comparisons between our model and the experimental data. For large spontaneous curvature [22] but a relatively modest complementary mid-plane slope, the free energy difference between the two states due to spontaneous curvature is

$$\Delta G_C \sim 2\pi(R_O - R_C)K_B C H' = -16 \left( \frac{20 \text{ \AA}}{C^{-1}} \right) \left( \frac{H'}{-0.2} \right) kT, \quad (3.7)$$

an energy typically large enough to stabilize the open state. In section 3.2, we have made some rather general arguments about the shape of the bilayer deformation energy landscape. We now return to this picture briefly to discuss the consequences of spontaneous curvature. In our discussion, we

assumed that the line tension,  $f$ , was typically positive, but we remarked that this need not be the case in the presence of large spontaneous curvature. If  $f$  is negative, as depicted by the dotted curve in Fig. 3.2, the only state stabilized by the bilayer is the open state, which very naturally gives rise to the open state stabilization observed by Perozo *et al.* [6]. Alternatively, this result can be understood from the predicted opening tension in equation 3.6. When  $\Delta G_0$  is bilayer deformation dominated, a negative  $f$  implies that the opening tension is itself negative! A compressive force is required to stabilize the closed state. This argument gives a tantalizingly simple explanation for the open state stabilization but in the absence of measured values for the spontaneous curvature induced by LPC, we can only conclude that spontaneous curvature could stabilize the open states for rather generic values of the parameters. An experimental consistency check of these results is fairly simple. Perozo *et al.* have incorporated LPC asymmetrically. The same experiment might be repeated with  $H_{II}$  phase inducing lipids which can also be used to generate spontaneous curvature but of the opposite sign. For the DOPC/DOPE system of Keller *et al.* [22], the spontaneous curvature is known and tunable as a function of concentration. Our results predict that  $\Delta G_0$  should be linear in  $C$  [16] and compatible with equation 4.3.3.

In the argument above, we focused on the radial dependence of bilayer deformation free energy, and fixed the other components of the state vector,  $X$ . In principle, there is a potentially important piece of radial dependence we are missing. The internal conformation may effectively couple the radius to the other parameters in the state vector  $X$ , adding additional implicit radial dependence. For example, the thickness of the inclusion,  $W$ , is almost certainly a function of radius. It is also very natural to couple the mid-plane slope to the radius. We have ignored these dependences in order to develop an intuitive and simple one dimensional picture with as few undetermined constants and couplings as possible. Provided that the bilayer deformation energy change is dominated by the radial change, this simplified model is a useful tool for understanding the bilayer-inclusion interaction. More elaborate models might easily be built from the general analytic framework we have constructed. This framework will be described in a forthcoming paper.

### 3.4 Discussion

We have argued that the bilayer deformation energy is harnessed by MscL to govern channel gating. Indeed, we have shown that a model which attributes the entire free energy difference between the open and closed states to the bilayer deformation energy is compatible with the experimental data. These results are somewhat surprising since it has been shown experimentally that the mutation of a single residue in the vicinity of the channel gate, can significantly effect channel gating [23], [24]. The protein conformational energy cannot be neglected in general. In fact, we have assumed that the protein conformational energy is large enough to constrain the channel geometry since we

have assumed it is the bilayer that deforms rather than the protein. In principle, the closed state could have been stabilized by protein conformation alone, rather than mismatch, but exploiting bilayer deformation provides a robust mechanism for mechanotransduction, a design principle which functions in spite of the enormous number of nearly degenerate microstates endemic to proteins. Even for proteins as simple as myoglobin, Frauenfelder *et al.* [25] have shown that the macroscopic conformation corresponds to an enormous number of structurally distinct microstates. These ideas have already been exploited for channel proteins. Goychuk and Hänggi [26] have used this degenerate landscape to derive the empirical rate law for voltage gated channels. In light of these results, it is very natural to suppose that the protein conformational energy of the MscL protein gives rise to a vast number of nearly degenerate states as well. The bilayer deformation energy naturally breaks this degeneracy and forms a mechanotransducing channel. The ensemble of microstates we observe as the closed states is stabilized at low applied tension by the line tension, while the ensemble of microstates we observe as the open state is stabilized by high applied tension. The importance of bilayer deformation in mechanotransduction may help to explain why there are no obvious sequence motifs associated with mechanosensitivity [27] since a mismatch requirement does not imply sequence specificity. Harnessing bilayer elasticity does have one noted disadvantage. The gating of a channel will be affected by the membrane environment that surrounds it. This is precisely what the experiments of Perozo *et al.* [6] have shown. In realistic cell membranes there is an enormous diversity of proteins and lipids which would imply that the free energy, and therefore opening tension, in these membranes would be heterogeneous. Sukharev and co workers [21] have evidence for exactly this variability for MscL in giant spheroplasts.

The reader may be concerned that we are attempting to invalidate the structural models of Betanzos *et al.* [9], Sukharev *et al.* [10], Perozo *et al.* [7], and other investigators of the MscL channel. This could not be further from the truth. Indeed much of the input to our model comes from these investigations. Our aim is rather to model the *physical principles* [6] that have been proposed with a simple, self-consistent model for channel membrane interaction. An objection to our model as proposed above is that we fail to account for the change in the hydrophobic thickness from closed to open-state. Indeed, it is difficult to envision a consistent atomic-scale model where the thickness of the channel is not reduced as the radius is increased. Furthermore, data from Betanzos *et al.* [9], Perozo *et al.* [7], and new data from Powl *et al.* [28] suggest that this added complexity is probably more experimentally accurate. Although these more detailed considerations complicate the story theoretically, in a forthcoming paper we will show that they do not significantly change the energetic results of the model. The failure of our model to predict the same zero mismatch lipid length for the closed-state as Powl *et al.* [28] is a consequence of the choice of one channel thickness for both states. The price of the clarity and simplicity of our coarse-grained model is an insensitivity to the degrees of freedom we ignore. For the sake of brevity in this short paper, we

have focused on the physical mechanism we believe to be most essential to understanding the MscL channel mechanics.

The correspondence between our simple theoretical model for the gating of the MscL channel and experiment is at least strongly suggestive that this mechanism is exploited by the MscL channel. Our model can also naturally explain the stabilization of the open state by LPC [6] as well as the ephemeral nature of the substates [5]. The tractable nature and simplicity of the model allow extensive analytic calculations to be made, which have in turn lead to numerous experimental predictions, discussed in section 3.3. Specifically we have predicted (i) a shift in the curve relating the free energy difference and acyl chain length when the hydrophobic thickness of the channel is altered and (ii) the dependence of the free energy on spontaneous curvature and, in particular, on the concentration of spontaneous curvature-inducing molecules.

We have developed an extensive framework for studying bilayer-inclusion interactions in the MscL system. The model we have discussed here is the simplest implementation of these results and a more thorough description of the model will appear in a future paper. There are several very natural extensions to the current work. For example, we have focused here on the radial dependence only, but, as we have briefly alluded to in section 3.3, there are two additional geometric parameters which may also play important roles in the function of the MscL channel. More detailed measurements of the rates and free energies of the various states will no doubt prove our simplified model incomplete and provide motivation and insight into a more detailed model of channel gating. The simplicity and generality of the competition between applied tension and a line tension, regardless of its source, suggests that it may be a quite general phenomena for mechanotransduction. We hope to apply similar ideas to other mechanosensitive systems. More generally, we are also intrigued by the possibility of finding analogous bilayer deformation driven conformational changes for other transmembrane proteins that do not exhibit mechanosensitive function, perhaps illuminating a more general qualitative design principle for the function of transmembrane proteins.

# Bibliography

- [1] Paul A. Wiggins and Rob Phillips. Analytic models for mechanotransduction: Gating a mechanosensitive channel. *Proc. Nat. Acad. Sci. USA*, 101:4071–4076, 2004. [25](#)
- [2] P. Blount and P. C. Moe. Bacterial mechanosensitive channels: Integrating physiology, structure and function. *Trends. Microbiol.*, 7:420–424, 1999. [25](#)
- [3] P.G. Gillespie and R.G. Walker. Molecular basis of mechanosensory transduction. *Nature*, 413:194–202, 2001. [25](#)
- [4] Owen P. Hamill and Boris Martinac. Molecular basis of mechanotransduction in living cells. *Physiol. Rev.*, 81(2):685–740, 2001. [25](#), [28](#), [33](#)
- [5] S. I. Sukharev, W. J. Sigurdson, C. Kung, and F. Sachs. Energetic and spatial parameters for gating of the bacterial large conductance mechanosensitive channel, MscL. *J Gen Physiol*, 113(4):525–40, 1999. [25](#), [26](#), [31](#), [37](#)
- [6] Eduardo Perozo, Anna Kloda, D. Marien Cortes, and Boris Martinac. Physical principles underlying the transduction of bilayer deformation forces during mechanosensitive channel gating. *Nat Struct Biol*, 9(9):696–703, 2002. [25](#), [27](#), [28](#), [31](#), [32](#), [33](#), [34](#), [35](#), [36](#), [37](#)
- [7] Eduardo Perozo, D. Marien Cortes, Pornthep Sompornpisut, Anna Kloda, and Boris Martinac. Open channel structure of MscL and the gating mechanism of mechanosensitive channels. *Nature*, 418(6901):942–8, 2002. [25](#), [26](#), [31](#), [36](#)
- [8] G. Chang, R. H. Spencer, A. T. Lee, M. T. Barclay, and D. C. Rees. Structure of the mscl homolog from mycobacterium tuberculosis: A gated mechanosensitive ion channel. *Science*, 282(5397):2220–6, 1998. [26](#), [31](#)
- [9] Monica Betanzos, Chien-Sung Chiang, H. Robert Guy, and Sergei Sukharev. A large iris-like expansion of a mechanosensitive channel protein induced by membrane tension. *Nat Struct Biol*, 9(9):704–10, 2002. [26](#), [36](#)
- [10] S. Sukharev, S. R. Durell, and H. Robert Guy. Structural models of the MscL gating mechanism. *Biophys J*, 81(2):917–36, 2001. [26](#), [27](#), [31](#), [36](#)

- [11] J. Gullingsrud and K. Schulten. Gating of MscL studied by steered molecular dynamics. *Biophys. J.*, 85:2087–2099, 2003. [26](#)
- [12] H. W. Huang. Deformation free energy of bilayer membrane and its effect on gramicidin channel lifetime. *Biophys. J.*, 50:1061–1070, 1986. [26](#), [28](#), [42](#)
- [13] W. Helfrich. Elastic properties of lipid bilayers: Theory and possible experiments. *Z Naturforsch [C]*, 28(11):693–703, 1973. [26](#), [41](#)
- [14] C. Nielsen, M. Goulian, and O. Andersen. Energetics of inclusion-induced bilayer deformations. *Biophys. J.*, 74:1966–1983, 1998. [26](#), [28](#)
- [15] M. Goulian, O.N. Mesquita, D.K. Fygenson, C. Nielsen, O.S. Andersen, and A. Libchaber. Gramicidin channel kinetics under tension. *Biophys. J.*, 74:3280–337, 1998. [26](#), [28](#), [42](#)
- [16] N. Dan and S.A. Safran. Effect of lipid characteristics on the structure of transmembrane proteins. *Biophys. J.*, 75:1410–1414, 1998. [26](#), [28](#), [29](#), [35](#), [42](#)
- [17] J. A. Killian. Hydrophobic mismatch between proteins and lipids in membranes. *Biochimica et Biophysica Acta*, 1376:401–416, 1998. [28](#)
- [18] J. N. Israelachvili. *Intermolecular and Surface Forces*. Academic Press, London, 2nd edition, 1991. [28](#)
- [19] Sol M. Gruner. Stability of lyotropic phases with curved interfaces. *J. Phys. Chem.*, 93:7562–7570, May 1989. [28](#)
- [20] C. Kittel and H. Kroemer. *Thermal Physics*. W.H. Freeman and Company, New York, 2nd edition, 1980. [29](#)
- [21] Chien-Sung Chiang, Andriy Anishkin, and Sergei Sukharev. Gating of the large mechanosensitive channel in situ: estimation of the spatial scale of the transition from channel population responses. *Biophys. J.*, 86(5):2846–61, 2004. [31](#), [36](#)
- [22] S. L. Keller, S. M. Bezrukov, S. M. Gruner, M. W. Tate, and I. Vodyanoy. Probability of alamethicin conductance states varies with nonlamellar tendency of bilayer phospholipids. *Biophys. J.*, 65:23–27, 1993. [34](#), [35](#)
- [23] X. Ou, P. Blount, R. J. Hoffman, and C. Kung. One face of a transmembrane helix is crucial in mechanosensitive channel gating. *Proceeding of the National Academy of Science USA*, 95:11471–11475, 1998. [35](#)

- [24] K. Yoshimura, A. Batiza, M. Schroeder, P. Blount, and C. Kung. Hydrophilicity of a single residue within MscL correlates with increased channel mechanosensitivity. *Biophys. J.*, 77:1960–1972, 1999. 35
- [25] H. Frauenfelder, S.G. Sligar, and P.G. Wolynes. The energy landscapes and motions of proteins. *Science*, 254:1598–1603, 1991. 36
- [26] I. Goychuk and P. Hänggi. Ion channel gating: A first-passage time analysis of the kramers type. *Proc. Natl. Acad. Sci. USA*, 99:3552–3556, 2002. 36
- [27] P. Strop, R. Bass, and D. C. Rees. Prokaryotic mechanosensitive channels. *Adv. Prot. Chem.*, 63:177–209, 2003. 36
- [28] Andrew M. Powl, J. Malcolm East, and Anthony G. Lee. Lipid-protein interactions studied by introduction of a tryptophan residue: the mechanosensitive channel MscL. *Biochemistry*, 42(48):14306–17, 2003. 36
- [29] W. Rawicz, K. C. Olbrich, T. McIntosh, D. Needham, and E. A. Evans. Effect of chain length and unsaturation on elasticity of lipid bilayers. *Biophys. J.*, 79(328–339), 2000. 41

### 3.5 Acknowledgments

We are grateful to Doug Rees, Tom Powers, Jané Kondev, Klaus Schulten, Evan Evans, Sergei Sukharev, Eduardo Perozo, Olaf Andersen, Sylvio May, Ben Freund, Mandar Inamdar, and the anonymous referee for useful discussions, suggestions, and corrections. We also acknowledge support from the Keck Foundation, NSF grant CMS-0301657 and the NSF funded Center for Integrative Multiscale Modeling and Simulation. PAW acknowledges support through an NSF fellowship.

### 3.6 Appendix: Lipids

When discussing the lipids used by other authors, we have used the same naming convention they employed: 10:0 dicaproyl-phosphatidylcholine (PC10), 12:0 dilauroyl-phosphatidylcholine (PC12), 14:1 dimirstoyl-phosphatidylcholine (PC14), 16:1 dipalmitoleoyl-phosphatidylcholine (PC16), 18:1 dioleoyl-phosphatidylcholine (PC18,DOPC), 20:1 Eicosenoyl-phosphatidylcholine (PC20), lysophospholipid (LPL), lysophosphatidylcholine (LPC), dioleoyl-phosphatidylethanolamine (DOPE).

## 3.7 Supporting Methods

### 3.7.1 Lipids

We performed calculations based on elastic moduli measured by Rawicz *et al.* [29]. To extrapolate the effects of changes in the acyl chain length, we use the moduli for a typical 18:1 phospholipid (1,2-dioleoyl-*sn*-glycero-3-phosphocholine) and the scaling relations listed below,

$$\begin{aligned}
 2a &= 40.7 \text{ \AA} && \propto a^1 \\
 K_A &= 0.576 kT \text{ \AA}^{-2} && \propto a^1 \\
 K_B &= 21 kT && \propto a^3 \\
 \mathcal{K} &= 2.1 \times 10^{-3} kT \text{ \AA}^{-2} && \propto a^0,
 \end{aligned} \tag{3.8}$$

where  $2a$  is the equilibrium thickness of the bilayer,  $K_A$  is the area expansion modulus,  $K_B$  is the bending modulus, and

$$\mathcal{K} \equiv \sqrt{2} \left( \frac{K_A^3 K_B}{a^6} \right)^{1/4}, \tag{3.9}$$

is the composite elastic modulus appearing in the line tension,  $f_U$ . The proportionality to bilayer thickness is approximate only and is deduced from treating the bilayer as a thin shell. For more elaborate models and scaling arguments, see Rawicz *et al.* [29]. By fitting the Peak-to-Peak head group thickness [29] for saturated and monounsaturated lipids, we find that the relation between bilayer thickness and acyl chain length is roughly

$$2a = 1.3n + 17 \text{ \AA}. \tag{3.10}$$

Again, more elaborate models and scaling arguments are found in Rawicz *et al.* [29].

### 3.7.2 Line Tension

In terms of  $h(r)$ , the bilayer mid-plane position, and  $u(r)$ , half the difference of the bilayer thickness and the equilibrium thickness, the mean curvature contributions to the free-energy density are [13]

$$\mathcal{G}_B = \frac{K_B}{2} \underbrace{[(\nabla^2 h)^2 + (\nabla^2 u)^2]}_{\mathcal{M}} - \underbrace{C_+ \nabla^2 [h + u] - C_- \nabla^2 [u - h]}_{\partial \mathcal{M}}, \tag{3.11}$$

where the variation of the  $\mathcal{M}$  terms contribute to the action in the bulk (bilayer), the  $\partial \mathcal{M}$  terms are total derivatives and can be evaluated at the interface, the constant terms are dropped,  $K_B$  is the bending modulus for the bilayer, and  $C_+$  and  $C_-$  are the spontaneous curvatures of the upper

and lower leaflets, respectively. The tension contribution to the free energy density is [15]

$$\mathcal{G}_\alpha = \underbrace{\frac{\alpha}{2} (\nabla h)^2}_{\mathcal{M}}, \quad (3.12)$$

where the thickness deformation term can be ignored. The interaction free energy density between the two layers is [12]

$$\mathcal{G}_I = \underbrace{\frac{K_A}{2a^2} u^2}_{\mathcal{M}}, \quad (3.13)$$

where  $K_A$  is the area expansion modulus and  $a$  is the equilibrium thickness of a leaflet.

The equilibrium equations that result from the minimization of  $u(r)$  and  $h(r)$  are

$$0 = \frac{\delta G[u, h]}{\delta u} = \left[ K_B \nabla^4 + \frac{K_A}{a^2} \right] u(r), \quad (3.14)$$

$$0 = \frac{\delta G[u, h]}{\delta h} = [K_B \nabla^4 - \alpha \nabla^2] h(r). \quad (3.15)$$

In the asymptotic regime, large  $R$ , we can ignore the curvature of the interface and replace the Laplacians with  $d^2/dr^2$ . For  $u(r)$ , the radially decreasing solutions are exponentials with complex wave numbers

$$\beta_\pm = - \left( \frac{K_A}{a^2 K_B} \right)^{1/4} e^{\pm i\pi/4}. \quad (3.16)$$

For  $h(r)$ , there is only a single radially decreasing solution with decay length,

$$\beta_h = \sqrt{\frac{\alpha}{K_B}}. \quad (3.17)$$

At the interface, the bilayer deforms to match the hydrophobic thickness of the protein,

$$u(R) = U = \frac{1}{2}W - a. \quad (3.18)$$

If the inclusion interface is relatively flat and the top and bottom surfaces of the bilayer are normal to the inclusion interface as depicted in Fig. 1, the radial slope of  $u(r)$  is zero at the interface,

$$u'(R) = 0, \quad (3.19)$$

although this too may be used as a geometrical parameter [16]. For  $h(r)$ , we set the radial slope at the interface,

$$h'(R) = H'. \quad (3.20)$$

At infinity, the bilayer is unperturbed, implying

$$u(\infty) = 0, \quad (3.21)$$

$$u'(\infty) = 0, \quad (3.22)$$

$$h(\infty) = 0. \quad (3.23)$$

The equilibrium solutions can be found by matching the boundary conditions above.

The line tension is

$$f = \int_R^\infty dr (\mathcal{G}_B + \mathcal{G}_\alpha + \mathcal{G}_I). \quad (3.24)$$

Integrating this equation by parts twice yields a bulk term proportional to the equilibrium equations, which is zero because the equations are satisfied, and surface terms. The total line tension is,

$$f = \underbrace{\frac{1}{2}\mathcal{K}U^2}_{f_U} + \underbrace{\frac{1}{2}\sqrt{K_B\alpha}H'^2}_{f_H} + \underbrace{K_BCH'}_{f_C}, \quad (3.25)$$

where  $\mathcal{K}$  has been defined in Eq. 2,  $C \equiv \frac{1}{2}(C_+ - C_-)$  is the composite spontaneous curvature, and  $f_H$  is the midplane deformation contribution to the line tension, which is typically small enough to ignore.

## Chapter 4

# The membrane-protein interactions of mechanosensitive channels

*This chapter is a reproduction of Wiggins and Phillips, 2005.*

In this paper, we examine the mechanical role of the lipid bilayer in ion channel conformation and function with specific reference to the case of the mechanosensitive channel of large conductance (MscL). In a recent paper (Wiggins and Phillips, 2004), we argued that mechanotransduction very naturally arises from lipid-protein interactions by invoking a simple analytic model of the MscL channel and the surrounding lipid bilayer. In this paper, we focus on improving and expanding this analytic framework for studying lipid-protein interactions, with special attention to MscL. Our goal is to generate simple scaling relations that can be used to provide qualitative understanding of the role of membrane mechanics in protein function and to quantitatively interpret experimental results. For the MscL channel, we find that the free energies induced by lipid-protein interaction are of the same order as the free energy differences between conductance states measured by Sukharev *et al.* (1999). We therefore conclude that the mechanics of the bilayer plays an essential role in determining the conformation and function of the channel. Finally, we compare the predictions of our model to experimental results from the recent investigations of the MscL channel by Perozo *et al.* (2002a,b), Powl *et al.* (2003), Yoshimura *et al.* (2004), and others and suggest a suite of new experiments.

### 4.1 Introduction

The mechanosensitive channel of large conductance (MscL) is a compelling example of the interaction of a membrane protein and the surrounding lipid bilayer membrane. MscL is gated mechanically (Blount and Moe, 1999) and belongs to a growing class of proteins that have been determined to be mechanosensitive (Gillespie and Walker, 2001; Hamill and Martinac, 2001). In a recent short paper (Wiggins and Phillips, 2004), we have argued that the mechanics of the bilayer is an

important partner in the phenomena of mechanotransduction and channel function. In particular, we considered a simplified model where only the radius of the channel changes in transitions between the open and closed state. In this paper, we present our free energy calculations in more generality and detail. Specifically, we have calculated the free energy due to the bilayer deformation as a result of the presence of a membrane protein using an analytic model developed for the study of bilayer mechanics (Canham, 1970; Helfrich, 1973; Evans, 1974). Many of the theoretical techniques exploited here have already been used with success in describing the role of the bilayer in the mechanics of the Gramicidin channel (e.g., Huang, 1986). In this paper, we have applied asymptotic approximations to the exact solutions of this model, permitting many of the important results to be expressed, estimated, and understood with simple scaling relations. These scaling relations are then applied to estimate the relative importance of each and every term in the bilayer free energy budget. We find that the bilayer deformation free energy can be of the same order as the free energy differences between conformational states of the MscL channel as measured by Sukharev *et al.* (1999). These results strongly suggest that bilayer deformation plays an important role in determining the protein conformation, and therefore function, of transmembrane proteins in general, and MscL in particular. Although we have explicitly estimated the size of the bilayer deformation energy exclusively for the geometry of MscL, the results can easily be re-evaluated and reinterpreted in the context of other transmembrane proteins and mechanosensitive channels, in particular MscS (Bass, 2002) Alamethicin (Opsahl and Webb, 1994), etc. We emphasize that our goal in this current work is not to attempt a quantitative understanding of all of the degrees of freedom of the channel and bilayer, but rather to build a tractable model for the role of bilayer mechanics in the function of the MscL channel, while developing the model in more detail than in our previous paper (Wiggins and Phillips, 2004).

The MscL channel is gated by membrane tension and has been studied extensively in patch clamp experiments (Sukharev *et al.*, 1999; Perozo *et al.*, 2002a). While several substates have been identified (Sukharev *et al.*, 1999), the channel typically resides in one of two primary conductance states. At low tension the channel is almost exclusively closed (C). As the tension is increased the open state (O) becomes ever more prevalent, until it dominates at high tension. Rees and coworkers have solved the structure for one conformation using X-ray crystallography which appears to be the closed state (Chan *et al.*, 1998). The open state has been modeled by a number of groups (Sukharev *et al.*, 2001; Betanzos *et al.*, 2002; Perozo *et al.*, 2002b).

The outline of the paper is as follows. In section 2, we briefly discuss the bilayer model, then present a table of results which shows the relative importance of different free energy penalties for bilayer deformation and then define the generalized forces we use to discuss the effects of bilayer deformation induced by protein conformational change. In section 3, we estimate the sizes of the bilayer deformation energy and forces for MscL, give a brief physical discussion of mechanisms that

give rise to the bilayer deformation energy, and discuss the scaling of these bilayer deformation energies. In section 4, we compare our predictions for a two state MscL model to experimental measurements made by Perozo *et al.* (2002a,b), Powl *et al.* (2003), Yoshimura *et al.* (2004), and others. In the Appendix, we provide a unit conversion table, bilayer parameters and full names, detailed derivations, and a discussion of the approximations used.

## 4.2 Free Energy of the Bilayer-Inclusion System

We begin by considering the free energy of the system as a whole: protein and bilayer. We assume that the system is in thermal equilibrium and define the free energy differences between states in the standard way

$$\Delta G_{(i)} \equiv -kT \log \left( \frac{\mathcal{P}_i}{\mathcal{P}_C} \right), \quad (4.1)$$

where  $\mathcal{P}_i$  is the probability of state  $i$  and the free energy differences are defined with respect to the closed state. We can divide each of these free energies into two parts

$$G = G_P + G_{\mathcal{M}}, \quad (4.2)$$

where  $G_P$  is the free energy associated with the protein's conformation and  $G_{\mathcal{M}}$  is the free energy induced in the bilayer by the protein inclusion and includes both a deformation free energy from the bulk of the bilayer and an interaction energy at the interface between the inclusion and bilayer. For the sake of brevity we will usually refer to both of these bilayer-related contributions to the free energy as the bilayer deformation energy. While a complete understanding of channel gating and function must encompass knowledge of both components of the free energy,  $G_P$  and  $G_{\mathcal{M}}$ , our analysis in this paper centers almost entirely on the bilayer deformation energy,  $G_{\mathcal{M}}$ . Several groups have used molecular dynamics (MD) and related techniques to study  $G_P$  or  $G$  in its entirety (Gullingsrud *et al.*, 2001; Gullingsrud and Schulten, 2002; Bilston and Mylvaganam, 2002; Elmore and Dougherty, 2003; Gullingsrud and Schulten, 2003) but as is often the case for biological systems, these studies have been handicapped by the size of the MscL system. It is too complex for direct simulation on biologically relevant time scales. From an experimental standpoint, Sukharev *et al.* have measured the free energy differences between different states (Sukharev *et al.*, 1999) in MscL and have found differences of order  $10 kT$ . These results reveal the energy scale associated with MscL gating and provide a reference by which different contributions to the free energy will be judged for their importance.

Our first goal in what follows is to persuade the reader that  $G_{\mathcal{M}}$  is large enough to be of interest. That is, since it is clear that there are several distinct contributions to the overall free energy budget, we illustrate that the contribution due to the inclusion-induced bilayer deformation is comparable

to the measured free energy differences between states. Since these contributions to  $G_{\mathcal{M}}$  are of the same order of magnitude as  $\Delta G$ , we conclude that the effects of bilayer deformation are potentially interesting. Perozo *et al.* (2002a) have already answered this question experimentally, demonstrating that bilayer characteristics such as lipid acyl chain length significantly effect the free energy.

### 4.2.1 The Calculation of the Bilayer Free Energy

The elastic deformation of the bilayer surrounding the channel is approximated with a model developed by Canham (1970), Helfrich (1973), and Evans (1974). Huang (1986) has applied this model to calculate the deformation energies induced by inclusions. These calculations have been elaborated upon by others, notably by Andersen and coworkers (Nielson *et al.*, 1998; Lundbæk *et al.*, 1996; Lundbæk and Andersen, 1994; Goulian *et al.*, 1998) and Dan and coworkers (Dan *et al.*, 1994; Dan *et al.*, 1993; Dan and Safran, 1995; Dan and Safran, 1998). Specifically, Goulian *et al.* (1998) have studied a similar model including applied tension. The bilayer deformation energy in this model is given by

$$G_{\mathcal{M}} = G_+ + G_- + G_{\text{I}}, \quad (4.3)$$

where

$$G_{\pm} = \int_{\mathcal{M}} d^2\sigma \left( \frac{1}{4}K_B[\text{tr } \mathbf{S}_{\pm}(\vec{x}) \mp C_{\pm}]^2 + \frac{K_G}{2} \det \mathbf{S}_{\pm}(\vec{x}) + \alpha_{\pm} \right), \quad (4.4)$$

and

$$G_{\text{I}} = \int_{\mathcal{M}} d^2\sigma \frac{1}{2}K_A \left( \frac{u}{a} \right)^2. \quad (4.5)$$

$G_{\pm}$  are the free energies due to the curvature and the tension in the top and bottom surfaces of the bilayer and  $G_{\text{I}}$  is the interaction free energy between these two surfaces. Locally, the curvature of the top (or bottom) surface of the bilayer is described by the shape operator,  $\mathbf{S}_{\pm}(\vec{x})$ , a rank two tensor. The trace of this tensor is twice the mean curvature and its determinant is the Gaussian curvature. The energetic cost for increasing the mean curvature of the top (or bottom) surface of the bilayer is the bending modulus,  $K_B/2$ . The energetic cost for increasing the Gaussian curvature of the top (or bottom) surface is the Gaussian bending modulus,  $K_G/2$ . We have chosen this normalization so that the effective moduli for the bilayer as a whole are  $K_B$  and  $K_G$ .

The addition of certain surfactants and non-bilayer lipids results in the lowest energy conformation of a single layer of lipids being curved (Israelachvili, 1991; Gruner, 1989). This spontaneous curvature is introduced into the model through non-zero values of  $C_{\pm}$ , the spontaneous curvatures of the upper and lower layers of the bilayer, respectively. We define the composite and the mean

spontaneous curvatures for the bilayer as

$$C \equiv \frac{1}{2}(C_+ - C_-), \quad (4.6)$$

$$\bar{C} \equiv \frac{1}{2}(C_+ + C_-), \quad (4.7)$$

respectively. The energetic penalty associated with changes in the area of the top and bottom surfaces of the bilayer are the tensions,  $\alpha_{\pm}$ , respectively. We assume that the tensions in the two layers are equal since, on long time scales, the lipids can switch between the two leaflets in order to equalize the tension. The total tension,  $\alpha = 2\alpha^{\pm}$ , is an externally tunable parameter. (See Appendix 4.7.5 for further discussion.)  $2u$  is the difference between the local thickness of the bilayer and the equilibrium thickness  $2a$ . The energetic cost for changing the thickness of the bilayer is the compression-expansion modulus,  $K_A$ . For further discussion of the model, the reader is invited to view the extensive discussions in the literature (Helfrich, 1973; Huang, 1986; Dan *et al.*, 1994; Goulian *et al.* 1998; etc.)

The presence of the channel will perturb the bilayer locally. To calculate the perturbation to the free energy due to the channel, we will assume that the radius of curvature corresponding to the vesicle or cell in which the inclusion is embedded is very large in comparison to the length scale of the inclusion itself and that the perturbation due to the bilayer inclusion is small enough to allow the equations to be linearized. In this approximation scheme, the bilayer deformation energy is

$$G_{\mathcal{M}} = \int_{\mathcal{M}'} d^2x \mathcal{G}, \quad (4.8)$$

where  $\mathcal{G}$  is the expanded effective free energy density (written out in its expanded form in the Appendix) and  $\mathcal{M}'$  is a Cartesian plane minus a circular inclusion of radius  $R$ . We can safely integrate out to infinity since the perturbation to the free energy density is localized around the inclusion. To construct the effective free energy density we describe the out-of-plane displacements of the upper and lower surfaces of the bilayer with the functions  $h_+(\vec{x})$  and  $h_-(\vec{x})$ , respectively, on  $\mathcal{M}'$ , as shown in Fig. 4.2.1. It is more transparent to work with the linear combinations of these two functions (Fournier, 1999), namely,

$$h(\vec{x}) = \frac{1}{2}(h_+ + h_-), \quad (4.9)$$

$$u(\vec{x}) = \frac{1}{2}(h_+ - h_-) - a, \quad (4.10)$$

where  $h$  is the average position of the upper and lower surfaces of the bilayer which we will refer to as the mid-plane and  $u$  is half the difference of the bilayer thickness and the equilibrium thickness. The overall structural picture is shown in Fig. 4.2.1 where the localized perturbation of the bilayer is depicted schematically.

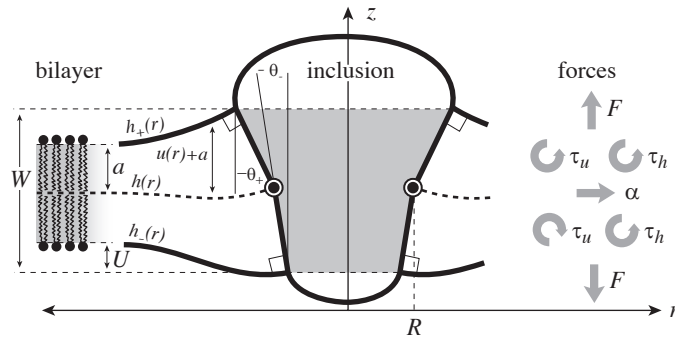


Figure 4.1: A schematic picture of the bilayer-inclusion model. The geometry of the inclusion is described by four parameters: the radius  $R$ , the thickness  $W$ , and the radial slopes  $H'_\pm$  of the top and bottom surfaces of the bilayer, respectively. If the surfaces of the bilayer are locally normal to the interface of the inclusion, as depicted above,  $H'_\pm = \theta_\pm$  in the small angle approximation. The bilayer equilibrium thickness is  $2a$ . The fields  $h_\pm(r)$  are the  $z$  displacements of the top and bottom surfaces of the bilayer, respectively. Their average is the mid-plane displacement,  $h(r)$ , and half their difference is  $u(r) + a$ .  $u(r)$  is the local thickness deformation of a single leaflet of the bilayer. At the interface, twice this deformation,  $2U$ , is the hydrophobic mismatch,  $W - 2a$ . The generalized forces on the inclusion induced by the bilayer are depicted for positive values.  $F$  is the expansion-compression force,  $\alpha$  is the tension,  $\tau_h$  is the mid-plane torque, and  $\tau_u$  is the shape torque.

A minimization of the effective free energy (Huang, 1986) gives two decoupled differential equations (Fournier, 1999) for the equilibrium configuration in the fields  $u(\vec{x})$  and  $h(\vec{x})$ , namely,

$$0 = [K_B \nabla^4 - \alpha \nabla^2 + \frac{K_a}{a^2}] u \quad (4.11)$$

$$0 = [K_B \nabla^2 - \alpha] h, \quad (4.12)$$

which are again discussed at length in the literature (Huang, 1986; Nielsen *et al.*, 1998; Fournier, 1999). The solution to these equations for the fields  $h(\vec{x})$  and  $u(\vec{x})$  can be written in terms of modified Bessel functions in cylindrical coordinates (Huang, 1986).

Due to the hydrophobic residues of the protein inclusion, we assume that the bilayer adheres to the external surface of the protein. As will be described in more detail below, the matching condition at this surface dictates half the boundary conditions for the bilayer (the remaining boundary conditions dictate that the bilayer is unperturbed at infinity). We consider proteins with azimuthal (cylindrical) symmetry. While the MscL channel is not truly azimuthally symmetric, as a homo-pentamer, it is highly symmetric, at least in the closed state as the X-ray crystallography structure has demonstrated (Chang *et al.*, 1998). In order to clearly distinguish values of the functions at the boundaries from the corresponding functions themselves, we will denote these parameters with capital letters. We fix the bilayer thickness,  $2U + 2a$ , to match the hydrophobic thickness of the protein,  $W$ , at the interface,  $r = R$ :

$$u(R) = U = \frac{1}{2}W - a. \quad (4.13)$$

$2U$  is called the hydrophobic mismatch since it is the difference between the equilibrium thickness of the bilayer,  $2a$ , and the thickness of the protein,  $W$ . For real proteins it is quite difficult to define exactly what one means by this region since real structures are not purely hydrophobic in the transmembrane region. The closed state and a proposed model of the open state colored by hydrophobicity are depicted in Fig. 4.2.1.

We also specify the radial derivatives of  $h_{\pm}$  at the boundary as

$$h'_{\pm}(R) = H'_{\pm} \quad (4.14)$$

or alternatively,

$$H' \equiv h'(R) = \frac{1}{2}(H'_+ + H'_-), \quad (4.15)$$

$$U' \equiv u'(R) = \frac{1}{2}(H'_+ - H'_-), \quad (4.16)$$

where  $'$  is the derivative with respect to  $r$ , the radial distance from the inclusion. A physical interpretation of these slopes might be to assume the bilayer's surfaces are normal to the protein's surface at the boundary, although this need not be the case (Nielson *et al.*, 1998). At infinity we assume that the bilayer is unperturbed which may be cast in mathematical terms as

$$h(\infty) = 0, \quad (4.17)$$

$$u(\infty) = 0. \quad (4.18)$$

Solving the equilibrium equations for a given set of boundary conditions and plugging these solutions into the surface integral for bilayer deformation energy results in the bilayer deformation energy for a given configuration of the protein (Huang, 1986). Each protein configuration corresponds to a different outcome for the bilayer deformation energy. This energy has been divided into several contributions based on the physical mechanism giving rise to it. In Table 6.1, we present a summary of these results. Brief derivations may be found in the Appendix. Generally, the bilayer deformation energies lend themselves to simple scaling laws, except for two cases: thickness and mid-plane deformation. In these cases the exact results to the model are somewhat complicated and the results that appear in the table are limits which are derived and discussed in the Appendix.

## 4.2.2 Connection between $H'_{\pm}$ and Channel Geometry

Recall from the discussion above that the energetics of the composite system of the inclusion and the bilayer depends in part on the geometric parameters  $H'_{\pm}$  that determine how the bilayer joins the protein at the interface. The appropriate bilayer slope boundary condition is still somewhat

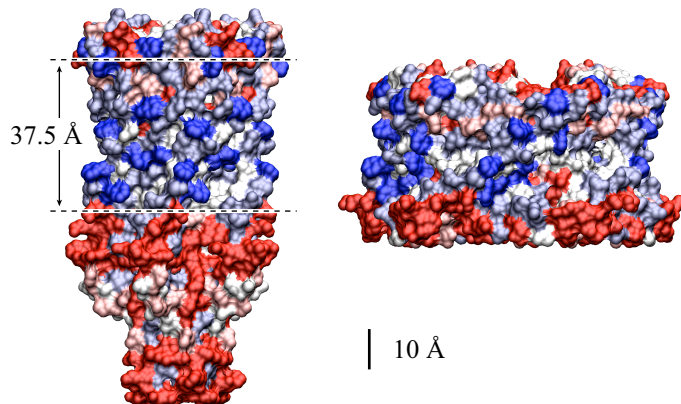


Figure 4.2: Models of the closed and open states colored by hydrophobicity (Sukharev *et al.*, 2001). While the general region spanned by the membrane is evident from the hydrophobic regions on the protein interface, it is difficult to precisely define the thickness of this region. A closed states thickness has been inferred from the data of Powl *et al.* (2003) and this region is schematically marked on the model of the closed state. Additional confirmation of this estimate for the hydrophobic thickness comes from the simulation of Elmore and Dougherty (2003).

of an open question. Some authors have treated these conditions as free, minimizing the bilayer deformation energy with respect to them, while others have assumed that the bilayer surfaces are normal to the protein surface (see refs. in Nielson *et al.*, 1998). Most of our results will be expressed in terms of  $H'_\pm$  which is independent of any particular assumption about these boundary conditions, though we will assume the normal interface boundary conditions in our concrete physical discussions. We will also discuss the free boundaries briefly. If we assume that the mid-plane of the lipid bilayer interface is normal to the protein and that transmembrane domains M1 and M2 are rigid and aligned this dictates that

$$H' = H'_+ = H'_- \quad (4.19)$$

$$U' = 0. \quad (4.20)$$

This can be recast verbally as the statement that the top and bottom surfaces of the bilayer have the same slope at the boundary and there is no bend in the inclusion interface. In the small angle limit,  $H'$  can be replaced by the angle away from normal of the interface. If we do introduce a bend in the middle of the interface, the orientations of the upper and lower interfaces are independent. Assuming that the interface of the bilayer is normal to the protein surface, we can replace the slopes with the angles away from normal,  $\theta_\pm$ , (Dan and Safran, 1998) in the small angle limit, as pictured schematically in Fig. 4.2.1.

### 4.2.3 Forces, Torques, and Tensions

The physical effects of bilayer deformation on the inclusion conformation can be recast in a more intuitive form by appealing to forces, tensions, and torques rather than free energies. For example, most of the bilayer deformation energies will generate a tension on the interface due to their radial dependence. The applied tension,  $\alpha$ , is not the whole story! The generalized forces are obtained by differentiating the bilayer deformation energy with respect to bilayer excursions. Implicitly, these generalized forces are defined through

$$dG_{\mathcal{M}} = -\alpha_{\Sigma}dA - \tau_+dH'_+ - \tau_-dH'_- - FdW, \quad (4.21)$$

where  $A \equiv \pi R^2$  is the area of the protein,  $H'_{\pm}$  are the slopes of the bilayer surfaces at the interface, and  $W$  is the thickness of the hydrophobic region of the protein. Explicitly, these generalized forces may be written as

$$\alpha_{\Sigma} \equiv -\frac{1}{2\pi R} \left( \frac{\partial G_{\mathcal{M}}}{\partial R} \right)_{T,W,H'_{\pm}}, \quad (4.22)$$

$$\tau_{\pm} \equiv -\left( \frac{\partial G_{\mathcal{M}}}{\partial H'_{\pm}} \right)_{T,A,W,H'_{\mp}}, \quad (4.23)$$

$$F \equiv -\left( \frac{\partial G_{\mathcal{M}}}{\partial W} \right)_{T,A,H'_{\pm}}. \quad (4.24)$$

Since we have already used  $\alpha$  to denote the applied tension, we use  $\alpha_{\Sigma}$  to denote the net radial tension on the inclusion interface; the sum of the applied tensions and other bilayer deformation induced contributions. When the tension is positive, it is tensile.  $F$  is the compression-expansion force, normal to the plane of the bilayer, acting on the inclusion. When the compression-expansion force is positive, it acts to induce inclusion-thickness expansion.  $\tau_{\pm}$  are cylindrical torques acting on the top and bottom surfaces of the inclusion around the mid-plane. It will usually be more convenient to work with the torques complementary to  $H'$  and  $U'$  rather than  $H'_{\pm}$ . We define the mid-plane torque as the cylindrical torque on the interface as a whole

$$\tau_h \equiv \tau_+ + \tau_- = -\left( \frac{\partial G_{\mathcal{M}}}{\partial H'} \right)_{T,A,W,U'}. \quad (4.25)$$

When the mid-plane torque is positive, it acts to induce increases in the mid-plane slope. This cylindrical torque is generated by bending stresses alone and is therefore related to the principal curvatures at the boundary (Landau and Lifshitz, 1986) through the relation

$$\frac{\tau_h}{C} = -K_B \left( R_{\parallel}^{-1} + R_{\perp}^{-1} - C \right) - K_G R_{\parallel}^{-1}, \quad (4.26)$$

where  $\mathcal{C}$  is the circumference of the inclusion,  $R_{\parallel}^{-1}$  and  $R_{\perp}^{-1}$  are the principal curvatures at the boundary of the midplane, in the directions parallel and perpendicular to the boundary, respectively. (For azimuthally symmetric surfaces the principal curvatures are always radial and azimuthal, and furthermore the azimuthal curvature is  $R_{\parallel}^{-1} = -r^{-1} \sin \theta_N$  where  $r$  is the cylindrical radius, and  $\theta_N$  is the angle of the upward surface normal away from vertical. For example, see Boal, 2002.) We can define the shape torque as the cylindrical torque complementary to  $U'$

$$\tau_u \equiv \tau_+ - \tau_- = - \left( \frac{\partial G_{\mathcal{M}}}{\partial U'} \right)_{T,A,W,H'} . \quad (4.27)$$

When the shape torque is positive, it induces radial expansion at the mid-plane and radial compression at the outer surfaces of the bilayer. When the shape torque is negative, it induces radial compression at the mid-plane and radial expansion at the outer surfaces of the bilayer. The bending stress picture of the shape torque is somewhat more complicated than for the mid-plane torque due to the interaction between the two layers. The generalized forces are depicted in Fig. 4.2.1 for positive values and their physical interpretation and size are discussed in Sect. 4.3.

#### 4.2.4 Relation between pressure gradients and generalized forces

Another way to recast the interaction between the membrane protein and the surrounding bilayer is by introducing the notion of pressure gradients. Cantor (1997, 1999) has made calculations of the out-of-plane pressure gradients in the bilayer. He has shown that the pressure is compressive in the middle of the bilayer and expansive near the surface. Cantor (1997) and de Kruijff (1997) have discussed the effects of this gradient on protein conformation. If the  $\alpha$ -helices (MscL's transmembrane domains M1 and M2) can be interpreted (to a first approximation) as rigid, the effects of this pressure gradient are to produce a tension and cylindrical torques. The tension on the interface is the integrated bilayer pressure,

$$\alpha_P = \int_{-a}^a dz P(z), \quad (4.28)$$

where  $z$  is the position in the bilayer, running from  $-a$  to  $a$ . This integrated tension must be the net tension  $\alpha_{\Sigma}$ . If we allow the inclusion to have a hinge at  $z = 0$ , cylindrical torques about this circumference are induced on each section of the inclusion. (See Fig. 4.2.1) In the small angle limit, these cylindrical torques are

$$\tau_{+,P} = R \int_0^{2\pi} d\phi \int_0^a dz P(z)z, \quad (4.29)$$

$$\tau_{-,P} = -R \int_0^{2\pi} d\phi \int_{-a}^0 dz P(z)z, \quad (4.30)$$

Physical Mechanism	Energy ( $G_{\mathcal{M}}$ )	for MscL
Areal Deformation	$G_A = -\alpha \cdot A$	$10kT$
Gaussian Curvature	$G_G = -\pi K_G (H'^2 + U'^2)$	$1kT$
Spontaneous Curvature	$G_C = K_B (CH' + \overline{CU}') \cdot \mathcal{C}$	$10kT$
Bilayer Interface	$G_\sigma = \sigma W \cdot \mathcal{C}$	$10kT$
Mid-Plane Deformation †	$G_H = \frac{1}{2} \sqrt{\alpha K_B} H'^2 \cdot \mathcal{C}$	$< kT$
Thickness Deformation †	$G_U = \frac{1}{2} \mathcal{K} U^2 \cdot \mathcal{C}$	$10kT$

Table 4.1: Summary of results for inclusion-induced bilayer free energies. The free energies are written symbolically followed by an estimate of the size of the contribution to the nearest order of magnitude for a typical MscL system in patch clamp experiments. In the following section more detailed estimates are made. The free energies have been factored to emphasize their radial dependence. Tension-like terms are proportional to the area,  $A \equiv \pi R^2$ . Line-tension-like terms are proportional to the circumference,  $\mathcal{C} \equiv 2\pi R$ .  $\mathcal{K}$  is a composite elastic constant defined in Sect. 4.3.6.  $\sigma$  is an interface energy discussed in Sect. 4.3.4. †Dominant scaling for asymptotic results.

where the torques have been defined to match our previous definitions in Sect. 4.2.3, when the angles made by two surfaces of the interface,  $\theta_\pm$ , are defined such that

$$\theta_\pm = H'_\pm. \quad (4.31)$$

The  $\tau_{\pm,P}$  must correspond to our  $\tau_\pm$ . The effects of the pressure gradient on our constrained system are neatly reduced to three of the generalized forces we have already discussed. The fourth force,  $F$ , is just the integrated shear stress.

### 4.3 Free Energy Estimates and Physical Interpretation

In Sect. 4.2, we summarized the bilayer model and presented the lowest order contributions to the bilayer deformation energy in Table 6.1. The aim of the present section is to revisit each of these individual contributions to the overall free energy, estimate its magnitude for MscL, and discuss the scaling and physical mechanism giving rise to the bilayer deformation energy. In order to estimate the bilayer deformation energies, we need structural information for MscL. From X-ray crystallography data (Chang *et al.*, 1998), in the closed state, MscL appears to have an external radius of roughly 23 Å. Sukharev *et al.* (2001) have speculated that the open state's external radius is roughly 35 Å. We use typical bilayer elastic parameters as summarized in the Appendix. In addition, the Appendix contains a brief discussion of the scaling of these parameters with bilayer thickness.

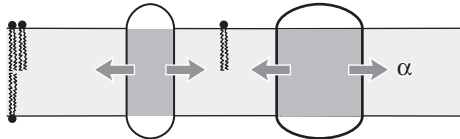


Figure 4.3: A cartoon of areal deformation. Tension, represented by the arrows, is transmitted through the bilayer to the inclusion. For positive biaxial tension, radial expansion of the inclusion reduces the free energy of the bilayer. The vesicle or cell can be viewed as a bilayer reservoir where tension is the energetic cost per unit area of bilayer in the local system.

Numerical results are multiplied by scaling relations to remind the reader what values have been used in their computation and how the free energies scale with changes in inclusion geometry, tension, etc.

### 4.3.1 Areal Deformation

The areal deformation free energy is the dominant tension-dependent term and typically provides the mechanism for opening the MscL channel. The physical interpretation of this term is shown schematically in Fig. 4.3.1. The form of this contribution is well understood (for example, see Hamill and Martinac, 2001) and is analogous to the  $-PdV$  term for an ideal gas in three dimensions. For areal deformations, the bilayer lipids act like a two-dimensional gas with a free energy change given by

$$dG_A = -\alpha dA, \quad (4.32)$$

where  $\alpha$  is the tension. At high tension, the open state is favored due to its larger area. Sukharev *et al.* (1999) have measured the opening tension to be  $\alpha_* = 1.2 \text{ pN } \text{\AA}^{-1}$ . ( $\alpha_*$  is the tension at which the channel is open half the time. This tension will depend on the bilayer in which the channel is reconstituted but we use this number as the typical size of the opening tension.) The areal deformation energy is

$$G_A = -\alpha A = -\alpha \pi R^2 \approx -47 \left( \frac{\alpha}{\alpha_*} \right) \left( \frac{A}{A_C} \right) kT, \quad (4.33)$$

and is plotted as a function of applied tension in Fig. 4.3.1. The way in which this free energy is expressed is to normalize the tension in units of the opening tension,  $\alpha_*$ , and the area in terms of the closed state area,  $A_C$ . As we expect, the typical free energies generated by radial changes are large. This is no surprise since the tension acts as the switch between the closed state and the larger open state. The most striking feature of this energy in comparison with those we will discuss below is its areal dependence. This free energy scales as the square of the channel radius, whereas almost all other contributions will roughly scale as the circumference. This scaling difference has important consequences for the stability of the conductance states and will give rise to a picture

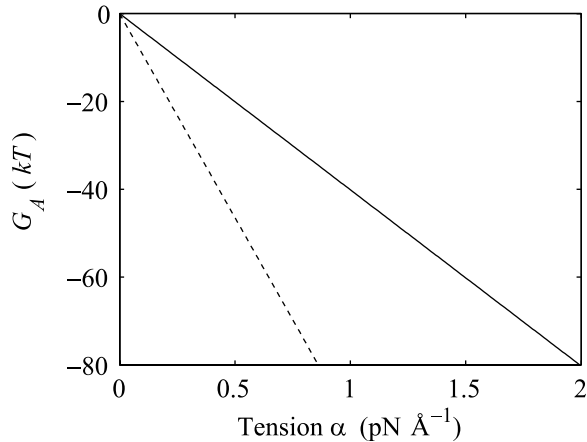


Figure 4.4: The theoretical areal deformation free energies for the open (dashed line) and closed state (solid line) as a function of applied tension.

of the tension-induced opening of the channel much like the picture used to discuss nucleation of second phases. We have gone to some length to develop the importance of this scaling difference in our previous paper (Wiggins and Phillips, 2004).

Experimental measurements have roughly confirmed the linear dependence of the free energy difference on tension (Sukharev *et al.*, 1999). This would suggest that the open and closed states are relatively well defined, at least with respect to the channel radius. If the closed state, for example, actually consisted of a heterogeneous mix of states, this would lead the dependence of the free energy on tension to deviate from the linear relation predicted above. The fact that this has not been seen indicates that well defined states are compatible with experiment.

### 4.3.2 Gaussian Curvature

Gaussian curvature normally contributes to the free energy topologically (independent of the local shape of the bilayer). However, at the inclusion, the bilayer has a boundary which will allow non-topological contributions to the free energy (E. Evans, personal communication). In the small-angle limit, the Gaussian curvature free energy is

$$G_G = -\pi K_G (U'^2 + H'^2) \quad (4.34)$$

as demonstrated in the Appendix. Measurements of the Gaussian curvature modulus are compatible with a wide range of values:  $K_G < -K_B/2$  (see references in Boal, 2002). We estimate that for MscL, the free energy contribution from the mid-plane slope is

$$G_G \approx 0.7 \left( \frac{-K_G}{K_B} \right) \left( \frac{H'}{0.1} \right)^2 kT, \quad (4.35)$$

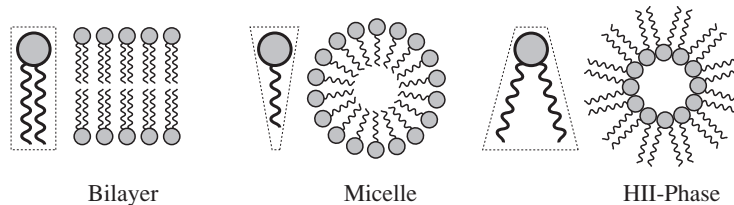


Figure 4.5: A schematic depiction of molecular shapes which influence spontaneous curvature (Israelachvili, 1991). Molecules with a cylindrical shape, such as phospholipids, will assemble into bilayers. Cone shaped molecules, such as lysophospholipids will assemble into micelles, the lowest energy configurations. For our sign conventions, these cone shaped molecules induce negative spontaneous curvature. Inverted cone shape molecules, such as cholesterol, DOPC, and DOPE assemble into  $H_{II}$  phases (Gruner, 1989) and induce positive spontaneous curvatures. The size of the spontaneous curvature is thought to be related to the difference in size between the polar head group and the acyl tails. Figure adapted from Lundbæk and Andersen, 1994.

where the deformation energy has been written in a dimensionless form in terms of the bending modulus,  $K_B$ , the closed state radius, and a modest interface angle of 0.1. (We expect the contribution from  $U'$  to be of the same order.) We have chosen this small angle since a large tilt angle for the interface is not evident from the closed state structure or the modeled open state (see Fig. 4.2.1). As indicated above, the free energy is typically fairly small unless  $H'$  or  $U'$  are large. Since  $G_G$  is radially independent, it induces no tension. On the other hand, Gaussian curvature does induce a torque of the form

$$\tau_{\pm} = \pi K_G H'_{\pm}, \quad (4.36)$$

which points toward  $H'_{\pm} = 0$  if  $K_G < 0$ . The induced mid-plane torque is exactly what is expected from the bending stresses in Eq. 4.26.

### 4.3.3 Spontaneous Curvature

Spontaneous curvature arises from the addition of detergents and non-bilayer forming lipids to the bilayer. These molecular additions cause the lowest energy configuration of a single layer of lipids to be curved. The general phenomenon of spontaneous curvature in lipid structures is reviewed by Gruner (1989). In general, measurements of the spontaneous curvature,  $C$ , have been for  $H_{II}$  phase forming molecules where the positive spontaneous curvature can be deduced from the lattice structure (Gruner, 1989; Chen and Rand, 1997; Keller *et al.*, 1993). Values of  $C^{-1} = 20 \text{ \AA}^{-1}$  (DOPE) are experimentally attainable (Keller *et al.* 1993). Less is known about negative spontaneous curvature, induced by micelle-inducing detergents and lysophospholipids. See Fig. 4.3.3 for a brief discussion of molecular shape and spontaneous curvature. To induce a composite bending modulus for the bilayer, the layers must be asymmetrically doped, though the molecules can exchange between the leaflets and move within a leaflet to energetically favorable locations caused by localized regions



Figure 4.6: A schematic depiction of spontaneous curvature induced by several species of lipids in the bilayer. The gray colored lipids depict a non-bilayer lipid which induces positive spontaneous curvature. A tilted inclusion interface can lead to a reduction in the stress caused by the non-bilayer lipids as depicted above. Spontaneous curvature induces both torques and tension at the interface. For energetically favorable tilt, the tension acts to open the channel. The torque on the inclusion from a bilayer leaflet with positive spontaneous curvature acts to increase tilt by expansive pressure at the surface and compressive pressure at the mid-plane. When only one leaflet of the bilayer is doped, both a mid-plane and a shape torque are induced but they cancel for the undoped leaflet.

of high complementary curvature (de Kruijff *et al.*, 1977; Kumar *et al.*, 1989). For the sake of making an explicit estimate, we ignore these complications.

In the linearized theory, the spontaneous curvature contributes an interface term to the free energy. In Fig. 4.3.3 an energetically favorable curvature is depicted. The free energy arising from spontaneous curvature is

$$G_C = 2\pi R K_B (CH' + \bar{C}U') \approx 15 \left( \frac{R}{23 \text{ \AA}} \right) \left( \frac{20 \text{ \AA}}{C^{-1}, \bar{C}^{-1}} \right) \left( \frac{H', U'}{0.1} \right) kT. \quad (4.37)$$

These symbolic results are equivalent to those in Dan and Safran (1998). To estimate the size of this contribution for MscL, we have written the free energy in a dimensionless form using the large positive spontaneous curvature of a DOPE monolayer ( $C^{-1} = 20 \text{ \AA}$ ) (Keller *et al.* 1993), a relatively modest tilt angle ( $H' = 0.1$ ), and the closed state radius. The comma notation is meant to denote that this estimate is for either these values of  $C$  and  $H'$  or  $\bar{C}$  and  $U'$ . The resulting free energy can be the same order of magnitude as the areal deformation energy, implying it may play an important role in channel function.

Physically, the scaling can be easily understood with the example schematically illustrated in Fig. 4.3.3. A protein that has a conical shape, which increases toward the periplasm, induces membrane stress that may be relieved by complementary shaped lipids (which give rise to a positive composite spontaneous curvature) as illustrated in the figure. The bilayer illustrated in the figure also has positive mean spontaneous curvature ( $\bar{C} > 0$ ), which relieves the stress induced by the hour glass shaped inclusion. This deformation energy is our first example of a line tension (a free energy with a linear radial dependence.) This deformation energy is caused by interaction at the protein interface whose size is proportional to the interface area and therefore proportional to the radius of the inclusion. We have described in detail the significance of this linear dependence for mechanotransduction elsewhere (Wiggins and Phillips, 2004).

Spontaneous curvature gives rise to both a tension, due to the radial dependence of the free energy, and torques, due to the dependence of the free energy on  $H'$  and  $U'$ . The tension on the boundary of the protein is

$$\alpha_C = -\frac{K_B}{R} (CH' + \bar{C}U') \approx -0.19 \left( \frac{23 \text{ \AA}}{R} \right) \left( \frac{23 \text{ \AA}}{C^{-1}, \bar{C}^{-1}} \right) \left( \frac{H', U'}{0.1} \right), \quad (4.38)$$

where we have estimated the size of the induced tension by writing it in a dimensionless form using the same parameters as the deformation energy described above. This induced tension can have either sign resulting in contributions which are either tensile or compressive. If curvature stress is relieved by spontaneous curvature, it is energetically favorable to increase the radius and the tension tends to open the channel while if the curvature stress is increased by the spontaneous curvature, the tension will be compressive. The mid-plane torque is

$$\tau_{h,C} = -2\pi R K_B C \approx -1.5 \times 10^2 \left( \frac{R}{23 \text{ \AA}} \right) \left( \frac{20 \text{ \AA}}{C^{-1}} \right) kT, \quad (4.39)$$

which is again written in a dimensionless form as described above. The torque induces inclusion conformations that would allow energetically favorable bending as explained above and depicted in Fig. 4.3.3. The mid-plane torque is non-zero only for asymmetrically doped bilayers and its symbolic form matches the spontaneous curvature term deduced from bending stress in Eq. 4.26. The shape torque is

$$\tau_{u,C} = -2\pi R K_B \bar{C} \approx -1.5 \times 10^2 \left( \frac{R}{23 \text{ \AA}} \right) \left( \frac{20 \text{ \AA}}{\bar{C}^{-1}} \right) kT, \quad (4.40)$$

which, for positive mean spontaneous curvature, acts to compress the mid-plane and expand the outer surface region of the inclusion. (Again, we have written the torque in a dimensionless form as described above.)

Keller *et al.* (1993) have studied the Alamethicin channel reconstituted into DOPC/DOPE bilayers. This is a particularly beautiful system since the spontaneous curvature of the mixed bilayer interpolates linearly with the relative concentration of the components, allowing a continuous range of spontaneous curvatures. The bilayers of Keller *et al.* are symmetric, implying that  $C = 0$ . In this case, the spontaneous curvature free energy is (Dan and Safran, 1998)

$$G_C = 2\pi R K_B \bar{C} U', \quad (4.41)$$

which would predict free energy differences between states to be linear in  $\bar{C}$  which Keller *et al.* (1993) have shown experimentally.

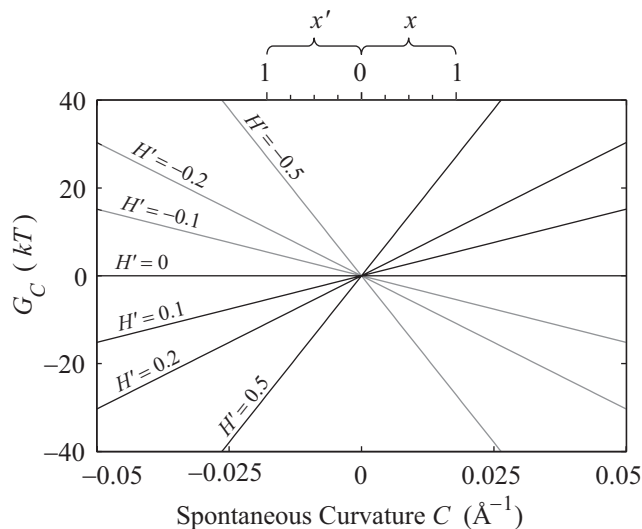


Figure 4.7: The spontaneous curvature free energy as a function of the composite spontaneous curvature  $C$  for various mid-plane slopes. At the top we have shown the corresponding concentration ratio for the DOPE/DOPC system of Keller *et al.* (1993). For positive  $C$ , the bottom leaflet consists of pure DOPC and the top leaflet is a DOPE/DOPC mix with mole fraction  $x$  of DOPE. For negative  $C$ , the top leaflet consists of pure DOPC and the bottom leaflet is a DOPE/DOPC mix with mole fraction  $x'$  of DOPE. We have plotted the free energy for a range of spontaneous curvatures that are larger than those that can be realized for DOPC/DOPE bilayers, since they may be relevant for other lipids or detergent-lipid bilayers.

#### 4.3.4 Bilayer Interface Energy

The bilayer and protein are glued together by hydrophobic-hydrophilic interaction forces which are strong enough to hold the protein in the bilayer at a typical cytoplasmic pressure of several atmospheres. It is natural to assume that in addition to the internal protein and bulk bilayer energies there will be an interaction term from the interface. There are many complicated scenarios which might be dreamed up, but the simplest is to assume that there is free energy proportional to the area of protein and bilayer in contact, resulting in a free energy

$$G_W = \sigma 2\pi RW, \quad (4.42)$$

where  $W$  is the thickness of the hydrophobic region. The constant of proportionality,  $\sigma$ , is the interface energy and has units of energy/area. Thus far, we have concentrated exclusively on the bilayer bulk for two reasons: (i) the continuum model is almost certainly a reasonable rough model for the processes of interest, and (ii) the material parameters for the bilayer are known from earlier experiments (Rawicz *et al.* 2000). In contrast, little is known about the validity of this model for the interface nor is there any estimate for the size of  $\sigma$ , the interface energy. This class of interface

terms gives rise to a tension and a compressive-expansive force

$$\alpha_W = -\sigma \frac{W}{R}, \quad (4.43)$$

$$F_W = -\sigma 2\pi R. \quad (4.44)$$

The effects of the tension and compressive force depend on the sign  $\sigma$ , the interface energy density. When  $\sigma$  is positive, the interface is minimized, leading to compressive forces. When  $\sigma$  is negative (the affinity of lipid and protein are high), the interface is maximized and the forces are expansive.

We have introduced this energy as a sanity check for our boundary conditions. We have somewhat naively assumed that the membrane adapts to an arbitrary protein shape. This assumption certainly fails when the adhesive forces attaching the membrane to the protein are not large enough to sustain the strain in the membrane. It is therefore useful to develop an approximate expression for these adhesive forces. We know the interface energy for a typical hydrophobic-hydrophilic mismatch (Hamill and Martinac, 2001)

$$\sigma_* = 25 \text{ cal mol}^{-1} \text{ \AA}^{-2} = 0.0418 k_B T \text{ \AA}^{-2}, \quad (4.45)$$

which is large compared to the other tensions in the problem. The compressive force countering the creation of this interface is

$$F_{W*} = -\sigma_* 2\pi R \approx -2.5 \times 10^2 \left( \frac{R}{23 \text{ \AA}} \right) \text{ pN}, \quad (4.46)$$

where we have used the closed state radius to write the force in a dimensionless form. This force can be interpreted as the critical force required to strip the protein from the bilayer. As we have reasoned above, this force will be important when we consider the large deformation limit on forces and energies due to thickness deformation.

### 4.3.5 Mid-Plane Deformation

The free energy associated with the deformation of the mid-plane of the bilayer is another contribution in the overall free energy budget. These constant thickness deformations like those pictured in fig. 4.3.5, are induced by conically shaped proteins. Mid-plane deformation contributes to the bilayer deformation energy through both bending of the bilayer and from a corresponding increase in bilayer area. The exact result to the linearized model is derived in the Appendix, but the dominant contribution at high applied tension is given by

$$G_H = \pi R \sqrt{\alpha K_B} (H')^2 \approx 0.6 \left( \frac{R}{23 \text{ \AA}} \right) \left( \frac{2a}{40.7 \text{ \AA}} \right)^{3/2} \left( \frac{\alpha}{\alpha^*} \right)^{1/2} \left( \frac{H'}{0.1} \right)^2 kT, \quad (4.47)$$

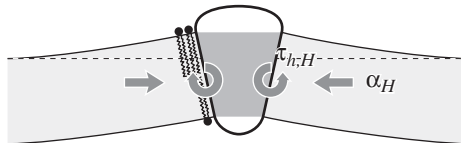


Figure 4.8: A conically shaped protein induces bilayer bending. In order to match a conical inclusion interface, the bilayer must deform. The deformation leads to energetic contributions both from an increase in bilayer area and from bilayer bending. Mid-plane deformation induces both a mid-plane torque and a tension. The tension is always compressive. The mid-plane torque acts to reduce interface tilt and restore the bilayer to its undeformed configuration. We estimate that the mid-plane deformation energy is probably not important for MscL gating.

where the parameters used to write the deformation energy in a dimensionless form are the closed state radius, the opening tension, and a modest interface tilt angle ( $H' = 0.1$ ). The  $H'^2$  dependence of the mid-plane deformation energy is as one would expect since no bending corresponds to  $H' = 0$  and results in the minimum energy (in the absence of spontaneous curvature). Dan and Safran (1998) have discussed deformation energies with a similar dependence on  $H'$ , but with a different size and physical origin. Note that mid-plane deformation scales differently with the applied tension ( $\alpha^{1/2}$ ) from the other contributions and can therefore be distinguished from the other bilayer deformation energies by measuring the tension dependence of the free energy. The approximation we have used is not really valid for MscL at experimentally realizable tensions since the elastic decay length is given by

$$\sqrt{\frac{K_B}{\alpha}} \approx 27 \left( \frac{2a}{40.7 \text{ \AA}} \right)^{3/2} \left( \frac{\alpha_*}{\alpha} \right)^{1/2} \text{ \AA}, \quad (4.48)$$

where we have estimated the typical size of the decay length by writing it in a dimensionless form using the opening tension. (The size and scaling of the bending moduli are described in the Appendix.) This decay length is roughly the same size as the channel radius. At high tension this length scale is reduced thus improving the asymptotic result and also increasing the size of the energy. For MscL, unless the bending modulus is significantly softened, we are unlikely to be able access this regime since the lysis tension for bilayers is typically not much more than  $\alpha_*$  (Olbrich *et al.*, 2000). The scaling result we have derived overestimates the bilayer deformation energy. (See the Appendix for further discussion.) Both the exact result and asymptotic result are plotted as a function of applied tension in Fig. 4.3.5. In spite of this overestimate, the energy is still small compared with the areal deformation, so we conclude that mid-plane deformation is probably not a key player in the free energy budget for MscL. This effect has also been explored in a recent paper by Turner and Sens (2004).

The dominant term in the mid-plane deformation energy scales linearly with  $R$  since the area of the bilayer deformation is roughly proportional to the circumference. This radial dependence gives

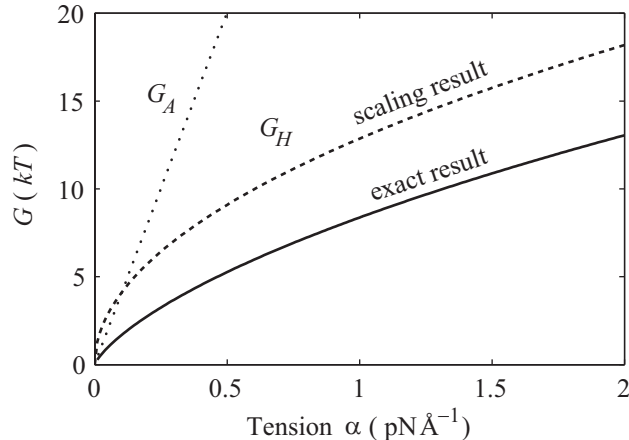


Figure 4.9: The mid-plane deformation energy is illustrated above as a function of tension. We have plotted the approximate scaling result (dashed line) discussed below, the exact result to the model (solid line) discussed in the Appendix 4.7.5, as well as the areal deformation energy for the closed state, the opening tension  $\alpha^*$  (dotted line). All the energies are computed for the closed state using an unrealistically large mid-plane slope ( $H=0.5$ ) to exaggerate the effect. While the scaling result is several  $kT$  larger than the exact result, it accurately reflects the scaling at high tension, and provides a limit for the exact result. The  $\alpha^{1/2}$  dependence of the mid-plane deformation energy has not been observed experimentally.

rise to a tension:

$$\alpha_H = \frac{1}{2R} \sqrt{K_B \alpha} H'^2 \approx 7.0 \times 10^{-3} \left( \frac{23 \text{ \AA}}{R} \right) \sqrt{\frac{\alpha}{\alpha^*}} \left( \frac{H'}{0.1} \right)^2 \text{ pN \AA}^{-1}, \quad (4.49)$$

which acts to inhibit channel opening. For the typical constants chosen here,  $\alpha_H$  is about a hundredth of the opening tension, again confirming that the mid-plane deformation is probably not important for MscL conformation or function. Like the spontaneous and Gaussian curvature contributions, the mid-plane deformation also places a torque on the protein

$$\tau_H = -2\pi R \sqrt{\alpha K_B} H' \approx -11 \left( \frac{R}{23 \text{ \AA}} \right) \sqrt{\frac{\alpha}{\alpha^*}} \left( \frac{H'}{0.1} \right) kT, \quad (4.50)$$

which we have written in a dimensionless form as described above. This is a restoring torque toward the lowest energy configuration  $H' = 0$  (in the absence of spontaneous curvature).

### 4.3.6 Thickness Deformation

The free energy contribution from thickness deformation results from changes in the separation between the upper and lower surfaces of the bilayer induced by the hydrophobic mismatch between the inclusion and the bilayer. This effect is depicted schematically in Fig. 4.3.6. The energetic contribution from this mismatch can be quite significant. Bilayer thickness deformation has been

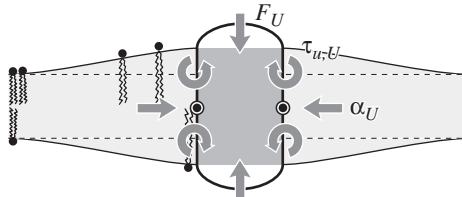


Figure 4.10: Bilayer thickness deformation due to a hydrophobic mismatch. In order to match the inclusion's hydrophobic boundary, the bilayer thickness must be deformed. Microscopically, the lipid tails are deformed as illustrated schematically above. The modulus for these deformations is  $K_A$ . For large mismatches, the energy contribution from thickness deformation can be quite significant. We estimate that this energy is important for MscL gating. Thickness deformation induces a compression-expansion force, a tension, and a shape torque which are also depicted above. The compression-expansion force acts to reduce the mismatch. The shape torque acts to induce interface tilt to reduce the bilayer bending. The tension generated by a mismatch is always compressive.

studied by many authors, Mouritsen and Bloom (1984), Huang (1986), etc. and more recently by Nielsen *et al.* (1998) and Goulian *et al.* (1998). These authors have all solved the model exactly, but we introduce a large radius asymptotic expansion to significantly simplify our results. Expanding the exact solution of the model in powers of the radius gives

$$G_U = G_U^{(0)} + G_U^{(1)} + \dots \quad (4.51)$$

where  $G_U^{(n)} \propto R^{1-n}$ . For MscL, the only important terms are the first two. In the Appendix we have plotted both the approximate and exact solutions to demonstrate that the interesting physics is captured by our approximations. Ignoring higher order terms, the resulting contribution is

$$G_U = \pi R [K_B (\beta_+ + \beta_-) (U' + [\beta_+ + \frac{1}{2R}] U) (U' + [\beta_- + \frac{1}{2R}] U) - \alpha U U'], \quad (4.52)$$

where

$$\beta_{\pm} \equiv \sqrt{\frac{\alpha \pm \sqrt{\alpha^2 - 4K_B K_A / a^2}}{2K_B}}. \quad (4.53)$$

We can simplify this expression further by defining a low tension limit (Goulian *et al.*, 1998):

$$\alpha \ll 2\sqrt{\frac{K_B K_A}{a^2}} \approx 0.34 \left( \frac{2a}{40.7 \text{ \AA}} \right) kT \text{ \AA}^{-2} \sim 10\alpha_* \quad (4.54)$$

which is roughly satisfied for the critical tension measured by Sukharev *et al.* (1999). (See the Appendix for details about the scaling and size of the elastic moduli. The tension above has been put into a dimensionless form using the parameters for a PC lipid of acyl length 18.) One might worry that for small bilayer thickness the small tension limit would no longer be satisfied, but we

will show that the opening tension is also reduced in this case. In the low tension limit,  $\beta_{\pm}$  is

$$\beta_{\pm} = e^{\pm \frac{i\pi}{4}} \left( \frac{K_A}{a^2 K_B} \right)^{\frac{1}{4}} = e^{\pm \frac{i\pi}{4}} \beta. \quad (4.55)$$

We will refer to  $\beta$  as the inverse decay length since it defines the length scale over which the thickness deformation perturbation decays. This length scale is given by

$$\beta^{-1} = \left( \frac{K_B a^2}{K_A} \right)^{1/4} \approx 11 \left( \frac{2a}{40.7 \text{ \AA}} \right) \text{ \AA}. \quad (4.56)$$

This decay length defines the large radius limit, which is satisfied even for the closed state of MscL since  $R_C > \beta^{-1}$ .

The dominant contribution at large radius is  $G_U^{(0)}$ , which corresponds to ignoring the curvature of the interface entirely (Dan *et al.*, 1993). To estimate the typical size of this contribution, we set  $U' = 0$

$$G_U^{(0)} = \pi R \mathcal{K} U^2 \approx 1.6 \left( \frac{R}{23 \text{ \AA}} \right) \left( \frac{U}{1 \text{ \AA}} \right)^2 kT, \quad (4.57)$$

where we have written the deformation energy in a dimensionless form using the closed state radius, a small mismatch ( $U = 1 \text{ \AA}$ ), and the effective elastic modulus  $\mathcal{K}$ , defined

$$\mathcal{K} \equiv \sqrt{2} \left( \frac{K_B K_A^3}{a^6} \right)^{\frac{1}{4}} \approx 2.16 \times 10^{-2} kT \text{ \AA}^{-3}. \quad (4.58)$$

This is the result listed in Table 6.1. Since large mismatches are possible and the deformation energy grows as the square of the mismatch, this contribution can be very significant. This  $U^2$  dependence, analogous to a linear spring, is exactly what we expect since the minimum energy occurs for a perfect thickness match between the protein and bilayer ( $U = 0$ ). Mouritsen and Bloom (1984, 1993) were the first to discuss this dependence. Its phenomenological significance has been stressed by Lundbæk *et al.* (1996). The thickness deformation energy is a function of both  $K_A$ , the local thickness deformation modulus, and the bending modulus,  $K_B$ . Physically,  $K_B$  provides a compatibility condition for adjacent lipids which sets the size of the deformed region. The thickness deformation energy is also roughly linear in  $R$  since the area of the bilayer deformed is roughly proportional to the channel circumference. The size of thickness deformation energy and its radial dependence imply that  $G_U^0$  is almost certainly important in the energetics of MscL. Unless both  $U'$  and  $U$  are zero or cancel, this term will contribute due to the radial expansion of the channel between the closed and open states. Even if the height of the hydrophobic region were to remain unchanged, this contribution would still be very significant (See Wiggins and Phillips, 2004). Let us mention, as a brief aside, that the functional form of  $G_U^0$  is a very pleasing result since, although the prefactor  $\mathcal{K}$  appears to depend on the bilayer width,  $a$ , it is roughly independent of  $a$ ! Please see

the Appendix for a brief argument. Because this scaling is not obvious and we will often use scaling arguments, we write the result in terms of  $\mathcal{K}$  to alleviate the temptation of thinking  $\mathcal{K} \propto a^{-3/2}$ .

One of the difficulties in implementing this model is the uncertainty concerning boundary conditions and in particular what slopes should be assigned for the bilayer-inclusion interface. One of the possibilities studied by other authors (Helfrich and Jakobsson, 1990), is to treat  $U'$  as a free parameter and minimize the free energy with respect to it. In the asymptotic limit this calculation becomes very simple. Taking the low tension limit ( $\alpha = 0$ ), and choosing  $U'$  to minimize  $G_U^{(0)}$ , gives a free energy half that which is obtained by naively assuming  $U' = 0$ , namely,

$$G_U^{(0),\text{Min}} = \frac{\pi R}{2} \mathcal{K} U^2. \quad (4.59)$$

As a result, we argue that the qualitative conclusions—the importance of this correction—are indifferent to the particular choice made for this boundary condition, but quantitatively the choice of boundary conditions can have a significant effect.

Although  $G_U^{(0)}$  dominates at large radius, for MscL-like geometries,  $G_U^{(1)}$  is roughly as large.  $G_U^{(1)}$ , which is radially independent, is

$$G_U^{(1)} = 2\pi \left( \frac{K_B K_A}{a^2} \right)^{1/2} U^2 \approx 1.1 \left( \frac{2a}{40.7 \text{ \AA}} \right) \left( \frac{U}{1 \text{ \AA}} \right)^2 kT, \quad (4.60)$$

for  $U' = 0$ , where the energy has been put in a dimensionless form using the closed state radius, and a small mismatch ( $U = 1 \text{ \AA}$ ). As can be seen above, for the closed state, this energy is almost as large as the dominant scaling term  $G_U^{(0)}$  and is also proportional to  $U^2$ . In general, the effects of this term on channel gating are not as pronounced since it is radially independent and will not contribute a term to the free energy difference between the open and closed states proportional to  $\Delta R$ . Likewise, it will not contribute to the tension. The asymptotic expressions for the thickness deformation energy are compared with the exact results to the linearized theory in Fig. 4.7.5 in the Appendix. We plot the thickness deformation energy for the closed state in Fig. 4.3.7, in the next section.

To develop physical intuition into how thickness deformation affects the channel conformation and function, we calculate the generalized forces induced on the inclusion. The tension is

$$\alpha_U = -\frac{\mathcal{K} U^2}{2R} \approx -2.0 \times 10^{-2} \left( \frac{23 \text{ \AA}}{R} \right) \left( \frac{U}{1 \text{ \AA}} \right)^2 \frac{\text{pN}}{\text{\AA}}, \quad (4.61)$$

which has been written in a dimensionless form as described above. The induced tension acts to close the channel. For a  $1 \text{ \AA}$  mismatch, the tension is roughly a sixtieth of what Sukharev *et al.* (1999) measured for the opening tension, but for larger mismatches, the tensions can become comparable, significantly reducing the net tension or, at small enough applied tension, becoming the dominant

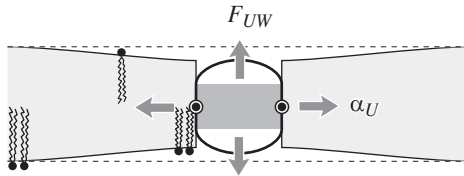


Figure 4.11: Bilayer thickness deformation saturates when the energy required to further deform the membrane is equal to the interface energy required to create a hydrophobic-hydrophilic interface. This failure of the bilayer to conform to the protein is depicted schematically above.

contribution. Since tensions of this size are responsible for triggering the channel to switch from the closed to the open conformation, this calculation strongly suggests that the thickness deformation energy plays an important role in channel function and conformation. The thickness deformation also generates a shape torque

$$\tau_{u,U} = -2\pi R \frac{\sqrt{K_A K_B}}{a} \left( 1 + \frac{1}{\sqrt{2}\beta R} \right) U \quad (4.62)$$

when  $U' = 0$ . We can estimate the dominant term at large radius

$$\tau_{u,U} \approx -25 \left( \frac{R}{23 \text{ \AA}} \right) \left( \frac{2a}{40.7 \text{ \AA}} \right) \left( \frac{U}{1 \text{ \AA}} \right) kT, \quad (4.63)$$

which has been written in a dimensionless form as described above. The shape torque can be quite large for large mismatches. Its sign depends on the mismatch  $U$ .

### 4.3.7 Saturation of Thickness Deformation

Due to the quadratic dependence of the thickness deformation energy on mismatch, it is initially energetically favorable to deform the thickness of bilayer, rather than expose the hydrophobic region of the protein to the solvent. But, this quadratic dependence also implies that the energetic cost of further deformation will continue to grow, until, at a critical mismatch, it becomes more costly than exposing this added region to the solvent. This critical mismatch is related to the compression force on the inclusion due to the thickness deformation. Recalling that  $U \equiv W/2 - a$ , the compressive force on the protein is

$$F_U = -\frac{\pi R}{2} \mathcal{K}(W - 2a) \left( 1 + \frac{\sqrt{2}}{\beta R} \right) \approx -54 \left( \frac{R}{23 \text{ \AA}} \right) \left( \frac{W - 2a}{1 \text{ \AA}} \right) \text{ pN}, \quad (4.64)$$

which has been written in a dimensionless form as described above. The change in the thickness deformation energy for increasing the hydrophobic region of the protein from  $W$  to  $W + dW$  is  $-F_U dW$  whereas to expose the added region to solvent results in an energy increase of  $-F_{W^*} dW$ .

At the critical mismatch, these two forces are equal

$$F_{W^*} = F_U(W). \quad (4.65)$$

Solving for  $2U$  gives the critical mismatch

$$2U_* \equiv |W - 2a| = \frac{4\sigma_*}{\mathcal{K}\left(1 + \frac{\sqrt{2}}{\beta R}\right)} \approx 5 \text{ \AA}, \quad (4.66)$$

which has been estimated for an acyl length 18 PC lipid bilayer and the closed state radius. The details of the saturated thickness deformation energy are worked out in the Appendix. This saturated deformation energy is compared to the thickness deformation energy and experimental deformation energies measured by Powl *et al.* (2003) in Fig. 4.3.7. For large mismatch, there are discrepancies between the experimental data and all the theoretical models. It is unclear whether the lipid finds a more energetically efficient method for offsetting the mismatch. In principle lipid packing calculations could answer these types of questions, but typically they are too constrained to capture this type of behavior. We shall return to this question in the next section.

Over the course of this entire section, we have provided a term-by-term dissection of the various contributions to the free energy of deformation associated with channel gating. The main point of this exercise has been to provide a framework for thinking about the connection between ion channel gating and the corresponding perturbations induced in the surrounding lipid bilayer membrane.

## 4.4 Application to MscL Gating

The conformational landscape of the MscL protein is certainly extremely complex, depending on a large number of microscopic degrees of freedom which are analytically intractable. Even from the standpoint of numerical calculations, this number is still very large (Gullingsrud *et al.*, 2001). What is the point of examining what is presumably only half the story by treating the bilayer analytically? The purpose of this model is to pose a theoretical problem simple enough to be completely soluble, yet not so simple that it bears too little resemblance to the complex system it represents. By understanding the consequences of the simplest models, we develop a framework in which to understand the richer dynamics of the real system, whether approximated by molecular dynamics simulations or studied in experiments. There is a wealth of useful, physical intuition to be gleaned from this model relating to both the function of the mechanosensitive channel (MscL) and that of mechanosensitive transmembrane proteins in general.

As we have argued in the previous section, the bilayer deformation energy is comparable to the measured free energy differences between states for the MscL channel. Therefore the bilayer must

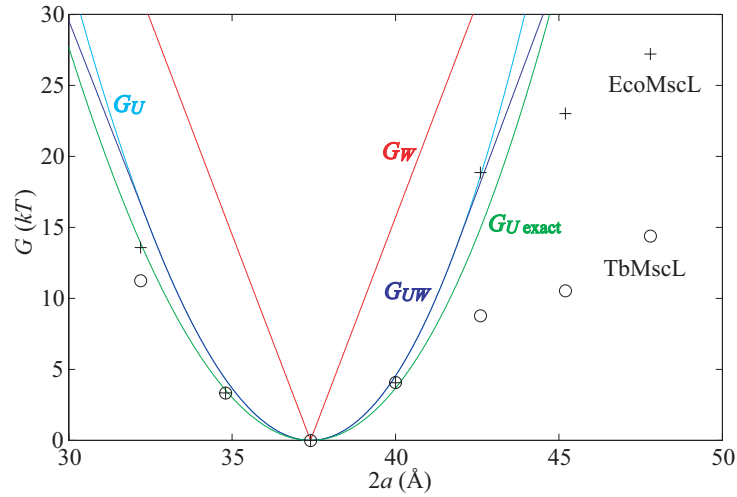


Figure 4.12: Interface and thickness deformation energy of the closed state compared to experimental data from Powl *et al.* (2003) as a function of lipid bilayer thickness. The red curve is the hydrophobic interface energy ( $G_W$ ) without thickness deformation (the limit as  $\mathcal{K} \rightarrow \infty$ .) The green curve is the exact thickness deformation energy ( $G_{U \text{ exact}}$ ) without saturation. The cyan curve is the asymptotic thickness deformation energy ( $G_U$ ) without saturation (the limit as  $\sigma_* \rightarrow \infty$ .) The blue curve is the saturating thickness deformation energy ( $G_{UW}$ , see the Appendix for details). The o's and +'s are the experimental values measured by Powl and coworkers for TbMscL and EcoMscL respectively. We have chosen the closed state thickness of the channel ( $W_C = 37.5 \text{ \AA}$ ) to match the thickness of the bilayer at the minimum of the experimental bilayer deformation energy. This thickness is compatible with the known closed state structure. For small mismatches there is a much better qualitative agreement between the thickness deformation energy than the hydrophobic interface theory. For large mismatch, the experimental data points are significantly smaller than the energy predicted by theory. We discuss this apparent discrepancy in the next section.

play an important role in determining the free energy balance between states, altering the channel function. It is also likely that the forces generated by bilayer deformation can significantly perturb the conformation of the states themselves. Indeed, to the extent that membrane deformations induce conformational changes in the protein itself, the structure of the protein itself becomes lipid context dependent, complicating predictions. At present, we treat the protein as a black box which gives us a fixed geometry for state  $i$  described by the state vector  $X_i$ , and a protein conformational free energy,  $G_{P,i}$ . As we have discussed above, the geometry of the channel in the  $i$ th conformational state is described by the radius ( $R_i$ ), the hydrophobic thickness ( $W_i$ ), and the two angular parameters that we usually interpret as the shape of the protein's interface ( $U'_i, H'_i$ ). Please see Fig. 4.2.1 and Sect. 4.2.2. These protein parameters are combined, for economy of notation, into the state vector  $X_i$ ,

$$X_i \equiv (R_i, W_i, U'_i, H'_i). \quad (4.67)$$

We assume these protein parameters are fixed by internal conformation and do not depend on the parameters of the bilayer membrane such as the lengths of the lipid tails or the concentration of spontaneous curvature inducing lipids, nor on the applied tension,  $\alpha$ . We will call this simplified picture the static conformation approximation. Explicitly, we assume the free energy takes the form

$$G_i = G_{P,i} + G_{\mathcal{M}}(X_i), \quad (4.68)$$

for state  $i$  where  $G_{P,i}$  and  $X_i$  are independent of the bilayer parameters and the applied tension. In principle, we can try to determine the unknown state vectors,  $X_i$ , by varying the membrane parameters and the applied tension. Of course the primary advantage of the static conformation approximation is that it allows simple predictions to be made relating to the channel gating. This model is probably reasonable for relatively modest changes to the bilayer parameters provided that the free energy wells corresponding to the conductance states are relatively sharp and well defined with respect to changes in the state vector  $X_i$ .

#### 4.4.1 Opening Probabilities for Two State System

The difference in free energy between the open and closed states is defined as

$$\Delta G = -kT \log \frac{\mathcal{P}_O}{\mathcal{P}_C} = \Delta G_P + \Delta G_{\mathcal{M}}, \quad (4.69)$$

where  $\mathcal{P}_i$  is the probability of state  $i$ , and  $\Delta$  here is the difference between open and closed. Notice that this expression is independent of the free energies of the other states as a result of working with the ratio of the open and closed probabilities. For ease of interpretation, it is convenient to further

subdivide the free energy by subtracting off the areal deformation contribution such that

$$\Delta G = \Delta G_P + \Delta G_{\mathcal{M}}^0 - \alpha \Delta A, \quad (4.70)$$

where the  $\Delta G_{\mathcal{M}}^0$  is the bilayer deformation energy less the areal contribution. Since we expect the only tension dependence to come from the linear areal deformation term, the measured  $\Delta G$  should be linear in tension. What would a non-linear behavior tell us? It would signal that there is additional tension dependence in the terms above. Provided that we are convinced the bilayer terms are correct, it would signal that the static conformation approximation is failing: the conformation of the state is tension dependent! Data from Sukharev *et al.* (1999) have shown that  $\Delta G$  is at least fairly linear in tension. Assuming that linear dependence discussed above is correct, the slope with respect to tension of the free energy gives us the area change:

$$\Delta A = -\frac{\partial \Delta G}{\partial \alpha} \quad (4.71)$$

and the free energy can be written in a convenient form (Hamill and Martinac, 2001)

$$\Delta G = \Delta A (\alpha_{1/2} - \alpha), \quad (4.72)$$

where  $\alpha_{1/2}$  is the opening tension (where the probability of being open or closed is equal) and is given by

$$\alpha_{1/2} = \frac{\Delta G_P + \Delta G'_{\mathcal{M}}}{\Delta A} = \frac{\Delta G_0}{\Delta A}, \quad (4.73)$$

where  $\Delta G_0$  is the free energy change with the areal deformation contribution removed or alternatively the free energy difference at zero tension. When the free energy is written in terms of the opening tension (Eq. 4.72), it is clear that changes in the lipid parameters, such as the equilibrium thickness for example, lead to a simple offset of the opening tension, leaving the dependence of the ratio of open to closed probabilities versus applied tension otherwise unchanged, as Perozo *et al.* (2002a) have observed. This observed offset behavior is indirect evidence that the change in the area between the closed and open states is roughly independent of the bilayer parameters, implying that the open and closed states are fairly well defined, at least radially. In the rest of the paper we will refer to  $\Delta G_0$  as the free energy difference, dispensing with the subscript.

In patch clamp experiments, the tension is controlled indirectly via the pipette pressure. The pressure and tension are related using Laplace's law:

$$P = \frac{2\alpha}{\mathcal{R}}, \quad (4.74)$$

where  $\mathcal{R}$  is the radius of curvature of the membrane patch. Typically it is assumed that this curvature

is roughly constant during the experiment (e.g., Hamill and Martinac, 2001) which implies that opening pressure is proportional to the opening free energy

$$\Delta G_0 = P_{1/2} \left[ \frac{\partial G}{\partial P} \right]_{P_{1/2}}, \quad (4.75)$$

where the derivative of  $G$  is expected to be constant since it is  $\Delta A \mathcal{R}/2$ .

#### 4.4.2 Mismatch and Gating

Before we begin our analysis in earnest, we wish to quickly remind the reader of the differences in the current model from that in our recent short paper (Wiggins and Phillips, 2004). In our previous paper we developed a simplified version of the model described above. The only geometrical change between the open and closed states was in the channel radius. In that model, the energetics of the bilayer deformation energy is one dimensional and can be analyzed as a competition between the bilayer line tension and the applied tension (Wiggins and Phillips, 2004)

$$G_{\mathcal{M}} = f \cdot 2\pi R - \alpha \cdot \pi R^2, \quad (4.76)$$

where  $f$  is the line tension and where the only free parameter is the effective thickness of the protein which we fit using the data of Perozo *et al.* (2002a). On the other hand, the simplifications associated with this model (i.e., we did not differentiate between the thickness of the open and closed states) leave it unable to reproduce the data of Powl *et al.* (2003) which essentially measures the bilayer deformation of the closed state. In spite of this limitation, this simple theory based upon the competition between the line tension and applied tension reveals that (i) the acyl chain length dependence of the opening free energy as measured by Perozo *et al.* (2002a,b) is very naturally explained by the thickness deformation energy and can qualitatively explain that (ii) spontaneous curvature could lead to open state stabilization and that (iii) the substates of the channel should be short lived. In this section, we undertake a more quantitative analysis in which we allow the open and closed states to have different hydrophobic thicknesses. In particular, we analyze the experimental data from three different classes of experiments in detail. First, we focus on the opening free energy measurements by Perozo *et al.* (2002a). Next, we analyze the lipid-MscL interaction data from Powl *et al.* (2003) and finally, we consider the recent mutation studies by Yoshimura *et al.* (2004) who altered amino acids in the transmembrane region of MscL. Note that we argue that our model should be viewed more as serving as an interpretive tool than as a scheme for fitting experimental data. As will be seen in the discussion to follow, the act of interpreting the data from these various experiments consistently suggests that the usual view of static protein structures that are lipid independent may have to be amended.

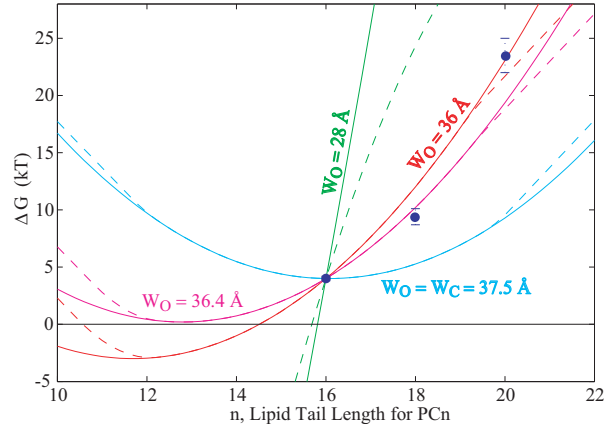


Figure 4.13: The theoretical free energy difference compared to the experimental data of Perozo *et al.* (2002a) for different choices of the geometric parameters characterizing the open state thickness. The thickness deformation energy is plotted for a closed state thickness of  $W_C = 37.5 \text{ \AA}$  and several different open state thicknesses. Each curve is shifted to pass through the data point at an acyl chain length of 16. An open state thickness of  $W_O \sim 36 \text{ \AA}$  give a reasonable fit to the experimental data. Perozo and coworkers also have electron paramagnetic resonance data for bilayers with acyl chain lengths  $n \geq 10$  which suggest that the channel is closed ( $\Delta G \geq 0$ ) in the absence of applied tension.

Perozo *et al.* (2002a) have measured the opening free energy of the channel for three bilayers with acyl chain lengths 16, 18, and 20. We will fix the thickness of the closed state ( $W_C = 37.5 \text{ \AA}$ ) based on experimental data from Powl *et al.* (2003) and corroborating computational evidence from Elmore and Dougherty (2003). This assignment seems reasonable based on the distribution of the hydrophobic residues in the closed state crystal structure as illustrated in Fig. 4.2.1. We now vary the open state thickness,  $W_O$ , and compare the resulting opening free energy versus lipid acyl chain length to the experimental data of Perozo *et al.* (2002a). While Perozo and coworkers have measured the opening free energy for only three acyl chain lengths, their electron paramagnetic resonance (EPR) data suggests that even in acyl chain length 10 lipid bilayers, the channel does not open spontaneously in the absence of applied tension. This qualitative information provides an additional constraint for the theory to satisfy ( $\Delta G \geq 0$  for  $n \geq 10$ ). We find that for  $W_O \sim 36 \text{ \AA}$ , we have the best agreement with the experimental data. The comparison between the theoretical opening free energy and the measured values as a function of acyl chain length is depicted in Fig. 4.4.2. Our fit with the experimental data is reasonable considering the complexity of the channel system and the naivete of the static conformation model. The inability of the theory to fit the data exactly is to be expected from a model where the elastic constants have been fit to scaling laws and the subtle conformational changes of the protein are ignored. As noted earlier, we view our model as a framework for interpreting previous experiments and suggesting new ones, as well as for providing intuition, rather than as a fitting scheme. As is clear from the figure, it is quite difficult to satisfy

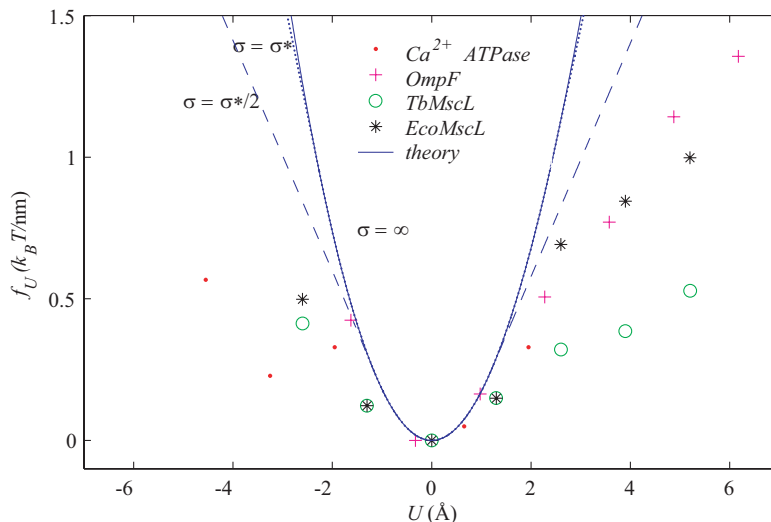


Figure 4.14: The theoretical line tension for MscL compared with the line tension estimated from the measurements of East, Lee and coworkers (East and Lee, 1982; O’Keeffe *et al.*, 2000; Powl *et al.*, 2003). The experimental data for several different proteins has been aligned so that the minimum line tension is assumed to correspond to zero mismatch. In the small mismatch regime, there is very reasonable agreement between theory and the measurements. At large mismatch the story becomes more complicated. There is significant variation between proteins, and even between Eco and Tb MscL. These variations may signal conformational changes in the protein. The methods of East and Lee are only sensitive to the free energy in the first layer of lipids surrounding the proteins. It is therefore natural to expect the theoretical line tension to be larger than the measured line tension. We have plotted the saturating thickness deformation energy ( $G_{UW}$ ) for interface energies  $\sigma = \infty$  (solid),  $\sigma = \sigma_*$  (dotted), and  $\sigma = \sigma_*/2$  (dashed) since  $\sigma_*$  probably underestimates the saturation effect since the interface of the bilayer which would initially be exposed to solvent is not extremely hydrophobic (e.g. White and Wimley, 1999).

both the large mismatch opening free energy for acyl length  $n = 20$  and the constraint that the channel be closed ( $\Delta G \geq 0$ ) for acyl length  $n \geq 10$ . In light of the proposed structures for the open state (Sukharev *et al.*, 2001a,b; Betanzos *et al.*, 2001; Perozo *et al.*, 2002a,b), our predicted change in channel thickness is quite modest. (See Fig. 4.2.1.) An open state with a smaller thickness satisfies neither the large  $n$  nor the small  $n$  limits.

We must treat the predictions of the theory with care when the mismatch is large since the theoretically predicted bilayer deformation energies are probably large enough to lead to protein conformational changes, violating our static geometry approximation. That is to say, either or both the closed and open states of the protein deform significantly. This systematic uncertainty is not a peculiarity of our models but a quite general uncertainty. For example, it is unclear that the lysophosphatidylcholine (LPC) stabilized conformation observed by Perozo *et al.* (2002a,b) is in precisely the same conformation as the open state of the channel stabilized by applied tension, reconstituted in a PC18 bilayer. One experimentally accessible probe to conformational changes is a precise measurement of the applied tension dependence of the free energy difference between

states. If the open and closed states are significantly perturbed by the applied tension, we would expect a deviation from the linear dependence (Eq. 4.71) of the free energy on applied tension. Alternatively, precise measurements of the area change between the open and closed states in different bilayers might show that the area change is lipid context dependent. We revisit the question of conformational changes below. At present, we conclude that experimental data of Perozo *et al.* (2002a,b) is compatible with the model. Due to both the approximate nature of the static geometry approximation and the systematic uncertainties inherent in patch clamp measurements of channel opening free energies (E. Evans, personal communication) it is important not to place too high a premium on the precise fitting of the data of Perozo *et al.* (2002a).

A more direct experimental method for analyzing the free energy of the MscL closed state has been exploited by Powl *et al.* (2003). East, Lee and coworkers (East and Lee, 1982; O’Keeffe *et al.*, 2000; Powl *et al.*, 2003) have developed Trp fluorescence spectroscopy to study lipid-protein interactions. Their technique measures the lipid-protein binding constant for channels reconstituted in liposomes. The log of this binding constant is the free energy difference between lipids at the boundary and lipids in the bulk of the bilayer (See Powl *et al.*, 2003 for details.) This free energy per lipid can then be converted into a line tension at the interface. While this experimental technique provides a very direct measurement of the free energy per lipid, it is only sensitive to the free energy in the first layer of lipids surrounding the protein where there is direct interaction between lipid and protein. Powl *et al.* (2003) measure a minimum line tension for an acyl chain length of 16, which roughly corresponds to a thickness of 37.5 Å. We assume that this chain length corresponds to zero mismatch, implying that the thickness of the closed state equals the equilibrium thickness of the bilayer:

$$W_C = 2a_{16}. \quad (4.77)$$

We can now compute a theoretical line tension for the closed state as a function of acyl chain length. In Fig. 4.4.2, we compare the experimental measurements of this line tension to the thickness deformation line tension predicted by theory. In the small mismatch regime, there is very reasonable agreement between theory and measurement. This is a nontrivial result since although we have fit the data to choose the minimum of the line tension, the curvature of the line tension (the second derivative with respect to the protein thickness) is predicted by the bending moduli of the membrane measured at very small curvature on  $\mu\text{m}$  length scales! At large mismatch, the predictions of the theoretical model are significantly higher than the experimentally measured values. There are several possible explanations for this discrepancy: (i) the predictions of the theory are too large for large mismatch signaling the onset of nonlinear elastic effects, for example, (ii) there are systematic problems comparing this competition assay to the deformation energy, or (iii) conformational changes in the protein reduce the size of the mismatch. For the moment, let us assume that the theory is

incorrect for large mismatch (i). If we use the measured line tension,  $f_U^{\text{exp}}$ , for a given mismatch, we can estimate the bilayer deformation free energy change between the open and closed states

$$\Delta G' = [f_U^{\text{exp}} \cdot 2\pi R]_O - [f_U^{\text{exp}} \cdot 2\pi R]_C, \quad (4.78)$$

where the ' is used to differentiate this computed free energy difference from that measured by Perozo *et al.* (2002a).  $\Delta G'$  can then be compared to the measured values of Perozo *et al.* (2002a) ( $\Delta G$ ) with the aim of examining the internal consistency of the model and both datasets. For  $W_O = 36 \text{ \AA}$ , the free energies are presented in Table 4.2. Remember that the numbers from Perozo are the total free energy change between states, the sum of both the membrane and protein free energy changes, while those we have estimated from the data of Powl include only the membrane interaction term. As before we will assume that the conformation and energy of the protein are roughly static, independent of the bilayer lipid acyl chain length. We therefore expect the free energy differences of Perozo and Powl to differ by a constant, corresponding to the protein conformational free energy difference,  $\Delta G_P$ . To eliminate the  $\Delta G_P$  contribution, we examine the relative changes in the opening free energy relative to the opening free energy for the acyl chain length 16 bilayer

$$\Delta\Delta G \equiv \Delta G - \Delta G_{16}. \quad (4.79)$$

The data of Powl *et al.* (2003) predicts the difference between the acyl chain lengths 16 and 18 ( $\Delta\Delta G_{18} \approx \Delta\Delta G'_{18}$ ), but fails spectacularly to predict the difference between the acyl chain lengths 16 and 20 ( $\Delta\Delta G_{20} \neq \Delta\Delta G'_{20}$ ). The agreement for small mismatch is no surprise since there is reasonable agreement between the measured line tension of Powl *et al.* (2003) and theory. But for large mismatch the measured line tension is just far too small to match the data of Perozo *et al.* (2002a). The reader may wonder whether this situation might be mitigated by changing the value of  $W_O$ . However, it is very difficult to reconcile such small values of the line tension with the measured free energy differences of Perozo. Perhaps the most distinct characteristic of the data of East, Lee and coworkers is the variation in the line tension for large mismatch between proteins and even between Eco and Tb MscL. This would seem to suggest, as they have speculated (Powl *et al.*, 2003) that conformational changes in the protein (iii) are the most attractive explanation for large mismatch dependence of the line tension. As we have already speculated, we expect the static conformation approximation to break down for large mismatch. It is difficult to rule out that there may be systematic problems with comparing the results of this competition assay to theoretical estimates for a single component bilayer. The environment in the bulk of the mixed bilayer is different from that of a single component bilayer. Furthermore, for large mismatches, a very significant fraction of the deformation energy is not localized in the first ring of lipids surrounding the protein and hence, is not revealed in the measurements of Powl *et al.* We would expect these membrane related

$n$	$\Delta G$ (kT)	$\Delta\Delta G$ (kT)	$\Delta G'$ (kT)	$\Delta\Delta G'$ (kT)
16	4	0	1.5	0
18	9.4	5.4	6.6	5.1
20	23.5	19.5	7.5	6

Table 4.2: Summary of the free energy differences measured by Perozo *et al.* (2002a) and those predicted from the line tension measured by Powl *et al.* (2003).  $n$  is the acyl chain length,  $\Delta G$  is the free energy differences between the open and closed state measured by Perozo *et al.* and  $\Delta G'$  is the deformation free energy difference predicted using the data of Powl *et al.* The relative free energy changes are defined  $\Delta\Delta G \equiv \Delta G - \Delta G_{16}$  and  $\Delta\Delta G' \equiv \Delta G' - \Delta G'_{16}$ . (See the Appendix for more details on this calculation.)

systematic errors to be independent of the protein, in contrast to experimental observations. A much more meaningful comparison to the data of Perozo *et al.* (2002a) might be attempted if the same measurements were repeated for the MscL channel trapped in the open state (perhaps via crosslinking). This direct measurement of the bilayer interaction free energy would be a useful addition to the experimental story and provide a direct experimental test of our predicted value of the open channel thickness,  $W_O$ .

In our previous paper (Wiggins and Phillips, 2004) we proposed that the width of the hydrophobic region of the protein could be engineered to adjust the gating tension of the channel. Shortly after our paper appeared, Yoshimura *et al.* (2004) published data describing precisely this type of experiment. Yoshimura and coworkers mutated residues in the hydrophobic region of the protein to hydrophilic asparagine and studied the gain/loss of function in the mutants. Single mutations were shown to possess significant loss of function phenotypes especially for mutations at the boundaries of the hydrophobic interface region of the channel. Yoshimura and coworkers also measured the the relative increase in gating pressure which is roughly proportional to the ratio of the opening free energies (see Eq. 4.75). Of the mutated channels which Yoshimura and coworkers were able to gate, there were mutations which gated at 1.5 times the wild-type pressure. The most severe loss of function mutations did not gate up to pressure of roughly twice the wild type gating pressure. Theoretically, we can estimate the change in the opening free energy due to these alterations in the protein-lipid interface. For a small change in the hydrophobic width of the channel ( $dW = dW_O = dW_C$ )

$$d\Delta G = -(\Delta F_U) dW \approx -3.5 \left( \frac{dW}{1 \text{ \AA}} \right) kT, \quad (4.80)$$

for typical values ( $W_O = 36 \text{ \AA}$ ,  $W_C = 37.5 \text{ \AA}$ , and  $n = 18$ ). (Since these patch-clamp measurements were performed in spheroplasts rather than synthetic liposomes, the effective lipid parameters are unknown.) We expect the change in the opening tension to be roughly

$$\Delta\alpha_{1/2} = \frac{d\Delta G}{\Delta G_A} \alpha_{1/2} \approx 0.3 \left( \frac{dW}{1 \text{ \AA}} \right) \alpha_{1/2}, \quad (4.81)$$

where we used the same parameters as above to estimate the relative change in the opening tension. (Remember that the relative change in the opening tension and pressure will be the same if the patch radius is roughly constant.) The free energy changes corresponding to reducing the size of the hydrophobic interface of the protein by a few Angstrom might energetically account for the observed increase in gating pressure and perhaps for those channels which did not gate. We hope to see this experiment repeated in synthetic liposomes where we would have more theoretical control of the system or alternatively studied with the methods employed by Powl *et al.* (2003) so that the change in the line tension for the closed state might be measured. We cannot rule out that more subtle mechanisms are responsible for the changes in the gating sensitivity. For example, in molecular dynamics simulations Gullingsrud and Schulten (2003) have drawn attention to the significance of the region of the protein interface on which the tension is applied.

Computationally, thickness deformation of the membrane has been observed in molecular dynamics simulations performed by Elmore and Dougherty (2003). Their simulations of MscL in the closed conformation for lipid acyl chain lengths 10-18 reveal that the lipids at the interface deform to offset the mismatch, at least *in silico*. Their simulations have also captured a complementary reduction in the protein hydrophobic interface thickness, a conformational change which violates our static conformation approximation (as well as the implicit static conformation approximation in Perozo *et al.*, 2002b, or Sukharev *et al.*, 2001) but which we have speculated may play a role in the discrepancy between our theoretical predictions and experimental measurements. This protein deformation could, in principle, be used to further generalize our analytic model, replacing the static conformation approximation with a model allowing protein deformation induced by the membrane, though the effective spring constant penalizing lipid-induced protein shape changes would need to be determined computationally. In fact, the spring constant for the closed state could be deduced from the data already provided by Elmore and Dougherty (2003). This more general model would be a natural extension to the model discussed here.

#### 4.4.3 Spontaneous Curvature and Gating

While we have discussed several quantitative studies of acyl chain length versus free energy, the effects of spontaneous curvature on gating has, to our knowledge, only been studied by Perozo *et al.* (2002a,b). Perozo and coworkers have shown that bilayers asymmetrically doped with LPC, a spontaneous-curvature-inducing surfactant, can stabilize the open state in the absence of tension. In our recent paper (Wiggins and Phillips, 2004) we showed that spontaneous-curvature-induced line tension could result in precisely this effect. However, we have been unable to make a quantitative analysis of this idea since the opening free energy has not been measured as a function of LPC concentration. (See predictions in Fig. 6.11.) We expect the concentration dependence of the free energy difference to be linear in LPC concentration. More complicated scenarios are also possible.

If the interface tilt is induced by LPC, we would expect a roughly quadratic rather than linear dependence on LPC concentration.

## 4.5 Conclusion

The MscL channel is an appealing system in which to study lipid-protein interactions since its function is to couple tension in the lipid membrane to protein conformation. During the gating transition, the channel undergoes a very large conformation change, dramatically expanding radially and leading to a significant local rearrangement of the lipid bilayer. The deformation free energies induced by this rearrangement and their role in channel gating has been the focus of this paper. While many uncertainties remain, we believe the start of a consistent story has begun to emerge from experiment. Indeed, we speculate that the framework described here might prove useful in analyzing the function of any ion channel whose gating leads to perturbations in the surrounding membrane.

Our goal in this paper has been to build an analytic framework in which to provide quantitative interpretation and compare experimental results on MscL gating. To that end, we have expanded and improved upon an existing simple analytic membrane-protein model and applied it to mechanotransduction and the MscL system. In Sect. 4.3, we have estimated the size of various contributions to the deformation energy of the membrane and have discussed the scaling of these contributions. In Sect. 4.4, we have shown how this model, when coupled with a simple two state static conformational model of the MscL channel qualitatively and quantitatively agrees with most all of the experimental features of channel gating, although one important geometrical parameter, the open state thickness of the protein, must still be fit. As part of our analysis, the model suggests that the assumption that protein conformational states are independent of their lipid context (such as the lengths of the lipids that the channel is reconstituted in) is perhaps not borne out experimentally, making structural models of gating even more subtle. Beyond the interpretation of existing experimental data, we have proposed a number of experiments which we believe will further elucidate the mechanisms of channel gating. Specifically, additional experiments analogous to those performed by Powl *et al.* (2003) with the channel locked into the open state could provide topical information about the conformation of the open state and its interaction with the membrane. Such data, when combined with the data already available for the closed state, would allow a direct comparison to the gating free energies measured by Perozo *et al.* (2002a) and a test of our predictions of how the free energy depends on the geometry of the open state. We still believe that a more controlled version of the experiments performed by Yoshimura *et al.* (2004), when combined with careful modeling would allow the sensitivity of the channel to be tuned by changing the size of the hydrophobic interface. We hope that these experiments will be repeated in synthetic liposomes where the theoretical model

is easier to apply. Finally, we suggest the need for a detailed test of the static conformation approximation by a careful measurement of the area change between states as a function of both applied tension and acyl chain length. We hope that the approximations developed in this paper will be useful in precisely formulating quantitative experimental questions.

## 4.6 Acknowledgments

We are grateful to Doug Rees, Tom Powers, Jané Kondev, Klaus Schulten, Sergei Sukharev and Evan Evans for useful discussions, suggestions, and corrections. We also acknowledge support from NSF grant CMS-0301657 and the NSF funded Center for Integrative Multiscale Modeling and Simulation as well as the Keck Foundation. PAW acknowledges support through an NSF fellowship.

## Bibliography

Aranda-Espinoza, H., A. Berman, N. Dan, P. Pincus, S. A. Safran. 1996. Interaction Between Inclusions Embedded in Membranes. *Biophys. J.* 71:648-656.

Bass, R. B., P. Srop, M. Barclay, D. C. Rees. 2002. Crystal Structure of Escherichia coli MscS, a Voltage-Modulated and Mechanosensitive Channel. *Science.* 298:1582-1587.

Ben-Shaul, A. 1995. Molecular theory of chain packing, elasticity and lipid protein interaction in lipid bilayers. *In Structure and Dynamics of Membranes*, Vol 1, 2nd Ed. R. Lipowsky and E. Sackmann, editors. Elsevier, Amsterdam. 359-402.

Betanzos, M., C. S. Chiang, H. R. Guy, et al. 2002. A large iris-like expansion of a mechanosensitive channel protein induced by membrane tension *Nat. Struct. Biol.* 9:704-710

Bilston, L. E., K. Mylvaganam. 2002. Molecular simulations of the large conductance mechanosensitive (MscL) channel under mechanical loading. *FEBS. Lett.* 512:185-190.

Blount, P., P. C. Moe. 1999. Bacterial mechanosensitive channels: integrating physiology, structure and function. *Trends. Microbiol.* 7 (10):420-424.

Boal D. 2002. *Mechanics of the Cell.* Cambridge:Cambridge University Press.

Canham, P. B. 1970. The Minimum Energy of Bending as a Possible Explanation of the Biconcave Shape of the Human Red Blood Cell. *J. Theoret. Biol.* 26:61-81.

Cantor, R. S. 1999. Lipid Composition and the Lateral Pressure Profile in Bilayers. *Biophys. J.*

76:2625-2639.

Cantor, R. S. 1997. Lateral Pressure in Cell Membranes: A Mechanism for Modulation of Protein Function. *J. Phys. Chem. B* 101:1723.

Chang, G., R. H. Spencer, A. T. Lee, M. T. Barclay, D. C. Rees. 1998. Structure of the MscL homologue from *Mycobacterium tuberculosis*: A gated mechanosensitive ion channel. *Science*. 282 (5397):2220-2226.

Chen, Z., R. P. Rand. 1997. The Influence of Cholesterol on Phospholipid Membrane Curvature and Bending Elasticity. *Biophys. J.* 73:267-276.

Chiang C. S., A. Anishkin, S. Sukharev. 2004. Gating of the large mechanosensitive channel in situ: Estimation of the spatial scale of the transition from channel population responses. *Biophys. J.* 86: 2846-2861.

Dan, N., A. Berman, P. Pincus, and S. A. Safran. 1994. Membrane-induced interactions between inclusions. *J. Phys. II France*. 4:1713-1725.

Dan, N., P. Pincus, and S. A. Safran. 1993. Membrane-Induced Interactions between Inclusions. *Langmuir*. 9:2768-2771.

Dan, N., S. A. Safran. 1995. Solubilization of Proteins in Membrane. *Israel J. Chem.* 35:37-40.

Dan, N., S. A. Safran. 1998. Effect of Lipid Characteristics on the Structure of Transmembrane Proteins. *Biophys. J.* 75:1410-1414.

de Kruijff, B. 1997. Lipids beyond the bilayer. *Nature*. 386:129-130.

de Kruijff, B., A. M. H. P. van den Besselaar, L. L. M. van Deene. 1977. Outside-inside distribution and translocation of lysophosphatidylcholine in phosphatidylcholine vesicles as determined by  $^{13}\text{C}$ -NMR using (N- $^{13}\text{CH}_3$ )-enriched lipids. *Biochimica et Biophysica Acta*. 465:443-453.

East, J. M., A. G. Lee. 1982. Lipid selectivity of the calcium and magnesium-ion dependent adenosine-triphosphatase, studied with fluorescence quenching by a brominated phospholipid. *Biochem-US* 21:4144-4151.

Elmore, D. E., D. A. Dougherty. 2003. Investigating Lipid Composition Effects on the Mechanosensitive Channel of Large Conductance (MscL) Using Molecular Dynamics Simulations. *Biophys. J.* 85:1512-1524.

- Evans, E. A. 1974. Bending Resistance and Chemically Induced Moments in Membrane Bilayers. *Biophys. J.* 14:923-931.
- Evans, E. A. personal communication.
- Fattal, D. R., A. Ben-Shaul. 1993. A molecular model for lipid protein interaction in membranes: the role of hydrophobic mismatch. *Biophys. J.* 65:1795-1809.
- Fournier, J. B. 1999. Microscopic membrane elasticity and interactions among membrane inclusions: Interplay between the shape, dilation, tilt and tilt-difference modes. *Eur. Phys. J. B.* 11 (2):261-272.
- Gillespie, P. G., R. G. Walker, 2001. Molecular basis of mechanosensory transduction. *Nature.* 413:194-202.
- Goulian, M., O. N. Mesquita, D. K. Fygenson, C. Nielsen, O. S. Andersen, A. Libshaber. 1998. Gramicidin Channel Kinetics under Tension. *Biophys. J.* 74:328-337.
- Gruner S. M. 1989. Stability of Lyotropic Phases with Curved Interfaces. *J. Phys. Chem.* 93:7562-7570.
- Gullingsrud, J. R., D. Kosztin, K. Schulten. 2001. MscL gating studied by molecular dynamics simulations. *Biophys. J.* 80:2074-2081.
- Gullingsrud, J. R., K. Schulten. 2002. Gating mechanisms of MscL studied by molecular dynamics simulations using applied surface tension. *Biophys J.* 82:3066.
- Gullingsrud, J. R., K. Schulten. 2003. Gating of MscL Studied by Steered Molecular Dynamics. *Biophys J.* 85:2087-2099.
- Hamill, O., B. Martinac. 2001. Molecular Basis of Mechanotransduction in Living Cells. *Physiol. Rev.* 81:685-740.
- Helfrich, P., E. Jakobsson. 1990. Calculations of deformation energies and conformations in lipid membranes containing gramicidin channels. *Biophys J.* 57:1075-1084.
- Helfrich, W. 1973. Elastic Properties of Lipid Bilayers. *Z. Naturforsch. C.* 28:693-703.
- Howard, J. 2001. *Mechanics of Motor Proteins and the Cytoskeleton*. Sunderland, Massachusetts: Sinauer Associates, Inc.
- Huang, H. W. 1986. Deformation Free Energy of Bilayer Membrane and its Effect on Gramicidin

- Channel Lifetime. *Biophys. J.* 50:1061-1070.
- Israelachvili, J. N. 1991. *Intermolecular and Surface Forces*. 2nd edn. London: Academic Press.
- Keller, S. L., S. M. Bezrukov, S. M. Gruner, M. W. Tate, I. Vodyanoy. 1993. Probability of Alamethicin Conductance States Varies with NonLamellar Tendency of Bilayer Phospholipids. *Biophys. J.* 65:23-27.
- Killian, J. A. 1998. Hydrophobic mismatch between proteins and lipids in membranes. *Biochimica et Biophysica Acta.* 1376:401-416.
- Kumar, V. V., B. Malewicz, W. J. Bauman. 1989. Lysophosphatidylcholine stabilizes small unilamellar phosphatidylcholine vesicles. Phosphorus-31 NMR evidence for the wedge effect." *Biophys. J.* 55:798-792.
- Landau, L. D., E. M. Lifshitz. 1986. *Theory of Elasticity*. 3rd edn. Oxford:Butterworth-Heinemann.
- Lundbæk, J. A., O. S. Andersen. 1994. Lysophospholipids Modulate Channel Function by Altering the Mechanical Properties of Lipid Bilayers. *J. Gen. Physiol.* 104:645-673.
- Lundbæk, J. A., A. M. Maer, O. S. Andersen. 1997. Lipid Bilayer Electrostatic Energy, Curvature Stress, and Assembly of Gramicidin Channels. *Biochem.* 36:5695-5701.
- Lundbæk, J. A., P. Birn, J. Girshman, A. J. Hansen, O. S. Andersen. 1996. Membrane Stiffness and Channel Function. *Biochem.* 35:3825-3830.
- Mandersloot, J. G., F. C. Reman, L. L. M. van Deenen, J. de Gier. 1975. Barrier properties of Lecithin/Lysolecithin mixtures. *Biochimica et Biophysica Acta.* 382:22-26.
- Marsh, D. 1996. Intrinsic Curvature in Normal and Inverted Lipid Structures and in Membranes. *Biophys. J.* 70:2248-2255.
- May, S., A. Ben-Shaul. 1999. Molecular Theory of Lipid-Protein Interaction and the  $L_{\alpha}$ - $H_{II}$  Transition. *Biophys. J.* 76:751-767.
- Mouritsen, O. G., M. Bloom. 1984. Mattress model of lipid-protein interactions in membranes. *Biophys. J.* 46:141-153.
- Mouritsen, O. G., M. Bloom. 1993. Models of Lipid-Protein interactions in Membranes. *Annu. Rev. Biophys. Biomol. Struct.* 22:145-171.

- Nielsen, C., M. Goulian, O. Andersen. 1998. Energetics of Inclusion-Induced Bilayer Deformations. *Biophys. J.* 74:1966-1983.
- Olbrich, K., W. Rawicz, D. Needham, E. A. Evans. 2000. Water Permeability and Mechanical Strength of Polyunsaturated Lipid Bilayers. *Biophys. J.* 79:321-327.
- O’Keeffe, A. H., J. M. East, A. G. Lee. 2000. Selectivity in lipid binding to the bacterial outer membrane protein OmpF. *Biophys. J.* 79:2066-2074.
- Opsahl, L. R., W. W. Webb. 1994. Transduction of Membrane Tension by the Ion Channel Alame-thicin. *Biophys. J.* 66:71-74.
- Ou, X. R., P. Blount, R. J. Hoffman, et al. 1998. One face of a transmembrane helix is crucial in mechanosensitive channel gating *Proc. Natl Acad. Sci. USA.* 95:11471-11475
- Perozo, E., A. Kloda, D. Marien Cortes, B. Martinac. 2002. Physical principles underlying the transduction of bilayer deformation forces during mechanosensitive channel gating. *Nature Structural Biology.* 9,9:696-703.
- Perozo, E., A. Kloda, D. Marien Cortes, B. Martinac. 2002. Open channel structure of MscL and the gating mechanism of mechanosensitive channels. *Nature.* 418:942-948.
- Polchinski, J. 1998. *String Theory, An Introduction to the Bosonic String.* Cambridge: Cambridge University Press.
- Powl, A. M., A. M. East, A. G. Lee. 2003. Lipid-Protein Interactions Studied by Introduction of a Tryptophan Residue: The Mechanosensitive Channel MscL. *Biochem.* 42, 14306-14317.
- Rawicz, W., K. C. Olbrich, T. McIntosh, D. Needham, E. A. Evans. 2000. Effect of Chain Length and Unsaturation on Elasticity of Lipid Bilayers. *Biophys. J.* 79:328-339.
- Ridder, A. N. J. A., W. van de Hoef, J. Stam, A. Kuhn, B. de Kruijff, J. A. Killian. 2002. Importance of Hydrophobic Matching for Spontaneous Insertion of a Single-Spanning Membrane Protein. *Biochem.* 41:4946-4952.
- Seifert, U. 1997. Configurations of fluid membranes and vesicles. *Adv. Phys.* 46:13-137.
- Sokabe, M., K. Nunogaki, K. Naruse, H. Soga. 1993. Mechanics of patch clamped and intact cell membranes in relation to SA channel activation. *Jpn. J. Physiol.* 43:s197-204.
- Spencer, R. S., D. C. Rees. 2002. The  $\alpha$ -Helix and the Organization and Gating of Channels. *Annu.*

*Rev. Biophys. Biomol. Struct.* 31:207-33.

Sukharev, S. I., W. J. Sigurdson, C. Kung, F. Sachs. 1999. Energetic and Spatial Parameters for Gating of the Bacterial Large Conductance Mechanosensitive Channel, *MscL. J. Gen Physiol.* 113:525-539.

Sukharev, S. I., S. R. Durell, H. R. Guy. 2001. Structural Models of the MscL Gating Mechanism. *Biophys. J.* 81:917-936.

Turner, M. S., P. Sens. 2004. Gating-by-tilt of mechanosensitive membrane channels cond-mat/0311574.

White, S. H., W. C. Wimley. 1999. Membrane Protein Folding and Stability: Physical Principles. *Annu. Rev. Biophys Biomol Struct.* 28:319-365.

Wiggins, P. A., R. Phillips. 2004. Analytic models for mechanotransduction: Gating a mechanosensitive channel. *Proc. Nat. Acad. Sci. USA*, 101:4071-4076.

Wiggins, P. A., R. Phillips. 2005. Membrane-Protein Interactions in Mechanosensitive Channels. *Biophys. J.*, 88: 880-902.

Yoshimura, K., A. Batiza, M. Schroeder, et al. 1999. Hydrophilicity of a single residue within MscL correlates with increased channel mechanosensitivity. *Biophys J.* 77:1960-1972.

Yoshimura, K., T. Nomura, M. Sokabe. 2004. Loss-of-function mutations at the rim of the funnel of mechanosensitive channel MscL. *Biophys. J.* 86::2113-2120.

## 4.7 Appendix

### 4.7.1 Units and Conversions

Throughout the paper, we use  $kT$  at  $T = 300$  K as our energy scale and  $\text{\AA}$  as our fundamental length scale. Tension is in units of  $\text{pN \AA}^{-1}$ . This table provides the conversion to “real life” units:

$$T = 300 \text{ K} \tag{4.82}$$

$$1 kT = 4.143 \times 10^{-14} \text{ erg} = 4.143 \times 10^{-21} \text{ J} = 0.5988 \text{ kcal mol}^{-1} \tag{4.83}$$

$$1 kT \text{\AA}^{-1} = 41.43 \text{ pN} = 4.143 \times 10^{-11} \text{ N} \tag{4.84}$$

$$1 kT \text{\AA}^{-2} = 41.43 \text{ pN \AA}^{-1} = 4.143 \times 10^{-1} \text{ N m}^{-1} \tag{4.85}$$

$$1 kT \text{\AA}^{-3} = 4.143 \times 10^{10} \text{ dyne cm}^{-2} = 4.143 \times 10^9 \text{ Pa} = 3.0570 \times 10^7 \text{ mmHg} \tag{4.86}$$

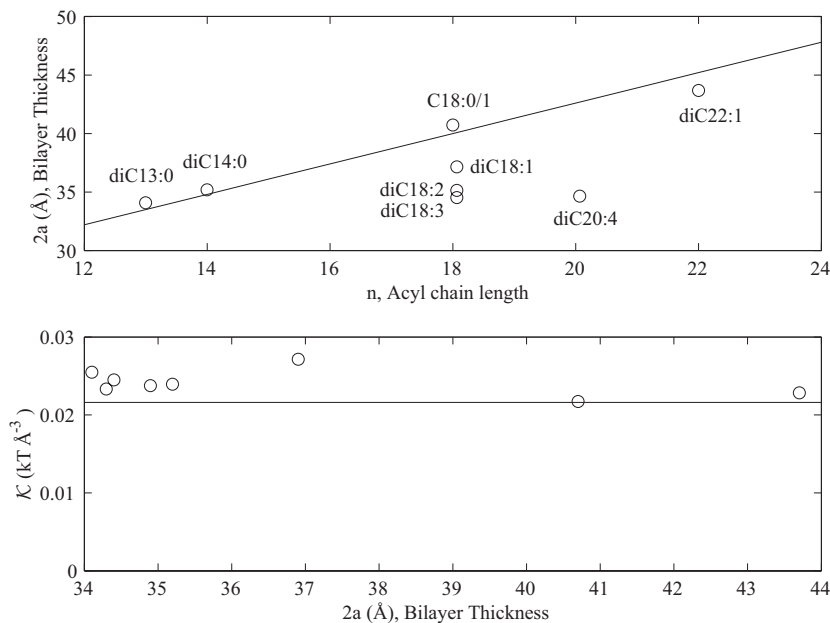


Figure 4.15: Accuracy of lipid model. In the top panel, we plot lipid bilayer thickness versus acyl chain width. There is reasonable agreement between the linear fit and the data provided that the lipid is not poly-unsaturated. In the bottom panel the effective spring constant  $\mathcal{K}$  is plotted versus lipid bilayer width.  $\mathcal{K}$  is roughly independent of the bilayer thickness. All data from Rawicz *et al.* (2000).

#### 4.7.2 Bilayer Parameter Model

We recommend Rawicz *et al.* (2002) (from which we have taken the table below) for a brief review of the mechanics of bilayers. There is a subtlety which we haven't discussed in the paper relating to the difference between peak to peak head group thickness which is measured from X-ray crystallography and mechanical thickness—that portion of the tail of the lipid which is deformed. The mechanical thickness of the bilayer is roughly 1 nm less than the peak to peak thickness (Rawicz *et al.*, 2000). When we discuss the scaling of the moduli, it is this thickness that we really consider. This uncertainty is compounded by the question of how this thickness relates to the hydrophobic thickness of the bilayer. The thickness of the interface between the hydrophobic region and the hydrophilic region is also difficult to define (White and Wimley, 1999). The MscL protein itself does not really have a sudden transition between hydrophobic residues and hydrophilic ones, meaning that one cannot really start with the structure and say definitively what the hydrophobic thickness is. This model is at best a caricature which attempts to capture the essential mechanics and it is for this reason we have not tried to differentiate between all these different thickness and replaced them all with a single approximation.

Having taken this spartan view of the bilayer, we assume the bilayer acts as if there were only

Lipid	Length (atoms)	$2a$ Å	$K_A$ ( $kT/\text{Å}^2$ )	$K_B$ ( $kT$ )
diC13:0	13	$34.1 \pm 0.5$	$0.576 \pm 0.03$	$14 \pm 2$
diC14:0	14	$35.2 \pm 0.6$	$0.565 \pm 0.05$	$14 \pm 2$
C18:0/1*	18	$40.7 \pm 0.6$	$0.568 \pm 0.03$	$21 \pm 2$
diC18:1 <sub>c9</sub>	18	$36.9 \pm 0.4$	$0.638 \pm 0.04$	$20 \pm 2$
diC18:2	18	$34.9 \pm 0.3$	$0.596 \pm 0.05$	$10 \pm 2$
diC18:3	18	$34.3 \pm 0.6$	$0.588 \pm 0.08$	$9.3 \pm 1$
diC20:4	20	$34.4 \pm 0.7$	$0.603 \pm 0.02$	$10 \pm 1$
diC22:1	22	$43.7 \pm 0.5$	$0.634 \pm 0.02$	$29 \pm 3$

Table 4.3: Lipid bilayer parameters.  $kT$  for  $T = 300$  K. \* indicates the lipid numbers used for standard values in calculations. Tail Length is the number of Carbon atoms which comprise each of the two tails. The full names of the lipids are: 1,2-ditridecanoyl-sn-glycero-3-phosphocholine (diC13:0); 1,2-dimyristoyl-sn-glycero-3-phosphocholine (diC14:0); 1-oleoyl-2-stearoyl-sn-glycero-3-phosphocholine (C18:0/1); 1,2-dioleoyl-sn-glycero-3-phosphocholine (diC18:1<sub>c9</sub>); 1,2-dilinoleoyl-sn-glycero-3-phosphocholine (diC18:2); 1,2-dilinoleoyl-sn-glycero-3-phosphatidylcholine (diC18:3); 1,2-diarachidonoyl-sn-glycero-3-phosphocholine (diC20:4); 1,2-dierucoyl-sn-glycero-3-phosphocholine (diC22:1).

one elastic constant governing its behavior, the (effective) Young's Modulus of the lipid tails

$$\mathcal{E} = \frac{\epsilon}{2} \left( \frac{\Delta V}{V} \right)^2 \quad (4.87)$$

where  $\mathcal{E}$  is the elastic energy density,  $V$  is the volume and  $\epsilon$  is the Young's modulus. The only length scale for the bilayer is its thickness  $2a$  so all the rest of the elastic moduli for the bilayer scale with  $\epsilon$  and the number of powers of  $a$  required to get the right units. These dimensional analysis arguments predict

$$K_B \propto a^3, \quad (4.88)$$

$$K_A \propto a^1, \quad (4.89)$$

$$\mathcal{K} \propto a^0. \quad (4.90)$$

This is a rough scaling, not a physical law, but it is sufficient for our calculations. (See Fig. 4.7.2.) For a more rigorous argument and experimental results, see Rawicz *et al.*, 2000. Table 4.7.2 gives the measured values for the elastic constants of a typical bilayer taken from Rawicz.

For estimates of bilayer thickness as a function of acyl chain length, we have fit the peak to peak head group separation to acyl chain length for the saturated lipids above as shown in Fig. 4.7.2. We have used the relation:

$$2a = 1.3n + 16.6 \text{ Å}, \quad (4.91)$$

although slightly more elaborate formulas are offered in Rawicz *et al.* (2000). When discussing the

lipids used by other authors, we have used the same naming convention they employed: PC12 (12:0 dilauroyl-phosphatidylcholine), PC10 (10:0 dicaproyl-phosphatidylcholine), PC16 (16:1 dipalmitoleoyl-phosphatidylcholine), PC18 (18:1 dioleoyl-phosphatidylcholine), PC20 (20:1 Eicosenoyl-phosphatidylcholine), PE (18:1 dioleoyl-phosphatidylethanolamine), LPL (lysophospholipid), LPC (lysophosphatidylcholine), DOPC (dioleoylphosphatidylcholine), and DOPE (dioleoylphosphatidylethanolamine).

### 4.7.3 Effective free energy density

The mean curvature contributions to the free energy density are

$$\mathcal{G}_B = \frac{K_B}{2} \left[ \underbrace{(\nabla^2 h)^2 + (\nabla^2 u)^2}_{\mathcal{M}} - 2 \underbrace{(C\nabla^2 h + \bar{C}\nabla^2 u)}_{\partial\mathcal{M}} \right], \quad (4.92)$$

where the variation of the  $\mathcal{M}$  terms contribute to the action in the bulk (bilayer), the  $\partial\mathcal{M}$  terms are total derivatives and can be evaluated at the interface, and constant terms are dropped. The Gaussian curvature contributes only at the boundary, not in the bulk, and will be calculated exactly below. The tension contributions to the free energy density are

$$\mathcal{G}_\alpha = \frac{\alpha}{2} \underbrace{[(\nabla h)^2 + (\nabla u)^2]}_{\mathcal{M}} \quad (4.93)$$

where as before, the variation of the  $\mathcal{M}$  terms contribute to the action in the bulk (bilayer). The interaction free energy density is

$$\mathcal{G}_I = \underbrace{\frac{K_A}{2a^2} u^2}_{\mathcal{M}}. \quad (4.94)$$

### 4.7.4 Equilibrium equations and solutions

The equations that result from the variation of  $u$  and  $h$  are

$$0 = \frac{\delta G[u, h]}{\delta u} = \left[ K_B \nabla^4 - \alpha \nabla^2 + \frac{K_A}{a^2} \right] u, \quad (4.95)$$

$$0 = \frac{\delta G[u, h]}{\delta h} = [K_B \nabla^4 - \alpha \nabla^2] h. \quad (4.96)$$

One Laplacian can be dropped from the equation for  $h$  and amounts to the freedom for rotations of the bilayer in the  $x, z$  and  $y, z$  planes and displacements along the  $z$  axis. We choose a configuration by specifying the equilibrium position of the plane. Assuming cylindrical symmetry, these equations are satisfied by the modified Bessel function  $K_0$

$$\frac{1}{r} \partial_r r \partial_r K_0(\beta r) = \beta^2 K_0(\beta r), \quad (4.97)$$

resulting in the solutions

$$u(r) = A_+ K_0(\beta_+ r) + A_- K_0(\beta_- r), \quad (4.98)$$

$$h(r) = B K_0(\beta_H r), \quad (4.99)$$

where  $\beta_{\pm}$  and  $\beta_H$  are given by

$$\beta_{\pm} \equiv \sqrt{\frac{\alpha \pm \sqrt{\alpha^2 - 4K_B K_A/a^2}}{2K_B}}, \quad (4.100)$$

$$\beta_H \equiv \sqrt{\frac{\alpha}{K_B}}, \quad (4.101)$$

where the branch cuts for the square roots are along the negative real axis.  $\beta_{\pm}$  need not be real and in fact if

$$\alpha^2 < 4K_B K_A/a^2, \quad (4.102)$$

the  $\beta_{\pm}$  are complex and  $u$  oscillates as it decays. The boundary conditions can be used to determine the constants  $A_{\pm}$  and  $B$  as

$$A_{\pm} = -\frac{K_{\mp} U' + \beta_{\mp} U K'_{\mp}}{\beta_{\pm} K'_{\pm} K_{\mp} - \beta_{\mp} K_{\pm} K'_{\mp}}, \quad (4.103)$$

$$B = \frac{H'}{\beta_H K'_0(\beta_H R)}, \quad (4.104)$$

where

$$K_{\pm} \equiv K_0(\beta_{\pm} R),$$

$$K'_{\pm} \equiv K'_0(\beta_{\pm} R).$$

For large  $z$ , the Bessel functions can be replaced by their asymptotic approximation as

$$K_0(z) \rightarrow \sqrt{\frac{\pi}{2z}} \exp(-z) \quad (4.105)$$

$$K'_0(z) \rightarrow -\left(1 + \frac{1}{2z}\right) \sqrt{\frac{\pi}{2z}} \exp(-z). \quad (4.106)$$

The relevant length scale for  $u$  is the decay length for thickness deformation:

$$\beta^{-1} \equiv \left(\frac{K_A}{K_B a^2}\right)^{-1/4} \sim 11 \text{ \AA} < R_{\text{MscL}}. \quad (4.107)$$

Since the decay length is shorter than the channel radius, we can expand our results in  $\beta R$ . By way of contrast, the length scale for mid-plane deformation is typically much larger since the restoring

force, in the form of the tension, is relatively weak

$$\beta_H^{-1} = \sqrt{\frac{K_B}{\alpha}} \sim 27 \sqrt{\frac{\alpha_*}{\alpha}} \text{ \AA}. \quad (4.108)$$

At low tension the length scale is even larger. Fortunately we will see that when the analytic approximation breaks down, the mid-plane energy is irrelevant in comparison with the other contributions anyway.

#### 4.7.5 Calculation of Free Energy

Except for the areal deformation term, the free energy can be calculated on the boundary by integrating by parts:

$$G[h, u] = \int_{\mathcal{M}'} d^2x \mathcal{G}, \quad (4.109)$$

$$= \int_{\mathcal{M}'} d^2x \left( u \frac{\delta G}{\delta u} + h \frac{\delta G}{\delta h} + \alpha \right) + \int_{\partial \mathcal{M}'} ds \hat{n} \cdot (...), \quad (4.110)$$

where the variations in the integral over the bilayer  $\mathcal{M}$  are zero since the equations for equilibrium are satisfied. The surface integrals come from integration by parts. The spontaneous and background curvature contributions are

$$G_C \equiv - \int_{\mathcal{M}'} d^2x (C_+ \nabla^2 h_+ - C_- \nabla^2 h_-), \quad (4.111)$$

$$= - \oint_{\partial \mathcal{M}'} d\hat{n} \cdot \frac{K_B}{2} (C_+ \nabla h_+ - C_- \nabla h_-), \quad (4.112)$$

$$= \pi R K_B (C_+ H'_+ - C_- H'_-). \quad (4.113)$$

The energy contributions from thickness deformations of the bilayer are

$$G_U = \frac{1}{2} \oint_{\partial \mathcal{M}'} d\hat{n} \cdot (K_B [\nabla u \nabla^2 u - u \nabla^3 u] + \alpha u \nabla u), \quad (4.114)$$

$$= \pi R (-\hat{r}) \cdot (K_B [\nabla u \nabla^2 u - u \nabla^3 u] + \alpha u \nabla u) |_R, \quad (4.115)$$

$$= \pi R K_B \frac{(\beta_+^2 - \beta_-^2) (K_+ U' - \beta_+ U K'_+) (K_- U' - \beta_- U K'_-)}{\beta_- K_+ K'_- - \beta_+ K_- K'_+} - \alpha U U', \quad (4.116)$$

$$= \pi R [K_B (\beta_+ + \beta_-) (U' + [\beta_+ + \frac{1}{2R}] U) (U' + [\beta_- + \frac{1}{2R}] U) - \alpha U U'], \quad (4.117)$$

where  $G_U$  contains all the free energy terms in  $u$  except those proportional to  $C_{\pm}$  and the asymptotic approximation has been used in the last line of the derivation. Consider the simple limit when  $U' = 0$ , namely,

$$G_U = \pi K_B (\beta_+ + \beta_-) [\beta_+ \beta_- R + (\beta_+ + \beta_-)] U^2 \quad (4.118)$$

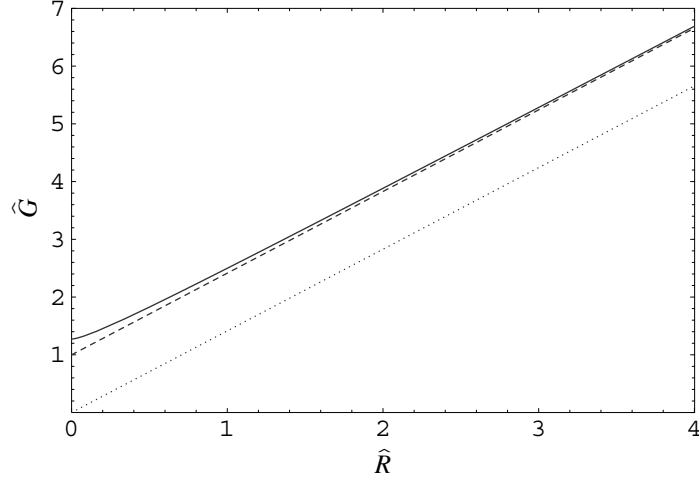


Figure 4.16: Validity of asymptotic approximation for dimensionless thickness deformation free energy. The curves above depict the difference between the exact result (eqn. 4.116, solid curve), the asymptotic expansion (eqn. 4.118, dashed curve), and the dominant scaling result (shown in Table 6.1, dotted curve). There is excellent agreement between the approximate result and exact result for radii relevant for MscL:  $\hat{R} > 1$ .

where we have discarded terms in lower powers of  $R$ . To address the validity of this approximation, we compare this result with the exact result. We make the radius dimensionless using the inverse decay length in the low tension limit

$$\beta \equiv \left( \frac{K_A}{K_B a^2} \right)^{1/4}, \quad (4.119)$$

$$\hat{R} \equiv \beta R. \quad (4.120)$$

We define a dimensionless thickness deformation free energy,

$$G_U = \pi K_B U^2 \beta^2 \hat{G}_U. \quad (4.121)$$

The exact result and the approximation are compared in Fig. 4.7.5.

The free energy associated with the deformation of the mid-plane is

$$G_H = \frac{1}{2} \oint_{\partial \mathcal{M}'} d\hat{n} \cdot (K_B [\nabla h \nabla^2 h - h \nabla^3 h] + \alpha h \nabla h), \quad (4.122)$$

$$= \pi R (-\hat{r}) \cdot [\alpha h \nabla h]_R, \quad (4.123)$$

$$= \pi K_B H'^2 \hat{R} \left[ \frac{K_0}{|K'_0|} \right]_{\hat{R}} \quad (4.124)$$

where  $\hat{R} \equiv \beta_H R$ . The last line is the exact result of the model. If we apply the asymptotic

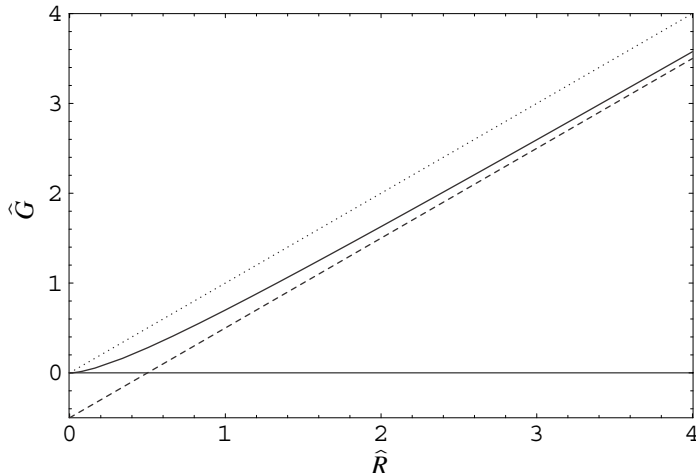


Figure 4.17: Validity of asymptotic approximation for dimensionless mid-plane deformation free energy (Eq. 4.126). The curves above depict the difference between the exact result (eqn. 4.124, solid curve), the asymptotic expansion (eqn. 4.125, dashed curve), and the dominant scaling result (Table 6.1, dotted line). For MscL the prefactor  $\pi K_B H'^2$  is typically less than  $kT$  implying that the greatest error (when the tension is 0) is a fraction of a  $kT$  at most.

approximation, the result reduces to

$$G_H = \pi K_B H'^2 \left[ \hat{R} - \frac{1}{2} + \mathcal{O}\left(\frac{1}{\hat{R}}\right) \right]. \quad (4.125)$$

The asymptotic approximation is violated for small tensions but the result is typically acceptable since the relative error in the energy when the tension is small is irrelevant. The prefactor is typically less than a  $kT$  and as can be seen in fig. 4.7.5 the error is at most half this prefactor. We define a dimensionless mid-plane deformation free energy

$$G_H = \pi K_B H'^2 \hat{G}_H. \quad (4.126)$$

The dimensionless energy defined above is compared with the approximate value in Fig. 4.7.5.

The Gaussian curvature contribution can be calculated exactly and has no local effect because it is related to a well known topological invariant, the Euler characteristic:

$$2\pi\chi \equiv \int_{\mathcal{M}} d^2\sigma \det \mathbf{S} - \int_{\partial\mathcal{M}} ds k, \quad (4.127)$$

where  $\det \mathbf{S}$  is the Gaussian curvature and

$$k \equiv t^a n_b \nabla_a t^b, \quad (4.128)$$

is the curvature of the boundary where  $\vec{t}$  is the unit tangent on the boundary and  $\vec{n}$  is the outward pointing unit normal to the boundary. See Polchinski, 1998, for example. In terms of the Euler Characteristic, the Gaussian curvature contribution is

$$G_G = K_G \left( 2\pi\chi + \int_{\partial\mathcal{M}} ds k \right). \quad (4.129)$$

$\chi$  depends on membrane topology alone and can be dropped since changes in protein conformation do not effect the membrane topology. The Gaussian bending energy is therefore exactly

$$G_G = K_G 2\pi \cos \theta, \quad (4.130)$$

where  $\theta$  is the angle of the bilayer away from horizontal at the interface. For the bilayer model in the small angle approximation this is

$$G_G = -\frac{K_G\pi}{2} (H_+^{\prime 2} + H_-^{\prime 2}) = -K_G\pi (H^{\prime 2} + U^{\prime 2}). \quad (4.131)$$

The Gaussian curvature contribution induces bending of the protein to relieve the bending of the bilayer. Existing measurements are consistent with

$$K_G < -\frac{1}{2}K_B, \quad (4.132)$$

(see Boal, 2002 for references) but we will assume that the magnitudes are similar. If this is the case, none of these corrections is particularly relevant for MscL.

Finally we calculate the areal deformation term. Before explaining the calculation, let us define precisely what we mean by the tension. The tension we are discussing is the applied tension, not a surface tension. Changes in the inclusion conformation do not effect the area of the bilayer—it is assumed that there is some small change in the global conformation which absorbs this area change. Furthermore these conformational changes do not change the tension since we assume that the bilayer is much larger than the size of the inclusion. Since the area of the bilayer is essentially fixed—at least the number of lipid molecules in the bilayer is fixed—the tension we discuss here is the applied tension rather than a surface tension.

The global conformation of the bilayer acts as a bilayer reservoir. The free energy cost for increasing the bilayer area of our small system is

$$dG_A = \alpha dA_{\mathcal{M}} = -\alpha dA_P \quad (4.133)$$

where the change in the proteins area is minus that of the bilayers. As mentioned above we assume that the reservoir is large enough that changes in the protein conformation have no effect on the

$W_O = 28.0 \text{ \AA}$	$2a \text{ (\AA)}$	$U_O \text{ (\AA)}$	$U_C \text{ (\AA)}$	$f_O \text{ (kTnm}^{-1}\text{)}$	$f_C \text{ (kTnm}^{-1}\text{)}$	$\Delta G \text{ (kT)}$
$n$						
16	37.4	4.7	0.0	0.93	0.0	20
18	40.0	6.0	1.3	1.1	0.15	22
20	42.6	7.3	2.6	1.2	0.7	16
$W_O = 36 \text{ \AA}$	$2a \text{ (\AA)}$	$U_O \text{ (\AA)}$	$U_C \text{ (\AA)}$	$f_O \text{ (kTnm}^{-1}\text{)}$	$f_C \text{ (kTnm}^{-1}\text{)}$	$\Delta G \text{ (kT)}$
$n$						
16	37.4	0.7	0.0	0.07	0.0	1.5
18	40.0	2.0	1.3	0.4	0.15	6.6
20	42.6	3.3	2.6	0.8	0.7	7.5

Table 4.4: Details of the computation for the comparison between the data of Perozo and Powl.

tension.

#### 4.7.6 Saturation of Thickness Deformation

If the mismatch  $2|U|$  is less than  $2U_*$ , then the mismatch is entirely absorbed by thickness deformation. The maximum thickness deformation free energy, corresponding to a mismatch of  $2U_*$ , is

$$G_U^{\text{Max}} = \frac{4\pi R\sigma_*^2}{\mathcal{K}\left(1 + \frac{\sqrt{2}}{\beta R}\right)} = 14 kT, \quad (4.134)$$

evaluated for the closed state. For larger mismatches,  $2U_*$  is absorbed by the thickness deformation while  $2(|U| - U_*)$  is exposed to the solvent. The combined interface and thickness deformation free energy for  $|U| > U_*$  is

$$G_{UW} = \sigma_* 2\pi R (2|U| - U_*). \quad (4.135)$$

This correction does not dramatically effect the qualitative picture of the thickness deformation discussed above. In fact, in fig. 4.3.7 we have plotted the deformation energies for interface energy alone, thickness deformation alone, and the corrected thickness deformation to show that for the range of bilayer widths of interest in this problem, there is little difference between thickness deformation and the corrected thickness deformation, while ignoring thickness deformation altogether in favor of interface energy alone results in a significant error.

#### 4.7.7 Details of the Perozo vs Powl comparison

Below we have estimated the bilayer deformation energy based on the EcoMscL data of Powl *et al.* (2003). For the closed states, we have simply used the values measured by Powl and coworkers. For the open state, we have used a fixed value of  $W_O$  listed below and estimated the mismatch. From the mismatch, we have reinterpreted the data of Powl *et al.* (2003) as a function of mismatch (see Fig. 4.4.2) to estimate the line tension. From the line tensions, we then compute the deformation

energy difference ( $\Delta G \equiv 2\pi [f_O R_O - f_C R_C]$ ). These computations appear in Table ??comp.

## Chapter 5

# All about DNA mechanics

“Why is this interesting?”, Jané Kondev remembers asking John Marko after hearing him describe his recent seminal work with Carlos Bustamante [1] on the extension of single DNA molecules with an optical trap. When Bustamante’s article appeared in *Science*, many of the practitioners of traditional biology were probably thinking the same thing. Was there a better reason for physicists to be pulling on single molecules of double stranded DNA than a demonstration of technical prowess? Did this experiment tell biologists anything they did not already know about DNA?

Phil Nelson (U. Penn.), Rob Phillips, and I have recently been reexamining the accepted models of DNA statistical mechanics with these very questions in mind. This work was motivated by some very striking experimental results from Tim Cloutier and Jon Widom (Northwestern) [2], which suggested that DNA is very much more flexible on short length scales than suggested by force-extension experiments. What makes these results particularly exciting is that DNA bending, on the short length scales probed by the experiments of Cloutier and Widom, plays an integral role in many biological processes. These experimental results seemed to upend much we thought we knew about DNA mechanics and therefore much we thought we knew about biological systems which bend DNA.

In these next four chapters, I shall describe a lot of work, only part of which is completely finished (Chapter 6). The DNA bending project has been an active collaboration between experimentalists and theorists. In the last two or three months, the experimental picture has changed significantly, several times! In fact, as I am writing this chapter, the wind has shifted yet again. These new experiments are outlined in Chapter 7.

In this chapter, I will briefly motivate our work on the mechanics of DNA. In Sect. 5.1, I explain why DNA bending is interesting from a biological perspective. In Sect. 5.2, I quickly outline the accepted model of DNA mechanics, the wormlike chain model, and briefly derive some technical results that we shall use in later chapters. In Sect. 5.3, I explain the concept of “effective concentration” and describe how this concept links DNA looping and DNA cyclization experiments. In particular, I relate the  $J$  factor, measured in cyclization measurements (like the experiments of Cloutier and

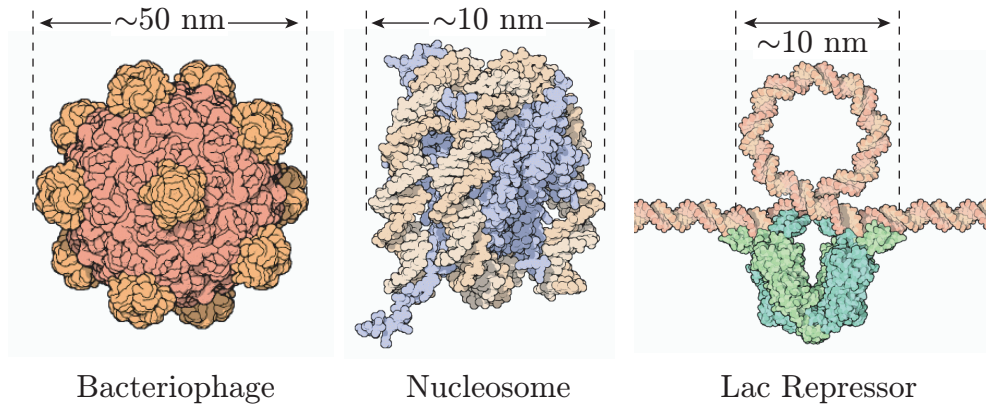


Figure 5.1: The bending of DNA is ubiquitous in the cellular processes associated with genome management. In the figure above, we depict cartoons of the crystal structures of three biological processes that bend DNA. The bacteriophage  $\phi$ X174, a virus that infects bacteria, is a DNA bending expert. The protein capsid shell, shown in the figure, is densely packed with the virus genome which assumes a spool conformation. Our own genome is tightly wrapped around many protein spools, called histone core particles (shown in the second panel). The complex, consisting of the protein and the DNA, is called a nucleosome. DNA bending is also intimately involved in gene regulation. The *lac* repressor is a simple example of a very common motif in which gene regulatory proteins loop DNA. (These images are taken from David Goodsell, the Protein Data Bank.)

Widom) to chain statistics. In Sect. 5.4, I present the experimental results of Cloutier and Widom [2] and discuss their implication for high-curvature DNA bending. Finally, in Sect. 5.5, I present a summary of the following chapter on DNA mechanics in which I describe an exact statistical mechanics theory of kinkable semi-flexible polymers and discuss the application of this theory to DNA mechanics.

## 5.1 Translating genetic code into biological function

DNA was referred to by Francis Crick as one of the two great polymer languages of biology [3], the repository of the genetic information that makes us what we are [4]. This genetic code contains the blueprint for the construction of proteins, Crick’s “second great polymer language of biology.” Proteins are the machines responsible for biological function on a microscopic scale.

The basic set of processes associated with protein *expression* (synthesis) are called the central dogma of molecular biology. The DNA sequence, the genetic code, is first *transcribed* into a messenger RNA transcript. I think of this process as going to the library and copying a paper from a journal. The library is the permanent repository of papers, but when I need to use something, I make a temporary copy of just that piece of the archive. The cell’s genome is the library’s archive and my photocopy is the messenger RNA. The cell, like me, cannot copy the entire archive, it is too costly.

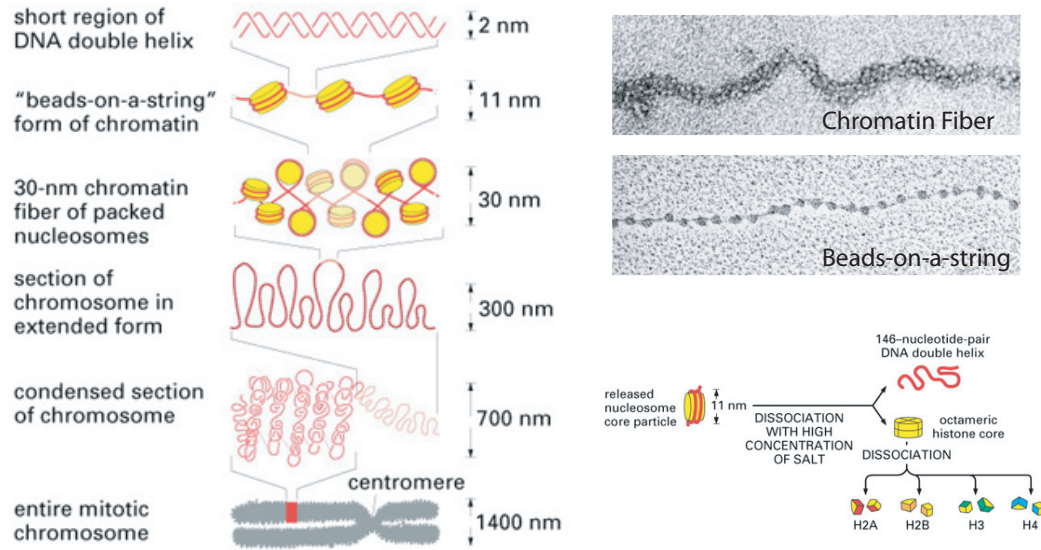


Figure 5.2: DNA packaging in eukaryotic cells. The figure above is a schematic illustration of the many levels of structural organization that exist in a mitotic chromosome. The fundamental packaging unit of chromatin is the nucleosome complex: a histone core (yellow) tightly wrapped one-and-three-quarter times by double-stranded DNA (red). This figure is from Ref. [5].

Nor can it use the original copy. It might damage this copy or another process might need use the same gene. In fact, at any one time in the cell, there are typically many RNA transcripts of a few, essential genes. The RNA transcripts are then *translated* into many copies of the *gene product*, the protein.

### 5.1.1 DNA packaging

Of course things are not quite that simple. A eucaryotic cell's library is called the *nucleus*. The nucleus is the organelle in which the genome is stored. Much like the complicated system in our own Caltech library, the cell also has an organized system for storing its genome. Consider the physical length of our genome: there are roughly three billion base pairs, each a third of a nanometer in length. If the genome were stretched out, it would be roughly a meter in length! The cell nucleus has just one millionth this diameter ( $\sim 1 \mu\text{m}$ )!

Different organisms have learned to cope with this “DNA packaging problem” in different ways. eukaryotic cells—like those that we are composed of—have several scales of DNA packaging. On the shortest length scale, DNA is tightly wrapped around protein “spools” called *histone core particles*. These protein spools are roughly 11 nm in diameter. One complex,  $\sim 200$  bp of DNA wrapped around the histone core, is called the nucleosome (See Fig. 5.1.1). Nucleosomes collectively form fibers called *chromatin*. Due to the large number of nucleosomes required to package our genome, histones are by far the most common DNA binding protein in eukaryotic cells [4]. The typical state

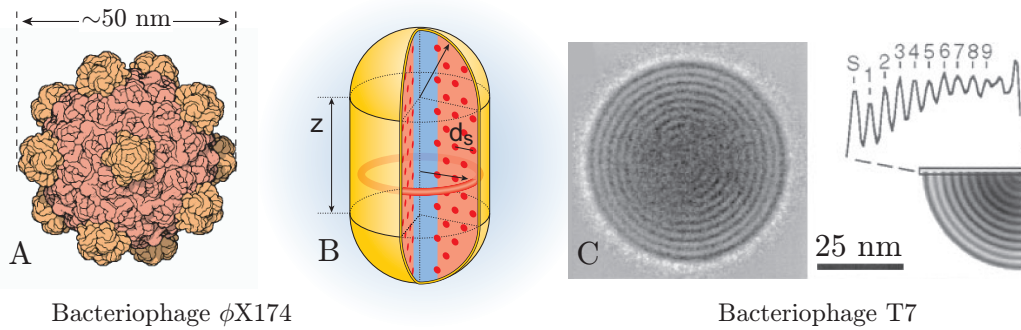


Figure 5.3: DNA bacteriophages are protein capsids tightly packed with DNA. Panel A shows a cartoon of the crystal structure of the capsid of bacteriophage  $\phi$ X174. The genome is believed to be packaged in an inverse-spool configuration, starting from large radius coils and working inwards as depicted schematically in panel B. Panel C shows experimental evidence for the spool packaging hypothesis. This image is from a three dimensional reconstruction of a T7 phage, generated by cryo-electron tomography [6]. The dark rings in the image correspond to the ordered DNA spool. The inner radius of the DNA spool is believed to be a few nm [6, 7]. (Panel A is from David Goodsell, at the Protein Data Bank. Panel C is from Ref. [6].)

of our DNA, due to the high-curvature induced by histones, is very much more condensed than free DNA in solution.

To see what a huge affect histones have on DNA condensation, it is useful exercise to estimate how much space the DNA would take up in absence of any confinement. As we shall discuss later, thermal fluctuations bend DNA spontaneously. The mean squared end-to-end distance of a long polymer in solution is [8]

$$\langle \Delta \vec{X}^2 \rangle = bL, \quad (5.1)$$

where  $L$  is the polymer contour length and  $b$  is the Kuhn length which is proportional to the stiffness of the polymer. (We shall define it more precisely later in the chapter.) For DNA, the Kuhn length is 100 nm. The mean squared end-to-end distance is approximately the square of physical length of the polymer in solution. To estimate the volume that DNA occupies in solution, we shall cube this approximate length

$$V_{\text{free}} \sim (bL)^{3/2} \sim 10^{-10} \text{ m}^3 = 0.1 \mu\text{L}. \quad (5.2)$$

A tenth of a micro-liter may seem pretty small, but in lab we routinely pipette volumes of just 2  $\mu\text{L}$ ! By contrast the volume of the nucleus is

$$V_{\text{nucleus}} \sim (1 \mu\text{m})^3 = 10^{-9} \mu\text{L}, \quad (5.3)$$

one one-hundred-millionth of the free DNA volume! This incredible condensation is predominantly the work of the histone.

The properties of nucleosomes are of great biological interest because chromatin forms the substrate for all eukaryotic-cellular processes associated with DNA: from transcription to replication, recombination, DNA repair, and cell division [9]. The chemical and physical properties of chromatin are intimately related to the mechanics of tightly bent DNA. I shall give one explicit example of this interplay in Sect. 5.4.

Perhaps viruses face a more pronounced “DNA packaging problem” than even eukaryotic cells. Although biologists argue about whether viruses should be counted as organisms, they replicate their genetic information with amazing efficiency. Viruses are parasites that cannot self replicate, but they are one of the smallest replicating genetic units [4]. Viruses are weight conscious. For example, nearly all of the genome sequence of a virus is *coding sequence*; whereas a very large fraction of our own genome (90%) does not appear to code for proteins at all! In fact, there are many known examples of regions of virus genomes that code for multiple proteins at once.

The virus is a parsimonious traveler to meet the challenges of efficient transfer from host to host, while protecting its genome. Like eukaryotic cells, viruses must pack their long genomes by tightly bending their DNA. Many bacteriophage, viruses which infect bacteria like that pictured in Fig. 5.1, achieve this tight packaging by compressing their DNA into a very small protein capsid shell, typically less than 50 nm in diameter. The DNA is packed into the capsid in an inverse spool configuration by a DNA packaging motor. As the capsid fills from its periphery, the motor must insert DNA coils of increasingly high curvature (See Fig. 5.1.1). The end of the genome is probably packed with a radius of curvature of just a few nanometers! The energy expended in this packaging processes to bend the DNA is not wasted, but stored, like a compressed spring, to be used to infect another host. This amazing story is told in many other places [7], but by almost all accounts the mechanics of tightly-bent DNA plays a starring role!

### 5.1.2 Transcriptional regulation

In the previous section, I alluded to the fact that only ten percent of our genome codes for proteins. Even in the coding regions, not all proteins are expressed (synthesized) at once. In fact, only very few “housekeeping genes” are generically expressed in all of our cells all of the time. The rest are “turned on” only when they are needed. How does the cell control its genetic information and ensure that the correct genes are expressed?

Many gene regulatory mechanisms have been discovered over the past fifty years but one of the most important and universal mechanisms controls the transcriptional process itself. If no protein is needed, no RNA transcript is produced. This regulatory mechanism is called *transcriptional regulation*. On the microscopic scale, *gene regulatory proteins* that bind particular sequences of DNA, called *operators*, interact with the cellular machinery responsible for transcription. Gene regulatory proteins exist which exert both positive (activation) and negative (repression) control

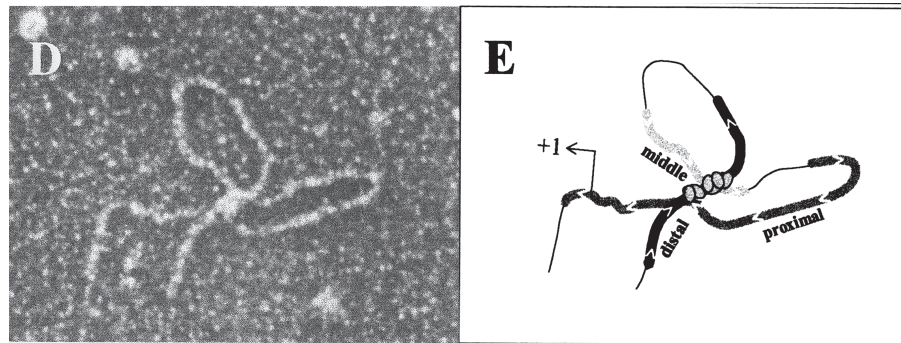


Figure 5.4: DNA looping is a common functional motif in eukaryotic gene regulation. The EM micrograph shows two DNA loops formed in the *CyIIIa* cis-regulatory region of the sea urchin genome. These DNA loops are the result of regulatory proteins trapping rare looped DNA conformations. (This figure is taken from Ref. [10].)

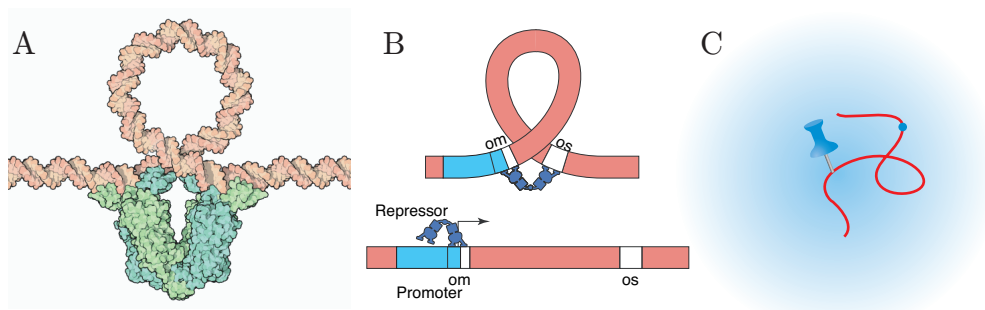


Figure 5.5: Transcriptional regulation and chain statistics. DNA looping is a common motif in transcriptional regulation, the mechanism by which the cell regulates transcription. The *lac* operon is an example of regulatory looping in a prokaryotic cell. The gene regulatory protein *lac* repressor can bind to two operators and induce a loop, increasing its affinity for the DNA. Panel A shows the crystal structure of the repressor bound to DNA. (This panel is taken from David Goodsell, the Protein Data Bank.) Panel B shows a schematic drawing of the looping mechanism. The *lac* repressor can capture rare thermal fluctuation that bring the auxiliary operator into proximity with the DNA binding domain of the protein. (This panel is taken from Ref. [11].) Panel C shows a schematic depiction of the effective concentration of the auxiliary operator (blue dot) once the primary operator is bound to the repressor (the pin). The intermediate DNA (red line) acts as a tether which increases the local, effective concentration of the auxiliary operator in the vicinity of DNA binding domain. (This panel is adapted from Ref. [4].)

over transcription.

One extremely important and common motif in transcriptional regulation is DNA looping. DNA looping is induced by gene regulatory complexes which bind the DNA at more than one operator. (See Fig. 5.1.2) DNA looping implies that the regulatory control region can be thousands of base pairs in length and can include many different operators and therefore it can be sensitive to many different stimuli. Such complicated regulatory machinery is generic in eukaryotic cells and especially in multicellular organisms. A typical example is the 2500 base pair *Endo16* cis-regulatory region in the Sea Urchin. In this regulatory circuit, more than 40 different looping configurations are possible [12, 10]! (See Fig. 5.1.2.)

From a biological perspective, we would like to understand and predict the levels of gene transcription in these systems. The formation of DNA loops implies that DNA chain statistics plays an integral role in determining the function of these regulatory circuits. Once the gene regulatory complex has bound one operator, the DNA, between this operator and those adjacent to it, acts as a tether, increasing the effective concentration of the adjacent operators at the regulatory complex. This mechanism is illustrated in Fig. 5.1.2. If the operators are too closely spaced, the inherent stiffness of the DNA can hold the two operators apart, preventing a gene regulatory complex from binding both operators. As a result, the behavior of gene regulatory circuits depends sensitively on the base pair spacing of the operators. In Sect. 5.3, we shall return to the idea of effective concentration and develop it more rigorously.

Fortunately, procaryotic cells exhibit regulatory circuits which do not loop in forty different configurations! These systems provide an *in vivo* proving ground for understanding gene regulatory looping. For example, in *E. coli*, the *lac* operon has been extensively studied. The binding of the *lac* repressor induces a DNA loop and represses the transcription of the gene *lacZ*. (See Fig. 5.1.2.) The stability of the induced DNA loop is measured indirectly by measuring protein expression as a function of inter-operator spacing (loop length) [13, 14, 15, 16]. (See Fig. 5.1.2.)

## 5.2 DNA chain statistics and the wormlike chain model

How do we describe the conformation of double-stranded DNA quantitatively? The molecular scale of DNA implies that the correct language is statistical mechanics. The thermal forces that buffet DNA molecules play an essential role in dictating its conformation and physical properties. For instance, consider the physical size of DNA molecules in solution. Thermal fluctuations bend DNA randomly. In fact thermal forces bend DNA so efficiently on the length scales observable by visible light microscopy that DNA must be stretched out in order to see its linear structure. Fig. 5.2.1 depicts the thermally induced bending of DNA molecules adsorbed to mica and then visualized via Atomic Force Microscopy (AFM). On the length scales accessible by visible light microscopy

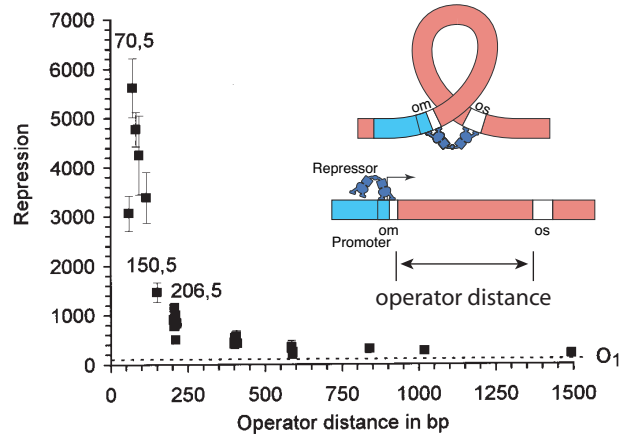


Figure 5.6: Gene expression depends sensitively on the inter-operator spacing (loop size). When the *lac* repressor binds to DNA, it induces the formation of a DNA loop by binding two DNA sequences called operators [14, 15]. The inset panel shows a schematic diagram of this process. When the repressor is bound, the gene is not expressed. Repression is proportional to the inverse of the protein expression. The plot shows the level of repression as a function of inter-operator spacing in base pairs (the length of the loop). The peak repression occurs when the looped complex is most stable. Mysteriously, this optimum loop length is just 70 base pairs, just half the persistence length of DNA and roughly one sixth of the optimum cyclization contour length. (Plot from Ref. [14]. Inset figure from Ref. [11].)

( $\gtrsim 250$  nm), DNA is typically bent. But on length scales shorter than about 50 nm, DNA is not efficiently bent by thermal forces and the polymer remembers its orientation. The length scale at which thermal bending “switches off” is called the persistence length.

### 5.2.1 The random walk model

If we concern ourselves only with the gross spatial distribution of long polymers, a random walk model will suffice to describe the polymer. (This model is known as the freely jointed chain.) Since the polymer begins to forget its orientation after a persistence length, we can treat the conformation as a series of steps in random directions. We shall define the length of these steps to be the Kuhn length,  $b$ . (We shall relate this length to the persistence length in a moment.) Since the directions of all steps are uncorrelated in the random walk model, it is straightforward to work out the average squared displacement

$$\langle \Delta \vec{X}^2 \rangle = b^2 N = bL, \quad (5.4)$$

where  $\langle \rangle$  denotes the average over all random flights,  $N$  is the number of steps, and the contour length  $L$  is the number of steps times the length of each step. We have already taken advantage of this result in Sect. 5.1.1 to discuss the physical size of DNA in solution.

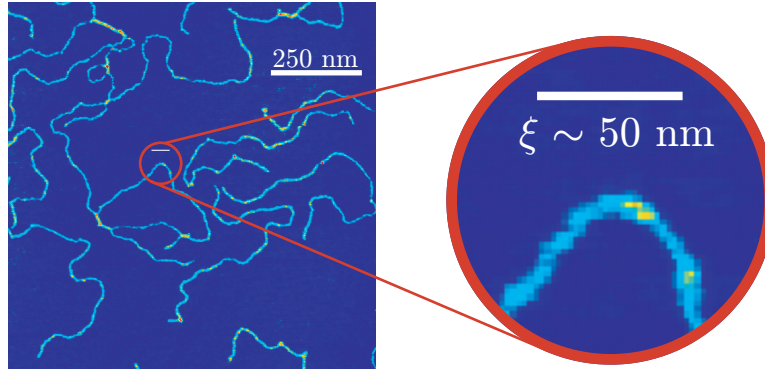


Figure 5.7: DNA configurations in two dimensions. DNA will adsorb to mica in 10 mM Mg. The mica binds the DNA weakly enough that the DNA can equilibrate on the surface. The equilibrated DNA configurations can then be traced with an Atomic Force Microscope (AFM). Thermal fluctuations bend the DNA randomly as is evident from the two dimensional DNA conformations pictured above. On sufficiently short length scales, DNA is typically straight as illustrated by the enlargement of one short section of the chain. The length scale above which DNA is efficiently bent by thermal forces is the persistence length ( $\xi \sim 50$  nm). (The data in this figure is from Thijn van der Heijden, Fernando Moreno, and Cees Dekker at Delft.)

## 5.2.2 The wormlike chain model

Although the freely jointed chain model is useful for describing long sequences of DNA, we need a more quantitative model for studying DNA on length scales on order the persistence length. Clearly a model of freely-jointed, rigid links does not realistically describe DNA on length scales comparable to the Kuhn length.

Semi-flexible polymers have been described with great success by a surprisingly simple statistical mechanics theory: the wormlike chain (WLC) model [17, 18]. This model is equivalent to the statistical mechanics of fluctuating linear-elastic rods [18]. In its simplest incarnation (twist free), the model is completely specified by a single parameter, the bending modulus of the rod [18].

We begin by coarse graining the conformation of the polymer to a space curve  $\vec{X}(s)$ , parameterized by its arc-length  $s$

$$\left| d\vec{X}(s)/ds \right| = 1. \quad (5.5)$$

The polymer tangent vector and curvature are

$$\vec{u}(s) = d\vec{X}(s)/ds, \quad (5.6)$$

$$\vec{\kappa}(s) = d\vec{u}(s)/ds, \quad (5.7)$$

respectively. The magnitude of the curvature is the inverse radius of curvature; the radius of the circle locally fit to the conformation at arc length  $s$ . The polymer is assumed to be inextensible, which is a very good approximation for DNA. There is a well defined total contour length  $L$ .

The bending energy density of a linear elastic rod ( $\epsilon$ ) is quadratic in the curvature

$$\epsilon(s) = \frac{1}{2}\xi\kappa^2(s), \quad (5.8)$$

where  $\xi \approx 50 \text{ nm } kT_{300 \text{ K}}$  is the bending modulus in thermal units<sup>1</sup>. This expression is the canonical bending energy of a slender rod from continuum mechanics. On dimensional grounds, this is the dominant contribution to the bending energy for small deflections. This expression can be derived for toy rod models like that illustrated in Fig. 5.2.3. The total energy is the integrated bending energy density

$$E = \int_0^L ds \epsilon(s). \quad (5.9)$$

Note that we neglect chain-chain interactions which play a negligible role in the high-curvature chain statistics that will be our focus.

### 5.2.3 The mechanical limit

For highly-bent DNA configurations, the contribution of thermal fluctuations can be ignored. The free energy is dominated by the lowest energy configuration. For example, consider the free energy associated with wrapping DNA tightly around the histone core particles to form nucleosomes. (See Fig. 5.1.1.) The roughly cylindrical shape of the histone core particle determines the DNA conformation. The bending energy of the wrapped DNA can be estimated from Eq. 5.9

$$E \approx 1.75 \times \frac{\xi\pi}{R} \approx 50 kT, \quad (5.10)$$

where 1.75 is the number of times the DNA wraps the histone core particle and the radius of curvature is roughly 5.5 nm. The estimated bending energy predicted by the wormlike chain is extremely large, but is thought to be offset by the coulomb attraction between the negatively charged DNA and the positively charged histone core particle [9]. There is a variation of roughly 7 kT in the relative histone binding free energies of different sequences [9]. I leave it as an exercise for the reader to show that a 14 percent sequence dependent change in the elastic constant could account for this variation.

As we have already discussed, the tight-bending of DNA is ubiquitous in biology. The bending energies predicted by the elastic-rod model are typically very large compared with  $kT$ . Polymer physics experiments that probe DNA mechanics typically probe a different bending regime where the entropic contribution to the mechanics is of central importance.

---

<sup>1</sup> The thermal units in this paper assume that the temperature is 300 K.

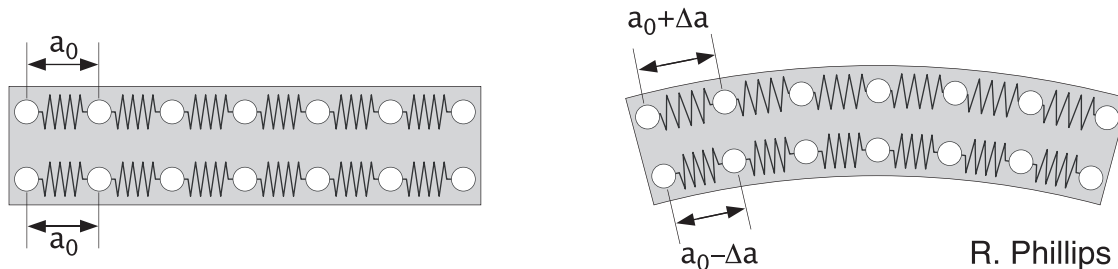


Figure 5.8: The bending of elastic rods. Above is a schematic spring model that can be used to derive the slender rod bending energy. This energy is understood to be the small deflection limit for continuum rods. The balls represent schematic atoms and the springs represent bonds. (This figure is taken from Ref. [19].)

#### 5.2.4 Chain Statistics

For most applications, thermal fluctuations of DNA cannot be neglected and we must consider the statistical mechanics of the polymer. In the canonical ensemble, the Boltzmann distribution relates probability of a particular micro-state  $\Gamma$  to its energy

$$\mathcal{P}_\Gamma = Z^{-1} \exp -E_\Gamma, \quad (5.11)$$

where  $Z$  is the partition function, determined by normalization, and we work in energy units of  $kT$ . The distribution functions of the polymer theory are calculated by performing path integrals over all possible intermediate chain configurations. For example, the tangent distribution function, the probability density of final tangent  $\vec{u}_f$  given initial tangent  $\vec{u}_i$  for a chain contour length  $L$ , is written

$$G(\vec{u}_f, \vec{u}_i; L) = Z^{-1} \left[ \int [d\vec{u}(s)] \exp -E[\vec{u}(s)] \right]_{\vec{u}_i}^{\vec{u}_f}, \quad (5.12)$$

where the measure  $[d\vec{u}(s)]$  denotes integrations over all intermediate tangents between  $\vec{u}_i$  at arc-length 0 and  $\vec{u}_f$  at arc-length  $L$ , and  $Z$  is the partition function determined by normalization.

#### 5.2.5 The equivalence of the WLC model to a free quantum particle

*Note to the reader:* This section is somewhat technical in nature and is not essential for understanding the rest of the chapter.

To evaluate the path integral in Eq. 5.12, we exploit a well-known trick that relates the path integral and Schrödinger equation methods of quantum mechanics [20]. The quantum propagator for a free particle written in the path integral formalism is

$$K(\vec{u}_f, t; \vec{u}_i, 0) = Z^{-1} \left[ \int [d\vec{u}(t)] \exp iS[\vec{u}(t)] \right]_{\vec{u}_i}^{\vec{u}_f}, \quad (5.13)$$

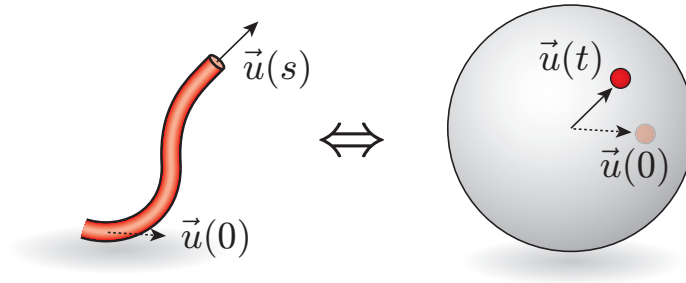


Figure 5.9: The equivalence of the WLC model to a free quantum particle on a unit sphere. The WLC model tangent distribution function and the quantum propagator for a free particle on a unit sphere are mathematically related by an analytic continuation of time to imaginary arc length. The tangent of the polymer is reinterpreted as the position of the particle. The sum over all intermediate tangents in the statistical mechanics model is mathematically equivalent to the sum over all classical trajectories in the quantum propagator.

where  $K$  is the propagator or Greens function for the time evolution of a state in the spatial representation,  $\vec{u}$  is interpreted as a position vector,  $Z$  is a constant determined by unitarity (normalization), and  $S$  is the classical free particle action which is a functional of the position  $\vec{u}$

$$S[\vec{u}(s)] = \int_0^t dt' \frac{1}{2} m \dot{\vec{u}}^2, \quad (5.14)$$

which, like the energy, is a functional quadratic in the derivative of  $\vec{u}$ . Comparing the free quantum particle (FQP) and the wormlike chain (WLC) path integrals, the only significant difference is that the exponent of the FQP path integral is imaginary. We “fix” this problem by analytically continuing time to imaginary arc-length. The table below summarizes the equivalence relation:

WLC	$\Leftrightarrow$	FQP
$G$	$\Leftrightarrow$	$K$
$\vec{u}(s)$	$\Leftrightarrow$	$\vec{u}(t)$
$s$	$\Leftrightarrow$	$it$
$\xi$	$\Leftrightarrow$	$m$ .

Note in particular that time has been analytically continued to imaginary arc-length and the target space in which the particle moves is not three dimensional Euclidian space ( $\mathbb{R}^3$ ) but the surface of a unit sphere ( $S_2 = \{\vec{u} \in \mathbb{R}^3 | \vec{u}^2 = 1\}$ ).

Having specified the equivalence between the quantum propagator ( $K$ ) and the tangent distribution function ( $G$ ), we now exploit the Schrödinger equation method to find the quantum propagator. Remember that the propagator is the transition amplitude of the time evolution operator  $\mathcal{U}$  [21]:

$$K(\vec{u}_f, t; \vec{u}_i, 0) = \langle \vec{u}_f | \mathcal{U}(t) | \vec{u}_i \rangle, \quad (5.15)$$

where  $|\vec{u}\rangle$  is a ket state in the spatial representation on  $S_2$ . For a time independent Hamiltonian, the time evolution operator is

$$\mathcal{U}(t) = \exp -i\mathcal{H}t, \quad (5.16)$$

where  $H$  is the Hamiltonian operator. For a free quantum particle on  $S_2$ , the Hamiltonian operator is

$$\mathcal{H} = \frac{p^2}{2m} = -\frac{\nabla^2}{2m} = \frac{\mathcal{L}^2}{2m}, \quad (5.17)$$

where  $p$  is the momentum operator on  $S_2$  which is the Laplace-Beltrami operator on  $S_2$  in the spatial representation. The Laplace-Beltrami operator can be reinterpreted as the orbital angular momentum operator ( $\mathcal{L}^2$ ) in three dimensions.

The eigenstates of  $\mathcal{L}^2$  are well known; they describe the angular wave functions for the Hydrogen atom and other quantum central force problems. Typical we choose a set of states which simultaneously diagonalize both  $\mathcal{L}^2$  and  $\mathcal{L}_z$ , the  $z$  component of the angular momentum

$$\mathcal{L}_z |lm\rangle = m |lm\rangle \quad (5.18)$$

$$\mathcal{L}^2 |lm\rangle = l(l+1) |lm\rangle, \quad (5.19)$$

for non-negative integers  $l$  and integers  $m$  on the interval  $[-l, l]$ . The states of this “angular momentum” representation are the spherical harmonics in the spatial representation

$$\langle \vec{u} | lm\rangle = Y_l^m(\vec{u}), \quad (5.20)$$

which form a complete set of states.

We have implicitly solved the Schrödinger equation by finding the spatial representation of the angular momentum states. Eq. 5.15 relates this solution of the Schrödinger equation to the path integral approach. By applying the substitutions outlined in the table, we have solved for the tangent distribution function exactly [18]

$$G(\vec{u}_f, \vec{u}_i; L) = K(\vec{u}_f, L/i; \vec{u}_i, 0) = \sum_{l=0}^{\infty} \sum_{m=-l}^l Y_l^m(\vec{u}_f) Y_l^{*m}(\vec{u}_i) \exp -\frac{l(l+1)L}{2\xi}. \quad (5.21)$$

This result forms the basis for the derivation of many other important results. In particular, Andy Spakowitz and Zhen-Gang Wang have used this result to derive exact results for the tangent-spatial and spatial distribution functions for the WLC model [22, 23].

### 5.2.6 What is the persistence length?

Let us return briefly to the definition of the persistence length. In Sect. 5.2, we defined the persistence length as the length scale on which the polymer “remembered its direction.” We now return to make a more precise definition.

Consider the expectation of the tangent at arc-length  $s$  dotted into a tangent at arc-length  $s'$

$$\langle \vec{u}(s) \cdot \vec{u}(s') \rangle = f(|s - s'|), \quad (5.22)$$

where the brackets  $\langle A \rangle$  denote the ensemble average of  $A$  and  $f$  is a function determined by the chain statistics. Eq. 5.22 is a quantitative measure of how well the polymer remembers its orientation. For tangents separated by many persistence lengths of contour length, we expect the tangents to be uncorrelated and Eq. 5.22 is zero. If  $s$  equals  $s'$ , the tangents are clearly the same and Eq. 5.22 is 1. Qualitatively, the persistence length defines the contour length on which the tangents are correlated. Eq. 5.21 allows a direct computation of Eq. 5.22:

$$\langle \vec{u}(s) \cdot \vec{u}(s') \rangle = \exp -\frac{|s-s'|}{\xi}, \quad (5.23)$$

where  $\xi$  is the bending modulus (Eq. 5.8) which has units of length (when  $kT=1$ ). This bending modulus has exactly the right physical properties to be what we have qualitatively called the persistence length. We shall therefore define the persistence length as the decay length in Eq. 5.23.

The functional form of Eq. 5.23 applies more generally. In fact, it is straightforward to show that Eq. 5.23 holds for polymers that bend isotropically (no preferred direction) and whose curvature is uncorrelated. This property is called multiplicativity [24]. Eq. 5.23 can be integrated twice to find the mean squared end-to-end distance [18]. In the long contour length limit, the mean squared end-to-end distance is the same as the freely jointed chain model when the relation between the Kuhn length (Eq. 5.4) is twice the persistence length.

In this section we have given a brief outline of the wormlike chain model and derived some of its basic properties. Although the model was originally proposed in a slightly different form [17], the WLC model describes the statistical mechanics of fluctuating linear-elastic rods. The model is characterized by a single parameter, the persistence length. The persistence length is the correlation length of the polymer tangent (Eq. 5.23), but it is also equal to the bending modulus divided by  $kT$ . In the next three chapters, we shall investigate whether this simple model applies to the mechanics of tightly-bent DNA. In the next section, we turn our attention to an important experimental technique for probing DNA mechanics: cyclization.

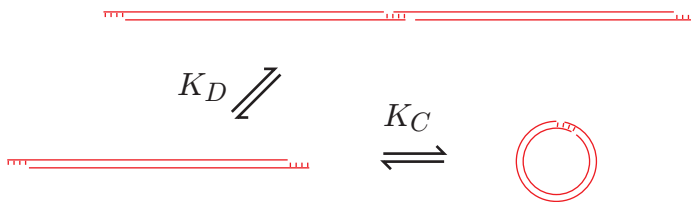


Figure 5.10: The cyclization assay: a schematic diagram. The linear monomer is a double-stranded DNA sequence with single-stranded complementary ends. These single-stranded ends can hybridize to form double stranded DNA. In standard cyclization experiments, the DNA backbone is then covalently joined by the enzyme DNA Ligase.

### 5.3 Effective concentration

To understand how the experiments of Cloutier and Widom [2] probe high-curvature chain statistics of DNA, we have to develop the concept of effective concentration. This concept is more generally applied than simply analyzing the results of cyclization experiments. There are many biological processes, like regulatory looping, for which the influence of DNA chain statistics on biological function can be factored into an effective concentration. Experiments that measure the effective concentration are important since these experiments sample the chain statistics in processes which are functionally analogous to many biological processes that capture rare DNA conformations [13, 16].

In the DNA cyclization assay, double stranded DNA sequences with complementary single stranded ends are cyclized into DNA loops and oligomers [25, 26, 27]. The effective concentration measured in this assay is called the  $J$  factor [25]. To understand this experiment, we shall first consider an equilibrium DNA cyclization reaction. When sequences cyclize, the closed conformations are stabilized by the hybridization (or base pairing) of the single stranded ends to form double-stranded DNA. This process is drawn schematically in Fig. 5.3. There are still two nicks in the DNA backbone, one on each side of the hybridized single-stranded DNA. Let us ignore these nicks for the moment [28].

When describing the cyclization reaction, there are two important free energies to consider. The first component is the free energy associated with the chain statistics; the free energy cost of bringing the two ends into the configuration required to hybridize. The second component is the free energy associated with the hybridization reaction itself which stabilizes the cyclized configuration. Our interest is exclusively in the former although both contribute to the cyclization equilibrium constant. Therein lies the problem with measuring the cyclization equilibrium constant for the purpose of studying the chain statistics; it depends on the affinity of the ends for each other.

The trick for isolating the chain statistics is to compare the cyclization equilibrium constant ( $K_C$ ) to the dimerization equilibrium constant ( $K_D$ ) for the same sequence. Remember that since

the ends are complementary, two ends of the same molecule can hybridize but so can the ends of two different molecules. Both processes involve the same hybridization reaction. The ratio of these equilibrium constants is known as the  $J$  factor [25]

$$J \equiv \frac{K_C}{K_D}. \quad (5.24)$$

Remember that we define the equilibrium constants

$$K_C \equiv \frac{[C]}{[L]} \quad (5.25)$$

$$K_D \equiv \frac{[D]}{[L]^2} \quad (5.26)$$

for the equilibrium concentrations of linear monomer  $[L]$ , cycle  $[C]$ , and dimer  $[D]$ . The  $J$  factor therefore has units of concentration. Note that the definition of the  $J$  factor implies that when the linear monomer concentration equals the  $J$  factor, cyclized and dimerized sequences are at equal concentration. For lower linear monomer concentration, the cyclization reaction is dominant. For higher linear monomer concentration, the dimerization reaction is dominant.

But in what sense is the  $J$  factor a concentration? Since we divide the cyclization equilibrium constant by the dimerization equilibrium constant, the dependence on the interaction of the single-stranded ends divides out. We shall show this more explicitly in a moment. If we think about the reaction physically, the hybridization rate should depend linearly on the local concentration of complementary ends, whether they be the complementary end of the same molecule or another. The  $J$  factor is therefore proportional to the effective concentration of one end at the other with the correct configuration to hybridize [25]. In the next section we shall derive this assertion.

### 5.3.1 Chain statistics and the $J$ Factor

Consider the interaction between two complementary ends. The free energy change upon binding is [28]

$$\Delta G = \Delta U_{\text{bond}} + \Delta G_{\text{config}} \quad (5.27)$$

where  $\Delta U_{\text{bond}}$  is the binding energy of the bond and  $\Delta G_{\text{config}}$  is the change in chain-configurational free energy due to the formation of the bond. We consider the free energy change for both cyclization and dimerization reactions

$$\Delta G_C \equiv -kT \log K_C, \quad (5.28)$$

$$\Delta G_D \equiv -kT \log K_D [L], \quad (5.29)$$

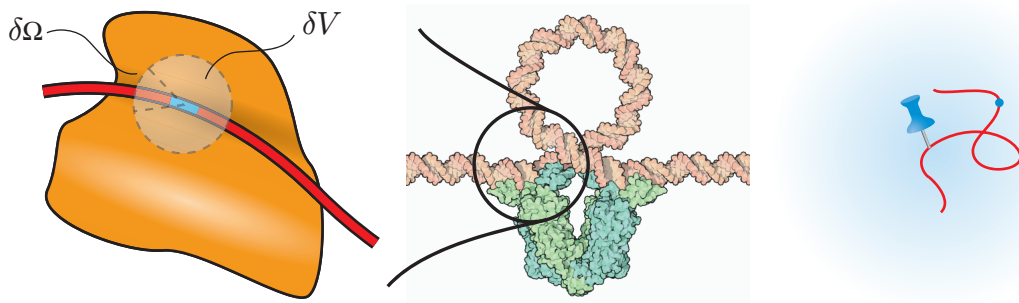


Figure 5.11: A schematic picture of a DNA operator binding to a protein binding site. In the  $J$  factor calculation, we imagine a range of configurations in which DNA can bind. This range is given by a volume  $\delta V$  and an orientational volume  $\delta\Omega$ . In the calculation, we assume is that this range is small. These parameters divide out of the resulting  $J$  factor. In the rightmost panel, we display the intuitive picture of effective concentration. The DNA is fixed at one end, resulting in an effective concentration of the operator (blue dot).

where we have introduced a factor of the monomer concentration into the dimerization free energy definition so that the derivations for the two free energies are analogous.

We shall denote the generalized coordinates describing the relative displacement and orientation of the end  $\{q_i\}$ . In our case, these degrees of freedom include the relative spatial displacement of the ends, the tangent of the polymer, as well as the relative twist [26].

The probability of the chain having some particular end configuration, specified by the coordinates  $\{Q_i\}$  and within admissible range  $\{\delta q_i\}$ , is

$$\mathcal{P} = \rho(Q_i) \prod dq_i, \quad (5.30)$$

where  $\rho$  is the probability density with respect to the coordinates  $\{q_i\}$ . The free energy change associated with assuming this configuration is therefore

$$\Delta G_{\text{config}} = -kT \log \rho(Q_i) \prod_i \delta q_i. \quad (5.31)$$

Note that this free energy depends on the admissible range  $\{\delta q_i\}$  which is not directly observable [26]. This scenario is drawn schematically for a DNA-protein complex in Fig. 5.3.1.

For DNA hybridization, the ends of the DNA must not only be spatially coincident, but their tangents must be aligned, and the twist of the helix must also be in registry. Therefore the  $q_i$  and

$Q_i$  are:

$$q_i = (\vec{x}, \cos \theta, \phi, \psi) \quad (5.32)$$

$$Q_i = (0, 1, 0, 0) \quad (5.33)$$

where  $\vec{x}$  is the end-to-end displacement,  $\theta$  and  $\phi$  describe the orientation of the final tangent with respect to the initial tangent, and  $\psi$  is the twist mismatch. The  $Q_i$  are the values of these coordinates required for hybridization.

We can now write the  $J$  factor in terms of the free energy change Eq. 5.27:

$$J = [L] \exp[-(\Delta G_C - \Delta G_D)/kT]. \quad (5.34)$$

We shall assume that the hybridization energy is identical in the two configurations. The  $J$  factor then depends only on the chain-configuration free energy

$$J = \rho_C [L] / \rho_D, \quad (5.35)$$

where  $\rho_C$  and  $\rho_D$  are the probability densities for cyclization and dimerization respectively.  $\rho_C$  depends on the chain statistics but dimerization probability density is simply the monomer concentration times the orientational density which is isotropic in solution  $\rho_D = [L]/(4\pi \cdot 2\pi)$ . The  $J$  factor is therefore [26, 27, 29, 18]

$$J = 8\pi^2 \rho_C, \quad (5.36)$$

where  $\rho_C$  is simply the polymer distribution function evaluated for the cyclization end configuration.

For the most part, we shall be interested in the mechanics of DNA when the twist is unobservable. Of course, the twist is observable in  $J$  factor, since DNA can only hybridize in twist registry, much like an electric cord will not plug into the wall unless it is in twist registry with the wall socket. We can approximately integrate out the twist degree of freedom by averaging the  $J$  factor over a helical repeat since the helical repeat is 10 bp and reasonably small compared with the total length of the sequence. In this case, the  $J$  factor becomes [29, 18]

$$J = 4\pi \rho'_C, \quad (5.37)$$

where  $\rho'_C$  is the probability density summed over the twist degrees of freedom, which results in a twist free theory.

To generalize this calculation to protein-induced DNA looping, we need only change the definition of  $\rho_C$ . That is, if the protein is stiff compared to DNA, it determines configuration of the DNA operators. Instead of the probability density for the cyclization boundary conditions, the protein

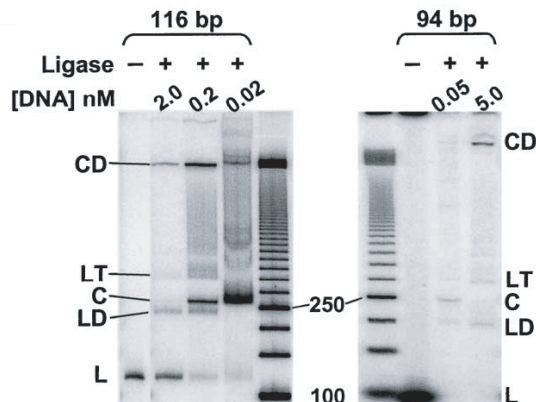


Figure 5.12: The results of a cyclization assay for DNA sequences of 116 bp and 94 bp. Gel electrophoresis is exploited to separate the bands of different length and topology. Above,  $L$  is linear monomer,  $C$  is cyclized monomer,  $LD$  is linear dimer,  $LT$  is linear trimer,  $CD$  is cyclized dimer, etc. The DNA is radio labeled and the concentration of DNA in each band is determined by the band intensity. Note that in the Ligase – column (Ligase is absent), there is only linear monomer. The unligated sequences are not stable enough to maintain their structure when run on the gel. For the 116 bp sequence, there are three Ligase + columns run at different DNA concentrations. As the DNA concentration is reduced, the bands corresponding to cyclized monomer increase in relative intensity while the bands corresponding to linear dimer decrease in relative intensity in agreement with the predictions of the kinetic equations. This concentration dependence is just one consistency check that the bands are correctly labeled. Note also that the bands corresponding to linear sequences run at the correct speed relative to the base pair ladder on the right-hand-side of the gel. This gel is from Ref. [2].

would dictate some more general set of boundary conditions which would give rise to an effective concentration. The relation between this looping  $J$  factor and the equilibrium constant is analogous to that derived for cyclization. For instance for the lac repressor looping reaction shown in Fig. 5.1.2 panel B, the looping equilibrium constant is

$$K_{\text{loop}} = \frac{[\text{looped}]}{[\text{unlooped}]} = K_{\text{op}} J', \quad (5.38)$$

where  $J'$  is the  $J$  factor evaluated for the correct operator-binding end configuration and  $K_{\text{op}}$  is the equilibrium constant for the repressor binding the free (unlooped) auxiliary operator sequence. The looping equilibrium constant depends on both DNA mechanics ( $J'$ ) as well as chemistry ( $K_{\text{op}}$ ) [13, 16, 11, 30].

### 5.3.2 Ligation, kinetics, and the cyclization assay

In the previous sections, I described a theoretical experiment in which the equilibrium concentrations of monomer, dimer, and cyclized sequences could be measured. Experimentally tractable biochemical cyclization assays are a little more complicated. Once the backbone nicks have been covalently sealed

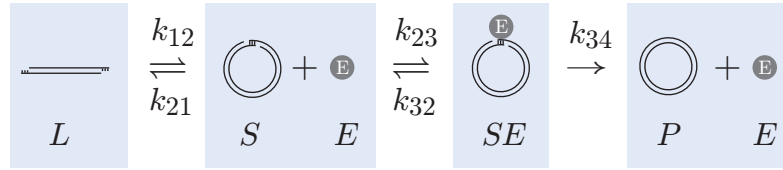


Figure 5.13: A schematic picture of the DNA cyclization assay. The linear monomer ( $L$ ) can cyclize or dimerize to form the ligation substrate ( $S$ ). The ligase enzyme ( $E$ ) can bind to this substrate to form a substrate enzyme complex ( $SE$ ). The ligation step then proceeds irreversibly to form the ligated product ( $P$ ) on ligase release. (The figure is adapted from Ref. [26].)

(ligated), it is straightforward to measure the relative populations via gel electrophoresis.<sup>2</sup> It is well known that the gel mobility of sequences decreases with sequence length. (“Longer sequences run more slowly.”) Fortunately, the circular topology of the cyclized sequences also reduces their gel mobility, implying that the various products of the cyclization reaction can be separated on a gel, and their concentrations measured by radio labeling. (See Fig. 5.3.2.)

The ligation reaction is performed with the enzyme T4 DNA ligase ( $E$ ) which covalently joins the backbone of a nicked substrate ( $S$ ). The biochemical process is picture schematically in Fig. 5.3.2. The kinetic equations are [26]



where  $L$  is linear monomer,  $S$  is the ligase substrate,  $E$  is ligase, and  $P$  is the ligated product. Despite the presence of the irreversible ligation step, we still wish to measure the ratio of the cyclization to the dimerization equilibrium constants for the linear monomer to nicked substrate reaction. In the kinetic regime where the ligation reaction is ligase limited,

$$k_{21} \gg k_{23}[E], \quad (5.41)$$

the equilibrium populations of cyclized and dimerized nicked substrates are sampled. Experimentally, this condition is straightforward to check since the product concentration is linear in the ligase concentration when the reaction is ligase limited. In this kinetic regime, the ratio of the ligated cyclization rate to the ligated dimerization rate is the  $J$  factor [26].

<sup>2</sup>The lifetime of the un-ligated products is not long enough to run the gel.

## 5.4 A startling discovery?

The nucleosome complex, the fundamental packing unit of DNA in Eukaryotic chromosomes, consists of a histone octamer tightly wrapped by DNA. (See Fig. 5.1.) One interesting and unresolved aspect of nucleosome formation is the sequence dependence of DNA-histone affinity. There is roughly a three-order-of-magnitude variation in the affinity of different DNA sequences for the histone core. Crystal structures of the nucleosome complex do not appear to support the common chemical motifs of sequence specificity (helix-turn-helix, zink finger motif, etc. [4, 9]). It has therefore been proposed that this variation in DNA-histone affinity could have an elastic origin.

The radius of curvature of the DNA that wraps the histone core is roughly 5 nm, a tenth of the persistence length. The bending energy is therefore large compared to  $kT$ . Small, sequence-dependent variations in the compliance of DNA could therefore lead to large variations in the overall free energy of nucleosome formation. Rough, order-of-magnitude estimates suggest that variations of only fifteen percent in the elastic modulus might be responsible for the observed variation in affinity. (See Sect. 5.2.3.)

To test this proposal, Cloutier and Widom compared the relative free energies of cyclization and nucleosome formation for 94 bp sequences. These DNA sequences were long enough to wrap the nucleosome just once, implying that the end state conformation of the DNA is roughly the same in both processes. These experiments confirmed that the sequenced induced variation in the relative free energies of cyclization and nucleosome formation were linearly correlated with slope one. The variation in the affinity of DNA for histones was predicted by their cyclization free energy, implying that the variation in the affinity of DNA for histones was a result of DNA conformation only, rather than the result DNA-protein interactions. This data is reproduced in Fig. 5.4.

The correspondence between cyclization and nucleosome formation was not unexpected, but Cloutier and Widom also reported a much more surprising result, the measured  $J$  factor (the propensity for sequences to spontaneously cyclize) was at least three orders of magnitude larger than that predicted by the WLC theory [2]. This data is plotted in Fig. 5.4. These results suggested that high-curvature DNA configurations might be orders of magnitude more probable than previously estimated based on other measurements of the chain statistics. The cyclization measurements for long-contour-length sequences were in excellent agreement with the WLC model, as were the results from force-extension experiments. Could DNA really be significantly softer at high curvature than predicted by the WLC model and yet still remain in excellent agreement with a host of previous measurements, which all seemed to implicate chain statistics described by the WLC model? What physical mechanisms could give rise to such a dramatic failure in the WLC model at high curvature?

These questions were of great relevance to biological systems. As we discussed in Sect. 5.1, high-curvature DNA bending in DNA-protein complexes is ubiquitous. If the work of Cloutier and

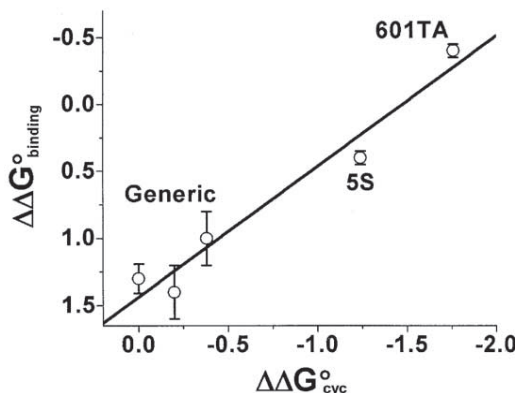


Figure 5.14: Histone affinity is DNA elasticity. In the plot above, the relative cyclization free energy is compared to the relative nucleosome formation free energy for 94 bp sequences. These sequences wrap the histone core once, implying that the DNA conformation in the nucleosome complex is similar to conformation of the cyclized sequence. The linear correlation of these free energies with slope one implies that the three-order-of-magnitude variation in DNA-histone affinity is mechanical in origin since it is identical to the variation in the cyclization free energy. That is to say that this variation is roughly independent of the presence of the protein and depends on the DNA conformation only. (Plot from Ref. [2].)

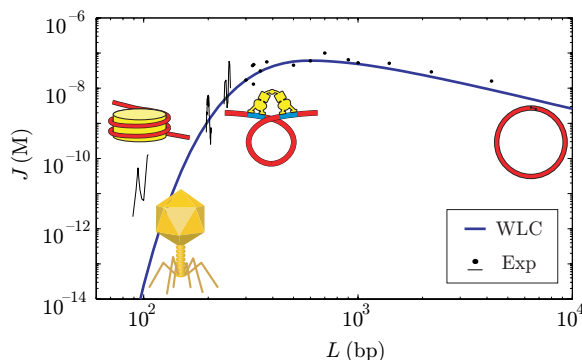


Figure 5.15: The WLC  $J$  factor (blue) is compared with measurements of the  $J$  factor from several authors (black) [2, 31, 27, 26, 32]. The  $J$  factor measurements made for sequences in length increments of 1 or 2 bp are plotted with solid lines connecting the data points. Other measurements are plotted as points. The WLC model does not include the twist modulation of the  $J$  factor evident in the continuous sets of experimental data and discussed in Sect. 5.3.1. Our interest is in the twist-free  $J$  factor (the  $J$  factor averaged over a 10 bp window). For long-contour-length sequences ( $L > 200$  bp), the experimental data is well described by the WLC model. For 94 bp sequences, the  $J$  factors measured by Cloutier and Widom [2] lie three to four orders of magnitude above the theoretical predictions of the WLC model. To give the reader a feeling for the biological systems that induce DNA bending on the length scales probed by cyclization experiments, we have drawn schematic pictures of biological bending at the contour length corresponding to the same induced radius of curvature. Nucleosome formation, phage packing, and transcriptional regulation all induce curvatures of the size probed by short-contour-length cyclization experiments of Cloutier and Widom. We have also drawn plasmid cyclization schematically at long-contour-length to show that some biological bending also explores the entropic regime of the  $J$  factor.

Widom was correct, it would dramatically change the way we thought about DNA bending. For example, these experiments suggested that DNA regulatory looping might remain active for very small DNA loops that would have been energetically forbidden in the WLC model. There was already evidence from *in vivo* regulatory looping studies that seemed to suggest exactly this [13, 14, 15, 16]! To understand DNA bending quantitatively in a biological context, the short-contour-length chain statistics would need to be reexamined.

## 5.5 What's wrong with the wormlike chain model

The experimental data of Cloutier and Widom [2] opened the door to the possibility that WLC model might fail dramatically for tightly bent DNA configurations. What are the possible mechanisms of this failure? Within the accepted framework of DNA mechanics, there are already two possible explanations. It is already known that DNA was pre-bent [33, 34, 35, 32]. There are sequences, so called A tracks, that are spontaneously curved in the absence of thermal fluctuations [36]. Also the stiffness of DNA is also a function of sequence [37, 9, 2]. Could either of these complications lead to the three-order-of-magnitude anomaly that Cloutier and Widom had observed? The answer is no. In the interest of brevity I will not make these extensive arguments here.

Rob Phillips, Phil Nelson, and I became convinced that the problem could only be resolved by changing the bending energy of DNA. Certainly from the perspective of macroscopic rods, it is well known that the linear-elastic model breaks down at high curvature. How can this intuitive picture be reconciled with years of experiments that showed that the WLC model described DNA statistics? One possible answer is that the cyclization experiments of Cloutier and Widom [2] probe a high-curvature regime of DNA bending that very few studies had probed before.

Our idea was to explore a model that included a rare, catastrophic breakdown of elasticity that would only appreciably change the chain statistics at high curvature. Many macroscopic systems kink, or localize curvature, in response to tight bending. Perhaps the most pedestrian example of this phenomena is the drinking straw which has a very small elastic bending regime before undergoing a kinking transition which buckles the straw. Back-of-the-envelope calculations showed that this model could reproduce exactly the behavior observed by Cloutier and Widom [2] for very rare kinking events. Not only that, but we would show that these kinks were nearly irrelevant to force-extension experiments that fit the WLC model so well. Does DNA kink?

# Bibliography

- [1] C. Bustamante, J. F. Marko, E. D. Siggia, and S. Smith. Entropic elasticity of lambda phage DNA. *Science*, 265:1599–1600, 1994. [5](#), [96](#), [195](#)
- [2] T. E. Cloutier and J. Widom. Spontaneous sharp bending of double-stranded DNA. *Molecular Cell*, 14(3):355–362, 2004. [5](#), [6](#), [7](#), [96](#), [97](#), [110](#), [114](#), [116](#), [117](#), [118](#), [124](#), [145](#), [148](#), [152](#), [164](#), [169](#), [172](#), [173](#), [174](#), [179](#), [181](#), [185](#), [198](#), [199](#), [200](#), [203](#)
- [3] Graeme K. Hunter. *Vital forces: The discovery of the molecular basis of life*. Academic Press, San Diego, 2000. [97](#)
- [4] Bruce Alberts, Dennis Bray, Julian Lewis, Martin Raff, Keith Roberts, and James D. Watson. *Molecular Biology of the Cell*. Garland Publishing, New York, NY, 3rd edition, 1994. [1](#), [11](#), [12](#), [13](#), [16](#), [97](#), [98](#), [100](#), [101](#), [116](#), [167](#), [179](#)
- [5] Bruce Alberts. The cell as a collection of protein machines: Preparing the next generation of molecular biologists. *Cell*, 92(3):291–294, 1998. [1](#), [2](#), [98](#)
- [6] Mario E. Cerritelli, Naiqian Cheng, Alan H. Rosenberg, Catherine E. McPherson, Frank P. Booy, and Alasdair C. Steven. Encapsidated conformation of bacteriophage T7 DNA. *Cell*, 91(2):271–280, October 1997. [99](#)
- [7] Prashant Purohit, Jané Kondev, and Rob Phillips. Mechanics of DNA packaging in viruses. *Proc. Natl. Acad. Sci. USA*, 100:3173–3178, 2003. [99](#), [100](#)
- [8] M. Doi and S. F. Edwards. *The Theory of Polymer Dynamics*. Oxford University Press, 1986. [99](#), [190](#)
- [9] Jonathan Widom. Role of DNA sequence in nucleosome stability and dynamics. *Quarterly Reviews of Biophysics*, 34(3):269–324, 2001. [100](#), [105](#), [116](#), [118](#), [179](#), [181](#), [201](#)
- [10] Carmen V. Kirchhamer, Chiou-Hwa Yuh, and Eric H. Davidson. Modular cis-regulatory organization of developmentally expressed genes: Two genes transcribed territorially in the sea urchin embryo, and additional examples. *Proc. Natl. Acad. Sci. USA*, 93:9322–9328, 1996. [101](#), [102](#)

- [11] Lacramioara Bintu, Nicolas E Buchler, Hernan G Garcia, Ulrich Gerland, Terence Hwa, Jané Kondev, and Rob Phillips. Transcriptional regulation by the numbers: models. *Current Opinion in Genetics & Development*, 15:116–124, 2005. [101](#), [103](#), [114](#)
- [12] R. W. Zeller, J. D. Griffith, J. G. Moore, C. V. Kirchhamer, R. J. Britten, and E. H. Davidson. A multimerizing transcription factor of sea urchin embryos capable of looping DNA. *Proc. Natl. Acad. Sci. USA*, 92:2989–2993, 1995. [102](#)
- [13] Karsten Rippe, Peter R. von Hippel, and J org Langowski. Action at a distance: DNA-looping and initiation of transcription. *Trends Biochem. Sci.*, 20(12):500–506, 1995. [2](#), [102](#), [110](#), [114](#), [118](#), [124](#), [152](#), [179](#)
- [14] J. Muller, S. Oehler, and B Muller-Hill. Repression of lac promoter as a function of distance, phase and quality of an auxiliary lac operator. *J. Mol. Biol.*, 257:21–29, 1996. [2](#), [102](#), [103](#), [118](#), [124](#), [152](#), [202](#)
- [15] J. Muller, A. Barker, S. Oehler, and B. Muller-Hill. Dimeric lac repressors exhibit phasedependent co-operativity. *J. Mol. Biol.*, 284:851–857, 1998. [2](#), [102](#), [103](#), [118](#), [124](#), [152](#)
- [16] Karsten Rippe. Making contacts on a nucleic acid polymer. *Trends Biochem. Sci.*, 26(12):733–740, 2001. [2](#), [102](#), [110](#), [114](#), [118](#), [124](#), [152](#)
- [17] O. Kratky and G. Porod. Rotgenuntersuchung geloster fadenmolekule. *Rec. Trav. Chim.*, 68(12):1106–1122, 1949. [104](#), [109](#), [123](#), [125](#)
- [18] H. Yamakawa. *Helical Wormlike Chains in Polymer Solutions*. Springer, Berlin, 1997. [5](#), [104](#), [108](#), [109](#), [113](#), [123](#), [125](#), [137](#), [146](#), [160](#), [164](#), [192](#), [199](#), [202](#)
- [19] Rob Phillips and Jan’e Kondev. *Physical Biology of the Cell*. Garland Press, 2006. To be published. [106](#)
- [20] R. P. Feynman and A. R. Hibbs. *Quantum Mechanics and Path Integrals*. McGraw-Hill, New York, 1965. [106](#), [130](#)
- [21] J. J. Sakurai. *Modern Quantum Mechanics*. Addison-Wesley, Reading, Massachusetts, 2nd edition, 1994. [107](#), [131](#), [186](#), [187](#), [188](#), [207](#), [208](#)
- [22] A. J. Spakowitz and Z.-G. Wang. Exact results for a semiflexible polymer chain in an aligning field. *Macromolecules*, 37:5814–5823, 2004. [108](#), [133](#), [138](#), [140](#), [144](#), [159](#), [169](#), [180](#), [193](#), [196](#), [211](#)
- [23] A. J. Spakowitz and Z.-G. Wang. End-to-end distance vector distribution with fixed end orientations for the wormlike chain model. *Phys. Rev. E*, 2005. In preparation. [108](#), [169](#), [180](#), [192](#), [193](#), [211](#), [212](#)

- [24] A. Y. Grosberg and A. R. Khokhlov. *Statistical physics of macromolecules*. AIP Press, New York, 1994. [109](#), [130](#), [137](#)
- [25] H. Jacobson and W. H. Stockmayer. Intramolecular reaction in polycondensations 1. The theory of linear systems. *J. Chem. Phys.*, 18(12):1600–1606, 1950. [110](#), [111](#), [146](#), [198](#), [199](#)
- [26] D. Shore, J Langowski, and R. L. Baldwin. DNA flexibility studied by covalent closure of short fragments into circles. *Proc. Natl. Acad. Sci. USA*, 170:4833–4837, 1981. [110](#), [112](#), [113](#), [115](#), [117](#), [148](#), [173](#), [179](#), [198](#), [199](#)
- [27] D. Shore and R. L. Baldwin. Energetics of DNA twisting 1. Relation between twist and cyclization probability. *Journal of Molecular Biology*, 170(4):957–981, 1983. [110](#), [113](#), [117](#), [148](#), [173](#), [198](#), [199](#)
- [28] P. J. Hagerman. Investigation of the flexibility of DNA using transient electric birefringence. *Biopolymers*, 20:1503–1535, 1981. [110](#), [111](#)
- [29] J. Shimada and H. Yamakawa. Ring-closure probabilities for twisted wormlike chains – applications to DNA. *Macromolecules*, 17:689–698, 1984. [113](#), [123](#), [149](#), [198](#), [199](#)
- [30] Lacramioara Bintu, Nicolas E Buchler, Hernan G Garcia, Ulrich Gerland, Terence Hwa, Jané Kondev, Thomas Kuhlman, and Rob Phillips. Transcriptional regulation by the numbers: applications. *Current Opinion in Genetics & Development*, 15:125–135, 2005. [114](#)
- [31] T. E. Cloutier and Jonathan Widom. DNA twisting flexibility and the formation of sharply looped protein–DNA complexes. *Proc. Natl. Acad. Sci. USA*, 102:3634–3650, 2005. [117](#)
- [32] M. Vologodskaia and A. Vologodskii. Contribution of the intrinsic curvature to measured DNA persistence length. *J. Mol. Biol.*, 317(2):205–213, 2002. [117](#), [118](#), [148](#), [199](#)
- [33] E. N. Trifonov, R. K.-Z. Tan, and S. C. Harvey. Static persistence length of DNA. In W. K. Olson, M. H. Sarma, and M. Sundaralingam, editors, *DNA bending and curvature*, pages 243–254. Adenine Press, Schenectady NY, 1987. [118](#), [137](#)
- [34] Jan Bednar, Patrick Furrer, Vsevolod Katritch, Alicja Z Stasiak, Jacques Dubochet, and Andrzej Stasiak. Determination of DNA persistence length by cryo-electron microscopy. Separation of static and dynamic contributions to the apparent persistence length of DNA. *Journal of Molecular Biology*, 254:579–594, 1995. [118](#), [167](#), [184](#)
- [35] P. Nelson. Sequence-disorder effects on DNA entropic elasticity. *Phys. Rev. Lett.*, 80:5810–5812, 1998. [118](#), [137](#)

- [36] J. C. Marini, S. D. Levene, D. M. Crothers, and P. T. Englund. Bent helical structure in kinetoplast. *Proc Natl Acad Sci USA*, 79:7664–7668, 1982. [118](#)
- [37] J. D. Kahn, E. Yun, and D. M. Crothers. Detection of localized DNA flexibility. *Nature*, 368(6467):163–166, 1994. [118](#), [173](#)

## Chapter 6

# Exact theory of kinkable elastic polymers

*This chapter is a reproduction of Ref. [1].*

The importance of nonlinearities in material constitutive relations has long been appreciated in the continuum mechanics of macroscopic rods. Although the moment (torque) response to bending is almost universally linear for small deflection angles, many rod systems exhibit a high-curvature softening. The signature behavior of these rod systems is a kinking transition in which the bending is localized. Recent DNA cyclization experiments by Cloutier and Widom have offered evidence that the linear-elastic bending theory fails to describe the high-curvature mechanics of DNA. Motivated by this recent experimental work, we develop a simple and exact theory of the statistical mechanics of linear-elastic polymer chains that can undergo a kinking transition. We characterize the kinking behavior with a single parameter and show that the resulting theory reproduces both the low-curvature linear-elastic behavior which is already well described by the Wormlike Chain model, as well as the high-curvature softening observed in recent cyclization experiments.

### 6.1 Introduction

The behavior of many semiflexible polymers is captured by the Wormlike Chain model [2, 3]. This model amounts to the statistical mechanics of linearly-elastic rods[4] where the elastic energy is microscopically a combination of both energetic and entropic contributions[5]. The mechanics of DNA, a polymer of particular biological interest, has been studied extensively experimentally and theoretically and its mechanical properties have been very well approximated by the Wormlike Chain model (WLC)[6] and its successors such as the Helical Wormlike Chain model[3]. For example, accurate force-extension experiments have shown that DNA is surprisingly well described by WLC[6, 7, 5], at least until the effects of DNA stretching become important at tensions of order 50 pN.

Despite the success of the WLC in describing DNA mechanics, recent DNA cyclization experi-

ments by Cloutier and Widom[8] have shown a dramatic departure from theoretical predictions for highly-curved DNA. These experiments suggest that the effective bending energy of small, cyclized sequences of DNA is significantly smaller than predicted by existing theoretical models based upon linear-elastic constitutive relations, in which the bending energy is quadratic in curvature. Similar anomalies have been revealed in transcriptional regulation where DNA looping by regulatory proteins remains active down to 60 base pair (bp) separations between the binding sites[9, 10, 11, 12, 13, 14].

From a continuum-mechanics perspective, this failure of the model at high-curvature is hardly surprising; the importance of material nonlinearities has been appreciated for many years. In fact, anyone who has ever tried to bend a drinking straw has observed that the straw will at first distribute the bending, as predicted by the linear theory, but as the curvature increases, the straw will eventually kink, localizing the bending. This kinking behavior is the signature of nonlinear constitutive softening at high curvature. Nonlinearities are certainly important in microscopic physical systems, such as polymers, because the effective bending free energy, a combination of interaction potentials and entropic effects, is only approximately harmonic. The possibility of kinking in DNA was realized long ago by Crick and Klug, who proposed a specific atomistic structure for the kink state [15]. Many authors have since found kinked states of DNA in protein–DNA complexes (see for example [16]), but less attention has been given to *spontaneous* kinking of free DNA in solution, even though Crick and Klug pointed out this possibility.

Our goal in this paper is to develop a simple, generic extension of the WLC model, introducing only one additional parameter, the average number of kinks per unit length for the unconstrained chain. The “kinks” are taken to be freely-bending hinge elements in the chain. This model is an extension of the well known Wormlike Chain (WLC); we refer to it as the Kinkable Wormlike Chain (KWLC). Although our model is not a detailed microscopic picture for DNA, it does capture the key consequences of any more detailed picture of kink formation. As such, it serves as a useful coarse-grained model to describe high-curvature phenomena in many stiff biopolymers, not just DNA [17]. Our main results are summarized in Figs. 6.5.2, 6.5.2, 6.6.2, and 6.6.3.

The KWLC is the simplest example of a class of theories that have been proposed and studied by Storm and Nelson[18] and more recently by Levine[19]. It is simple enough that many results are exact or nearly so. The method by which we obtain our exact results is analogous to the Dyson expansion for time-dependent quantum perturbation theory. For the KWLC, the perturbation series can be re-summed exactly.

For small values of our kinking parameter the KWLC model predicts nearly identical behavior to the WLC—except when the rod is constrained to be highly curved. Such constraints induce kinking, even when the kinking parameter is small. We will show in detail how the energy relief caused by this alternative bending conformation can account for the observed anomalously high cyclization rate of short loops of DNA[8] and anomalously high levels of gene expression[11, 12]. Further discussion

of the applications of KWLC to DNA, will appear elsewhere[20]; the present paper focuses on the mathematical details of the theory. Yan and Marko, and Vologodskii, have independently obtained results related to ours [21, 22]. Also, Sucato *et al.* have performed Monte Carlo simulations of kinkable chains to obtain information about their structural and thermodynamic properties [23].

The outline of the paper is as follows: in Sect. 6.2, we introduce the KWLC model in a discrete form. In section 6.3, we compute the unconstrained partition function for the theory and show that there is a sensible continuum limit. In section 6.4, we give an exact computation of the tangent partition function of the continuum theory as well the moment-bend constitutive relation and the kink number for bent polymer chains. We show that kinking causes an exact renormalization of the tangent persistence length and we write exact expressions for the average squared end distance and the radius of gyration. In Sect. 6.5, we exactly compute the Fourier-Laplace transform of the spatial propagator and discuss various limits of these results. We also compute the exact force-extension relation and the structure factor for KWLC. In Sect. 6.6, we compute the KWLC correction to the Jacobson-Stockmayer  $J$  factor and the partition function for cyclized chains. We show that the topological constraint of cyclization induces kinking and we compute the kink number distribution explicitly. In Sect. 6.7, we discuss the limitations of KWLC. In the Appendix, we present a summary of the Faltung Theorem which is required for computations and develop the small and large contour length limits of the KWLC  $J$  factor.

## 6.2 Kinkable Wormlike Chain Model

Although the Wormlike Chain model was originally proposed to describe a purely entropic chain without a bending energy[2], it is often interpreted as the statistical mechanics of rods with bending energies quadratic in curvature[4, 24]. From a mechanical perspective, the success of the WLC model is not surprising since the small amplitude bending of rods universally induces a linear moment response. For WLC, the bending energy for a polymer in configuration  $\Gamma$  is

$$E_{\Gamma} = \int_0^L ds \frac{\xi}{2} \left( \frac{d\vec{t}}{ds} \right)^2, \quad (6.1)$$

where  $\vec{t}(s)$  is the unit tangent at arc length  $s$ ,  $L$  is the contour length, and  $\xi$  is the bending modulus. Throughout this paper we will express energies in units of the room-temperature thermal energy  $k_{\text{B}}T = 4.1 \times 10^{-21}$  J. For WLC it is well known that the bending modulus and persistence length (the length scale over which tangent are thermally correlated) are equal in these units [5].

It is most intuitive to define our new model in terms of the discretized definition of WLC. Accordingly, we divide a chain of arc length  $L$  into  $L/\ell$  segments of length  $\ell$ . There are then  $N = (L/\ell) - 1$  interior vertices, plus two endpoints (Fig. 6.2a). Next we replace the arc length

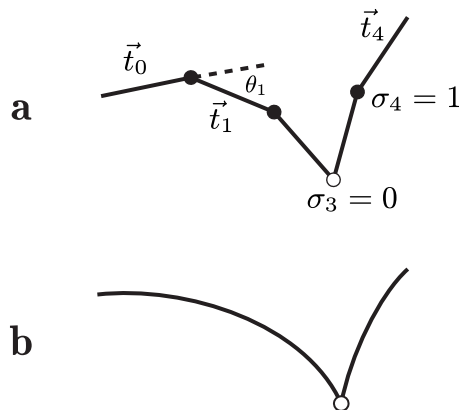


Figure 6.1: *a*: The discretized KWLC is a chain of wormlike and kink-like vertices. In this illustration  $N = 4$ ; thus there are four vertices, of which one is kink-like. When a vertex  $i$  is wormlike ( $\sigma_i = 1$ ), the energy is given by the normal Wormlike Chain energy; if it is kink like ( $\sigma_i = 0$ ), the energy is  $\epsilon$ , independent of  $\theta_i$ . *b*: The continuum version of this theory. Although the number of vertices is now infinite, the continuum limit maintains a finite average kink density.

derivative with the finite difference over the segment length  $\ell$ , replace the integral with a sum, and introduce the spring constant  $\kappa \equiv \xi/\ell$ . The resulting energy is

$$E_{\Gamma} = \sum_{i=1}^N \kappa (1 - \vec{t}_i \cdot \vec{t}_{i-1}), \quad (6.2)$$

where  $\vec{t}_i$  is the vector joining vertices  $i$  and  $i + 1$ .

We introduce a similar discretized energy for the Kinkable Wormlike Chain model (KWLC). In addition to the bending angle, there is now a degree of freedom at each vertex describing whether the vertex is kink-like or wormlike. To describe this degree of freedom, we introduce a state variable,  $\sigma_i$  at each vertex. When  $\sigma_i = 1$ , we say that the vertex is wormlike and the energy is given by the discrete WLC energy at that vertex. When  $\sigma_i = 0$ , the vertex is kink-like and the energy is independent of the bend angle at that vertex, but there is an energy penalty  $\epsilon$  to realize the kink state. This model is depicted schematically in Fig. 6.2. The energy for the model we have just described can be concisely written as

$$E_{\Gamma}^* = \sum_{i=1}^N [\kappa (1 - \vec{t}_i \cdot \vec{t}_{i-1}) \sigma_i + \epsilon(1 - \sigma_i)] , \quad (6.3)$$

where the  $*$  denotes that this is the energy of the KWLC theory and  $\epsilon$  is the energetic cost of introducing a kink in the chain. Note that in general we denote KWLC results or equations with a  $*$ . We will recover the WLC results when we take the kinking energy  $\epsilon$  to infinity. While Storm

and Nelson[25] and others[26, 27, 28, 29, 25, 19] have considered more general theories where the kink energy is not assumed to be independent of the kink angle, much of the important physics can already be studied in the simpler KWLC theory. Moreover, this theory has the significant advantage of being analytically exact to a much greater extent than more general theories; it applies in the limit where the kinks are only weakly elastic compared to the elastic rod.

### 6.3 Partition functions

For a summary of notation used in this article, see Appendix 6.12.

We have defined the KWLC model in terms of a discrete set of degrees of freedom. In the next section, however, we shall wish to take advantage of the continuum WLC machinery. To this end, this section formulates the continuum limit of the KWLC model. Beyond the computational advantage, there is also an additional reason to go to the continuum limit. Fig. 6.2 describes the kinking with two parameters, a density  $\ell^{-1}$  of kinkable sites and the kink energy  $\epsilon$ . We wish to describe the kinking in terms of a *single* parameter, to be called  $\zeta$  (see Eq. 6.7).  $\zeta$  essentially sets the average number of kinks per contour length for a long, unstressed chain. In the continuum limit of WLC, we take  $\ell \rightarrow 0$  while holding the persistence length  $\xi$  and chain length  $L$  constant. To take the corresponding continuum limit for KWLC, we will also hold  $\zeta$  constant as  $\ell \rightarrow 0$ .

We begin by computing the partition functions for the WLC and KWLC and demonstrating that there is a continuum limit of the KWLC. These unconstrained partition functions are required for later computations. For this case, the partition function factors into independent contributions from each interior vertex. In the continuum limit ( $\kappa \rightarrow \infty$ ), the partition function for each vertex in the WLC model is

$$Q \equiv \lim_{\kappa \rightarrow \infty} \int d^2 \vec{t}_i \exp[-\kappa(1 - \cos \theta_i)] = \frac{2\pi}{\kappa}, \quad (6.4)$$

where  $\theta_i$  is the polar angle of  $\vec{t}_i$  defined using  $\vec{t}_{i-1}$  as the polar axis, that is,  $\cos \theta_i \equiv \vec{t}_i \cdot \vec{t}_{i-1}$ . The measure  $d^2 \vec{t}_i = d(\cos \theta_i) d\phi_i$  denotes solid angle on the unit sphere. The total discretized partition function for the chain of  $N + 1$  segments is then

$$\mathcal{Z}_{\text{discrete}}(L) = 4\pi Q^N. \quad (6.5)$$

The factor of  $4\pi$  reflects one overall orientation integral, for example the integral over  $\vec{t}_0$ .

Similarly, the partition function for a single vertex of the KWLC theory is

$$Q^* \equiv \lim_{\kappa \rightarrow \infty} \int d^2 \vec{t}_i (\exp[-\kappa(1 - \cos \theta_i)] + \exp[-\epsilon]) = Q (1 + 2\kappa e^{-\epsilon}), \quad (6.6)$$

which we have written in terms of the corresponding WLC quantity  $Q$ . The total partition function

for the chain of  $N + 1$  segments is  $\mathcal{Z}_{\text{discrete}}^*(L) = 4\pi(Q^*)^N$ .

In the small segment length limit, Eq. 6.6 shows that the probability of a vertex being kink-like is  $2\kappa e^{-\epsilon}$ . Therefore the probability of kinking per unit length (for this unconstrained situation) is

$$\zeta \equiv \frac{2\xi}{\ell^2} e^{-\epsilon} = \frac{4\pi}{\ell Q} e^{-\epsilon}, \quad (6.7)$$

where we have eliminated the bending spring constant,  $\kappa$ , in favor of the persistence length,  $\xi = \kappa\ell$ . In order to recover a sensible continuum limit, we will hold the parameter  $\zeta$  constant as we take the segment length to zero. Note that we recover the WLC theory when we set  $\zeta \rightarrow 0$ . In later sections we will discuss a formal “zero temperature” limit, in which simple mechanics (no thermal fluctuations) describes the physics. This limit is a useful intuitive tool, not an experimental prediction of the behavior of polymers frozen in solution. The “zero temperature” limit is taken treating  $\zeta$  as temperature independent, which is equivalent to either the short rod limit or the large persistence length limit which we shall use interchangeably.

In the continuum limit, we must remove a divergent constant in the partition functions as  $N \rightarrow \infty$ . Thus we define the path integral measure

$$[d\vec{t}(s)]_{\vec{t}_i} \equiv \prod_{i=1}^N \frac{d^2\vec{t}_i}{Q}, \quad (6.8)$$

where  $Q$  is defined by Eq. 6.4. Note that unlike the discrete case, in this measure the starting tangent vector  $\vec{t}_0$  is *not* integrated, but is instead fixed to some given  $\vec{t}_i$ . The continuum partition function corresponding to  $\mathcal{Z}_{\text{discrete}}(L)$  is then

$$\mathcal{Z}(L) \equiv \int [d\vec{t}(s)]_{\vec{t}_i} e^{-E^*} = 1. \quad (6.9)$$

With our choice of integration measure,  $\mathcal{Z}(L)$  just equals one, independent of  $L$ .

The continuum KWLC partition function is now

$$\mathcal{Z}^*(L) = \lim_{N \rightarrow \infty} \left( 1 + \frac{\zeta L}{N} \right)^N = e^{\zeta L}. \quad (6.10)$$

The convergence of the partition function assures us that the continuum limit is well defined. As a consistency check, we now compute the average kink number for the unconstrained chain

$$\langle m \rangle = \frac{\partial \log \mathcal{Z}^*}{\partial \log \zeta} = \zeta L, \quad (6.11)$$

which confirms that  $\zeta$  is indeed density of kinks. The expansion of the partition function in a power series shows that the kink number distribution is also correct. We will repeat the average kink

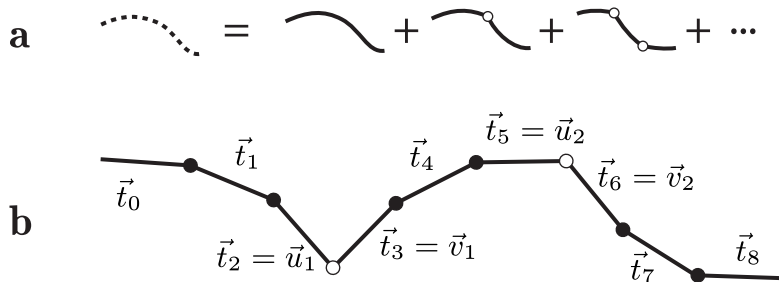


Figure 6.2: *a.* Diagrammatic representation of the kink expansion for the tangent partition function. The dashed curve represents the KWLC theory and the solid curves represent the WLC theory. It is convenient to collect the terms by kink number as shown. *b.* Detail of the two-kink term, showing the relation to the underlying discrete model.  $\vec{u}_i$  and  $\vec{v}_i$  are the tangent vectors flanking kink number  $i$ .

number calculation several times in the course of this paper for different constraints to show that constraining the chain will affect the kink number.

## 6.4 Tangent partition function and propagator

In this section we compute the tangent partition function and propagator by using a method symbolized in Fig. 6.4a. By tangent partition function  $\mathcal{Z}(\vec{t}_f, \vec{t}_i, L)$  we mean the partition function with the initial and final tangents constrained (Eq. 6.12 below). Dividing the tangent partition function by the unconstrained partition function  $\mathcal{Z}(L)$  gives the probability density  $H(\vec{t}_f, \vec{t}_i, L)$  for the final tangent vector, given the initial tangent. We will refer to  $H$  as the normalized tangent partition function, or propagator.

Most of the kink-related physics of the KWLC theory can be understood qualitatively from the tangent partition function. Furthermore, the computation of the tangent partition function is more transparent than the analogous spatial computation in which the end-to-end distance is constrained along with the initial and final tangents. The tangent partition function for WLC is defined as

$$\mathcal{Z}(\vec{t}_f, \vec{t}_i; L) \equiv \int [d\vec{t}(s)]_{\vec{t}_i} e^{-E} \delta^{(2)}[\vec{t}_N - \vec{t}_f], \quad (6.12)$$

where the path integral is regularized as described above (Eq. 6.8). Due to the tangent constraint, the partition function no longer factors into independent vertex contributions. The lower limit on the integration denotes that the initial tangent  $\vec{t}_0$  is held equal to  $\vec{t}_i$ ; the final tangent  $\vec{t}_N$ , is set to  $\vec{t}_f$  by the delta function. We integrate (or sum) over the infinite set of intervening tangents in order to generate the partition function. In this regularization scheme, the tangent partition function and

tangent propagator are identical

$$H(\vec{t}_f, \vec{t}_i; L) = \mathcal{Z}(\vec{t}_f, \vec{t}_i; L), \quad (6.13)$$

since with our conventions the unconstrained WLC partition function is one. However, we will see that this convenient identity does not hold for the KWLC:  $H^* \neq \mathcal{Z}^*$ .

While the direct evaluation of the path integral in Eq. 6.12 is difficult, it is well known that this calculation is equivalent to finding the quantum-mechanical propagator for a particle on the unit sphere[30, 31]. The tangents correspond to position, arc length corresponds to imaginary time, and persistence length corresponds to mass. Thus, the tangent partition function is

$$\mathcal{Z}(\vec{t}_f, \vec{t}_i; L) = \langle \vec{t}_f | e^{-\mathcal{H}L} | \vec{t}_i \rangle, \quad (6.14)$$

where the Hamiltonian operator is defined as

$$\mathcal{H} \equiv \frac{\vec{p}^2}{2\xi}, \quad (6.15)$$

where  $\vec{p}^2$  is the Laplace operator on the unit sphere. The Hamiltonian is diagonal in the angular momentum representation so the tangent partition function for WLC can be expressed as

$$\mathcal{Z}(\vec{t}_f, \vec{t}_i; L) = \sum_{l=0}^{\infty} \sum_{m=-l}^l Y_l^m(\vec{t}_f) Y_l^m(\vec{t}_i)^* C_l(L). \quad (6.16)$$

In this expression, the  $Y_l^m$ 's are the Spherical Harmonics and the coefficients  $C_l$  are

$$C_l(L) = \exp \left[ -\frac{l(l+1)L}{2\xi} \right]. \quad (6.17)$$

It can easily be shown that this partition function has the required normalization by summing over the final tangent to recover  $\mathcal{Z}(L) = 1$ .

To compute the tangent partition function for KWLC, we proceed with the path integral in exactly the same fashion, setting the initial tangent, integrating over an infinite set of intervening tangents, and summing over the state vectors:

$$\mathcal{Z}^*(\vec{t}_f, \vec{t}_i; L) = \sum_{\{\sigma_1, \dots, \sigma_N\}} \int [d\vec{t}(s)]_{\vec{t}_i} e^{-E^*} \delta^{(2)}[\vec{t}_N - \vec{t}_f]. \quad (6.18)$$

It is now convenient to collect the terms in contributions with a fixed number  $m$  of kinks and then express the result in the continuum limit.

The first step in going from the definition of the discrete KWLC tangent partition function to the

continuum limit is to reorganize the sum over  $\{\sigma_n\}$  as a sum over the number of kinks  $m$ . Each term of this sum is in turn a sum over the positions  $n_i$  of the kinks, for  $i = 1, \dots, m$ . The only subtlety here is introducing the correct limits on the sum to avoid over counting the kink states. The last kink can be chosen at any arc-length location, but additional kinks must always be chosen with smaller arc-length values than the following kink. This method is more convenient than introducing “time ordering” and a factor of  $1/m!$  to explicitly remove the over counting as is commonly done in the Dyson expansion for time-dependent quantum perturbation theory[32].

The next step is to replace the kink position sums with integrals over the position of the kinks as

$$\sum_{n_i=i}^{n_{i+1}-1} \rightarrow \int_0^{L_{i+1}} \frac{dL_i}{\ell}, \quad i = 1, \dots, m, \quad (6.19)$$

where  $L_i \equiv n_i \ell$  and we take  $L_{m+1} = L$ . The structure of the arc length integrals is that of a series of convolutions[33], which we write symbolically as  $\otimes$ . For example, if  $F(L)$  and  $G(L)$  are two functions, then

$$(F \otimes G)(L) \equiv \int_0^L dL_1 F(L - L_1)G(L_1). \quad (6.20)$$

In the intervals between kinks, the chain is described by the WLC energy function. We can therefore replace each partial path integral with a WLC propagator.

For every kink, there is one factor of  $Q^{-1}$  that has been introduced by the path integral normalization (Eq. 6.8) but is not absorbed by the definition of the WLC propagator (eqns 6.18 and 6.13). The  $m$  factors of  $\ell^{-1}$ ,  $e^{-\epsilon}$ , and  $Q^{-1}$  can now be written as  $(\zeta/4\pi)^m$  (see eqn 6.7). Defining  $\mathcal{Z}^* = \sum_m \mathcal{Z}_m^*$ , the terms in the kink-number expansion can thus be written (compare Fig. 6.4)

$$\mathcal{Z}_m^*(\vec{t}_f, \vec{t}_i; L) = \zeta^m \int \prod_{j=1}^m \frac{d^2 \vec{u}_j d^2 \vec{v}_j}{4\pi} \underbrace{(H(\vec{t}_f, \vec{v}_m) \otimes H(\vec{u}_m, \vec{v}_{m-1}) \otimes \dots \otimes H(\vec{u}_1, \vec{t}_i))}_{m+1}(L), \quad (6.21)$$

The  $2m$  angular integrations are over the incoming ( $\vec{u}_i$ ) and outgoing ( $\vec{v}_i$ ) tangents of the  $m$  kinks.

Eq. 6.21 has a very simple interpretation. The probability of creating a kink between  $L$  and  $L+dL$  is just  $\zeta dL$ . We then sum over all possible configurations being careful to choose the integration limits so as not to over count the kink states. At each kink, all orientational information is lost, so that only tangent independent terms of the propagator contribute (those with angular quantum number  $l = 0$ ).

To compute the contour length convolution of propagators, it is convenient to work with the contour length Laplace transformed propagators  $\tilde{H}$  (Eq. 6.80). We shall denote the contour length Laplace transformed functions with a tilde and use the variable  $p$  as the arc length Laplace conjugate variable. Although we could avoid Laplace transforming the partition function at this juncture, we use this method presently because it is analogous to our later computation of the spatial propagator.

By the well known Faltung theorem (Eq. 6.84), the convolution of propagators is just the product of Laplace transforms. Therefore, in terms of the transformed WLC propagators, the  $m$  kink KWLC Laplace transformed partition function is

$$\tilde{\mathcal{Z}}_m^*(\vec{t}_f, \vec{t}_i; p) = \zeta^m \begin{cases} \tilde{H}(\vec{t}_f, \vec{t}_i; p), & m = 0 \\ \tilde{C}_0^{m+1}(p)/4\pi, & m > 0. \end{cases} \quad (6.22)$$

To derive Eq. 6.22, note that Eq. 6.16 gives the WLC tangent propagator summed over the initial tangent as  $C_0(L)$ , which equals 1 from Eq. 6.17. The corresponding Laplace transform is just  $\tilde{C}_0(p) = 1/p$ .

The  $m$  kink contributions to the KWLC transformed tangent partition function can now be summed exactly (i.e.  $\mathcal{Z}^* = \sum_m \mathcal{Z}_m^*$ ) because they form a geometric series, resulting in

$$\tilde{\mathcal{Z}}^*(\vec{t}_f, \vec{t}_i; p) = \tilde{H}(\vec{t}_f, \vec{t}_i; p) + \frac{1}{4\pi} \frac{\zeta \tilde{C}_0^2(p)}{1 - \zeta \tilde{C}_0(p)}. \quad (6.23)$$

The  $m > 0$  kink terms clearly contribute no tangent dependence. The inverse Laplace transform can now be computed without complications, giving the exact KWLC tangent partition function

$$\mathcal{Z}^*(\vec{t}_f, \vec{t}_i; L) = H(\vec{t}_f, \vec{t}_i; L) + \frac{e^{\zeta L} - 1}{4\pi}. \quad (6.24)$$

Alternatively, we could have derived Eq. 6.24 by noting that the KWLC model is mathematically equivalent to a Quantum Mechanical system whose Hamiltonian is diagonal in the angular momentum representation:

$$\mathcal{H}^* = -\zeta |0, 0\rangle \otimes \langle 0, 0| + \mathcal{H}. \quad (6.25)$$

Here  $|l, m\rangle$  is the state with angular momentum quantum numbers  $l$  and  $m$  and  $\mathcal{H}$  is the Hamiltonian operator for the WLC. The only change to the theory is a “ground state energy” shift equal to  $-\zeta$ .

The KWLC tangent propagator and its Laplace transform can now be evaluated using Eq. 6.10:

$$H^*(\vec{t}_f, \vec{t}_i; L) = \frac{\mathcal{Z}^*(\vec{t}_f, \vec{t}_i; L)}{\mathcal{Z}^*(L)} = e^{-\zeta L} \left[ H(\vec{t}_f, \vec{t}_i; L) + \frac{e^{\zeta L} - 1}{4\pi} \right], \quad (6.26)$$

$$\tilde{H}^*(\vec{t}_f, \vec{t}_i; p) = \tilde{H}(\vec{t}_f, \vec{t}_i; p + \zeta) + \frac{\zeta}{4\pi p(p + \zeta)}. \quad (6.27)$$

Fig. 6.4a compares the KWLC tangent propagator to the WLC theory with an illustrative value  $\zeta = 0.01/\xi$ . The two theories appear indistinguishable, and in fact we will find that many, but not all, predictions of the models are essentially the same in this parameter regime.

In principle since the propagator is known exactly, everything in the theory can now be computed. Of course this is an exaggeration since, even though the tangent propagator for WLC has long

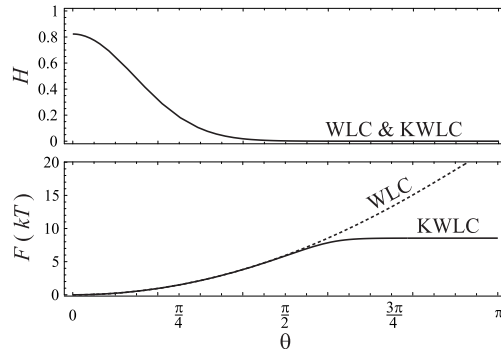


Figure 6.3: The tangent propagator and the tangent free energy as functions of the deflection angle for the illustrative values  $L = 0.2\xi$  and  $\zeta\xi = 10^{-2}$ . The solid curves are KWLC and the dashed curves are WLC with the same value of  $\xi$ . In the absence of kinking, the WLC distribution ( $H$ ) is essentially zero away from small deflection. For the small value of  $\zeta$  chosen above, WLC and KWLC are indistinguishable in the top panel. The presence of kinks adds a background level to the propagator which is independent of  $\theta$ , but is thermally inaccessible—too small to distinguish from zero in the top panel, but is visible in the free energy in the lower panel. The tangent free energy gives an intuitive picture of the system interpreted as a single-state system with an effective bending modulus which saturates due to kinking. Most thermally driven experiments measure the polymer distribution as it is pictured in the top panel and are therefore insensitive to the high-curvature constitutive relation. But experiments which do probe this regime, short-contour-length cyclization for example, will be extremely sensitive to the difference between the theories due to the large free energy difference at large deflection.

been known, only recently have the exact expressions for the transformed spatial propagator been derived[34, 35]. The free energy of the chains for both theories have the canonical relation with their respective partition functions

$$F(\theta; L) = -\log \mathcal{Z}(\vec{t}_f, \vec{t}_i; L), \quad (6.28)$$

where we have explicitly written the free energy in terms of the deflection angle defined by the dot product of the initial and final tangents:  $\cos \theta = \vec{t}_i \cdot \vec{t}_f$ . Up to this point we have written the partition function and propagator as explicit functions of both the initial and the final tangent but the rigid body rotational invariance of the energy implies that these functions depend only on the deflection angle. To express any quantity in terms of the deflection angle, we set the initial tangent to be the unit vector in the  $z$  direction and the final tangent to be the unit vector in the radial direction.  $\theta$  now assumes its canonical definition in spherical polar coordinates.

Fig. 6.4b compares the free energies of WLC and KWLC. Despite the similarity of propagators (Fig. 6.4a), the free energies are quite different. To understand the significance of this free energy, we imagine discretizing the chain at some segment length  $\ell$ . The free energy  $F(\theta; \ell)$  gives us the effective constitutive relation for single-state torsional springs in this new discretized theory. As depicted in Fig. 6.4b, the potential energy of these springs is initially quadratic in deflection, but saturates due to kink formation.

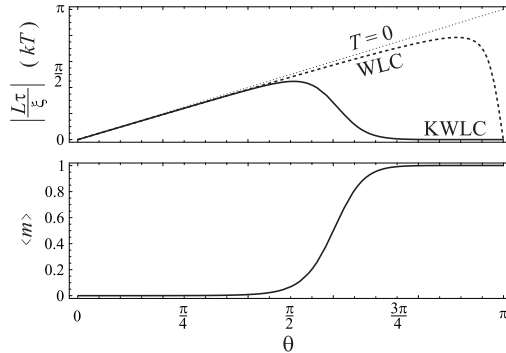


Figure 6.4: The bending moment  $\tau$  and average kink number  $\langle m \rangle$  as functions of the tangent deflection angle for illustrative values  $L = 0.2\xi$  and  $\zeta\xi = 10^{-2}$ . The solid curves are KWLC and the dashed curves are WLC with the same bend persistence length. At small  $\theta$ , the normalized bending moment exhibits a linear spring dependence and the chain is unknicked. The limiting linear behavior of the short rod limit is the dotted curve, labeled  $T = 0$  corresponding to the mechanical limit of WLC. For large deflection, the chain kinks and the moment drops to zero. This correspondence between kinking and the moment is clearly illustrated in the short length limit depicted above.

#### 6.4.1 Moment-Bend & kink number

To understand the interplay between chain kinking and deflection, it is helpful to explicitly compute the relation between the deflection angle and the restoring moment (torque), as well as computing the average kink number. Here we ask the reader to imagine a set of experiments analogous to force-extension but where the moment-bend constitutive relation is measured. We compute the constitutive relation in the usual way in terms of the deflection angle  $\theta$

$$\tau(\theta; L) \equiv -\frac{\partial}{\partial \theta} F(\theta; L), \quad (6.29)$$

where  $F(\theta; L)$  is the tangent free energy and  $\theta$  is the deflection angle. In terms of the WLC bending moment, Eq. 6.24 shows that the moment for KWLC has a very simple form:

$$\tau^*(\theta; L) = \tau(\theta; L) \frac{\mathcal{Z}(\theta; L)}{\mathcal{Z}^*(\theta; L)}, \quad (6.30)$$

where  $\tau$  is the WLC moment and  $\mathcal{Z}$  and  $\mathcal{Z}^*$  are the tangent partition functions for WLC and KWLC, respectively. The moment is plotted as a function of deflection in Fig. 6.4.1. For short chains, the small deflection moments of the two theories initially coincide. But as the deflection increases, there is a transition, corresponding to the onset of kinking, where the moment is dramatically reduced to nearly zero. In Eq. 6.30, this transition is clear from the ratio of the partition functions. Remember that the KWLC partition function is the sum of the WLC partition function and the  $m > 0$  kink partition functions. Before the onset of kinking, the WLC and KWLC partition functions are equal since the kinked states do not contribute significantly to the partition function. For large deflection,

the KWLC partition function is kink dominated and therefore the ratio in Eq. 6.30 tends to zero. Physically, once the chain is kink dominated, the moment must be zero since the kink energy is independent of the kink angle. At zero temperature, the moment would be zero, but fluctuations in which the chain becomes unkinked cause the moment to be nonzero. We discuss this effect in more detail below.

To explicitly see that the reduction in the moment corresponds to kinking, we compute the average kink number as a function of deflection

$$\langle m \rangle (\theta; L) = -\frac{\partial F^*}{\partial \log \zeta} = \frac{\zeta L}{4\pi H^*(\theta; L)}, \quad (6.31)$$

which is depicted in Fig. 6.4.1. Note that when we remove the tangent constraint, we again find that the average kink number is  $\zeta L$ . When the chain is constrained, the enhancement factor is proportional to  $(H^*)^{-1}$ . Note that this implies that the kink number will be reduced when the tangents are constrained to be aligned and enhanced when the chain is significantly bent. In Fig. 6.4.1, the kink-induced reduction in the moment can be seen to correspond to the rise of the kink number from zero to one kink.

We will now compare these exact results to the mechanical or “zero temperature” limit. This regime is equivalent to the large persistence length limit, where we can write the partition function concisely as

$$\lim_{L \rightarrow 0} \mathcal{Z}^*(\vec{t}_f, \vec{t}_i; L) = \frac{1}{4\pi} \left[ \frac{2\xi}{L} \exp\left(-\frac{\xi}{2L}\theta^2\right) + \zeta L \right]; \quad (6.32)$$

the WLC limit is recovered for  $\zeta = 0$ . In the short length limit, the moment of the WLC chain is simply linear in deflection:  $\tau = -\theta\xi/L$ . This moment is also plotted in Fig. 6.4.1. Even without the complication of kinking, there is already one interesting feature of the exact WLC moment-bend constitutive relation which needs explanation. For large deflection, the linear relation already fails in the WLC model! This is a thermal effect which is best understood by going to the extreme example of deflection  $\theta = \pi$ . For any configuration, the contribution of a chain reflected through the axis defined by the initial tangent will make the partition function symmetric about  $\vec{t}_f = -\vec{t}_i$ . This implies that the bending moments from these chains cancel. Away from  $\theta = \pi$ , the cancellation is no longer exact. In the mechanical limit, this effect is present but localized at  $\theta = \pi$  due to the path degeneracy.

In the mechanical limit, kinking is always induced by bending and at most one kink is nucleated. In this limit, the KWLC bend-moment can be rewritten in terms of the kink number

$$\tau^*(\theta; L) = \tau(\theta; L)(1 - \langle m \rangle), \quad (6.33)$$

where the kink number is just the Heaviside step function,

$$\langle m \rangle(\theta, L) = \Theta_H[\theta - \theta_0], \quad (6.34)$$

around a critical deflection angle

$$\theta_0 \equiv \left[ \frac{2L}{\xi} \log \frac{2\xi}{\zeta L^2} \right]^{1/2}. \quad (6.35)$$

For deflection less than the critical deflection, the kink number is zero and the moment is given by the WLC moment. At the critical deflection angle, there is an abrupt transition to the kinked state with kink number one and the moment zero. Precisely at the critical angle the free energy of the kinked state and the elastically bent state are equal. Note that we have not discussed dynamics and have assumed that the system is in equilibrium, not kinetically trapped.

The behavior of the KWLC theory for short contour lengths is nearly what one would expect from mechanical intuition. Bending of the chain on short length scales induces a moment which is initially linearly dependent on deflection. When the chain is constrained to a large deflection angle, kinking is induced and the response of the chain to deflection is dramatically weakened. In the mechanical limit, once kinking is induced, the moment is zero but for finite size rods, the ability of the chain to fluctuate between the kinked states and unkinked states blurs the dramatic zero-temperature transition between the kinked and unkinked bend response.

Our discussion here has focused principally on developing an intuition for the short chain limit. From an experimental perspective, it is difficult to measure the moment-bend relation directly as we have described, especially for short chains. While single molecule AFM experiments might probe this relation, most of the information about the moment-bend constitutive relation comes from indirect measurements of thermally-induced bending. For example light scattering, force-extension, and cyclization experiments are all measures of thermally induced bending. As we shall explain, only cyclization experiments with short contour length polymers are sensitive to the high curvature regime of the moment-bend constitutive relation. For the most part, these thermally driven bending experiments are only sensitive to the thermally accessible regime of the moment-bend constitutive relation which corresponds to small curvature and therefore small deflection on short length scales, a regime that is very well approximated by linear moment-bend constitutive relation. For long chains, the initial linear response is weaker implying that the kinking transition is less pronounced. In fact we shall see in the next section that for some of these indirect measurements of the low curvature regime of the constitutive relation, the effect of the kinking will be indistinguishable from the linear elastic response.

### 6.4.2 Persistence length

Since many polymer characterization experiments are most sensitive to the thermally-accessible weak-bending regime, it is clearly of interest to determine whether kinking changes this low-curvature physics. Intuitively, we have already argued that, at least for small kink densities, many properties of the polymer that do not explicitly probe the highly bent structure will remain essentially unchanged. In this section, we will derive a number of exact results that show that the effects of kinking can be described by a renormalization of the persistence length of WLC theory for some bulk features of the polymer distribution, regardless of the magnitude of  $\zeta$ .

The tangent-tangent correlation must be a decreasing exponential due to multiplicativity[5, 31] and therefore we can discuss the decay length. The tangent persistence is

$$\langle \vec{t}_\Delta \cdot \vec{t}_0 \rangle = e^{-(\zeta + \xi^{-1})\Delta}, \quad (6.36)$$

which can be computed by examining the limit of small  $\Delta$  and applying the tangent propagator (eqn 6.26). Since this result is identical to the WLC result except for the decay constant, we introduce the effective persistence length

$$\xi^* \equiv (\xi^{-1} + \xi_{\text{kink}}^{-1})^{-1}, \quad (6.37)$$

where the kink length is defined as  $\xi_{\text{kink}} \equiv \zeta^{-1}$ . The form of this effective persistence length is not surprising since a roughly analogous effect is observed adding two linear springs together or from the combination of static and dynamic persistence length[36, 37, 38]. This tangent persistence result immediately implies that an analogous exact renormalization occurs for both the mean squared end distance

$$\langle R^2 \rangle_{\text{KWLC}} = [\langle R^2 \rangle_{\text{WLC}}]_{\xi \rightarrow \xi^*} = 2L\xi^* - 2\xi^* \left(1 - e^{-L/\xi^*}\right) \quad (6.38)$$

and the radius of gyration

$$\langle R_g^2 \rangle_{\text{KWLC}} = [\langle R_g^2 \rangle_{\text{WLC}}]_{\xi \rightarrow \xi^*} = \frac{L\xi^*}{3} - \xi^{*2} + \frac{2\xi^{*3}}{L} - \frac{2\xi^{*4}}{L^2} \left(1 - e^{-L/\xi^*}\right), \quad (6.39)$$

since these result are simply integrations of the tangent persistence[4]. In experiments sensitive only to the radius of gyration (static scattering for small wave number) or the average square end distance (force-extension in the small force limit), the measured persistence length of the KWLC theory will be the effective persistence length,  $\xi^*$ , regardless of the magnitude of  $\zeta$ . In most systems of physical interest, the kink length is much larger than the bend persistence length implying that, even if the bend persistence were independently measurable, the difference between the effective persistence length and the bend persistence length would be very small. In other words, the loss of tangent

persistence due to kinking is negligible compared with the loss due to thermal bending since kinks are rare on the length scale of a persistence length.

The tangent persistence corresponds to the first moment of the tangent propagator. Clearly the renormalization we have discussed fails for higher order moments! At least in principle it is therefore possible to determine the bend persistence from higher order moments of the distribution. From an experimental perspective this corresponds to scattering experiments at large wave number, force extension for large force, or cyclization experiments for short contour length. To predict the effects of kinking in these experiments, we must compute the spatial propagator (the spatial distribution function).

## 6.5 Tangent-spatial and spatial propagators

The spatial propagator  $K(\vec{x}; L)$  is defined as the probability density of end displacement  $\vec{x}$  for a polymer of contour length  $L$ . Similarly, the tangent-spatial propagator  $G(\vec{x}; \vec{t}_f, \vec{t}_i; L)$  is defined as the probability density of end displacement  $\vec{x}$  with final tangent  $\vec{t}_f$ , given an initial tangent  $\vec{t}_i$ , for a chain of contour length  $L$ . Although in principle the theory is solved once the tangent propagator is known, the moments of the spatial propagator, or spatial distribution function, are more experimentally accessible than the tangent propagator. In particular, the  $J$  factor measured in cyclization experiments, the force-extension characteristics, and the structure factor measured in scattering experiments are all more directly computable from the propagators  $G$  and  $K$ . In this section, we first compute the spatial propagator and then discuss its application to experimental observables.

Following our computation of the tangent propagator, we compute the tangent-spatial and spatial partition functions. Our solution relies on the same Dyson-like expansion of the partition function in the kink number as was exploited to compute the tangent partition function. The only added complication is that, in addition to the arc length convolution, we must also compute convolutions over the 3d spatial positions of the kinks. By going to the Fourier-Laplace transformed propagator, the convolutions again become products and the  $m$  kink contributions can be summed exactly. Unfortunately the exact results of this computation will only be found analytically up to a Fourier-Laplace transform, in part because the WLC theory itself is only known analytically in this form[34, 35].

We begin by writing the tangent-spatial partition function for the KWLC theory in an form analogous to the tangent partition function in Eq. 6.18:

$$\mathcal{Z}^*(\vec{x}; \vec{t}_f, \vec{t}_i; L) = \sum_{\{\sigma_1, \dots, \sigma_N\}} \int [d\vec{t}(s)]_{\vec{t}_i} e^{-E^*} \delta^{(2)}[\vec{t}_N - \vec{t}_f] \delta^{(3)}[\vec{x}_{N+1} - \vec{x}], \quad (6.40)$$

where  $\vec{t}_0$  is the initial tangent vector. The additional spatial Dirac delta function in the equation sets a spatial constraint for the end displacement; in this expression,  $\vec{x}_{N+1} \equiv \ell \sum_{n=0}^N \vec{t}_n$ . We will again collect the terms in this sum by kink number  $m$ . In the intervals between kinks, we again introduce the WLC propagator, but this time we use the tangent-spatial propagator  $G$ , defined by an expression analogous to Eq. 6.40, but with  $E$  in place of  $E^*$ .

Because we have normalized the unconstrained WLC partition function such that  $\mathcal{Z} \equiv 1$ , the tangent-spatial partition function and propagator are identical. It is convenient to introduce the WLC spatial propagator

$$K(\vec{x}; L) \equiv \frac{1}{4\pi} \int d^2\vec{t}_1 d^2\vec{t}_2 G(\vec{x}; \vec{t}_1, \vec{t}_2; L), \quad (6.41)$$

where we sum over the final tangent and average over the initial tangent to derive the spatial probability density. We also introduce the one tangent summed tangent-spatial propagator

$$G'(\vec{x}, \vec{t}; L) = \int d^2\vec{t}_1 G(\vec{x}; \vec{t}, \vec{t}_1; L), \quad (6.42)$$

which will allow us to concisely express intermediate results. Finally for economy of notation, we write the convolutions over both the spatial position and arc length symbolically with  $\otimes$ , generalizing the notation introduced in Sect. 6.4.

The  $m > 0$  kink KWLC tangent-spatial partition function can be written in terms of the WLC propagators:

$$\mathcal{Z}_m^*(\vec{x}; \vec{t}_f, \vec{t}_i; L) = \frac{\zeta^m}{4\pi} \left( G'(\vec{t}_f) \otimes [K \otimes]^{m-1} G'(\vec{t}_i) \right) (\vec{x}, L), \quad m > 0. \quad (6.43)$$

We now introduce the WLC Fourier-Laplace transforms of the propagators  $G'$  and  $K$ . We denote the transformed functions with a tilde. The Laplace conjugate of contour length  $L$  is  $p$  and the Fourier conjugate of the end displacement  $\vec{x}$  is the wave number  $\vec{k}$ . The Faltung theorem (Eqs 6.79 and 6.84) allows us to replace the spatial-arc length convolutions with the products of the Fourier-Laplace transformed propagators. The  $m$  kink KWLC transformed partition function is

$$\tilde{\mathcal{Z}}_m^*(\vec{k}; \vec{t}_f, \vec{t}_i; p) = \zeta^m \begin{cases} \tilde{G}(\vec{k}, \vec{t}_f, \vec{t}_i; p), & m = 0 \\ \tilde{G}'(\vec{k}, \vec{t}_f; p) \tilde{K}^{m-1}(\vec{k}; p) \tilde{G}'(\vec{k}, \vec{t}_i; p) / 4\pi, & m > 0, \end{cases} \quad (6.44)$$

which is analogous to Eq. 6.22 for the tangent propagator.

As before, the transformed  $m$  kink contributions can be summed exactly in a geometric series. Abbreviating the notation somewhat, the resulting tangent-spatial transformed partition function

becomes

$$\tilde{\mathcal{Z}}^*(\vec{k}; \vec{t}_f, \vec{t}_i; p) = \tilde{G} + \frac{\zeta \tilde{G}' \tilde{G}'}{4\pi (1 - \zeta \tilde{K})}. \quad (6.45)$$

We can also derive the KWLC transformed spatial partition function by averaging over the initial tangent and summing over the final tangent. Applying the definition in Eq. 6.41 gives

$$\tilde{\mathcal{Z}}^*(\vec{k}; p) = \frac{\tilde{K}(\vec{k}; p)}{1 - \zeta \tilde{K}(\vec{k}; p)}. \quad (6.46)$$

To compute the KWLC spatial and tangent-spatial propagators, we divide the constrained partition functions by the unconstrained partition function (Eq. 6.10). The transformed tangent-spatial and spatial propagators are

$$\tilde{G}^*(\vec{k}, \vec{t}_f, \vec{t}_i; p) = \mathcal{L}\mathcal{F} \left[ \frac{\tilde{\mathcal{Z}}^*(\vec{x}, \vec{t}_f, \vec{t}_i; L)}{\tilde{\mathcal{Z}}^*(L)} \right] = \tilde{\mathcal{Z}}^*(\vec{k}; \vec{t}_f, \vec{t}_i; p + \zeta), \quad (6.47)$$

$$\tilde{K}^*(\vec{k}; p) = \mathcal{L}\mathcal{F} \left[ \frac{\tilde{\mathcal{Z}}^*(\vec{x}; L)}{\tilde{\mathcal{Z}}^*(L)} \right] = \tilde{\mathcal{Z}}^*(\vec{k}; p + \zeta), \quad (6.48)$$

where  $\mathcal{L}$  is the arc-length Laplace transform and  $\mathcal{F}$  is the spatial Fourier transform. The transformed WLC spatial propagator is exactly known[34, 35]

$$\tilde{K}(\vec{k}; p) = \frac{1}{P_0 + \frac{A_1 \vec{k}^2}{P_1 + \frac{A_2 \vec{k}^2}{P_2 + \frac{A_3 \vec{k}^2}{\dots}}}}, \quad (6.49)$$

where  $A_j$  and  $P_j$  are defined

$$A_j \equiv \frac{j^2}{4j^2 - 1}, \quad P_j \equiv p + \frac{j(j+1)}{2\xi}. \quad (6.50)$$

Because the KWLC transformed spatial partition function and propagator are functions of  $\tilde{K}$ , they are also known exactly. In principle, both  $K$  and  $K^*$  can be computed by inverting the transforms numerically. In order to compute the KWLC tangent-spatial partition function and propagator, the WLC tangent-spatial propagator,  $G$ , must also be known. Since  $\tilde{G}$  is not known analytically, our solution for the tangent-spatial partition function and propagator are formal. From the perspective of computing experimental observables,  $K^*$  will suffice for computation of the force-extension characteristic, the structure factor, and surprisingly, the  $J$  factor, despite the tangent constraint in its definition.

### 6.5.1 Wave number limits

While we have written the exact transformed propagators for KWLC, like WLC, these transforms cannot be inverted analytically. It is therefore useful to examine the exact transformed propagators in several limits which can be computed analytically. First we consider the long length scale ( $k \rightarrow 0$ ) limit. We find that KWLC and WLC are identical apart from the renormalization of the persistence length (see Eq. 6.37):

$$\lim_{k \rightarrow 0} \tilde{K}^* = \lim_{k \rightarrow 0} \tilde{K}_{\xi \rightarrow \xi^*} = \left[ p + \frac{1}{3} \frac{k^2}{p + (\xi^*)^{-1}} + \dots \right]^{-1}. \quad (6.51)$$

By expanding the exponential in the definition of the Fourier transform, it can be shown that this result is equivalent to showing that  $R^2$  is exactly renormalized. In our discussion of the  $J$  factor it will be convenient to consider an even more restrictive limit. We now add the additional restriction that the chain is long ( $p \rightarrow 0$ ). In this limit we must recover the Gaussian chain (Central Limit Theorem)

$$\lim_{k, p \rightarrow 0} \tilde{K}^* = \lim_{k \rightarrow 0} \tilde{K}_{\xi \rightarrow \xi^*} = \left[ p + \frac{\xi^* k^2}{3} + \dots \right]^{-1}, \quad (6.52)$$

which is the transformed Gaussian distribution function for Kuhn length  $2\xi^*$ . When applicable, the Gaussian distribution is a power tool due to its simplicity.

The opposite limit is the short length scale ( $k \rightarrow \infty$ ) and short contour length limit ( $p \rightarrow \infty$ ). In this limit WLC and KWLC are identical, both approaching the rigid rod propagator

$$\lim_{p, k \rightarrow \infty} \tilde{K}^* = \lim_{p, k \rightarrow \infty} \tilde{K} = \tilde{K}_{\xi \rightarrow \infty} = \frac{1}{k} \tan^{-1} \frac{k}{p}. \quad (6.53)$$

The rigid rod spatial propagator describes a polymer that is infinitely stiff. In the limit that we analyze very short segments of the polymer, both the WLC and KWLC models appear rigid since we have confined our analysis to length scales on which bending is thermally inaccessible. In this limit, the propagators take a very simple form which is more tractable than either WLC or KWLC. The rigid rod propagator is useful when discussing the limiting behavior of the  $J$  factor at short contour length and is discussed in more detail in the Appendix.

### 6.5.2 Partition function in an external field and force-extension characteristic

In force-extension experiments, a single polymer molecule is elongated by a bead in an external field. The average extension of the polymer is measured as a function of external field strength. The forces opposing extension are entropic. These entropic forces are caused by the reduction in the number of available microstates as the polymer extension is increased. The persistence length defines the

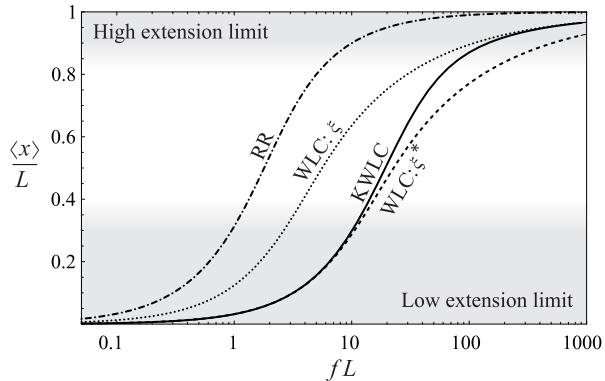


Figure 6.5: Force-extension characteristic for KWLC compared to WLC and Rigid Rod for  $L = 4\xi$  and  $\zeta\xi = 4$ . At low extension, the force-extension of KWLC (solid curve) approaches WLC (dashed curve) with a persistence length equal to the effective persistence length of KWLC. At high extension, the kink modes are frozen out and the KWLC force-extension characteristic approaches WLC (dotted curve) with a persistence length equal to the bend persistence length of KWLC. Rigid Rod (dot dashed curve) has been plotted for comparison. The extension of Rigid Rod corresponds to alignment only.

length scale on which the polymer tangents are correlated. For small persistence length, the number of statistically uncorrelated tangents is greater, which increases the size of the entropic contribution to the free energy relative to the external potential. This deceptively simple physics implies that a chain with a softer bending modulus acts as a stiffer entropic spring resisting extension.

To compute the force-extension relation, we must compute the partition function in an external field  $f$  which can be concisely written in terms of the spatial partition function

$$\mathcal{Z}_{\vec{f}}(L) = \int d^3x e^{\vec{f} \cdot \vec{x}} \mathcal{Z}(\vec{x}; L) = \tilde{\mathcal{Z}}(i\vec{f}; L), \quad (6.54)$$

which is a particularly convenient expression since it is the Fourier-transformed partition function with the wave number  $\vec{k}$  analytically continued to  $i\vec{f}$ . Note that this is the inverse Laplace transform of Eq. 6.45. The average extension is

$$\langle x(f) \rangle = \frac{\partial}{\partial f} \log \mathcal{Z}_{\vec{f}}, \quad (6.55)$$

which may be computed by taking the inverse Laplace transform numerically. (See Sect. 6.9.2 for the numerical method.) The results are plotted in Fig. 6.5.2. In this figure, the KWLC theory interpolates between two WLC limits at high and low extension. The low-force limit is clearly related to low wave number limit (Eq. 6.51) via an analytic continuation of the wave number. Therefore KWLC with effective persistence length  $\xi^*$  and WLC with persistence length  $\xi^*$  correspond in the low-extension limit as can be seen in Fig. 6.5.2.

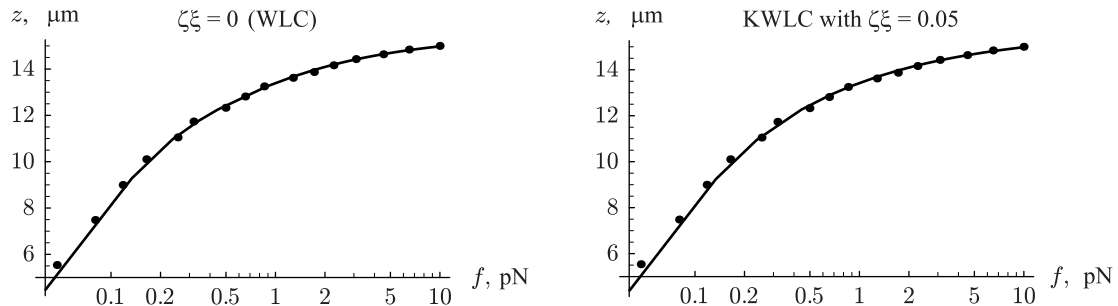


Figure 6.6: Left: Semilog plot of the best fit of the WLC model ( $\zeta = 0$ ) to experimental data on the force-extension relation of a single molecule of lambda DNA. Right: Best fit of the KWLC model to the same data, taking  $\zeta\xi = 0.05$ . The fits are equally good, even though this value of  $\zeta$  is larger than the one that we will argue fits cyclization data. Thus, force-extension measurements can only set a weak upper bound on the value of  $\zeta$ . (Data kindly supplied by V. Croquette; see [5].)

At high force, Fig. 6.5.2 shows that kinking becomes irrelevant and the extension of KWLC and WLC both with bend persistence  $\xi$  are identical. In this limit, the chain is confined to small deflection angles for which the effect of kinking is negligible, as can be seen in Fig. 6.4. In essence the kink modes freeze out and measurement of the extension versus force measures the bend persistence rather than the effective persistence length of the KWLC polymer chain.

These two regimes imply that in principle the value of  $\zeta$  could be determined by the difference between the persistence length measured at small and large extension. In practice, this is most likely not practical. We have purposely chosen an unrealistically large value of  $\zeta$  in Fig. 6.5.2, to illustrate clearly the low- and high-extension limits. In more realistic systems, the difference between the bend and effective persistence lengths would be small implying that it would be difficult to detect. Furthermore, at low extension the effects of polymer-polymer interactions can act to either increase or decrease the effective low extension persistence length. At high extension, polymer stretch also acts to increase the extension at high force most likely obscuring the effects of the entropy reduction due to the loss of the kink bending modes. Fig. 6.5.2 illustrates these remarks. The force-extension characteristic is therefore unlikely to detect the high-curvature softening induced by kinking.

### 6.5.3 Structure factor

Another experimental observable used to characterize polymers is the structure factor, measured by static light scattering, small-angle X-ray scattering, and neutron scattering experiments. Measurements of the structure factor can probe the polymer configuration on a wide range of length scales.

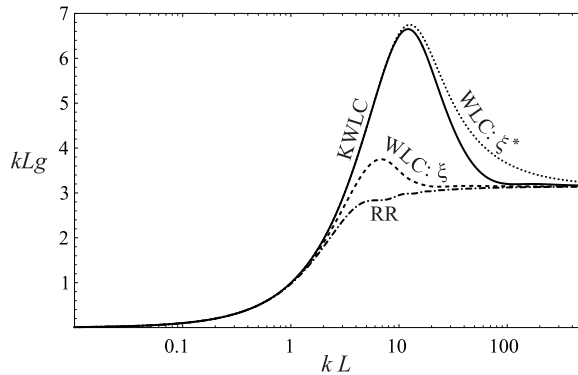


Figure 6.7: The structure factor and the role of effective persistence length. The solid curve is the structure factor for KWLC with contour length  $L = 4\xi$ , and kink parameter  $\zeta = 4/\xi$ . For comparison, we have plotted the structure factor for WLC of the same contour length for identical bend persistence lengths (dashed) and identical effective persistence length (dotted). At short length scales (large wave number) the KWLC structure factor approaches that for WLC with an identical bend persistence length. At long length scales (small wave number), the KWLC structure factor approaches that for WLC with a persistence length equal to its effective persistence length  $\xi^*$ . We have also plotted the structure factor for Rigid Rod (dot dashed curve) for comparison.

Symbolically the structure factor is

$$g(\vec{k}) \equiv \frac{1}{L^2} \int_0^L ds ds' \left\langle \exp \left[ i\vec{k} \cdot \left( \vec{X}(s) - \vec{X}(s') \right) \right] \right\rangle, \quad (6.56)$$

where  $\vec{X}(s)$  is the position of the polymer at arc length  $s$  and we have included an extra factor of the polymer contour length in the denominator to make the structure factor dimensionless[34]. At high wave number, the structure factor is sensitive to short length scale physics, whereas the polymer length and radius of gyration can be measured at low wave number. The structure factor can be rewritten in terms of the Laplace-Fourier transformed propagator

$$g(\vec{k}) = \frac{2}{L^2} \mathcal{L}^{-1} \left[ \frac{\tilde{K}(\vec{k}; p)}{p^2} \right], \quad (6.57)$$

where  $\mathcal{L}^{-1}$  is the inverse Laplace transform which can be computed numerically. (See Sect. 6.9.2 for the numerical method.) As we mentioned above, the leading-order contributions at small wave vector are the polymer length and the radius of gyration

$$Lg(k) = L \left( 1 + \frac{1}{3} k^2 R_g^2 + \dots \right) \quad (6.58)$$

$$\text{dashed circle} = \text{solid circle} + \text{solid circle with 1 kink} + \text{solid circle with 2 kinks} + \dots$$

Figure 6.8: The diagrammatic representation of the kink number expansion for cyclized polymers. The dashed curve represents the KWLC theory which is the sum of the  $m$  kink contributions. In the interval between the kinks, the polymer is described by WLC, represented by the solid curves. For each  $m$  kink contribution, we sum over the kink position. In order to meet the tangent alignment conditions for cyclized polymers, we close the chain at a kink for kink number one or greater.

where we have temporarily restored the length dimension of  $g$ . At large  $k$ , both WLC and KWLC are rod-like or straight which gives an asymptotic limit for large wave number

$$g(k) \rightarrow \frac{\pi}{Lk}, \quad (6.59)$$

since the chain is inflexible at short length scales.

To what extent can scattering experiments differentiate between WLC and KWLC? We have already argued that kinking merely leads to a renormalization of the persistence length for the radius of gyration,  $R_g$ , so both theories are identical at the low and high wave number limits. For the rest of the interval, the theories do predict subtly different structure factors, but for small values of  $\zeta$ , the theories are nearly indistinguishable. Again, we have chosen to illustrate the structure factor for an unrealistically large value of  $\zeta$ , to exaggerate its effect. Like force-extension measurements, scattering experiments are not sensitive to the high curvature physics since the signal is dominated by the thermally accessible bending regime which is essentially identical to WLC.

## 6.6 Cyclized chains and the $J$ factor

Although the theoretical study of the moment-bend constitutive relation is straightforward, it is problematic experimentally to apply a moment and measure the deflection directly on microscopic length scales. It is typically more convenient to let thermal fluctuations drive the bending, but as we have discussed above, experiments which measure thermally-driven bending are typically not sensitive to the rare kinking events. In contrast, cyclization experiments, although thermally driven, are sensitive to bending at any length scale. These experiments measure the relative concentrations of cyclized monomers to noncyclized dimers. By choosing the contour length of the monomers, any bending scale may be studied provided the concentration of cyclized molecules is detectable. Furthermore, these experiments are typically bulk rather than single molecule. In fact the data motivating this work comes from recent DNA cyclization measurements of Cloutier and Widom[8] who have shown that the cyclization probability is  $10^4$  to  $10^5$  times larger than that predicted by WLC for DNA sequences with a contour length  $L \approx 0.6\xi$ , while confirming that larger sequences

( $L > \xi$ ) do cyclize at the rate theoretically predicted by the WLC <sup>1</sup>

In cyclization measurements, the configurational free energy is isolated in the  $J$  factor which is ratio of the cyclization equilibrium constant to the dimerization equilibrium constant[39]. This ratio eliminates the dependence on the end-end interaction free energy. For non-twist storing polymers, the  $J$  factor is proportional to the tangent-spatial propagator[39]

$$J = 4\pi G(0; \vec{t}, \vec{t}; L), \quad (6.60)$$

which is the concentration of one end of the polymer chain at the other ( $\vec{x} = 0$ ) with the correct tangent alignment. The factor of  $4\pi$  is due to the isotropic angular distribution of monomer in free solution. Our analysis will neglect additional complications relevant to the study of real DNA. First, in DNA the twist must also be aligned, which requires the use of a variant of WLC, Helical Wormlike Chain[4]. This additional constraint modulates the  $J$  factor with a 10.5 bp period equal to the helical repeat. Our interest here is in the value of the  $J$  factor averaged over a helical repeat for which the effects of twist can be roughly ignored[4]. A second complication in real DNA is sequence dependent prebending[40, 41]. We argue elsewhere that prebending effects alone cannot explain the high cyclization rates observed for short DNA[20]; in this paper we focus instead on kink formation.

Although cyclization experiments are fairly straightforward, extracting mechanical information from the results poses a difficult theoretical problem due to the combination of tangent and spatial constraints. In fact, there is no exact analytic expression for the  $J$  factor in the WLC theory; the following sections and appendices will develop the numerical methods we need.

### 6.6.1 The looping $J$ factor

Due to these computational complications, we shall initially dispense with the tangent alignment condition and compute a modified  $J$  factor that is relevant for processes that do not fix the tangents of the chain. For example some protein-DNA complexes exhibit a behavior that is believed to be better represented by looping (free end tangents) than cyclization (end tangents aligned) [14]. We define the looping  $J$  factor as the ratio of the looping to the dimerization equilibrium constants. The KWLC looping  $J$  factor,  $J_L^*$ , can be written in terms of the spatial propagator as

$$J_L^* = K^*(0; L), \quad (6.61)$$

---

<sup>1</sup>Cloutier and Widom's discussion assumed that the ligase enzyme used in their experiments acts in the same way when ligating a single DNA or joining two segments. Although this assumption is standard in the field, it may be criticized when the length of the DNA loop becomes not much bigger than the ligase enzyme itself. We believe that effects of this type cannot account for the immense discrepancy between the measured  $J$  factor and that predicted by the WLC theory.

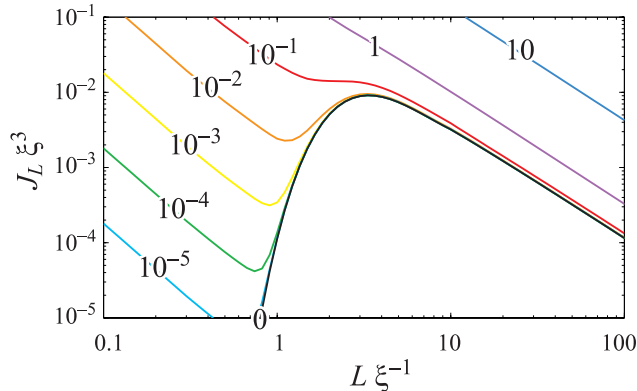


Figure 6.9: The KWLC looping  $J$  factor,  $J_L^*$ , as a function of contour length plotted for various values of the kinking parameter  $\zeta$ . The numbers labeling the curves indicate the value of the dimensionless quantity  $\xi\zeta$ . WLC is the curve labeled 0. For large contour length  $L$ , the effect of kinking can be accounted for by computing  $J_L$  for the effective persistence length,  $\xi^*$ . But as the contour length shrinks to a persistence length, the effect of kinking becomes dominant, even for small  $\zeta$ . At short contour length the looping  $J$  factor is one kink dominated and diverges in contrast to the WLC looping  $J$  factor which approaches zero precipitously for short contour length.

which can be interpreted as the concentration of one end at the other. We have again neglected the effect of twist. In this case the explicit  $4\pi$  in Eq. 6.60 is not needed, as the definition of  $K$  already includes an integral over angles. the angular distribution is irrelevant and therefore there is no additional factor of  $4\pi$ . Both from the standpoint of developing intuition and computational convenience it is useful to explicitly expand  $K^*$  in the kink number. We introduce the WLC closed spatial propagator convolutions which we denote

$$\mathcal{K}^{(m)} \equiv [K \otimes]^m (0; L), \quad (6.62)$$

where again the  $\otimes$  represents both spatial and arc length convolutions. The computation of the  $\mathcal{K}^{(m)}$  is discussed in Sect. 6.9.3. In terms of the  $\mathcal{K}^{(m)}$ , the free tangent  $J$  factor is

$$J_L^* = e^{-\zeta L} \sum_{m=0}^{\infty} \zeta^m \mathcal{K}^{(m+1)}, \quad (6.63)$$

where we have defined the  $\mathcal{K}^{(m)}$  to be independent of the kinking parameter  $\zeta$ . The kink number sum is illustrated with a diagrammatic expansion in Fig. 6.6. The probability of the  $m$  kink state can be concisely written in terms of the  $\mathcal{K}^{(m)}$

$$\mathcal{P}_m = e^{-\zeta L} \zeta^m \frac{\mathcal{K}^{(m+1)}}{J_L^*}. \quad (6.64)$$

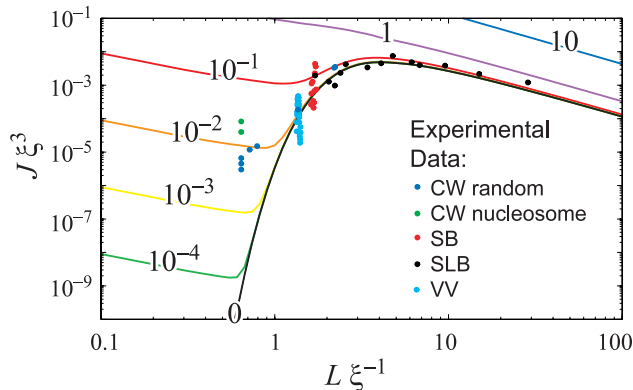


Figure 6.10: (Color.) The KWLC cyclization  $J$  factor as a function of contour length  $L$  for various values of the kink parameter  $\zeta$ . As discussed in the text, our theory does not include the twist induced 10.5 bp modulation of the  $J$  factor. The numbers labeling the curves indicate the value of the dimensionless parameter  $\xi\zeta$ . The WLC theory corresponds to  $\zeta = 0$ . For large contour length  $L$ , the effect of kinking can be accounted for by computing the  $J$  factor using the effective persistence length,  $\xi\zeta$ . As the contour length  $L$  falls below a persistence length, kinking dramatically increases the  $J$  factor, even for small  $\zeta$ . For small  $L$  the chain is two kink dominated and diverges, in contrast to the WLC theory which precipitously falls to zero at small  $L$ . Experimental cyclization data for DNA are plotted for comparison, assuming  $\xi = 50$  nm. (Data sources: CW[8], SB[42], SLB[43], and VV[44].) At contour length  $L = 0.6\xi$ , the experimentally measured  $J$  factor is  $\approx 10^4$  times larger than predicted by the WLC theoretical curve. The KWLC with  $\zeta\xi = 10^{-2}$  correctly captures this behavior, while matching the WLC theory at large contour length.

This expression can be interpreted as the kink number distribution for a looped chain, a constraint that induces kinking in a manner roughly analogous to the tangent constraints already discussed in detail. The looping  $J$  factor is plotted in Fig. 6.6.1. In this figure, we can see that the intuition we developed computing the moment-bend constitutive relation is borne out in the looping  $J$  factor, despite the fact that the process is thermally driven. In the short-length limit, the ability of the chain to kink dramatically reduces the bending energy and increases the looping  $J$  factor. In the short-length limit, a single kink is nucleated in a manner almost exactly analogous to the process we have described in detail for the moment-bend constitutive relation. We will discuss these results and their scaling in more detail after computing the KWLC  $J$  factor.

### 6.6.2 The cyclization $J$ factor

Although the computation of the free tangent  $J$  factor is more direct and intuitive, the  $J$  factor with tangent alignment is of more phenomenological interest. The computation begins with the tangent-spatial partition function defined in Eq. 6.45 for end distance zero and aligned tangents. Since the transformed WLC tangent-spatial propagator is unknown, it would initially appear to preclude exploiting the exact results derived above. But intuitively we know the chain may be closed at any point resulting in an identical  $J$  factor. For kinked chains, it is convenient to close the chain at a

kink where the tangent alignment condition is no longer required. The only chains for which this simplification cannot be applied are the unknicked chains for which the  $J$  factor is already known[3]. To show this explicitly, we write the transform of Eqn. 6.45 in its expanded form and specialize to  $\vec{t} = \vec{t}_0$  to obtain the cyclization partition function:

$$\mathcal{Z}_C^*(L) = G(0; \vec{t}, \vec{t}; L) + \sum_{m=0}^{\infty} (\zeta G'(\vec{t}) \otimes (\zeta K \otimes)^m G'(\vec{t})) (0; L). \quad (6.65)$$

We can now use the composition property of the propagators to replace the initial and final tangent-spatial propagators with a single spatial propagator. Some care is now required in performing the convolution, as described in Appendix 6.9.1. The cyclization partition function then becomes (Eqn. 6.87)

$$\mathcal{Z}_C^*(L) = G(0; \vec{t}, \vec{t}; L) + \frac{1}{4\pi} \sum_{m=1}^{\infty} \frac{\zeta^m L}{m} \mathcal{K}^{(m)}, \quad (6.66)$$

where we have expressed the result in terms of the zero end distance spatial propagator convolutions,  $\mathcal{K}^{(m)}$ . The kink number sum is illustrated with a diagrammatic expansion in Fig. 6.6. This equation has an analogous form to the looping  $J$  factor in Eqn. 6.63. The only complication here is that for kinked chains, the state counting has subtly changed since we close the chain at a kink. For inverse transform numerical computations, it is convenient to write a transformed partition function

$$\tilde{\mathcal{Z}}_C^*(k; p) = \tilde{G} + \frac{1}{4\pi} \frac{\partial}{\partial p} \log [1 - \zeta \tilde{K}], \quad (6.67)$$

although the expression is understood to only have physical meaning when the chain is closed ( $\vec{x} = 0$ ). Our derivation of the cyclized partition function implies that the KWLC tangent-spatial propagator is known for one special case

$$G^*(0; \vec{t}, \vec{t}; L) = e^{-\zeta L} \mathcal{Z}_C^*(L), \quad (6.68)$$

which is precisely the expression we need to compute the  $J$  factor. In terms of the KWLC tangent-spatial propagator, the KWLC  $J$  factor is

$$J^* = 4\pi G^*(0; \vec{t}, \vec{t}; L) = e^{-\zeta L} \sum_{m=0}^{\infty} \zeta^m \mathcal{J}^{(m)}, \quad (6.69)$$

where we have explicitly expanded the  $J$  factor in kink number. The  $\mathcal{J}^{(m)}$  are defined by

$$\mathcal{J}^{(m)} \equiv \begin{cases} J, & m = 0 \\ Lm^{-1} \mathcal{K}^{(m)}, & m > 0 \end{cases}. \quad (6.70)$$

Fig. 6.6.2 compares experimental data to our theoretical calculation of  $J^*$ . Details of the calcu-

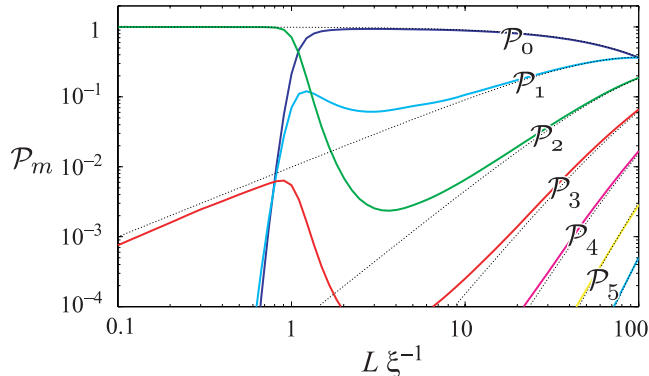


Figure 6.11: The kink-number distribution compared for cyclized chains (solid curves) and unconstrained chains (dashed curves) as a function of contour length  $L$ . To illustrate constraint-driven kinking, we have chosen the illustrative value  $\zeta\xi = 10^{-2}$ . At large contour length  $L$ , the cyclization constraint is irrelevant but as the arc length shrinks to roughly a persistence length, the bending energy required to cyclize the chain becomes significant and there is a dramatic transition to the two kink state which dominates at short contour length. The contributions of one and  $m > 2$  kink states are secondary.

lation are discussed in Appendix 6.9.3. Note that setting the kink density to  $\zeta \approx 10^{-2}/\xi = 0.2/\mu\text{m}$  roughly reproduces the experimental cyclization data. Eq. 6.7 connects  $\zeta$  to the density of vertices  $\ell$  and the free energy cost  $\epsilon$  of creating a kink. Assuming that the site density is just the DNA base pair length  $\ell = 0.34\text{ nm}$ , we can estimate the kink energy,

$$\epsilon = \ln \left[ \frac{2\xi}{\ell^2\zeta} \right] \approx 15 kT \approx 9\text{ kcal/mol} . \quad (6.71)$$

Although we do not discuss detailed microscopic models in this paper, it is interesting to note that molecular modeling studies have found that in B-form DNA, base pairs indeed open individually and noncooperatively with an activation energy of 10–20kcal/mol [45].

### 6.6.3 Topologically induced kinking

It is useful to discuss kink number in chains that are topologically confined to be cyclized. These chains have both the kink inducing tangent and spatial constraint. We can write the kink number distribution concisely in terms of the  $J$  factor

$$\mathcal{P}_m = e^{-\zeta L} \zeta^m \frac{\mathcal{J}^{(m)}}{J^*}, \quad (6.72)$$

which is analogous to Eq. 6.64 and depicted in Fig. 6.6.3.

The effects of kinking on the  $J$  factor are dramatic even when the kinking parameter  $\zeta$  is small! Fig. 6.6.2 shows that the WLC  $J$  factor precipitously decreases with loop contour length due to the

increasing elastic energy required to close the loop

$$J \sim e^{-2\pi^2\xi/L}. \quad (6.73)$$

In dramatic contrast, the KWLC  $J$  factor, while tracking the WLC  $J$  factor at large contour length, turns over at small contour length and increases divergently. Physically, this small contour length divergence can be understood as an increase in the ratio of available cyclized to noncyclized states which is roughly inversely proportional to the physical volume explored by the chain when one end is fixed. This divergent increase in the density of states can also be seen for the Gaussian chain in the short length limit, although this limit is not physical for polymer systems. For the Gaussian chain, the  $J$  factor is monotonically decreasing with contour length since the only obstruction to the ends finding each other is entropic, and the number of available noncyclized states scales like  $L^{3/2}$  (Eq. 6.104). For KWLC, once the chain is kinked twice, it is advantageous to shorten the chain which, while decreasing the degeneracy of the first kink location,  $\propto L$  (Eq. 6.70), increases the density of cyclized states,  $\propto L^{-2}$  (Eq. 6.95). Therefore, there is a net  $L^{-1}$  scaling of the two kink term  $\mathcal{J}^{(2)}$  (Eq. 6.70). In this limit, the contributions from chains with kink numbers greater than two scale like  $L^{m-3}$  (eqns 6.70 and 6.102), implying that at short lengths the two kink term dominates. In addition, in most physically interesting scenarios the kinking parameter  $\zeta$  is small. The probability of  $m$  kink number state scales roughly like the average kink number for the unconstrained chain to the  $m$ th power  $(L\zeta)^m$  (Eq. 6.69), which further decreases the importance of higher kink number states. The dramatic transition from the zero kink to the two kink state at short contour length is evident in Fig. 6.6.3. Interestingly, recent molecular-dynamics simulations on a 94 bp DNA minicircle indicate the presence of two sharply kinked regions [46].

Physically, we can understand the onset of this transition by roughly comparing the free energies of the two kink term and the zero kink term to find the length at which these two are roughly equal. Here we merely wish to motivate our results as clearly and simply as possible so we shall ignore the difference in the density of states, even though its effect is quantitatively important. We therefore treat the free energy of the zero kink term as the bending energy only and the free energy of the two kink term as twice the kink energy in the discrete model (Eq. 6.7):

$$2\epsilon \sim \frac{2\pi^2\xi}{L_{\text{crit}}}. \quad (6.74)$$

When the bending energy equals the energy required to nucleate two kinks, the transition occurs. It is important to remember that the  $\zeta$ -dependence is relatively weak while the bending energy scales like the inverse of the contour length. Below  $L \sim \xi$ , the bending energy grows divergently implying that even for very small kink densities, kinking always becomes important at short enough contour length. That is to say, we are almost assured of observing elastic breakdown effects below contour

lengths of roughly a persistence length.

Previously we had shown that for moment-bending, only a single kink was nucleated, in contrast to the current example where the one kink contribution to the  $J$  factor,  $\mathcal{J}^{(1)}$ , is of little scaling importance since the chain must still bend as illustrated schematically in Fig. 6.6. This will not be the case for the KWLC looping  $J$  factor,  $J_L^*$ , which lacks the tangent constraint implying that only one kink is required to relieve all the elastic bending. The one kink term of  $J_L^*$  therefore diverges like  $L^{-2}$  (Eq. 6.95) as explained above.  $J_L^*$  is plotted in Fig. 6.6.1.

## 6.7 Discussion

Our main results are summarized in Figs. 6.5.2, 6.5.2, 6.6.2, and 6.6.3. We formulated a generalization of the WLC model, in which a semiflexible polymer can develop flexible sites of an alternative conformation. We found that taking the density of kinks in the unstressed polymer to be about 0.01 per persistence length has negligible effect on the force–extension relation, but vastly enhances the probability of cyclization for chains shorter than a persistence length, as seen in recent experiments on DNA [8].

Various microscopic mechanisms could furnish the kinking mechanism in DNA, for example single-basepair flipout or strand separation [20]. But any complete, microscopic analysis of high-curvature DNA conformations would also have to include a variety of effects, for example those arising from the significant thickness of the DNA molecule on the few-nanometer scale of a short circle, strong polyelectrolyte effects, and so on. We have taken the attitude that any net nonlinear softening at high curvature will lead to generic new phenomena. By summarizing all such effects into a single phenomenological parameter, our model focuses attention on the general mesoscale physics of kinking. The KWLC’s generality also makes it a useful starting point for studying the conformations of other stiff biopolymers, such as actin.

Other diagnostics of low-curvature physics, for example light scattering, also turned out to be almost indistinguishable from the linearly-elastic Wormlike Chain model. It is only by conducting experiments that are explicitly sensitive to high curvature, that we can measure the nonlinear response to bending. DNA cyclization offers one experimentally tractable measurement sensitive to the high-curvature physics of free DNA in solution; we gave predictions for other, future tests, for example the moment–bend relation and the kink number as a function of constraints. Indeed, the predicted average number of kinks has direct structural implications for very small DNA loops, and for processes involving such loops, for example, the looping implicated in some gene-regulatory mechanisms [9, 10, 11, 12, 13, 14]. Recent simulations indeed suggest that spontaneous kinking may play a role in such situations [46].

Some mathematical aspects of the model, for example the divergence of the theoretical  $J$  factor

at small contour length (Fig. 6.6.2), are artifacts of the simplified picture we have proposed. The small contour length divergence is due to the two kink term, which can close a loop without elastic bending regardless of the contour length, via the creation of 180-degree kinks! Clearly due to the finite thickness of the chain, this divergence is unphysical. We can consider a number of modifications to the theory to fix this problem: kink angle cutoffs, kinks that are not perfectly flexible, etc. But all these proposals require adding additional parameters to the model, rendering it both less tractable and less predictive, since the additional parameter must then be fit to experimental data.

The KWLC is in essence a coarse-grained, effective theory for systems where kinking occurs and the kinks are localized compared with the chain persistence length. Its virtue is that it offers a simple way to characterize stiff biopolymers, and a quantitative guide to the mesoscale effects of kinking. Thanks to this simplicity, we were able to compute many results in this paper exactly, without extensive numerical simulation. We discuss the specific application of KWLC to DNA at length elsewhere[20].

## 6.8 Acknowledgments

We thank J. Widom and T. Cloutier for sharing their data and insights on DNA bending before they were generally available. PAW thanks A. Spakowitz for insightful conversations and his results before they were generally available, and T.-M. Yan for his careful instruction in the mysteries of quantum mechanics long ago. The authors would also like to acknowledge M. Inamdar, W. Klug, J. Maddocks and Z.-G. Wang for helpful discussions and correspondence, and Yongli Zhang for comments on the draft manuscript. We acknowledge grant support from an NSF graduate fellowship [PAW]; the Human Frontier Science Foundation and NSF grant DMR-0404674 [PN]; the Keck Foundation and NSF Grant CMS-0301657 as well as the NSF-funded Center for Integrative Multiscale Modeling and Simulation [RP and PAW].

# Bibliography

- [1] P. A. Wiggins, P. C. Nelson, and R. Phillips. Exact theory of kinkable elastic polymers. *Phys. Rev. E*, 71(021909), 2005. [123](#), [164](#), [184](#)
- [2] O. Kratky and G. Porod. Rotgenuntersuchung geloster fadenmolekule. *Rec. Trav. Chim.*, 68(12):1106–1122, 1949. [104](#), [109](#), [123](#), [125](#)
- [3] J. Shimada and H. Yamakawa. Ring-closure probabilities for twisted wormlike chains – applications to DNA. *Macromolecules*, 17:689–698, 1984. [113](#), [123](#), [149](#), [198](#), [199](#)
- [4] H. Yamakawa. *Helical Wormlike Chains in Polymer Solutions*. Springer, Berlin, 1997. [5](#), [104](#), [108](#), [109](#), [113](#), [123](#), [125](#), [137](#), [146](#), [160](#), [164](#), [192](#), [199](#), [202](#)
- [5] Philip C. Nelson. *Biological Physics: Energy, Information, Life*. W. H. Freeman and Co., New York, 1 edition, 2003. [123](#), [125](#), [137](#), [143](#)
- [6] C. Bustamante, S. B. Smith, J. Liphardt, and D. Smith. Single-molecule studies of DNA mechanics. *Curr. Opin. Struct. Biol.*, 10:279–285, 2000. [123](#), [179](#), [195](#)
- [7] C. Bouchiat, M. D. Wang, J. F. Allemand, T. Strick, S. M. Block, and V. Croquette. Estimating the persistence length of a worm-like chain molecule from force-extension measurements. *Biophys. J.*, 76:409–413, 1999. [123](#)
- [8] T. E. Cloutier and J. Widom. Spontaneous sharp bending of double-stranded DNA. *Molecular Cell*, 14(3):355–362, 2004. [5](#), [6](#), [7](#), [96](#), [97](#), [110](#), [114](#), [116](#), [117](#), [118](#), [124](#), [145](#), [148](#), [152](#), [164](#), [169](#), [172](#), [173](#), [174](#), [179](#), [181](#), [185](#), [198](#), [199](#), [200](#), [203](#)
- [9] G. R. Bellomy, M. C. Mossing, and M. T. Record. Physical properties of DNA in vivo as probed by the length dependence of the lac operator looping process. *Biochemistry*, 27:3900, 1988. [124](#), [152](#)
- [10] Karsten Rippe, Peter R. von Hippel, and Jörg Langowski. Action at a distance: DNA-looping and initiation of transcription. *Trends Biochem. Sci.*, 20(12):500–506, 1995. [2](#), [102](#), [110](#), [114](#), [118](#), [124](#), [152](#), [179](#)

- [11] J. Muller, S. Oehler, and B. Muller-Hill. Repression of lac promoter as a function of distance, phase and quality of an auxiliary lac operator. *J. Mol. Biol.*, 257:21–29, 1996. [2](#), [102](#), [103](#), [118](#), [124](#), [152](#), [202](#)
- [12] J. Muller, A. Barker, S. Oehler, and B. Muller-Hill. Dimeric lac repressors exhibit phasedependent co-operativity. *J. Mol. Biol.*, 284:851–857, 1998. [2](#), [102](#), [103](#), [118](#), [124](#), [152](#)
- [13] Karsten Rippe. Making contacts on a nucleic acid polymer. *Trends Biochem. Sci.*, 26(12):733–740, 2001. [2](#), [102](#), [110](#), [114](#), [118](#), [124](#), [152](#)
- [14] Yongli Zhang, Stephen D. Levene, and Donald M. Crothers. Statistical-mechanical theory of DNA looping. 2004. Preprint. [124](#), [146](#), [152](#)
- [15] F. H. C. Crick and A. Klug. Kinky helix. *Nature*, 255:530–533, 1975. [124](#)
- [16] R Dickerson. DNA bending: the prevalence of kinkiness and the virtues of normality. *Nucleic Acid Res.*, 26:1906, 1998. [124](#)
- [17] Yoshio Muroga. Conformational analysis of broken rodlike chains. 1. scattering function of rods joined together by flexible coils. *Macromolecules*, 21(9):2751–2755, 1988. [124](#)
- [18] C. Storm and P. Nelson. Theory of high-force DNA stretching and overstretching. *Phys. Rev. E*, 67:051906, 2003. Erratum *ibid.* **70**, 013902 (2004). [124](#)
- [19] A. J. Levine. The helix–coil transition on the worm–like chain. <http://arxiv.org/abs/cond-mat/0401624>, 2004. submitted to PRL. [124](#), [127](#)
- [20] P. A. Wiggins, P. C. Nelson, R. Phillips, and J Widom. The mechanics of highly curved DNA. 2004. In preparation. [125](#), [146](#), [152](#), [153](#)
- [21] A. Vologodskii. 2004. (To appear.). [125](#)
- [22] J. Yan and J. F. Marko. Localized single-stranded bubble mechanism for cyclization of short double helix DNA. *Phys. Rev. Lett.*, 93, 2004. [125](#)
- [23] Christopher A. Sucato, David P. Rangel, Dan Aspleaf, Bryant S. Fujimoto, and J. Michael Schurr. Monte carlo simulations of locally melted supercoiled DNAs in 20 mM ionic strength. *Biophys J*, 86(5):3079–96, 2004. [125](#)
- [24] L. D. Landau and E. M. Lifshitz. *Theory of Elasticity*. Butterworth-Heinemann, Oxford, 4 edition, 1986. [125](#)
- [25] C. Storm and P. Nelson. The bend stiffness of S-DNA. *Europhys. Lett.*, 62:760–766, 2003. [127](#)

- [26] J. F. Marko. DNAs under high tension: Overstretching, undertwisting, and relaxation dynamics. *Phys. Rev.*, E57:2134–2149, 1998. [127](#)
- [27] A. Ahsan, J. Rudnick, and R. Bruinsma. Elasticity theory of the B-DNA to S-DNA transition. *Biophys. J.*, 74:132–137, 1998. [127](#)
- [28] P. Cizeau and J. L. Viovy. Modeling extreme extension of DNA. *Biopolymers*, 42:383–385, 1997. [127](#)
- [29] I. Rouzina and V. A. Bloomfield. Force-induced melting of the DNA double helix 1. Thermodynamic analysis. *Biophys. J.*, 80:882–893, 2001. [127](#)
- [30] R. P. Feynman and A. R. Hibbs. *Quantum Mechanics and Path Integrals*. McGraw-Hill, New York, 1965. [106](#), [130](#)
- [31] A. Y. Grosberg and A. R. Khokhlov. *Statistical physics of macromolecules*. AIP Press, New York, 1994. [109](#), [130](#), [137](#)
- [32] J. J. Sakurai. *Modern Quantum Mechanics*. Addison-Wesley, Reading, Massachusetts, 2 edition, 1994. [107](#), [131](#), [186](#), [188](#), [207](#), [208](#)
- [33] G. B. Arfken and H. J. Weber. *Mathematical methods for physicists*. Academic Press, Inc., San Diego, 4th edition, 1995. [131](#), [157](#)
- [34] A. J. Spakowitz and Z.-G. Wang. Exact results for a semiflexible polymer chain in an aligning field. *Macromolecules*, 37:5814–5823, 2004. [108](#), [133](#), [138](#), [140](#), [144](#), [159](#), [169](#), [180](#), [193](#), [196](#), [211](#)
- [35] S. Stepanow and G. M. Schutz. The distribution function of a semiflexible polymer and random walks with constraints. *Europhys. Lett.*, 60(4):546–551, 2002. [133](#), [138](#), [140](#), [180](#)
- [36] E. N. Trifonov, R. K.-Z. Tan, and S. C. Harvey. Static persistence length of DNA. In W. K. Olson, M. H. Sarma, and M. Sundaralingam, editors, *DNA bending and curvature*, pages 243–254. Adenine Press, Schenectady NY, 1987. [118](#), [137](#)
- [37] P. Nelson. Sequence-disorder effects on DNA entropic elasticity. *Phys. Rev. Lett.*, 80:5810–5812, 1998. [118](#), [137](#)
- [38] P. A. Wiggins and P. C. Nelson. Prebend... 2004. In preparation. [137](#)
- [39] H. Jacobson and W. H. Stockmayer. Intramolecular reaction in polycondensations 1. the theory of linear systems. *J. Chem. Phys.*, 18(12):1600–1606, 1950. [110](#), [111](#), [146](#), [198](#), [199](#)
- [40] R. S. Manning, J. H. Maddocks, and J. D. Kahn. A continuum rod model of sequence-dependent DNA structure. *Journal of Chemical Physics*, 105(13):5626–5646, 1996. [146](#)

- [41] Y. L. Zhang and D. M. Crothers. Statistical mechanics of sequence-dependent circular DNA and its application for DNA cyclization. *Biophysical Journal*, 84(1):136–153, 2003. [146](#)
- [42] D. Shore and R. L. Baldwin. Energetics of DNA twisting 1. Relation between twist and cyclization probability. *Journal of Molecular Biology*, 170(4):957–981, 1983. [110](#), [113](#), [117](#), [148](#), [173](#), [198](#), [199](#)
- [43] D. Shore, J. Langowski, and R. L. Baldwin. DNA flexibility studied by covalent closure of short fragments into circles. *Proc. Natl. Acad. Sci. USA*, 170:4833–4837, 1981. [110](#), [112](#), [113](#), [115](#), [117](#), [148](#), [173](#), [179](#), [198](#), [199](#)
- [44] M. Vologodskaja and A. Vologodskii. Contribution of the intrinsic curvature to measured DNA persistence length. *J. Mol. Biol.*, 317(2):205–213, 2002. [117](#), [118](#), [148](#), [199](#)
- [45] J. Bernet, K. Zakrzewska, and R. Lavery. Modelling base pair opening: the role of helical twist. *Theochem-Journal of Molecular Structure*, 398:473–482, 1997. [150](#)
- [46] 2004. (F. Lankas, R. Lavery and J.H. Maddocks private communication.). [151](#), [152](#)

## 6.9 Fourier & Laplace Transforms & convolution theorems

The relations listed below are well known[33] but essential to our derivations. We define the 3D spatial Fourier Transform and inverse transform

$$\tilde{F}(\vec{k}) \equiv \mathcal{F}\{F(\vec{x})\} = \int d^3x F(\vec{x})e^{-i\vec{k}\cdot\vec{x}}, \quad (6.75)$$

$$F(\vec{x}) = \mathcal{F}^{-1}\{\tilde{F}(\vec{k})\} = \left(\frac{1}{2\pi}\right)^3 \int d^3k \tilde{F}(\vec{k})e^{i\vec{k}\cdot\vec{x}}. \quad (6.76)$$

The Faltung theorem states that Fourier Transform of a convolution is the product of the Fourier Transforms

$$\mathcal{F}\{F \otimes G\} = \tilde{F}\tilde{G}, \quad (6.77)$$

for functions  $F$  and  $G$  where the spatial convolution is defined

$$F \otimes G(\vec{x}) \equiv \int d^3x' F(\vec{x}')G(\vec{x} - \vec{x}'). \quad (6.78)$$

The generalization of the Faltung theorem is true for  $n$  functions

$$\mathcal{F}\{F_1 \otimes \dots \otimes F_m\} = \tilde{F}_1 \dots \tilde{F}_m. \quad (6.79)$$

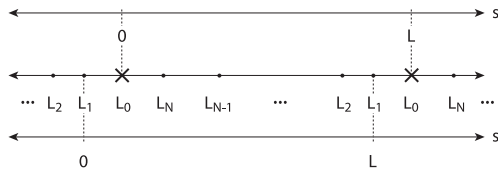


Figure 6.12: A schematic diagram of the coordinate transformation exploited to compute the circular convolution. The crosses represent chain ends and dots represent kinks. The center line represents a periodic coordinate system. For regular convolutions, we set the chain end to be the zero and we compute the convolution in the  $s$  coordinate system. For the circular convolution, it is more convenient to choose  $L_1$ , the first kink arc length position as the zero and sum over the chain end positions as represented by the  $s'$  coordinate system.

We define the 1D contour length Laplace Transform and inverse transform

$$\tilde{F}(p) \equiv \mathcal{L}\{F(L)\} = \int_0^\infty dL F(L)e^{-pL}, \quad (6.80)$$

$$F(L) = \mathcal{L}^{-1}\{\tilde{F}(p)\} = \frac{1}{2\pi i} \int_{\mathcal{L}} dp \tilde{F}(p)e^{pL}, \quad (6.81)$$

where  $\int_{\mathcal{L}}$  denotes a contour integral along the Laplace contour. The Faltung theorem states that Laplace Transform of a convolution is the product of the Laplace Transforms

$$\mathcal{L}\{F \otimes G\} = \tilde{F}\tilde{G}, \quad (6.82)$$

for functions  $F$  and  $G$ , where the arc length convolution is defined

$$F \otimes G(L) \equiv \int_0^L dL' F(L')G(L-L'). \quad (6.83)$$

The generalization of the Faltung theorem is true for  $m$  functions

$$\mathcal{L}\{F_1 \otimes \dots \otimes F_m\} = \tilde{F}_1 \dots \tilde{F}_m. \quad (6.84)$$

### 6.9.1 Circular convolutions

For the closed chain we need to evaluate a special type of convolution which is circular. By circular we mean that the end points are identified so that the arc-length position of the chain ends is not at an end point of the propagator. In this case it is convenient to redefine the arc-length coordinate system to be zero at the position of the first kink,  $L_1$ , and sum over the position of the chain ends as depicted in Fig. 6.9.1. The  $m$  kink contribution to the partition function is therefore

$$\mathcal{Z}_m^* = \frac{\zeta^m}{4\pi} \left[ (K \otimes)^{m-1} LK \right] (0; L), \quad (6.85)$$

where the factor of  $L$  comes from the integration over the end position and varies in the convolution. To simplify this result it is convenient to go to the transformed partition function

$$\tilde{\mathcal{Z}}_m^* = -\frac{\zeta^m}{4\pi} \tilde{K}^{m-1} \frac{\partial}{\partial p} \tilde{K} = -\frac{\zeta^m}{4\pi m} \frac{\partial}{\partial p} \tilde{K}^m, \quad (6.86)$$

where the  $L$  has been transformed into a  $p$  derivative. We now return from Fourier-Laplace space, giving

$$\mathcal{Z}_m^* = \frac{\zeta^m L}{4\pi m} [K \otimes]^m (0; L), \quad (6.87)$$

which is written in terms of convolutions of the spatial propagator only.

### 6.9.2 Numerical inverse transforms

To compute the numerical inversions of the Fourier and Laplace Transforms involving the spatial propagator, we first truncate the continued fraction [34] in Eq. 6.49, then we compute the numerical inversion with the built-in Mathematica functions `InverseLaplaceTransform` and `InverseFourierTransform`. In particular, the structure factor and partition function in an external field involve only a single numerical inverse Laplace Transform.

### 6.9.3 $J$ factor computation

We have chosen to present most of our results in the last section as explicit series in kink number rather than writing them in the summed form (Eq. 6.48 and 6.67). The purpose is two fold. First these expansions allow  $J$  to be computed efficiently for many small values of  $\zeta$ , because the  $\mathcal{K}^{(m)}$  are independent of  $\zeta$  and only the first few must be computed explicitly for sufficient numerical accuracy. Furthermore the  $\mathcal{K}^{(m)}$  are simply related to the kink number distribution allowing the same computation to suffice for both results. Our computational discussion will mainly focus on the short contour length limit where these kink number expansions converge quickly. As we have already discussed at length, the large contour length limit can trivially be computed with the WLC results using the renormalized effective persistence length,  $\xi^*$ . This corresponds to the  $k \rightarrow 0$  and  $p \rightarrow 0$  limit where the theories are identical. In fact, in this limit, we can use the Gaussian chain to compute the  $J$  factor. This computation appears briefly in Appendix 6.11.

It is at short contour length where the two theories significantly diverge and kinking is induced. As we have discussed above, in the limit as the contour length goes to 0, the polymer resembles a rigid rod. It is problematic to directly compute the inverse transforms of  $K^*$  or  $K$  numerically in this limit since

$$K(0; L \rightarrow 0) \propto \int_0^\infty dk k \sin kL, \quad (6.88)$$

which, although it can be computed analytically by expanding sine into two exponentials then

integrating them on different contours, is problematic numerically. It is therefore convenient to use the expanded definition of  $K^*$  in terms of the  $\mathcal{K}^{(m)}$  (eqn 6.62). In the short contour length limit, an asymptotic expression already exists[4] for  $J$  and  $K(0; L)$ .

Convolutions of  $K$  must still be computed. Numerical computations of the inverse transforms of powers of  $\tilde{K}$  are still problematic in the  $L \rightarrow 0$  limit since, while they are more convergent than  $K$ , they must be integrated to large  $k$  where it is difficult to compute accurate Laplace transforms. But this implies it is in precisely this limit that bending is really irrelevant and that the mechanics of these kinked chains becomes kink dominated. Once there are two or more kinks, the chain can now be closed without elastic bending. That is to say that, when these terms become difficult to calculate numerically, they can be well approximated by the kinkable rigid rod! The kinkable rigid rod is treated in Appendix 6.10. As a practical matter there is a small contour length regime ( $L \sim 1$ ), between the rigid rod limit and the contour length at which numerical transform inversion are rapidly convergent and where it is most convenient to use direct Monte Carlo integrations to compute the  $\mathcal{K}^{(m)}$ . These direct Monte Carlo integrations serve as a useful check on our other numerical and analytic computations. For large dimensionless kink densities, the kink-number expansion is not rapidly converging and direct numerical inversions of the exactly summed transformed results are required. For most computations of the  $J$  factor at small kink density, the rigid rod approximation suffices to compute the two kink term and the kink number sum can be truncated at this point as illustrated schematically by Fig. 6.6.3.

## 6.10 Kinkable rigid rod

In this section we develop the theory of kinkable rigid rods, the infinite persistence length limit of the KWLC. This theory is useful for discussing the short loop limit of the  $J$  factor. The rigid rod tangent-spatial propagator is

$$G(\vec{x}, \vec{t}_L, \vec{t}_0, L) = \delta^{(3)}[\vec{x} - L\vec{t}_L] \delta^{(2)}[\vec{t}_L - \vec{t}_0]. \quad (6.89)$$

The spatial propagator,  $K$ , is obtained by averaging and summing over the two tangents (Eq. 6.41)

$$K(\vec{x}, L) = \frac{1}{4\pi L^2} \delta[|\vec{x}| - L]. \quad (6.90)$$

The Fourier and Fourier-Laplace transform spatial propagator are

$$\tilde{K}(\vec{k}, L) = \frac{\sin kL}{kL}, \quad (6.91)$$

$$\tilde{K}(\vec{k}, p) = \frac{1}{k} \tan^{-1} \frac{k}{p}. \quad (6.92)$$

In order to discuss the  $J$  factor limit, we will need the convolutions

$$\mathcal{K}^{(m)} \equiv [K \otimes]^m(0, L), \quad (6.93)$$

which is proportional to the probability density of the end distance be 0 after arc length  $L$  and  $m-1$  kinks.  $\mathcal{K}^{(1)}$  is zero since the rod is rigid and the ends cannot meet unless the chain kinks.

$\mathcal{K}^{(2)}$  is also fairly straight forward. It is convenient to compute the convolution explicitly

$$\mathcal{K}^{(2)} = \frac{1}{2\pi^2} \int_0^L dL_1 \int_0^\infty dk k^2 \frac{1}{kL_1} \sin kL_1 \frac{1}{k(L-L_1)} \sin k(L-L_1) \quad (6.94)$$

$$= \frac{1}{2\pi L^2}, \quad (6.95)$$

where the Fourier transform delta function has been used to evaluate the integral.

The computation of  $\mathcal{K}^{(3)}$  requires some care. Again it is convenient to compute the convolution explicitly

$$\begin{aligned} \mathcal{K}^{(3)} &= \frac{1}{2\pi^2} \int_0^L dL_1 \int_0^L dL_2 \int_0^L dL_3 \int_0^\infty dk k^2 \times \\ &\quad \frac{1}{kL_1} \sin kL_1 \frac{1}{kL_2} \sin kL_2 \frac{1}{kL_3} \sin kL_3 \delta(L_1 + L_2 + L_3 - L), \end{aligned} \quad (6.96)$$

$$= \frac{1}{8\pi^3} \int_0^{L/2} dL_1 \int_{L/2-L_1}^{L/2} dL_2 \frac{1}{(L-L_1-L_2)L_1L_2}, \quad (6.97)$$

$$= \frac{\pi}{16L}. \quad (6.98)$$

For convolution number  $m > 3$ , we exploit the Fourier-Laplace transform method

$$\mathcal{K}^{(m)} = \frac{1}{2\pi^2} \int_0^\infty dk k^2 \int_{\mathcal{L}} dp \left( \frac{1}{k} \tan^{-1} \frac{k}{p} \right)^m e^{pL} \quad (6.99)$$

$$= \frac{1}{2\pi^2} \int_0^\infty dk' k'^2 \int_{\mathcal{L}} dp p^{3-m} \left( \frac{1}{k'} \tan^{-1} k' \right)^m e^{pL}, \quad (6.100)$$

where we have made the substitution  $k' = k/p$ . Now let us compute the  $k'$  integral, which must be done numerically. We now make the substitution  $\tan x = k'$ . The integral in  $k'$  becomes

$$I_m \equiv \frac{m}{m-3} \int_0^{\pi/2} dx \tan^{3-m} x x^{m-1}, \quad (6.101)$$

which we computed using *Mathematica*. The  $p$  integral is now a simple contour integral which gives

$$\mathcal{K}^{(m)} = \frac{I_m}{2\pi^2} \frac{L^{m-4}}{(m-3)!}, \quad (6.102)$$

for  $m > 3$ . The first few values of  $I$  are computed numerically in Table 6.1.

convolution number $m$	Integral $I_m$
4	2.249
5	0.841
6	0.461
7	0.300
...	...

Table 6.1: Values for the numerically computed integral  $I_m$  for the first few  $m$ .

The kinkable rigid rod theory, derived above, provides a very useful analytic check of the KWLC model at short contour length. For short cyclized polymers, the bending between kinks can be ignored since these segments are significantly shorter than a persistence length. As we have illustrated above, the computation of the dominant two kink contribution is straightforward in this limit.

## 6.11 Gaussian limit

The Gaussian limit provides a useful analytic limit to the KWLC theory for long contour length. In this limit, the length of the polymer makes the initial tangent condition irrelevant and describes the spatial distribution for chain extensions short compared with the contour length.

For large  $L$ , we can work with the Gaussian distribution. The Gaussian distribution is

$$G(\vec{x}; \vec{t}, \vec{t}'; L) = \frac{1}{4\pi} \left( \frac{3}{4\pi\xi L} \right)^{3/2} \exp \left[ -\frac{3\vec{x}^2}{4\xi L} \right] \quad (6.103)$$

for persistence length  $\xi$ . The  $J$  factor is

$$J = 4\pi G(0; \vec{t}, \vec{t}; L) = \left( \frac{3}{4\pi\xi L} \right)^{3/2}. \quad (6.104)$$

For KWLC, the persistence length is replaced by the effective persistence length  $\xi^*$ :

$$J^* = 4\pi G^*(0; \vec{t}, \vec{t}; L) = \left( \frac{3}{4\pi\xi^* L} \right)^{3/2}. \quad (6.105)$$

In the Gaussian limit, the convolution functions  $\mathcal{K}^{(m)}$  can be computed without difficulty:

$$\mathcal{K}^{(m)} = \frac{L^{m-1}}{(m-1)!} \left( \frac{3}{4\pi\xi L} \right)^{3/2}. \quad (6.106)$$

But this expression holds only when the number of kinks is small.

## 6.12 Summary of notation

We imagine a chain of total contour length  $L$ , with  $L/\ell$  elementary segments of length  $\ell$ . Individual segments will be referred to by their sequence number  $n = 0, \dots, N$ , where  $N = (L/\ell) - 1$ , or by arclength  $s = n\ell$ . A configuration  $\Gamma$  consists of a sequence of tangent vectors  $\{\vec{t}_0, \dots, \vec{t}_N\}$ .

The stiffness parameter (WLC persistence length)  $\xi$ , one-vertex partition function  $Q$ , kink formation energy  $\epsilon$ , and kinking parameter  $\zeta$  are defined in Sects. 6.2–6.3.  $\xi^*$  and  $Q^*$  are related quantities relevant to the KWLC. The kink length is  $\xi_{\text{kink}} \equiv \zeta^{-1}$ .

The measure  $d^2\vec{t}$  denotes solid angle on the sphere of unit vectors  $\vec{t}$ . Square brackets denote the functional measure  $[d\vec{t}(s)]_{\vec{t}_i}$ ; see Eq. 6.8.

The partition functions  $\mathcal{Z}(L)$  and  $\mathcal{Z}(\vec{t}_f, \vec{t}_i; L)$  refer to unconstrained and constrained functional integrals over a chain of length  $L$  in the continuum limit. Rotation invariance implies that the constrained function depends only on the angle  $\theta$  between the vectors, so we sometimes write it as  $\mathcal{Z}(\theta; L)$ . Discretized versions of the partition functions are denoted with the subscript “discrete,” and KWLC versions with a star. Related quantities include the free energy  $F(\theta; L) = -\log \mathcal{Z}(\theta; L)$  (Eq. 6.28) and the normalized tangent partition function (or propagator)  $H(\vec{t}_f, \vec{t}_i; L) = \mathcal{Z}(\vec{t}_f, \vec{t}_i; L)/\mathcal{Z}(L)$ . Laplace transforms of these functions on  $L$  are denoted with a tilde.

When it is important to maintain spatial information, we introduce space-dependent functions  $\mathcal{Z}(\vec{x}, \vec{t}_f, \vec{t}_i; L)$  (Eq. 6.40),  $K(\vec{x}; L)$  (Eq. 6.41), and  $G'(\vec{x}, \vec{t}; L)$  (Eq. 6.42). Fourier–Laplace transforms of these functions on  $\vec{x}, L$  are again denoted with a tilde.

Laplace and Fourier transformations, and the corresponding convolution operation  $\otimes$ , are defined in Appendix 6.9. Repeated convolutions of  $K$  give the functions  $\mathcal{K}^{(m)}$  (Eq. 6.62), and the related  $\mathcal{J}^{(m)}$  (Eq. 6.70).

The partition function in an external force is  $\mathcal{Z}_{\vec{f}}$  (Eq. 6.54); the cyclization partition function is  $\mathcal{Z}_C^*(L)$  (Eq. 6.65).

In an expansion in kink number,  $m$  labels the number of kinks and  $i = 1, \dots, m$  labels which kink is in question. The kinks are taken to be located at  $n_i$ , or at arc length position  $L_i = \ell n_i$ .

## Chapter 7

# On the experimental front

We now had an elegant model of DNA mechanics which could explain why DNA appeared to be described by the Wormlike Chain model in all experiments except those that explicitly probed the high-curvature bending of DNA. For the correct kink density, the KWLC model fit the experimental data of Cloutier and Widom [1], but was this model the right model? Did it actually describe DNA?

Answering these questions required more experimental input. We had already been working closely with Jon Widom, but in the ensuing months after publishing the KWLC paper (Chapter 6), we also began actively collaborating with the Dekker group at Delft. This work would eventually take me to the Netherlands to get to the bottom of some puzzling AFM data. Even more recently, there have been two other surprising and seemingly contradictory experimental results that cloud the interpretation of the experiments of Cloutier and Widom. This chapter informally describes this experimental odyssey and evolution in our thinking about DNA bending that lead to the final chapter on generalized models of polymer statistics.

### 7.1 Does DNA kink?

I had been fighting a quiet war against Rob Phillips and Phil Nelson. They were in favor of making the mathematics in the KWLC paper as explicit as possible and I had been quietly trying to move the mathematics into the Appendix. Eventually a truce of sorts was reached. We would write two papers. In the long paper for Physical Review E (Chapter 6) the math would remain explicit, but we would write a second paper for a biological audience. In this short paper, we would keep the mathematics implicit and employ an approximate method and analytic results from Shimada and Yamakawa [2] that allowed us to get to the answer without extensive calculations. The short paper was never written, but I will come to that in a moment. The Physical Review E paper [3] was published and very few people persisted with the paper long enough to reach the results, especially biologists who were familiar with neither our notation nor the techniques and mathematics we employed. It was an important lesson and a mistake I hope not to repeat.

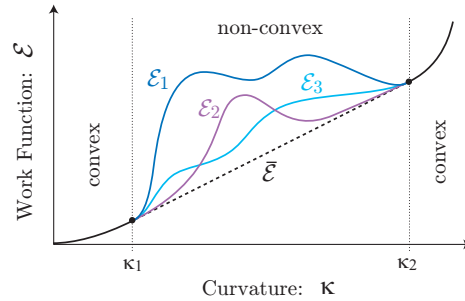


Figure 7.1: Non-convex bending energy densities induce kinking. Above are drawn three examples of non-convex bending energies. Each of the three functions is non-super-convex in curvature on the interval  $(\kappa_1, \kappa_2)$ . If the mean curvature of a rod, under a pure torque load, is on this interval, the lowest energy configuration consists of a combination of regions of curvature  $\kappa_1$  and  $\kappa_2$ . Examples of these “two phase” configurations are drawn in Fig. 7.1.1.

A few biologists did look at the paper. One of these was Bob Schleif. Bob had helped discover transcriptional DNA looping [4] twenty years ago and had seen many micrographs of bent DNA. One of most interesting plots in the KWLC paper was a plot of the distribution in the number of kinks for cyclized DNA. This plot made a clear prediction for tightly looped DNA. It was generically kinked twice! Bob’s message for us was not only had he not seen two kinks generically, he couldn’t remember seeing one! This was not irrefutable evidence against the KWLC model. In fact, kink-like structures have been observed under some conditions [5, 6], especially when DNA is bound tightly to proteins [7], but the KWLC model predicted that kinking should be generic for tightly bent DNA. The KWLC model made bold predictions, but tacitly accused biologists of sleeping on the job! Crick and Klug had in fact proposed that DNA might kink to bind to nucleosomes thirty years before [8]. In the ensuing years, biologists had not observed that kinking was the generic pathway of high-curvature DNA bending.

### 7.1.1 The kinking of macroscopic rods

The failure of the elastic constitutive relation does not necessarily imply kinking. Fosdick and James [9] have studied macroscopic rod systems with energy densities that are arbitrary functions of the curvature<sup>1</sup>. The lowest energy configuration of a rod under a pure torque load (no force) is found by identifying the intervals over which the energy density is super-convex. The super-convex domain of a function is defined as domain on which the tangent line at any point on the function lies below the function for the entire domain. Although this definition sounds technical, it is illustrated clearly in Fig. 7.1.1 for three different non-super-convex functions.

<sup>1</sup>In principle arbitrary derivatives of curvature must also be considered. Physically these terms give rise to a nucleation energy for kinks. I would like to thank Rick James for explaining this to me in June 2004 when he was at Caltech on some personal business. He inspired me to think very generally about the DNA bending problem.

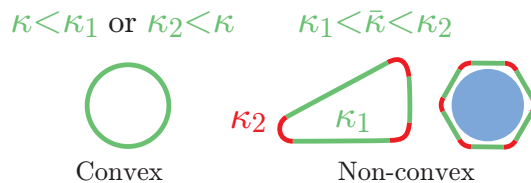


Figure 7.2: Kinking: the localization of curvature. For mean curvatures on the interval where the bending energy density is non-convex ( $\kappa_1, \kappa_2$ ), curvature is localized into kinks (regions of  $\kappa_2$ ). For mean curvatures outside this interval, the curvature of the lowest free energy configuration is uniform.

Let us assume there is only one interval,  $(\kappa_1, \kappa_2)$  over which the energy density fails to be super-convex for positive curvature. This scenario is illustrated in Fig. 7.1.1. For mean curvatures not on the interval  $(\kappa_1, \kappa_2)$ , the minimum energy configuration has constant curvature.

But, for mean curvatures on the interval over which the bending energy density is non-convex, the minimum energy configurations consists of regions of curvature  $\kappa_1$  and  $\kappa_2$ . Regions with curvature  $\kappa_2$  are the localized regions of high curvature or kinks. The kinked conformations are illustrated schematically in Fig. 7.1.1 and the corresponding non-convex bending energy density is depicted in Fig. 7.1.1. Increasing the mean curvature of the lowest energy configuration converts regions of  $\kappa_1$  to  $\kappa_2$ , resulting in a linear dependence of the mean bending energy density on the mean curvature <sup>2</sup>.

Kink-free DNA conformations imply that the bending energy density for DNA is not dramatically non-convex on the length scales observable in electron micrographs. Clearly, the KWLC theory—which kinks dramatically—is non-convex. Fig. 6.4 can be interpreted as the bending free energy for a 10 nm contour length chain. This bending energy is non-convex due to the kinking transition which saturates the bending energy after a kink is nucleated. The absence of kinking in micrographs is evidence for a less-abrupt elastic breakdown.

## 7.2 Beyond kinking

Like Bob Schleif, Jon Widom was also convinced that the high-curvature softening was less dramatic than that predicted by the KWLC model. Phil Nelson and I had favored the kink model in part because it led to a tractable theory. Of course this was not a relevant argument in favor of DNA being described by the KWLC model! Jon argued that he expected that the bending energy of the DNA had the same rough dependence as WLC for small deflection but that the bending energy was simply softer than the WLC model at high deflection but was not soft enough to kink. Based on

<sup>2</sup>In general there will also be a kink nucleation energy, an energy cost for the interfaces between kink regions and non-kink regions. This complication does not significantly change our conclusions.

the insight gained from continuum mechanics, the bending energy density must be approximately convex.

Shortly after finishing the KWLC paper, Rob Phillips, Jon Widom, Phil Nelson, and I began work on a short paper on DNA kinking for a biological audience. As we began to write a draft of the short paper, Jon discovered an interesting experimental paper. Cees Dekker and coworkers had published a measurement of the bending energy as a function of deflection angle for 5 nm segments of DNA. The measured bending energy had roughly the form that Jon had proposed and did not seem to fit either the WLC or the KWLC model.

### 7.2.1 AFM measurements of the bending energy of DNA

Individual DNA molecules are directly observable on the nm length scale in 2D via AFM [10, 11] and EM experiments [12], and in 3D via Cryo EM Tomography [13]. If these molecules are in thermal equilibrium, the chain statistics is also directly observable since it can be computed from the observed conformations. For example, the tangent distribution function  $G(\vec{t}_f; \vec{t}_i; L)$  for contour length  $L$  is the conditional probability density of a final tangent  $\vec{t}_f$  at contour length  $L$  given an initial tangent  $\vec{t}_i$  at contour length 0. This distribution function can be computed directly from observed conformations by histogramming the deflection angles ( $\theta \equiv \arccos \vec{t}_f \cdot \vec{t}_i$ ) for contour length  $L$  segments of the chain.

The bending energy for the contour length  $L$  segment is then defined by the Boltzmann distribution

$$E_L(\theta) = -kT \log G(\vec{e}_r(\theta); \vec{e}_z; L), \quad (7.1)$$

where  $\vec{e}_r$  and  $\vec{e}_z$  are the unit vectors in the  $r$  and  $z$  directions respectively. Of course, the bending energy as we have defined it here is really a bending free energy. For chain statistics calculations, the distinction between energy and free energy is not meaningful since we describe a coarse grained model. Note also that I have explicitly restored the thermal units in this equation in the interest of clarity.

A number of authors have studied the chain statistics of DNA adsorbed to mica [10, 11]. Bustamante and coworker showed that when DNA is adsorbed in the presence of  $\text{Mg}^{2+}$  at concentrations smaller than 10 mM, the persistence length of DNA is nearly identical to that measured in solution [10]. The authors interpreted these results to imply that at low magnesium concentration, (i) the DNA was weakly bound to the mica substrate and was free to equilibrate on the surface and (ii) the bending energy of the chain was not significantly altered by interaction with the surface.

Dekker, van Noort, and coworkers recently employed the mica deposition technique to study the effect of the DNA repair protein Rad50 on DNA curvature [11]. As a control, they computed the DNA bending energy as a function of the deflection angle for 5 nm segments of DNA. These measurements posit a bending energy of DNA, on the 5 nm length scale, that is poorly modeled by

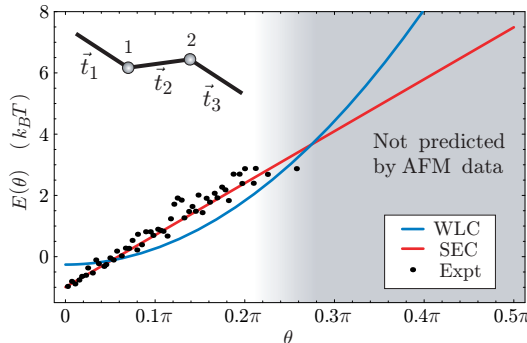


Figure 7.3: The bending energy of DNA on short length scales? The tangent distribution function is measured as a function of deflection angle for 5 nm sections of long sequences of DNA absorbed to mica via AFM [11]. The bending energy deduced from the tangent distribution function (Eq. 7.1) (black dots) is significantly non-harmonic and can be approximately fit to the functional form  $A|\theta|/\ell$  (red curve). For comparison, the WLC bending energy is also shown (blue curve) for persistence length 53 nm which accurately describes the long-length-scale DNA statistical mechanics but fits the short-length-scale experimental data very poorly. We shall call the model based on the fit to the experimental data the SEC model.

an elastic rod model. In fact the data is better fit by the bending-energy

$$E(\theta) = A|\theta| = 5.3|\theta|. \quad (7.2)$$

It is clear from Fig. 7.2.1 that the model is softer at high curvature than the WLC model with persistence length 53 nm (we shall show that the persistence length of the model defined by Eq. 7.2 is 53 nm) and the energy is not non-convex. We will refer to this model as the Sub-Elastic Chain model (SEC) since the constitutive relation (the bending energy) has a weaker dependence on the magnitude of the curvature than the elastic rod model.

It seemed immediately clear to all of us that this bending energy must be incorrect since the energy did not have a wide quadratic region at small deflection. The WLC model work well for force-extension experiments and long-contour-length cyclization measurements, both of which were sensitive to bending in this regime. To our surprise, when we computed the persistence length from the SEC energy, it was 53 nm, correct for DNA. I then proceeded to compute the long-contour-length tangent distribution functions. They were indistinguishable from the WLC model! How could a theory that was so different from the WLC model on short-length-scales still give the correct answer at long length scales? The answer was thermal fluctuations and the renormalization group.

The renormalization group was well known to me in other contexts (high-energy particle physics) but I had forgotten it should also apply for systems as simple as DNA bending. Many physical properties of complicated condensed matter systems have been described by a small set of theories described in terms of renormalizable operators [14]. Regardless of the complicated structure of

the theory at short length scales, the Renormalization Group guarantees that the long-length-scale chain statistics will be described by a theory of renormalizable operators only. For stiff polymers, only one such renormalizable operator exists with the right symmetries. As a consequence, all stiff polymers share generic long-length-scale behavior: that described by the WLC model. Physically, this loss of information is due to the averaging effect of thermal fluctuations. (Many microstates contribute to any given macrostate.) But, on short enough length scales, the underlying structure of the theory becomes important. Violations of the linear elastic theory, analogous to those observed in macroscopic bending, are therefore predicted in experiments that probe the short-length-scale bending of DNA: experiments like the cyclization experiments of Cloutier and Widom.

The renormalization group and the inextensibility of DNA essentially guaranteed that the force-extension of the SEC model would be identical to the WLC model. To check this, it was necessary to expand the machinery developed by Spakowitz and Wang [15, 16, 17] for computing the spatial distribution of the WLC model to analyze general theories. This turned out to be surprisingly easy! As expected, the force-extension of the SEC model was essentially indistinguishable from the WLC model. The last calculation was the most surprising. When we computed the  $J$  factor, it fit the Cloutier and Widom data [1] without a fitting parameter.

We had a cute story and no kinking was required. Was it really so surprising that DNA was not described by an elastic rod on short length scales? DNA was a complicated biomolecular polymer. How could the elastic model do it justice? The only reason the elastic rod model worked was that the renormalization group hid all the details.

### 7.3 On the experimental front...

Phil told our story at the Aspen Single Molecule Biophysics (Steve M. Block) conference. Cees Dekker, whose data was the basis for our model, was in the audience. Cees' paper had not been about DNA mechanics. Had it been, he would have had much better statistics. When Cees returned to Delft, he asked Fernando Moreno and Thijn van der Heijden to repeat the measurement of the bending energy more carefully. Two weeks after Aspen, we had a new set of data from the experimentalists (Fig. 7.3) which was as puzzling as it was exciting.

We had assumed that the bending energy was approximately linear in the deflection angle in part due to poor statistics. But the new data was amazingly linear! Back of the envelope estimates suggested that Dekker and coworkers had the resolution to measure the bending energy for 5 nm segments of DNA. Most disturbing was the fact that the linear elastic regime which we assumed must be there intuitively was nowhere to be seen. Cees seemed reasonably confident about the data, but it seemed to us too good (too linear) to be true<sup>3</sup>. The other problem was what kind of microscopic

---

<sup>3</sup>That being said, hind sight is always 20-20.

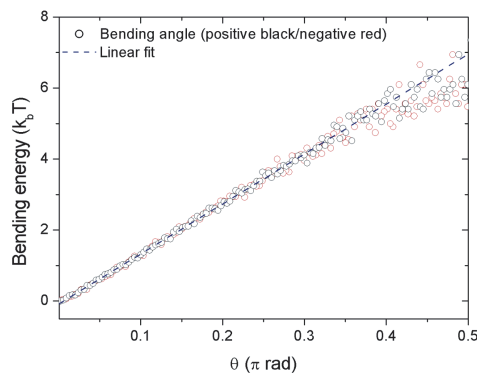


Figure 7.4: The new bending energy measurements of Dekker and coworkers. These new measurements of the bending energy were perplexingly linear in the deflection angle. Even at small deflection, where we intuitively expect the bending energy to be quadratic, the dependence resembled the SEC model ( $E = |\theta|$ ).

mechanism could be responsible for this linear dependence. Why was it so linear? Like us, everybody who had seen the bending energy was also bothered by this linearity, especially at small deflection. Carlos Bustamante had basically told us he didn't believe any of the data. Eventually, Rob and I decided that I should go to Delft so I could learn more about the details of the experiment.

### 7.3.1 Trip to Delft

Phil, Rob, and I had been curious for sometime about exactly how the DNA conformations were digitized and traced. (Carlos Bustamante had been especially vocal about checking this step very carefully.) This was an essential step that had to be done correctly, but until this point we had been unable to understand in detail how they had obtained their results. Cees and coworkers also agreed that checking this step was essential. I discovered that the tracing algorithm had been written a few years ago by van Noort, a postdoc who had since moved to another lab, with Thijn's help. No one remembered exactly how it worked. (My heart sank on hearing this.) Thijn and I eventually found the code responsible for the tracing algorithm, but it was without comments and we had to decipher the code to understand the algorithm.

After seeing the code, I knew we could do better. The next morning I wrote an improved tracing code in Matlab. (This code appears in the Appendix, Sect. A.1.) I expected the new code to make little difference since the tracing produced by the old code was to my eye good, although not perfect. The new code streamlined the tracing processes significantly, and the traces seemed to be a tighter fit to the AFM scan images. Fig. 7.3.1 shows a trace of AFM data generated by the new code.

Using the new code, we traced roughly one hundred, micron-length DNA molecules to get sufficient statistics to compute the tangent distribution function. To my consternation, the improved tracing algorithm did alter the bending energy as is evident in Fig. 7.3.1. It removed the sharp cusp

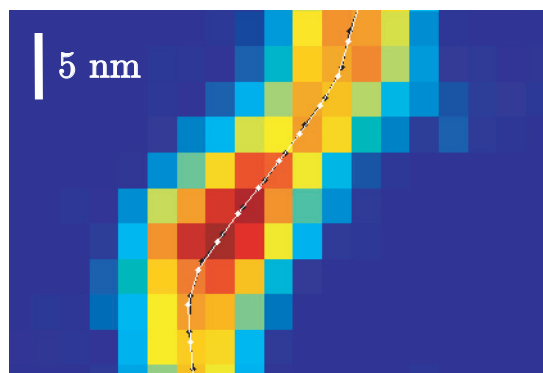


Figure 7.5: Traced DNA conformations. The results of two tracing runs with different initial points are shown in the figure above. The overlap of the black and white traces demonstrates that the tracing algorithm repeatedly finds the same trace independent of the starting point on the DNA molecule.

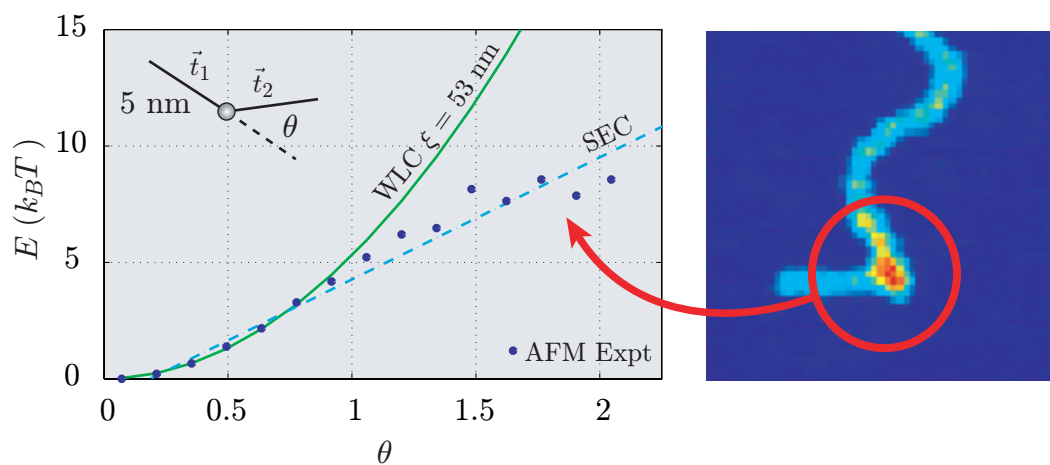


Figure 7.6: The bending energy of DNA revisited. The measured bending energy of DNA (blue dots) fits the WLC model for small deflection (green curve). For large deflection the bending energy may saturate. The SEC model (cyan) fits the data better than the WLC model at high deflection. It is unclear whether the high-curvature events are artifacts of the adsorption process. Some of these events resemble the bent conformation in the right-hand panel. The red coloring of the DNA indicates that this high-curvature region sits higher off the mica than the rest of the DNA. Data from Thijn van der Heijden, Fernando Moreno, and Cees Dekker (Delft).

at zero deflection that we always had suspected was an artifact. But the data now fit the WLC model in the small deflection regime. I had now had a chance to examine the data myself, and both Cees and I were suspicious of the high deflection data. We could check that these high-curvature events were not artifacts of the tracing procedure. But, were these highly-curved conformations artifacts of the surface deposition procedure? Some of these high-curvature conformation appeared raised off the mica surface in the AFM images. (See Fig. 7.3.1.) It was a difficult question to answer with AFM experiments alone<sup>4</sup>. The cyclization data of Cloutier and Widom [1] had seemed to justify the interpretation of these high-curvature events as representative of the chain statistics in solution—high-curvature softening was required to reproduce the observed  $J$  factor—but this evidence was now being challenged from another quarter!

### 7.3.2 Surprising results from Vologodskii

While I was still at Delft, I received a copy of a preliminary paper by Vologodskii and coworkers [18] which claimed to have repeated Cloutier and Widom’s experiment, but found that the  $J$  factor was in fact that described by the Wormlike Chain model! The paper claimed that Cloutier and Widom were working in the wrong kinetic regime and their measurements were therefore invalid! Jon Widom told us that the paper of Vologodskii and coworkers seemed solid and he could not immediately refute their claims. I was giving an invited talk on DNA bending at the March APS meeting in a few days. If the cyclization assay showed no anomaly, the AFM data was unconvincing alone. The data now seemed to point to the WLC model, at least on the length scales probed by the experiments of Vologodskii and coworkers.

### 7.3.3 New data from Jon Widom

As I write this chapter, the evidence is again shifting. Widom and coworkers claim that their  $J$  factor measurements are in the correct kinetic regime and the  $J$  factor for their experiment is as published. It is important to note that these experiments are not exactly identical. The experiments of Cloutier and Widom are at higher temperature<sup>5</sup> and use a different sequence for the single-stranded complementary ends which is more stable than that used by Vologodskii and coworkers [1, 18].

---

<sup>4</sup>The analysis we performed to check the consistency of the chain statistics measured by AFM does not appear here in the interest of brevity. Phil performed a lot of this work for which I am very grateful. It is also worth noting that Thijn van der Heijden and I performed some simulated experiments to try to estimate the accuracy of the AFM technique for measuring the bending energy. I do not have space to explain this work here, but let me simply state that the shape of the measured bending energy was suggestive even though the trace tended to underestimate the polymer bending. This effect had been noted before in Ref. [11]. The AFM results are therefore suggestive but not quantitative.

<sup>5</sup>The experiments of Cloutier and Widom are performed at 30°C versus 20° C for the experiments of Vologodskii and coworkers.

### 7.3.4 What have we learned?

As I write, there is no clear resolution to the inconsistencies between the measurements of Cloutier and Widom [1] and those of Vologodskii and coworkers [18]. Are both experiments correct? Widom and coworkers faced a lot of initial skepticism about their measurements but their reasoning seems to have stood the test of time. Widom, having rechecked the controls of their experiment, is convinced that their work is correct. It is worth noting that measurements of Cloutier and Widom for long-contour-length  $J$  factors match the accepted values. It is also very likely that the experiments of Vologodskii are also correct.

If both experiments are correct, they still differ in at least two aspects: temperature and the affinity of the single-stranded “sticky ends.” Could the stability of the hybridized, complementary, single-stranded ends be responsible for the three-orders-of-magnitude difference in the measured  $J$  factors? The rapid pre-equilibrium kinetic scheme used in the experiment is very well established. (For instance see reference in [19, 20].) Control experiments conclusively show that both experiments are in the correct kinetic regime since the ligation reaction is linear in the ligase concentration and is therefore ligase limited (Eq. 5.41). Although the kinetic regime should be carefully re-examined in light of these experimental discrepancies, failure of the cyclization experiment on account of the stability of the “sticky ends” is unlikely.

The temperature difference between the two conflicting experiments may be able to account for the discrepancy between the experiments of Cloutier and Widom [1] and Vologodskii [18]. There has been extensive work on the thermodynamic stability of DNA [21] due to its importance in the design of PCR primers. AT-rich regions of DNA sequence begin to melt at 50° C. Once short regions of double-stranded DNA melt (fully strand-separate), the short bubbles of melted DNA amount to flexible hinges [22, 23]. In fact, Yan and Marko [24] have already proposed that local melting may account for the high-curvature softening observed by Cloutier and Widom. Their model is very similar to the KWLC model developed in Chapter 6 and the authors estimate the energetic cost of nucleating a three-base-pair bubble is 6-10 kT (estimated from Ref. [21]). The kinking free energy required to reproduce the  $J$  factor measurements by Cloutier and Widom is (Chapter 6)

$$G \approx -kT \log \zeta \ell_{\text{bp}} \approx 10 kT, \quad (7.3)$$

where  $\zeta$  is the kink density and  $\ell_{\text{bp}}$  is the length of a basepair, which is in rough agreement with the bubble nucleation energy.

On-the-other-hand there are two convincing arguments against the canonical “melted-bubble” scenario: the presence of melted tracts would give the  $J$  factor a strong dependence on AT content in the DNA sequence and nearly eliminate the helical phasing effect in the  $J$  factor as the total DNA length is varied, both contrary to observation [25]. DNA melting is not clearly implicated or

ruled out by the experimental data. Certainly the experimental data leaves open the possibility of other, less-cooperative, thermally-activated bending significantly increasing the probability of high-curvature bending. Unfortunately, this new experimental work is too recent to have been analyzed in detail and it is too soon to draw any firm conclusions.

The AFM experiments performed by the Dekker group, while they hint about how the statistics may deviate from the Wormlike Chain model at short contour length, are alone unconvincing evidence for high-curvature softening. There are many possible systematic and experimental problems with interpreting the bending energy from AFM conformations absorbed to mica. For instance it is impossible to rule out the possibility that the mica substrate influences the chain statistics subtly. Rare high curvature bending events may correspond to some process unrelated to the equilibrium solution chain statistics. That being said, if cyclization experiments do continue to show that the chain statistics in solution deviates from the WLC model, these AFM experiments may provide a useful insight into the form of this failure.

### 7.3.5 General models for stiff polymers

Regardless of the outcome of the currently confusing experimental situation, these experiments have motivated a critical re-examination of the mechanics of DNA in tightly-bent conformations. The next chapter is a paper in preparation which quantitatively examines our central claim in this chapter: although the mechanics of DNA may be significantly different from an elastic rod on the short length scales most relevant for the description of biological processes, the Wormlike Chain model describes the chain statistics of DNA as measured in most polymer physics experiments.

Chapter 8 develops a near-exact theory of the chain statistics of a class of generalized stiff polymer models. These models have a bending energy density which is an arbitrary function of curvature. For explicit computations, we use the SEC model, proposed in Sect. 7.2.1. As described in Sect. 7.2.1, we show that a long contour length, the chain statistics of these generalized models is generically described by the WLC model. In particular, we show that the WLC model is sufficient to describe force-extension, solution scattering, and long-contour-length cyclization experiments. The short-contour-length statistics are model dependent. We explicitly show that the SEC model can reproduce the short-contour-length  $J$  factor measured by Cloutier and Widom [1]. Although the muddled experimental picture prevents us from drawing any firm conclusion about the short-length-scale statistics of DNA, these calculations explicitly demonstrate the importance of performing experiments, like short-contour-length cyclization, that are sensitive to the high-curvature DNA mechanics most relevant for biological systems.

# Bibliography

- [1] T. E. Cloutier and J. Widom. Spontaneous sharp bending of double-stranded DNA. *Molecular Cell*, 14(3):355–362, 2004. [5](#), [6](#), [7](#), [96](#), [97](#), [110](#), [114](#), [116](#), [117](#), [118](#), [124](#), [145](#), [148](#), [152](#), [164](#), [169](#), [172](#), [173](#), [174](#), [179](#), [181](#), [185](#), [198](#), [199](#), [200](#), [203](#)
- [2] H. Yamakawa. *Helical Wormlike Chains in Polymer Solutions*. Springer, Berlin, 1997. [5](#), [104](#), [108](#), [109](#), [113](#), [123](#), [125](#), [137](#), [146](#), [160](#), [164](#), [192](#), [199](#), [202](#)
- [3] P. A. Wiggins, P. C. Nelson, and R. Phillips. Exact theory of kinkable elastic polymers. *Phys. Rev. E*, 71(021909), 2005. [123](#), [164](#), [184](#)
- [4] K. Martin, L. Huo, and R. F. Schleif. The DNA loop model for ara repression: AraC protein occupies the proposed loop sites in vivo and repression-negative mutations lie in these same sites. *Proc Natl Acad Sci USA*, 83(11):3654–8, 1986. [2](#), [165](#)
- [5] Wenhai Han, M. Dlakic, Y. J. Zhu, S. M. Lindsay, and R. E. Harrington. Strained DNA is kinked by low concentrations of Zn<sup>2+</sup>. *Proc. Natl. Acad. Sci. USA*, 94:10565–10570, 1997. [165](#)
- [6] Wenhai Han, M. Dlakic, Y. J. Zhu, S. M. Lindsay, and R. E. Harrington. Kinked DNA. *Nature*, 386:563–563, 1997. [165](#)
- [7] Timothy J. Richmond and Curt A. Davey. The structure of DNA in the nucleosome core. *Nature*, 423:145–150, 2003. [165](#), [201](#)
- [8] F. H. C. Crick and A. Klug. Kinky helix. *Nature*, 255:530–533, 1975. [165](#)
- [9] R. L. Fosdick and R. D. James. The elastica and the problem of the pure bending for a non-convex stored energy function. *J. Elast.*, 11:165–186, 1981. [165](#), [184](#)
- [10] Claudio Rivetti, Martin Guthold, and Carlos Bustamante. Scanning force microscopy of DNA deposited onto mica: Equilibration versus kinetic trapping studied by statistical polymer chain analysis. *J. Mol. Biol.*, 264(5):919–932, 1996. [167](#), [185](#)
- [11] John van Noort, Thijn van der Heijden, Martijn de Jager, Claire Wyman, Roland Kanaar, and Cees Dekker. The coiled-coil of the human Rad50 DNA repair protein contains specific segments

- of increased flexibility. *Proceeding of the National Academy of Science USA*, 100(13):7581–7586, 2003. [167](#), [168](#), [172](#), [180](#), [184](#), [185](#), [186](#)
- [12] Bruce Alberts, Dennis Bray, Julian Lewis, Martin Raff, Keith Roberts, and James D. Watson. *Molecular Biology of the Cell*. Garland Publishing, New York, NY, 3rd edition, 1994. [1](#), [11](#), [12](#), [13](#), [16](#), [97](#), [98](#), [100](#), [101](#), [116](#), [167](#), [179](#)
- [13] Jan Bednar, Patrick Furrer, Vsevolod Katritch, Alicja Z Stasiak, Jacques Dubochet, and Andrzej Stasiak. Determination of DNA persistence length by cryo-electron microscopy. Separation of static and dynamic contributions to the apparent persistence length of DNA. *Journal of Molecular Biology*, 254:579–594, 1995. [118](#), [167](#), [184](#)
- [14] Michael Fisher. Renormalization group theory: Its basis and formulation in statistical physics. *Rev. Mod. Phys.*, 70:653–681, 1998. [168](#), [180](#), [183](#)
- [15] A. J. Spakowitz and Z.-G. Wang. Exact results for a semiflexible polymer chain in an aligning field. *Macromolecules*, 37:5814–5823, 2004. [108](#), [133](#), [138](#), [140](#), [144](#), [159](#), [169](#), [180](#), [193](#), [196](#), [211](#)
- [16] A. J. Spakowitz and Z.-G. Wang. End-to-end distance vector distribution with fixed end orientations for the Wormlike Chain model. *Phys. Rev. E*, 2005. In preparation. [108](#), [169](#), [180](#), [192](#), [193](#), [211](#), [212](#)
- [17] A. J. Spakowitz. 2005. In preparation. [169](#), [180](#), [193](#), [202](#)
- [18] Quan Du, Chaim Smith, Nahum Shiffeldrim, Maria Vologodskaja, and Alexander Vologodskii. Cyclization of short DNA fragments and bending fluctuations of the double helix. *Proc Natl Acad Sci USA*, 102(15):5397–402, 2005. [172](#), [173](#), [179](#), [181](#), [198](#), [200](#)
- [19] D. Shore, J Langowski, and R. L. Baldwin. DNA flexibility studied by covalent closure of short fragments into circles. *Proc. Natl. Acad. Sci. USA*, 170:4833–4837, 1981. [110](#), [112](#), [113](#), [115](#), [117](#), [148](#), [173](#), [179](#), [198](#), [199](#)
- [20] D. Shore and R. L. Baldwin. Energetics of DNA twisting 1. Relation between twist and cyclization probability. *Journal of Molecular Biology*, 170(4):957–981, 1983. [110](#), [113](#), [117](#), [148](#), [173](#), [198](#), [199](#)
- [21] J. Jr SantaLucia, H. T. Allawi, and P. A. Seneviratne. Improved nearest-neighbor parameters for predicting DNA duplex stability. *Biochemistry*, 35(11):3555–62, 1996. [173](#)
- [22] J. D. Kahn, E. Yun, and D. M. Crothers. Detection of localized DNA flexibility. *Nature*, 368(6467):163–166, 1994. [118](#), [173](#)

- [23] J. B. Mills, J. P. Cooper, and P. J. Hagerman. Electrophoretic evidence that single-stranded regions of one or more nucleotides dramatically increase the flexibility of DNA. *Biochemistry*, 33(7):1797–1803, 1994. [173](#)
- [24] J. Yan and J. F. Marko. Localized single-stranded bubble mechanism for cyclization of short double helix DNA. *Phys. Rev. Lett.*, 93, 2004. [173](#), [184](#), [212](#)
- [25] T. E. Cloutier and Jonathan Widom. DNA twisting flexibility and the formation of sharply looped protein–DNA complexes. *Proc. Natl. Acad. Sci. USA*, 102:3634–3650, 2005. [173](#), [198](#), [199](#), [202](#)

## Chapter 8

# A generalized theory of stiff polymers

DNA bending on length scales shorter than a persistence length plays an integral role in the translation of genetic information from DNA to cellular function. Quantitative experimental studies of these biological systems have led to a renewed interest in the polymer statistics relevant for describing the conformational free energy of DNA bending induced by protein-DNA complexes. The recent DNA cyclization studies of Cloutier and Widom have questioned the applicability of the canonical stiff polymer theory, the wormlike chain (WLC) model, to DNA bending on biological length scales.

In this paper, we develop a near-exact theory of the chain statistics of a class of generalized stiff polymer models. Our focus is on the theoretical development of these models and the computation of experimental observables. To perform explicit calculations, we also introduce a toy model of DNA bending. We show that the WLC model generically describes the long-length-scale chain statistics of stiff polymers, as predicted by the Renormalization Group. In particular, we show that the WLC model is sufficient to describe force-extension, solution scattering, and long-contour-length cyclization experiments. In contrast, in experiments sensitive to the short-length-scale chain statistics, the WLC model can fail dramatically. We demonstrate this explicitly by showing that our toy model can reproduce the anomalously large short-contour-length cyclization  $J$  factor measured by Cloutier and Widom. Finally, we discuss the applicability of these models to DNA chain statistics in the context of new experimental data.

### 8.1 Introduction

The statistical mechanics of linear polymers has long attracted the attention of physicists and chemists alike. A particularly important and successful application of polymer statistics has been in the description of double stranded DNA (dsDNA) by the wormlike chain model (WLC). The mechanics of DNA is of considerable biological relevance to describing the configurational free en-

ergy of protein-induced DNA bending. These protein-DNA interactions are of central importance to cellular function on a microscopic scale, from chromosomal DNA packaging, to transcription, and gene regulation, to viral packaging [1]. Protein-DNA interactions typically induce short-length-scale DNA bending which couples the chemical and physical properties of DNA [2, 3, 4]. In WLC model, DNA is modeled as fluctuating linear elastic rod. Despite the apparent simplicity of this model, it has been remarkably successful in describing many aspects of DNA mechanics and the statistics of stiff polymers generally. In particular, WLC describes the extension of a single dsDNA molecule under an external force with impressive precision [5].

Despite the notable theoretical and experimental success of the wormlike chain model, the recent DNA cyclization studies of Cloutier and Widom [6] have questioned the validity of the WLC model for describing the cyclization of short-contour-length sequences of DNA. In still more recent cyclization studies, Vologodskii and coworkers claim that the WLC model does accurately describe the cyclization of short DNA sequences [7]. Due to the current, muddled experimental picture, it seems imperative to reevaluate the WLC chain model theoretically. Specifically, we wish to answer the questions: (i) How can such a simple theory describe DNA? (ii) Can the WLC model fail to predict short-contour-length cyclization and still predict long-length-scale phenomena to great accuracy? (iii) If we do expect the WLC model to fail, for which experiments does it fail? (iv) Would the failure of the WLC model to describe DNA mechanics have any biological significance? The focus of this paper will be the theoretical analysis of these questions and the development and discussion of more general stiff polymer models. Although these ideas are widely applicable to polymers statistics in general, the focus of this paper will be exclusively the mechanics of DNA. We shall attempt a synthesis of the existing experimental knowledge to determine which aspects of DNA bending are probed by existing experiments. In particular, we determine which experiments are most sensitive to the DNA mechanics relevant for understanding biological systems. In the remainder of this introduction, we shall quickly motivate the answers to the questions posed above.

### 8.1.1 Confronting two world views

First, to put the possible failure of the WLC model into perspective, it is helpful to consider the bending of macroscopic rods. To engineers in the mechanics community, whose work has been the study of macroscopic bending, the failure of a linear elastic model at high curvature is more pedestrian than remarkable. The linear elastic theory is understood to apply only to the small deflection limit. What is perhaps more remarkable to some in this community is that a linear elastic model describes a macromolecular polymer at all, let alone to the accuracy illustrated by force-extension measurements and long-contour-length cyclization experiments!

To put the remarkable success of the WLC model into perspective, it is helpful to consider DNA mechanics from the perspective of the statistical mechanics of condensed matter systems. Many

physical properties of complicated condensed matter systems have been described by a small set of theories described in terms of renormalizable operators [8]. Regardless of the complicated structure of the theory at short length scales, the Renormalization Group guarantees that the long-length-scale chain statistics will be described by a theory of renormalizable operators only. For stiff polymers, only one such renormalizable operator exists with the right symmetries. As a consequence, all stiff polymers share generic long-length-scale behavior: that described by the WLC model. Physically, this loss of information is due to the averaging effect of thermal fluctuations. (Many micro-states contribute to any given macro-state.) But, on short enough length scales, the underlying structure of the theory becomes important. Violations of the linear elastic theory, analogous to those observed in macroscopic bending, are therefore predicted in experiments that probe the short-length-scale bending of DNA: experiments like the cyclization experiments of Cloutier and Widom.

### 8.1.2 Summary

In this paper, we develop the qualitative framework outlined above by introducing a near-exact generalization of the wormlike chain model. This generalized theory, introduced in Sect. 8.2, describes stiff polymers with local bending energies which are arbitrary functions of curvature. In Sect. 8.2.1, we introduce an explicit toy model of DNA bending, the Sub-Elastic Chain model (SEC), motivated by an experimentally measured tangent distribution function of DNA adsorbed to mica [9]. In Sect. 8.2.3, we illustrate a computational procedure for computing the tangent distribution function for arbitrary contour length in generalized theories. In Sect. 8.2.6, we introduce the persistence length in generalized theories. In Sect. 8.2.7, we explicitly show that these theories converge to the WLC model at long contour length.

In the second half of this paper, we turn our attention to the spatial distribution of the polymer. The spatial distribution is of particular importance for biological applications where the contribution of chain statistics to biological function can often be formulated in terms of an effective concentration or  $J$  factor. Physically, this effective concentration is just the probability density of the polymer having the correct configuration for binding to the binding site of a protein. In Sect. 8.3, we introduce a near-exact method for computing the spatial and tangent-spatial distributions of generalized stiff polymer models in terms of a framework developed by Spakowitz and Wang [10, 11, 12] and others [13]. In Sect. 8.3.1, we explicitly compute the spatial distributions for both the SEC and WLC models for various contour lengths. We discuss the Renormalization Group applied to spatial distributions and show the predicted convergence of the SEC and WLC models at long contour length. In Sect. 8.3.2 and Sect. 8.3.3, we show that the force extension and the structure factor computed for general theories are nearly identical to the WLC model results, implying that these experiments do not probe the high-curvature chain statistics important for many biological processes. In Sect. 8.3.4, we compute the cyclization  $J$  factor for generic theories. We show that the SEC model gives

rise to the enhanced cyclization efficiency for short-contour-length sequences observed by Cloutier and Widom [6] while leaving the long-contour-length  $J$  factor identical to that predicted by the WLC model. Finally, we discuss the results of this paper in the context of the recent cyclization measurements of Vologodskii and coworkers [7] and new preliminary AFM measurements of the tangent distribution function.

## 8.2 Defining discrete link theories

In this paper, we shall discuss a class of generalized elastic models for the statistical mechanics of isotropic, stiff, inextensible polymers. The theories we discuss in this paper will be applicable to the description of polymers on length scales long comparable to the molecular structural length scales. We shall idealize a stiff polymer as a space curve whose configurational free energy is a local functional of the spatial configuration. Microscopically this configurational free energy is the combination of entropic and energetic parts which depend on the underlying molecular structure of the polymer. We will ignore the effects of excluded volume since we will be principally interested in bending on very short length scales where these self interaction effects play a negligible role in describing the chain conformation.

The bending energy density of general theories can be written in terms of the arc length, tangent vector, and its derivatives:

$$\varepsilon = \varepsilon(\vec{t}, d\vec{t}/ds, d^2\vec{t}/ds^2, \dots, s), \quad (8.1)$$

where the energy density depends on arbitrarily high derivatives of the tangent vector  $\vec{t}$ . We shall not study this completely general model, but a restricted class of these models. First we shall assume that the energy density is not explicitly dependent on the arc length  $s$  (homogeneous). Strictly, this is not the case for DNA since both the helical pitch and the sequence dependence add arc length dependence [2, 6]. But, we shall study the mechanics of DNA on length scales longer than helical repeat (3.41 nm) where we can treat the DNA as rod like and assume that the sequence dependence is weak. We shall also make the assumption that the theory is rotationally invariant under rigid body rotations (isotropic). Last of all, we shall assume that the energy density depends on no higher derivative terms than the curvature

$$\vec{\kappa} \equiv d\vec{t}/ds. \quad (8.2)$$

Under these assumptions, the energy density is a function of the magnitude of the curvature only

$$\varepsilon = \varepsilon(\kappa), \quad (8.3)$$

since the curvature is orthogonal to the tangent vector.

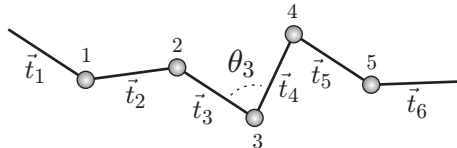


Figure 8.1: Link and vertex numbering. The energy is a function of the deflection angles. The deflection angle between links  $i$  and  $i + 1$  is  $\theta_i$ .

Of these assumptions, the most subtle is that associated with discarding the derivatives of the curvature. In the interest of brevity, we shall call this condition locality since it describes theories of stiff polymers with the fewest derivatives of the tangents. It is not manifestly imperative that this restricted class of models describes DNA. For example, on strictly dimensional grounds, there is no reason to keep a term in  $\kappa^4$  over a term in  $(d\kappa/ds)^2$ . We have chosen this subset of general models motivated by Atomic Force Microscopy (AFM) experiments which we shall discuss in Sect. 8.2.2. We shall return to this point again briefly in the discussion.

### 8.2.1 Statistical mechanics

We shall define the statistical mechanics theory in the canonical way. The probability of any microstate is given by the Boltzmann law:

$$\mathcal{P} = Z^{-1} \exp -E, \quad (8.4)$$

where  $Z$  is the partition function determined by normalization and we have defined the energies  $E$  in units of  $k_B T$ . In fact, we shall simply define the energy by Eq. 8.4.

To define a statistical mechanics theory, the notion of an energy density is not sufficient. We must also introduce a fundamental length scale on which to define the theory. To determine the partition function  $Z$ , we must have an explicit method for enumerating all possible states. To be explicit, we define the theory at scale  $\ell$  by discretizing the configuration into links length  $\ell$ , separated by torsional springs whose energy is a function of the deflection angle  $\theta_i$  between adjacent links  $i$  and  $i + 1$ . This discretized chain is pictured schematically in Fig. 8.2. We shall interpret (or define) the bending energy density by letting the bending energy be that for a uniformly bent arc with deflection angle  $\theta_i$  and length  $\ell$ :

$$E_i = \ell \varepsilon(\kappa_i), \quad (8.5)$$

where  $\kappa_i = \theta_i/\ell$ . The total bending energy  $E$  for a configuration of links is the sum of these vertex energies.

In mechanics, a continuum model would be defined by the limit as the link length goes to zero. In this limit, the energy is independent of the link length  $\ell$ . But this will not be the case in general

statistical mechanics theories. The behavior of the theory, and experimental observables, depend on the fundamental length scale  $\ell$ . There is however a one-parameter family of polymer theories in which the scale dependence vanishes. These theories are described by a linear-elastic energy density which is quadratic in the curvature

$$\varepsilon = \frac{1}{2}\xi\kappa^2. \quad (8.6)$$

The statistics is completely described by the bending modulus  $\xi$ . This family of theories is the wormlike chain model.

The systematic study of the length scale dependence of statistical mechanics theories is called the Renormalization Group [8]. If we confine our interest to the description of the tangents of the polymer, there is only one renormalizable term in the energy density with the right symmetries to meet our assumptions. It is the energy density which describes the wormlike chain model, Eq. 8.6. The fact that more general energy densities are not scale independent does not imply that these energy densities result in poorly defined theories, it implies only that these theories must be defined with respect to a fundamental length scale.

The assumption that the bending energy depends only on the curvature and not on higher order derivatives of the tangent, implies that the vertex bending energy depends on the tangents of nearest neighboring links only. This assumption implies that the partition function for an  $N$  link chain decouples into  $N - 1$  factors of the single-link partition function:

$$q = \int d\vec{t}_{i+1} e^{-E_i}, \quad (8.7)$$

where  $\vec{t}_{i+1}$  is the out-going tangent of link vertex  $i$ . (See Fig. 8.2.) In the expression above, we have written the sum over the final tangent implicitly since we do not wish to limit ourselves to a particular dimension since both two and three dimensions are of experimental interest.

We now introduce the fundamental tangent distribution function. The tangent distribution function is the conditional probability density for the final tangent, given an initial tangent. The fundamental tangent distribution function is the distribution function over just one link, length  $\ell$ , and is related to the vertex energy by the Boltzmann Law (Eq. 8.4)

$$g(\vec{t}_{i+1}, \vec{t}_i) \equiv q^{-1} e^{-E_i}, \quad (8.8)$$

where  $\vec{t}_i$  and  $\vec{t}_{i+1}$  are the initial and final tangent respectively and the deflection angle at vertex  $i$  is  $\cos\theta_i = \vec{t}_i \cdot \vec{t}_{i+1}$ . The chain statistics of the theory are completely determined by the fundamental tangent distribution.

### 8.2.2 Sub-Elastic Chain Model: A toy model

We shall now introduce an explicit toy model for DNA bending that is dramatically different from the WLC model. Although all the symbolic results can be applied to the analysis of general stiff polymer models, we shall use this simple model to compute experimental observables like the force extension, the cyclization  $J$  factor, etc for an explicit generalized theory. The model we wish to study has a bending energy which is softer than the elastic model for high curvature but reproduces the long-length-scale predictions of the WLC model with a persistence length of roughly 50 nm.

We have already described one such model in another paper [14] and a similar model has also been proposed by Yan and Marko [15]. In both cases, the high curvature softening was introduced via kinking, or curvature localization. Although these models could reproduce the two desired features mentioned above, they postulated that highly curved DNA should be generically kinked [14]. These dramatic predictions have not been observed experimentally for DNA visualized via EM or AFM experiments. It is well known in continuum mechanics that bending-energy densities that are non-convex in curvature induce kinking when highly bent [16]. To avoid kinking, we shall place an additional loose restriction on the model: the energy density is not dramatically non-convex in curvature on length scales observable via EM or AFM experiments.

As we have tacitly implied above, the tangent distribution function is, in principle, observable in 2D via AFM [9] and EM, and in 3D via Cryo EM Tomography [17]. Eq. 8.8, relating the bending energy and fundamental tangent distribution function, can be inverted and interpreted as a definition of the bending energy<sup>1</sup>:

$$E_i(\kappa) = \ell \varepsilon(\kappa) \equiv -\log g(\vec{t}_{i+1}, \vec{t}_i), \quad (8.9)$$

where the fundamental length scale, the link length  $\ell$ , is interpreted as the resolution of the experimental technique used to resolve the chain statistics. In Fig. 8.2.2, we show AFM data from van Noort *et al.* [9] for the bending energy of DNA absorbed to mica. The bending energy has been computed for a link length,  $\ell$ , of 5 nm. These measurements posit a bending energy of DNA, on the 5 nm length scale, that is poorly modeled by an elastic rod model. In fact the data is better fit by the bending-energy density

$$\epsilon(\kappa) = A|\kappa| = 5.3|\kappa|. \quad (8.10)$$

We shall show that this bending energy has many of the features we desire. In particular, it is already clear from Fig. 8.2.2 that the model is softer at high curvature than the WLC model with persistence length 53 nm (we shall show that the persistence length of the model defined by Eq. 8.10 is 53 nm) and the energy is not non-convex. We will refer to this model as the Sub-Elastic Chain model (SEC) since the constitutive relation (the bending energy) has a weaker dependence on the

---

<sup>1</sup>Of course, the bending energy as we have defined it here is really a bending free energy. For chain statistics calculations, the distinction between energy and free energy is not meaningful since we describe a coarse grained model.

magnitude of the curvature than the elastic rod model.

The reader may have several quite substantive objections to the claim that Eq. 8.10 correctly describes the bending energy of DNA in solution. These measurements were performed on DNA, adsorbed to mica at low Magnesium concentrations, then rinsed and dried before the DNA conformations were scanned using an AFM [9]. It is believed that (i) the adsorption of DNA to the mica substrate is weak enough that the chain can equilibrate on the surface and that (ii) the mica does not significantly affect the bending energy of the chain because the persistence length of the polymer is roughly the same as that measured in solution [18]. There are also important limitations on the accuracy of these measurements due to the AFM tip convolution, pixillation, and tracing algorithm used to extract the bending angles [9]. Another objection to the proposed model is that the energy is non-analytic at zero curvature.

We wish to use these experiments only to motivate a class of models in which the bending energy becomes softer than quadratic at large deflection. For the moment, let us lay our fears aside and analyze the SEC model to see what the consequences of the bending energy described by Eq. 8.10 are. Is this model, which is dramatically different from the WLC model on short length scales, compatible with other measurements of DNA chain statistics on long length scales as suggested by Renormalization Group arguments? Can this type of model reproduce the anomalously high  $J$  factor observed by Cloutier and Widom [6]? To answer these questions, the detailed form of the bending energy will not be particularly important. For instance, we could introduce a small quadratic regime to the bending energy without significantly affecting the predictions of the model or the fit to experiment. In the remainder of Sect. 8.2, we shall explicitly demonstrate that the tangent distribution function of the SEC model approaches that predicted by the WLC model as the contour length of the chain increases.

### 8.2.3 The propagator and composition

The locality assumption in the definition of the bending energy implies that each vertex bends independently. The fundamental tangent distribution function is the conditional probability of a final tangent, given an initial tangent for a single vertex. Computing the tangent distribution functions for chains of several links is therefore straightforward. These conditional probabilities are simply the product of conditional probabilities for single vertices, summed over the orientations of the intermediate tangents [19]

$$G(\vec{t}, \vec{t}'; N\ell) = \int \underbrace{d\vec{t}_1 \dots d\vec{t}_{N-2}}_{N-2} g(\vec{t}; \vec{t}_1) \underbrace{g(\vec{t}_1; \vec{t}_2) \dots g(\vec{t}_{N-3}; \vec{t}_{N-2})}_{N-2} g(\vec{t}_{N-2}; \vec{t}'), \quad (8.11)$$

where we have written the  $N$  link tangent distribution function as a function of the arc length,  $N\ell$ . This notation is needlessly cumbersome. It is therefore convenient to introduce the propagation

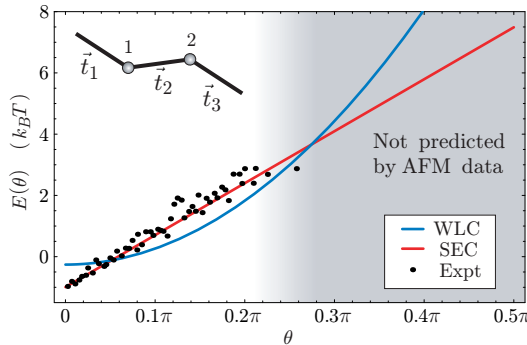


Figure 8.2: The bending energy of DNA on short length scales? The tangent distribution function is measured as a function of deflection angle for 5 nm sections of long sequences of DNA absorbed to mica via AFM [9]. The bending energy deduced from the tangent distribution function (Eq. 8.9) (black dots) is significantly non-harmonic and can be approximately fit to the functional form  $A|\theta|/\ell$  (red curve). For comparison, the WLC bending energy is also shown (dotted blue curve) for persistence length 53 nm which accurately describes the long-length-scale DNA statistical mechanics but fits the short-length-scale experimental data very poorly. We shall call the model based on the fit to the experimental data the SEC model. *Note to reader:* See also Fig. 7.3.1 for a fit to unpublished AFM data.

operator (or transfer matrix [19])

$$\mathcal{G} \equiv \int dt dt' |\vec{t}\rangle g(\vec{t}, \vec{t}') \langle \vec{t}'|, \quad (8.12)$$

where  $\langle |$  and  $| \rangle$  is the canonical bra ket notation of statistical mechanics (or quantum mechanics) [20]. These states are a continuum basis:

$$\langle \vec{t} | \vec{t}' \rangle = \delta [\vec{t} - \vec{t}'], \quad (8.13)$$

where  $\delta$  is the Dirac delta function on the space of unit tangent vectors.

The propagation operator,  $\mathcal{G}$ , applied on a state gives the probability distribution after one additional link. This property is called composition and is a direct result of the locality discussed above. We can now rewrite Eq. 8.11 more concisely

$$G(\vec{t}; \vec{t}'; N\ell) = \langle \vec{t} | \mathcal{G} \dots \mathcal{G} | \vec{t}' \rangle = \langle \vec{t} | \mathcal{G}^N | \vec{t}' \rangle, \quad (8.14)$$

where the weighted sum, or path integral, over all intermediate configurations is now implicit. By changing the basis in the next section, we shall show that this expression is also a convenient computational tool for understanding general theories [19].

### 8.2.4 Symmetry considerations

The tangent basis we have exploited to write the tangent distribution function is not particularly convenient computationally since the operator is not expressed in its eigenbasis in which it is diagonal. To find an eigenbasis for this operator, we exploit the rigid body rotational invariance of the tangent distribution function. In  $D$  dimensions, the rigid-body-rotational invariance of the model implies that the propagator commutes with the generators of rotation

$$[\mathcal{G}, \mathcal{L}_{ij}] = 0, \quad (8.15)$$

where  $\mathcal{L}_{ij} = -\mathcal{L}_{ji}$  are the generators of rotation in the  $ij$  plane. The propagator therefore also commutes with the Casimir operator, which corresponds to the total angular momentum:

$$\mathcal{L}^2 \equiv \frac{1}{2} \sum_{i,j=1}^D \mathcal{L}_{ij} \mathcal{L}_{ij}. \quad (8.16)$$

Since  $\mathcal{L}^2$  and  $\mathcal{G}$  commute, they share the same eigenbasis [20]. The angular momentum states span the tangent space and are eigenvalues of  $\mathcal{L}^2$ :

$$\mathcal{L}^2 |l \mathbf{m}\rangle = l(l + D - 2) |l \mathbf{m}\rangle, \quad (8.17)$$

where  $l$  is the total angular quantum number and we write the other angular quantum numbers collectively as  $\mathbf{m}$ . The propagator can therefore be expanded in this eigenbasis [19]

$$\mathcal{G} = \sum_{l\mathbf{m}} g_l |l\mathbf{m}\rangle \langle l\mathbf{m}|, \quad (8.18)$$

where the  $g_l$  are coefficients that depend only on the quantum number  $l$  but not on  $\mathbf{m}$ . (If this wasn't the case,  $\mathcal{L}^2$  and  $\mathcal{G}$  would not commute.) We have now achieved our goal of diagonalizing the propagator  $\mathcal{G}$ .

Explicitly, in two dimensions, it is convenient to use the eigenfunctions [20]

$$\langle \vec{t} | lm \rangle = \frac{1}{\sqrt{2\pi}} \exp -im\theta, \quad (8.19)$$

for  $m \in \mathbb{Z}$  and  $l \equiv |m|$ . Note that the quantum number  $m$  is sufficient to describe the state but we have introduced a second quantum number,  $l$ , which is invariant under a generalized notion of rotational invariance in two dimensions which includes the discrete transformation  $\theta \rightarrow -\theta$  which is a parity inversion.

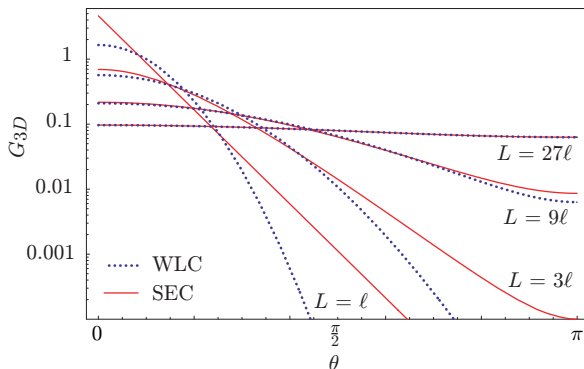


Figure 8.3: The evolution of the tangent distribution function. In the figure above, the WLC and SEC tangent distribution functions are plotted as a function of the deflection angle  $\theta$  for several contour lengths. The linear dependence of SEC bending energy on the deflection angle of the fundamental distribution function ( $L = \ell = 5$  nm) is lost at longer contour length. For  $L \gg \ell$ , the tangent distribution approaches the WLC distribution function with a persistence length of 53 nm despite dramatically different behavior at short contour length. This loss of the short length structure of the tangent distribution function is universal and explains the success of the WLC model in describing many stiff polymer phenomena.

In three dimensions, it is convenient to use the eigenfunctions [20]

$$\langle \vec{t} | l m \rangle = Y_{lm}(\theta, \phi), \quad (8.20)$$

where the  $Y_{lm}$  are the spherical harmonics where we typically choose  $m$  to be the quantum number of the  $z$  component of the angular momentum which we have written  $\mathcal{L}_{12}$ .

The orthonormality of the basis implies that the  $g_l$  are uniquely determined and can be determined in the usual way (Eq. 8.51 and Eq. 8.52). It is now straightforward to perform the  $N+1$  link path integral of Eq. 8.11

$$\mathcal{G}^N = \sum_{l\mathbf{m}} g_l^N |l\mathbf{m}\rangle \langle l\mathbf{m}|, \quad (8.21)$$

since the propagation operator is diagonal.

We return now to the SEC model proposed in Sect. 8.2.2. The  $N$  link tangent distribution function for the SEC model is shown in Fig. 8.2.4. This figure explicitly illustrates the scale dependence of statistical mechanics theories. For short contour length chains, the WLC and SEC theories make dramatically different predictions, but as the contour length of the chain increases, the differences between the distribution functions of the two theories decrease until at long contour length, the theories are essentially indistinguishable. This is the essence of the renormalization group: at short length scales, the mechanics of the chain can be extremely complicated but the thermal fluctuations sum over many intermediate configurations and hide the underlying complexity on longer length scales. We shall show this for general theories in Sect. 8.2.7.

### 8.2.5 Contour length continuation

Since we shall frequently be interested in the properties of the polymer on length scales much longer than the fundamental link length  $\ell$ , it is useful to introduce a continuum dependence on arc length. We therefore introduce the Hamiltonian operator defined

$$\mathcal{H} \equiv -\ell^{-1} \log \mathcal{G} = \sum_{l\mathbf{m}} h_l |l\mathbf{m}\rangle \langle l\mathbf{m}|, \quad (8.22)$$

where the eigenvalues of the Hamiltonian operator are  $h_l = -\ell^{-1} \log g_l$  and it is also diagonal in the angular momentum representation. We call this operator the Hamiltonian operator because in the WLC model, the statistical mechanics of the chain corresponds to a quantum particle on a  $D - 1$  sphere. The tangent distribution function is equal to the quantum propagator where time has been continued to imaginary arc length. The Hamiltonian operator is equal to the Hamiltonian of the corresponding particle system.

In terms of the Hamiltonian operator, we can rewrite the  $N$  link propagator

$$\mathcal{G}^N = \exp -\mathcal{H}N\ell, \quad (8.23)$$

where  $N\ell$  is the contour length corresponding to  $N$  links. The advantage of this reformulation of distribution function is that it introduces a natural extension to fractional numbers of links by replacing  $N\ell$  by the contour length  $L$  defined for all positive real numbers. We define the continuum tangent distribution function

$$\mathcal{G}(L) \equiv \exp -\mathcal{H}L, \quad (8.24)$$

although rigorously, it is understood that this function is only defined for contour lengths equal to an integral number of links.

### 8.2.6 The meaning of persistence length

What is the meaning of persistence length in general models like those of interest here? Persistence length describes the length scale on which the polymer maintains its tangent orientation. For the WLC model in  $D$  dimensions, the tangent persistence is

$$\langle \vec{t}(0) \cdot \vec{t}(L) \rangle = \exp [-L(D - 1)/2\xi], \quad (8.25)$$

where  $\xi$  is the persistence length, which also appears in the energy density as the bending modulus in Eq. 8.6. In general models, the tangent persistence (Eq. 8.25) has the same functional form but  $\xi$  no longer corresponds to a bending modulus. We shall therefore simply use Eq. 8.25 to define the persistence length of general models.

The tangent persistence corresponds to the  $l = 1$  mode of the propagator. (The tangent is a vector; therefore it is spin 1.) Comparing Eqs. 8.24 and 8.25, the persistence length is

$$\xi_D \equiv (D - 1)/2h_1, \quad (8.26)$$

where  $h_1$  is the  $l = 1$  eigenvalue of the Hamiltonian. Note that we have explicitly written a subscript to denote the dependence on dimension. In the WLC model,  $\xi$  is independent of dimension, but in more general models this is not the case.

The persistence length also controls the long-length characteristics of the polymer. Remember that the mean-squared end-to-end distance can be written in terms of the tangent persistence

$$\langle \bar{X}^2 \rangle = \int_0^L ds ds' \langle \vec{t}(s) \cdot \vec{t}(s') \rangle. \quad (8.27)$$

Since Eq. 8.25 applies to both the WLC model and general models, the dependence of the mean squared end-to-end distance on persistence length and contour length is identical to the WLC model. The same is true for radius of gyration, which can also be written in terms of an integration of Eq. 8.25. It is also well known that the long-contour-length spatial distribution of stiff polymers is described by the Gaussian Chain model [21]. (This is a consequence of renormalization.) The width of the Gaussian distribution is determined by the mean squared end-to-end distance therefore there is the same relation between the the Kuhn length and the persistence length for general models as for the WLC model.

We can immediately exploit Eq. 8.26 and Eq. 8.52 to analyze the SEC model. The persistence length, computed for the SEC model in three dimensions is 53 nm which matches solution measurements.

### 8.2.7 Stiff polymer limit

In this section, we examine the tangent distribution function in the stiff polymer limit and show that the WLC model is universal at long contour length as predicted by the Renormalization Group. Our explicit computations of the SEC tangent distribution function in Sect. 8.2.3 have already provided one explicit example of this behavior, but we address this question generally in this section.

The stiff polymer limit, by definition, implies that the fundamental tangent distribution function,  $g$ , is narrowly distributed around zero deflection. We will exploit this fact by expanding the basis functions in the deflection angle and computing the eigenvalues of the propagator (Eq. 8.18) to lowest order in the deflection angle. In dimension  $D$ , this calculation, although straightforward, requires some technical mathematics. We therefore relegate the details of this calculation to the appendix, Sect. 8.6.2, and present only the results.

The propagator in the stiff polymer limit is

$$\mathcal{G} = 1 - \frac{\ell}{2\xi} \mathcal{L}^2 + \mathcal{O}[\mathcal{L}^4(\ell/\xi)^2], \quad (8.28)$$

where  $\xi$  is the persistence length defined by the  $l = 1$  eigenvalue of the Hamiltonian operator (Eq. 8.26). Note that the  $\mathcal{L}^2$  term is understood to be small for small values of the angular quantum number  $l$  since, in the stiff polymer limit, the link length  $\ell$  is much shorter than the persistence length  $\xi$ . The corrections are order  $\mathcal{L}^4 \langle \theta^4 \rangle$  and scale as  $l^4$  for large  $l$ . Clearly this approximation holds only for small angular quantum number  $l$ . It is convenient to compute the Hamiltonian operator

$$\mathcal{H} = \frac{1}{2\xi} \mathcal{L}^2 + \mathcal{O}[\mathcal{L}^4(\ell/\xi)^2], \quad (8.29)$$

which is identical to the WLC Hamiltonian to lowest order in the deflection angle. Again, the correction scales like  $l^4$  which implies that this relation holds only for small angular quantum numbers.

The correspondence between the Hamiltonian operators for general models and the WLC model for small angular quantum numbers implies that the long-contour-length behavior of the polymer is universal and determined by the persistence length alone. This correspondence is shown explicitly for the SEC and WLC theories in Fig. 8.2.7. At long contour length, only states with small  $l$  contribute since higher momentum states decay quickly. Remember that the propagator is

$$\mathcal{G} = \exp -\mathcal{H}L, \quad (8.30)$$

and the eigenvalues of  $\mathcal{H}_{\text{WLC}}$  scale as  $l^2$  for large  $l$ . The tangent distribution function is therefore well approximated by the WLC model at long contour length:

$$\lim_{L \gg \ell} \mathcal{G}(L) = \mathcal{G}_{\text{WLC}}(L). \quad (8.31)$$

The details of the short-length-scale bending energy affect only the large  $l$  eigenvalues of the Hamiltonian operator and are therefore irrelevant at long contour length as predicted by the renormalization group.

Although we have yet to compute the spatial distribution function, we have already explicitly shown that measurements that are only sensitive to the long-length-scale chain statistics do not determine the short-length-scale behavior of the theory and that violations of the wormlike chain model, while disguised by thermal fluctuations at long contour length, are generic as the length scales probed by experiment approach the fundamental or structural length scale of the chain.

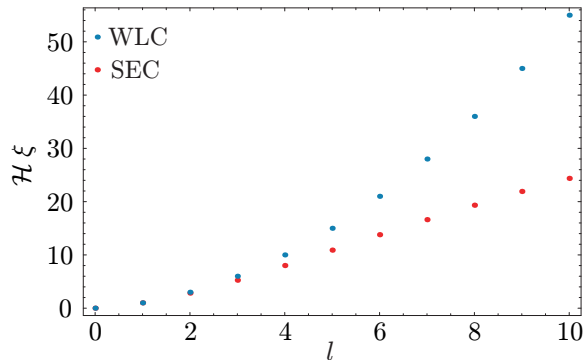


Figure 8.4: The eigen-spectrum of  $\mathcal{H}$  for the SEC and WLC models. The eigenvalues of the Hamiltonian operator for the WLC and SEC theories are compared as a function of the angular quantum number  $l$ . Both theories have an identical persistence length,  $\xi = h_1^{-1} = 53$  nm. The eigenvalues of the Hamiltonian are coincident for small  $l$  but diverge as  $l$  increases. The  $l$ th moment of the distribution function decays as  $\exp -h_l L$ . The larger eigenvalues of the Hamiltonian, for which the two theories differ, are therefore relevant only for small  $L$ , implying that the SEC and WLC chain statistics are identical for long-contour-length chains.

### 8.3 The spatial distribution

For most applications, it is the spatial distribution of the polymer rather than the tangent distribution function which is of phenomenological interest. From solution scattering to force-extension, cyclization to looping, the spatial distribution function is directly observable. In this section, we shall develop a near exact formalism for computing the spatial distribution function. Our focus will be exclusively three dimensions but computations in other dimensions are a simple extension of the methods discussed here.

The tangent-spatial distribution function is the probability density of end displacement  $\vec{X}$  and final tangent  $\vec{t}_f$  given an initial tangent  $\vec{t}_i$  for an arc length  $L$  chain. It is convenient to write the tangent spatial distribution in terms of the spatial delta function [22]

$$G(\vec{X}; \vec{t}_f, \vec{t}_i; L) = \langle \vec{t}_f | \exp[-\mathcal{H}L] \delta^3[\vec{X} - \int_0^L ds \vec{t}(s)] | \vec{t}_i \rangle, \quad (8.32)$$

where we have written the distribution function in the continuum limit. We shall reintroduce an operational definition of this continuum limit in a moment.

To compute the tangent-spatial distribution function, we introduce an operator-valued spatial distribution function [11]:

$$\mathcal{G}(\vec{X}; L) = \int d\vec{t} d\vec{t}' | \vec{t} \rangle G(\vec{X}; \vec{t}, \vec{t}'; L) \langle \vec{t}' |, \quad (8.33)$$

which allows us to keep the tangents implicit in our expressions. We shall call this operator the

spatial propagator since it obeys the composition property of Green Functions:

$$\mathcal{G}(\vec{X}; L + L') = \mathcal{G}(\vec{X}; L) \otimes \mathcal{G}(\vec{X}; L'), \quad (8.34)$$

where  $\otimes$  is the spatial convolution.

As usual, it will be convenient to work in the angular momentum basis with the matrix elements

$$G_{lm'l'}(\vec{X}; L) \equiv \langle l \ m | \mathcal{G}(\vec{X}; L) | l' \ m' \rangle, \quad (8.35)$$

since this basis diagonalizes the Hamiltonian (although not the spatial propagator). Finding the spatial propagator reduces to the ability to explicitly compute all the  $G_{lm'l'}$ .

We shall be able to derive exact expressions for the Fourier-Laplace Transform of the spatial propagator in the continuum theory in terms of the transformed matrix elements (Eq. 8.35). We adopt the Fourier Transform convention

$$G(\vec{k}; L) \equiv \mathcal{F}_{\vec{X} \rightarrow \vec{k}} G(\vec{X}; L) \equiv \int d^3 X G(\vec{X}; L) \exp -i\vec{k} \cdot \vec{X}, \quad (8.36)$$

and the Laplace transform convention

$$\tilde{G}(\vec{k}; p) \equiv \mathcal{L}_{L \rightarrow p} G(\vec{k}; L) \equiv \int_0^\infty dL G(\vec{k}; L) \exp -pL. \quad (8.37)$$

The derivation of the transformed matrix elements exploits the same techniques used recently by Spakowitz and Wang [10, 11, 12] to derive exact results for the WLC model. The extension of these results to the generalized theories considered here is straightforward. We shall therefore include only a brief derivation in the Appendix (Sect. 8.6.3) although we discuss the results in the main text.

### 8.3.1 The spatial distribution function

In force-extension and solution scattering experiments the tangents of the polymer are not directly probed by experiment; it is only the spatial distribution function rather than the tangent-spatial distribution function which is observed. We shall therefore introduce the spatial distribution function,  $K(\vec{X}; L)$ , which is defined as the probability density that a contour length  $L$  polymer has end displacement  $\vec{X}$ . The spatial distribution function is the tangent-spatial distribution function summed over the final tangent and averaged over the initial tangent:

$$K(\vec{X}; L) \equiv \frac{1}{4\pi} \int d\vec{t}_f d\vec{t}_i G(\vec{X}; \vec{t}_f, \vec{t}_i; L) = G_{0000}(\vec{X}; L), \quad (8.38)$$

where the last equality expresses the spatial distribution function in terms of a matrix element of the spatial propagator.

The Fourier-Laplace transform of this matrix element, a continued fraction, is computed in Eq. 8.78. For convenience, we write the explicit expression for the transformed spatial distribution function below

$$\tilde{K}(\vec{k}; p) = \frac{1}{p + h_0 + \frac{B_1 k^2}{p + h_1 + \frac{B_2 k^2}{\dots}}}, \quad (8.39)$$

where the  $h_l$  are the eigenvalues of the Hamiltonian operator, Eq. 8.22, and the  $B_n$  coefficients are defined as

$$B_n \equiv \frac{n^2}{4n^2 - 1}. \quad (8.40)$$

This expression is identical to that derived for the WLC model, except that the eigenvalues of the Hamiltonian operator,  $h_l$ , are those for a generic theory rather than the WLC eigenvalues. Otherwise the expression is unchanged.

The spatial distribution functions for the WLC and SEC models are plotted in Fig. 8.3.1 for several contour lengths. Again, what is striking about these results is the renormalization group flow towards the WLC model at long contour length. Although the two theories make dramatically different predictions for short-contour-length chains, the predictions converge at long contour length! We also explicitly show the convergence with the gaussian chain model at contours lengths much longer than the persistence length.

The loss of the short-length-scale structure of the theory can again be understood in terms of the eigenvalues of the Hamiltonian operator. The levels of the continued fraction (Eq. 8.41) can be understood as contributions from transitions to states of increasing angular quantum number  $l$ . But these “high angular momentum” states decay quickly due to their large eigenvalues of the Hamiltonian. (These eigenvalues of the Hamiltonian produce poles in the transformed propagator at large-magnitude, negative values of  $p$ .) We can also understand the irrelevance of “high angular momentum” states at long length in terms of the wave number  $k$ . Long length scales correspond to small wave number. The levels of the continued fraction are multiplied by  $k^2$  and are therefore suppressed for small wave number, implying that the “higher angular momentum” states have successively less relevance at long length scales.

It is also instructive to consider the long-length-scale limit of the spatial distribution function since we know that this limit is describe by the gaussian chain model. The long-length-scale limit corresponds to the limit of small  $k$  and contour dual number  $p$ . In this limit, the transformed spatial distribution function is

$$\tilde{K}(\vec{k}; p) \rightarrow \frac{1}{p + A_1 \vec{k}^2 / h_1}, \quad (8.41)$$

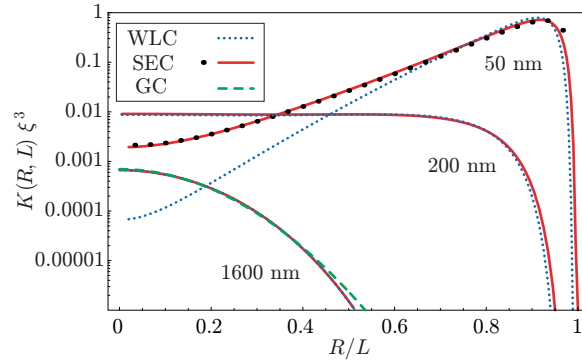


Figure 8.5: The spatial distribution for the WLC and SEC theories. All curves except the black dotted curve have been computed using the inverse transform technique. To reassure the reader of the validity of this technique, we have included a direct Monte Carlo integration for the shortest contour length SEC curve (red). We have chosen the contour lengths of the chains to illustrate two types of renormalization. At 50 nm for large deflection ( $R/L \sim 0$ ), The SEC (red) and WLC (blue) theories differ by two orders of magnitude. For a 200 nm contour length, SEC and WLC predict nearly identical distributions, but this distribution is clearly not Gaussian. For long contour length, these theories renormalize to the Gaussian chain model (green).

which is just a Gaussian distribution with a Kuhn length of twice the persistence length (Eq. 8.25) as we have already argued from computations of the mean-squared end-to-end distance and has also been shown schematically for the SEC model in Fig. 8.3.1.

### 8.3.2 Force-extension

The force-extension of single polymer molecules has recently been the subject of considerable experimental interest [5]. The experimental observable in these experiments, the extension of the polymer under an external force, can be directly computed from the spatial distribution function. Typically this force is applied to a bead, tethered to the polymer, using an optical or magnetic trap [23, 24, 5]. The restoring force against extension is entropic in nature (for inextensible polymers). This entropic force is induced by the reduction in the number of micro configurations available to the chain as the extension is increased. One of the triumphs of biophysics is the description of the extension of DNA by an external force by the WLC model and the precise agreement between experiment and theory as illustrated in Fig. 8.3.2. These experiments have been described as the strictest test of the WLC model [5]. How do other stiff polymer models compare? Can these models reproduce the precise fit to experiment? To answer these questions, we compute the force-extension for general models and explicitly compare the extension in the SEC and WLC models in Fig. 8.3.2.

The partition function for a polymer under a constant external tension is related to the Fourier

transform of the spatial distribution function via an analytic continuation of the wave number:

$$Z(\vec{f}) = \int d^D x K(\vec{x}; L) \exp[\vec{f} \cdot \vec{x}] \quad (8.42)$$

$$= \mathcal{L}_{L \rightarrow p}^{-1} \tilde{K}(i\vec{f}; p), \quad (8.43)$$

where  $\vec{f}$  is the external force or tension. The partition function can be computed numerically by truncating the continued fraction in Eq. 8.41 and applying the `InverseLaplaceTransform` function in *Mathematica*. The extension or mean end distance is computed in the usual way:

$$\langle x \rangle = \frac{\partial \log Z}{\partial f}. \quad (8.44)$$

The force-extension for the SEC and WLC models are compared in Fig. 8.3.2.

Despite the drastically different bending energy of the SEC model on short length scales, as illustrated in Fig. 8.2.2, thermal fluctuations disguise these differences and give rise to an extension almost identical to the WLC model. In retrospect, these results are hardly surprising. The theories are identical at small extension due to the renormalization group and at large extension due to inextensibility. Although, in principle, the high force limit is mathematically equivalent to probing short length scales—they are related by analytic continuation—these differences are not large enough to be experimentally observable. Physically, the rare high curvature bending regime, where the difference between the models is most pronounced, is further suppressed by the application of tension. For the study of DNA mechanics, force-extension measurements do probe the persistence length and the inextensibility of DNA, but these experiments do not efficiently probe DNA elasticity on the length scales of interest for many biological processes.

### 8.3.3 Structure factor

Another experimental observable used to characterize polymers is the structure factor, measured by static light scattering, small-angle X-Ray scattering, and neutron scattering experiments. Measurements of the structure factor can probe the polymer configuration on a wide range of length scales. Symbolically the structure factor is

$$g(\vec{k}) \equiv \frac{1}{L^2} \int_0^L ds ds' \left\langle e^{i\vec{k} \cdot [\vec{X}(s) - \vec{X}(s')]} \right\rangle, \quad (8.45)$$

where  $\vec{X}(s)$  is the position of the polymer at arc length  $s$  and we have included an extra factor of the polymer contour length in the denominator to make the structure factor dimensionless [10]. At high wave number, the structure factor is sensitive to short length scale physics, whereas the polymer length and radius of gyration can be measured at low wave number. The structure factor can be

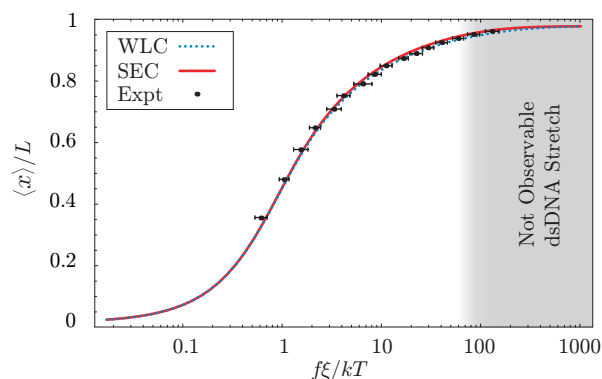


Figure 8.6: Force-extension for the WLC and SEC models compared with experimental measurements [24]. The WLC model was fit to the experimental data to determine the contour length and persistence length ( $\xi = 53$  nm). Despite the dissimilar short-length-scale tangent distribution function, the behavior of the polymer under an external force is nearly identical. For forces greater than 10 pN, the effects of DNA stretch becomes important, screening the entropic response.

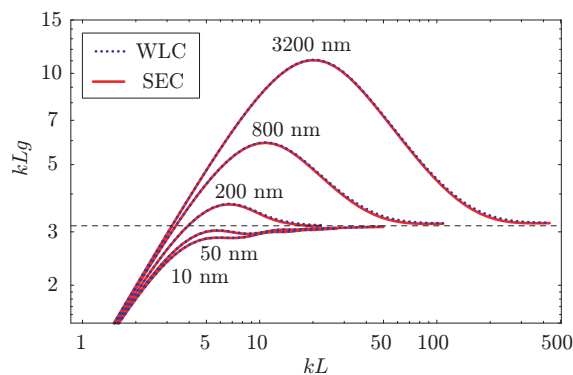


Figure 8.7: The structure factor for the SEC and WLC models. In the figure above, the structure factor, scaled by the wave number, is plotted for several contour lengths. The curves are nearly identical for the two theories since the structure factor is dominated by thermally accessible configurations. Although rare, high-curvature configurations are orders of magnitude more probable in the SEC than in the WLC theory, these configurations are still too rare to significantly affect the structure factor.

rewritten in terms of the transformed spatial distribution function

$$g(\vec{k}) = \frac{2}{L^2} \mathcal{L}_{L \rightarrow p}^{-1} \left[ \frac{\tilde{K}(\vec{k}; p)}{p^2} \right], \quad (8.46)$$

where  $\mathcal{L}^{-1}$  is the inverse Laplace transform which can be computed numerically. As we mentioned above, the leading-order contributions at small wave number are determined by the polymer length and the radius of gyration

$$Lg(k) = L(1 + \frac{1}{3}k^2 R_g^2 + \dots), \quad (8.47)$$

where we have temporarily restored the length dimension of  $g$ . At large  $k$ , both WLC and SEC are rod-like or straight which gives an asymptotic limit for large wave number

$$g(k) \rightarrow \frac{\pi}{Lk}, \quad (8.48)$$

since the chain is inflexible at short length scales.

The structure factor is compared for the SEC and WLC models in Fig. 8.3.3. Again we find that the two theories make nearly identical predictions. The reasoning is again similar to that explained for force-extension. The two theories make dramatically different predictions for rare, highly bent configurations but the structure factor is dominated not by these rare high curvature configurations but by typical thermal bending. We therefore find that the structure factor, like force extension, does not efficiently probe the high curvature statistics of the polymer.

### 8.3.4 Cyclization

The biochemical process of DNA cyclization is not in itself a process of particular biological importance<sup>2</sup> but cyclization experiments do provide a controlled, bulk experimental method for probing the probability of rare, highly-curved DNA configurations [6, 27, 7]. In these experiments, linear double stranded sequences with complementary single stranded ends are ligated into cyclized sequences or oligomers [28, 4, 25, 29, 30]. The cyclization reaction precedes via the capture of rare, thermally activated configurations and is thought to be very similar to the process by which many DNA-protein complexes are formed. Cyclization does have a very clear advantage over protein-induced DNA looping as a method of probing the high-curvature mechanics of DNA: the chain boundary conditions for cyclization (tangents aligned) are well known, in marked contrast to most DNA-protein complexes where the relevant chain boundary conditions must be determined.

The cyclization assay is performed under conditions such that ligation reaction samples the equilibrium populations of unligated cyclized and oligomerized polymers [4]. The ratio of the cyclization

---

<sup>2</sup>Bacteriophages are known to cyclize their genomes after ejection into a cell, but these genomes are typically many thousands of base pairs and the barrier to cyclization is purely entropic.

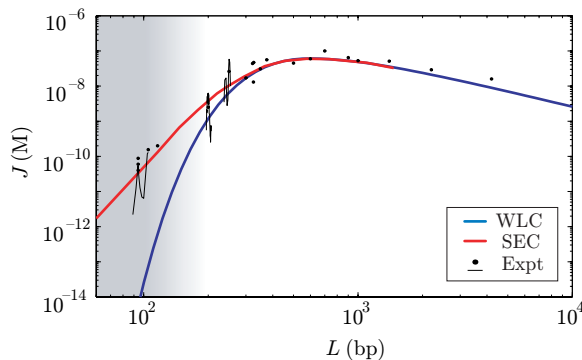


Figure 8.8: The cyclization  $J$  factor: probing the high-curvature chain statistics. In the figure above, the cyclization  $J$  factor is plotted for the WLC and SEC models and compared with experimental measurements [4, 25, 26, 6, 27]. The theoretical curves do not include the twist induced modulation visible in the three continuous sets of experimental data [25, 22, 26, 27]. The renormalization group predicts that the SEC model will be identical to the WLC model ( $\xi = 53$  nm) for long-contour-length sequences. But, for sequences shorter than two persistence lengths ( $\lesssim 200$  bp), the short-contour-length chain statistics become important and the SEC  $J$  factor diverges from the WLC prediction. In fact, for 94 bp sequences, the SEC  $J$  factor is three orders of magnitude larger than that predicted by the WLC model, roughly matching the  $J$  factors measured by Cloutier and Widom [6, 27]. Our theoretical results predict that this type of short-contour-length anomaly in the  $J$  factor is generic for sufficiently short sequences. But, the contour at which the WLC model fails is model dependent.

equilibrium constant ( $K_C$ ) to the dimerization equilibrium constant ( $K_D$ ) is called the Jacobson-Stockmayer factor [28] or  $J$  factor and is proportional to the tangent-spatial distribution function of the polymer [4, 29]

$$J \equiv K_C/K_D = 4\pi G(0; \vec{t}, \vec{t}; L) = \text{tr } \mathcal{G}(0; L), \quad (8.49)$$

where  $G$  is the tangent-spatial distribution function for end-to-end displacement 0 and aligned end tangents, for a contour length  $L$  polymer. The  $J$  factor can also be written as the trace of the spatial propagator, which is computed in Sect. 8.6.4. Physically, the  $J$  factor is proportional to the concentration of one end at the other with the correct (aligned) orientation for hybridization.

Our analysis neglects the condition that DNA twist must also be aligned, which requires the use of models including the twist degree of freedom. This additional constraint modulates the  $J$  factor with a 10.5 bp period equal to the helical repeat. Our interest here is in the value of the  $J$  factor averaged over a helical repeat for which the effects of twist can be roughly ignored [22].

We compare the cyclization  $J$  factor for the SEC and WLC theories in Fig. 8.3.4. The  $J$  factor for sequences with contour lengths greater than two persistence lengths have long been known to match the predictions of the WLC model [4, 25]. For sequences shorter than two persistence lengths, the figure illustrates the short-contour-length break down of the WLC model describing the chain statistics of the SEC model. For example, for contour lengths of roughly 0.6 persistence lengths, which correspond to loops with approximately the same radius of curvature as DNA bound to

histones in nucleosome complexes, the SEC model  $J$  factor is three orders of magnitude larger than predicted by the WLC model, in rough agreement with cyclization measurements of Cloutier and Widom [6], as illustrated in Fig. 8.3.4.

The qualitative picture illustrated in the Fig. 8.3.4 (the WLC model describes long-contour-length chain statistics, but fails at sufficiently short contour length) is the generic result from  $J$  factor computations in general models. These results were qualitatively predicted by the renormalization group ideas we have discussed throughout the paper. From an experimental perspective, the cyclization assay is clearly a powerful technique for probing the short-contour-length chain statistics of DNA. In particular, this technique has very clear advantages over force-extension and solution-scattering experiments since (i) cyclization assays probe the chain statistics of DNA in a way that is qualitatively similar to biological DNA looping applications and (ii) cyclization experiments are incredibly sensitive to the differences between models at short contour length. The main shortcoming of cyclization assays is that it is difficult to determine the chain statistics from cyclization experiments alone.

## 8.4 Discussion

In Sect. 8.2.2, we introduced the SEC model as a toy model for DNA bending, motivated by AFM measurements of the chain statistics on short length scales. We proceeded to show that this simple model exhibited the long-length-scale chain statistics of the WLC model, despite dramatically increasing the probability of high-curvature configurations. In particular, we demonstrated that the SEC model predicted a cyclization  $J$  factor in agreement with the measurements of Cloutier and Widom [6]. More generally, we showed that this type of short-length-scale anomaly was generic in generalized stiff chain models; but the length scale at which this failure occurs is model dependent, not universal.

Unfortunately, the experimental picture of DNA bending on short length scales is still somewhat muddled. Vologodskii and coworkers have recently made measurements which suggest that the experiments of Cloutier and Widom are flawed [7]. Their measurements suggest that the  $J$  factor is that predicted by the WLC model, at least down to a contour length of 100 bp. Widom and coworker have also recently repeated their own measurements and have confirmed their previous results. At the moment, it is difficult to reconcile these two conflicting experiments experiments. (Please see the extensive discussion in Sect. 7.3.4.) In this paper, we have argued that the failure of the WLC model at short length scales is generic for stiff polymers. Certainly the renormalization group predicts that WLC chain statistics are universal for stiff polymers at long length scales. On sufficiently short length scales, it is also clear that the WLC model fails to capture the statistics of the complicated macromolecular structure of DNA. But at what length scale does the WLC model begin to capture

the statistics of DNA quantitatively? This length scale is determined by the underlying, molecular structure of DNA. In our description of generalized theories, this length scale is integrally related to the link length parameter.

Until now, we have treated the link length as a parameter of the model without discussing its physical significance. In order to understand the role of the link length, it is useful to return to the equation describing the tangent distribution of the polymer (Eq. 8.24)

$$\mathcal{G}(L) \equiv \exp -\mathcal{H}L, \quad (8.50)$$

which we rewrite here for convenience. This equation gives a recipe for computing the tangent distribution function for any contour length, based on a fundamental tangent distribution function of a contour length  $\ell$  chain. But, this equation can also be evaluated for contour lengths shorter than the link length, violating the spirit of the renormalization group. These distribution functions, computed for contour lengths shorter than the link length, are not physically meaningful. On shorter length scales, the polymer may not even be described by a theory which meets the assumptions we made initially: (i) isotropic, (ii) homogeneous, and (iii) local. In fact, Eq. 8.29 implies that if the stiff polymer were described by a theory satisfying (i)-(iii) at arbitrarily short length scales and the bending energy was everywhere finite, the chain statistics would be described by the WLC theory! It is precisely because at least one of these assumptions breaks down on short length scales that polymers are not exactly described by the WLC model.

Determining the length scale on which the WLC theory breaks down is therefore related to determining on what length scale our assumptions fail—this is the fundamental length scale. On length scales sufficiently long compared with this fundamental length scale, the WLC model is applicable. The general models discussed in the text provide a framework that is more generally applicable than the WLC model. These models can describe the chain statistics before the WLC model becomes applicable.

Is the SEC model of DNA plausible? The SEC model essentially implies that the fundamental length scale is on order 5 nm. (If it were significantly smaller, the chain statistics at the 5 nm length scale would be described by the WLC model.) Such a proposal is not ridiculously far fetched since our assumption of homogeneity may fail. The link length, 5 nm, is not significantly longer than the helical repeat of DNA. It has been proposed, for instance, that DNA may bend preferentially into the minor groove and there is just one such location with the correct orientation every helical repeat [2, 31]. On the other hand, sequence induced heterogeneity is probably fairly well averaged over the 5 nm length scale since this corresponds to nearly 15 bp. Failure of the locality assumption (iii), the break down of the nearest neighbor interaction on these length scales, seems unlikely since it is difficult to understand such a phenomena without bending-induced, long-range structural changes.

Such structures have not been observed in the crystal structures of highly bent DNA on the 5nm length scale. Based on these theoretical and structural arguments alone, failure of the WLC model on these length scales, while possible, is not imperative.

*Note to the reader:* Please see the newly written experimental discussion in Sect. 7.3.4.

### 8.4.1 Unfinished business

For many biological applications of DNA chain statistics, the twist degrees of freedom are also of great importance. For instance for DNA looping, moving an operator (the DNA binding sequence) a few base pairs can change the looping probability by an order of magnitude [32]. This dramatic, short-contour-length dependence arises from the necessity of bring the DNA operator into twist registry with the binding site. The twist degree of freedom of DNA has also been described by a fluctuating elastic rod, the Helical Wormlike Chain model (HWLC) [22]. At long length scales, this modified WLC model has successfully described the twist dependence of DNA. But, there is mounting evidence that the HWLC model breaks down. Bryant *et al.* [33] have demonstrated that the restoring torque generated by twisted DNA saturates for high twist densities, implying that the linear elastic model breaks down for highly twisted DNA. Cloutier and Widom have also shown that the twist-induced modulation of the cyclization  $J$  factor is less for short sequences than predicted by the HWLC model [27]. Although the bending of DNA for small twist densities may be adequately described by the HWLC model, a generalized model of DNA, including twist, may be necessary to describe the chain statistics of short sequences of looped DNA which are not naturally in twist registry when bound. Such generalized models are in principle a straightforward extension of the theory presented in this paper and the exact results for the HWLC model that have recently been derived by Spakowitz [12].

## 8.5 Conclusion

In this paper, we have developed a class of generalized stiff polymer models in which the bending energy density is an arbitrary function of curvature. To analyze the chain statistics of these models, we develop a formalism which is analogous to the techniques used for describing the WLC model. We demonstrate that the statistics of these general models are described by the WLC model at long contour length, as predicted by the renormalization group. At short length scales, we show that the predictions of these models can be dramatically different from the WLC model. Of particular importance, we compute near-exact expressions for the transformed spatial and tangent-spatial distribution functions with a method analogous to that recently exploited to find exact results for the WLC model. These generalized models provide an explicit example of a non-renormalizable model which is nearly exactly solvable. We exploit these general theoretical results to compute several

important experimental observables: force-extension, the structure factor, and the cyclization  $J$  factor. We explicitly perform these computations for a toy model of DNA bending, the Sub-Elastic Chain (SEC) model. The predictions of this model are essentially indistinguishable from the WLC model for force-extension, solution scattering, and long-contour-length cyclization measurements, despite the dramatic differences between the bending energies of the two models on short length scales. For short-contour-length cyclization experiments, general models generically predict that the WLC model fails. In particular we compute the  $J$  factor for the SEC model and show that this model could account for the anomalously large cyclization  $J$  factor measured by Widom and Cloutier [6]. We expect these generalized models to be widely applicable for describing the high-curvature statistics of other semiflexible polymers.

# Bibliography

- [1] Bruce Alberts, Dennis Bray, Julian Lewis, Martin Raff, Keith Roberts, and James D. Watson. *Molecular Biology of the Cell*. Garland Publishing, New York, NY, 3rd edition, 1994. [1](#), [11](#), [12](#), [13](#), [16](#), [97](#), [98](#), [100](#), [101](#), [116](#), [167](#), [179](#)
- [2] Jonathan Widom. Role of DNA sequence in nucleosome stability and dynamics. *Quarterly Reviews of Biophysics*, 34(3):269–324, 2001. [100](#), [105](#), [116](#), [118](#), [179](#), [181](#), [201](#)
- [3] Karsten Rippe, Peter R. von Hippel, and J org Langowski. Action at a distance: DNA-looping and initiation of transcription. *Trends Biochem. Sci.*, 20(12):500–506, 1995. [2](#), [102](#), [110](#), [114](#), [118](#), [124](#), [152](#), [179](#)
- [4] D. Shore, J Langowski, and R. L. Baldwin. DNA flexibility studied by covalent closure of short fragments into circles. *Proc. Natl. Acad. Sci. USA*, 170:4833–4837, 1981. [110](#), [112](#), [113](#), [115](#), [117](#), [148](#), [173](#), [179](#), [198](#), [199](#)
- [5] C. Bustamante, S. B. Smith, J. Liphardt, and D. Smith. Single-molecule studies of DNA mechanics. *Curr. Opin. Struct. Biol.*, 10:279–285, 2000. [123](#), [179](#), [195](#)
- [6] T. E. Cloutier and J. Widom. Spontaneous sharp bending of double-stranded DNA. *Molecular Cell*, 14(3):355–362, 2004. [5](#), [6](#), [7](#), [96](#), [97](#), [110](#), [114](#), [116](#), [117](#), [118](#), [124](#), [145](#), [148](#), [152](#), [164](#), [169](#), [172](#), [173](#), [174](#), [179](#), [181](#), [185](#), [198](#), [199](#), [200](#), [203](#)
- [7] Quan Du, Chaim Smith, Nahum Shiffeldrim, Maria Vologodskaia, and Alexander Vologodskii. Cyclization of short DNA fragments and bending fluctuations of the double helix. *Proc Natl Acad Sci USA*, 102(15):5397–402, 2005. [172](#), [173](#), [179](#), [181](#), [198](#), [200](#)
- [8] Michael Fisher. Renormalization group theory: Its basis and formulation in statistical physics. *Rev. Mod. Phys.*, 70:653–681, 1998. [168](#), [180](#), [183](#)
- [9] John van Noort, Thijn van der Heijden, Martijn de Jager, Claire Wyman, Roland Kanaar, and Cees Dekker. The coiled-coil of the human Rad50 DNA repair protein contains specific segments of increased flexibility. *Proceeding of the National Academy of Science USA*, 100(13):7581–7586, 2003. [167](#), [168](#), [172](#), [180](#), [184](#), [185](#), [186](#)

- [10] A. J. Spakowitz and Z.-G. Wang. Exact results for a semiflexible polymer chain in an aligning field. *Macromolecules*, 37:5814–5823, 2004. [108](#), [133](#), [138](#), [140](#), [144](#), [159](#), [169](#), [180](#), [193](#), [196](#), [211](#)
- [11] A. J. Spakowitz and Z.-G. Wang. End-to-end distance vector distribution with fixed end orientations for the Wormlike Chain model. *Phys. Rev. E*, 2005. In preparation. [108](#), [169](#), [180](#), [192](#), [193](#), [211](#), [212](#)
- [12] A. J. Spakowitz. 2005. In preparation. [169](#), [180](#), [193](#), [202](#)
- [13] S. Stepanow and G. M. Schutz. The distribution function of a semiflexible polymer and random walks with constraints. *Europhys. Lett.*, 60(4):546–551, 2002. [133](#), [138](#), [140](#), [180](#)
- [14] P. A. Wiggins, P. C. Nelson, and R. Phillips. Exact theory of kinkable elastic polymers. *Phys. Rev. E*, 71(021909), 2005. [123](#), [164](#), [184](#)
- [15] J. Yan and J. F. Marko. Localized single-stranded bubble mechanism for cyclization of short double helix DNA. *Phys. Rev. Lett.*, 93, 2004. [173](#), [184](#), [212](#)
- [16] R. L. Fosdick and R. D. James. The elastica and the problem of the pure bending for a non-convex stored energy function. *J. Elast.*, 11:165–186, 1981. [165](#), [184](#)
- [17] Jan Bednar, Patrick Furrer, Vsevolod Katritch, Alicja Z Stasiak, Jacques Dubochet, and Andrzej Stasiak. Determination of DNA persistence length by cryo-electron microscopy. Separation of static and dynamic contributions to the apparent persistence length of DNA. *Journal of Molecular Biology*, 254:579–594, 1995. [118](#), [167](#), [184](#)
- [18] Claudio Rivetti, Martin Guthold, and Carlos Bustamante. Scanning force microscopy of DNA deposited onto mica: Equilibration versus kinetic trapping studied by statistical polymer chain analysis. *J. Mol. Biol.*, 264(5):919–932, 1996. [167](#), [185](#)
- [19] J. Yan, R. Kawamura, and J. F. Marko. preprint, 2004. [185](#), [186](#), [187](#)
- [20] J. J. Sakurai. *Modern Quantum Mechanics*. Addison-Wesley, Reading, Massachusetts, 2nd edition, 1994. [107](#), [131](#), [186](#), [187](#), [188](#), [207](#), [208](#)
- [21] M. Doi and S. F. Edwards. *The Theory of Polymer Dynamics*. Oxford University Press, 1986. [99](#), [190](#)
- [22] H. Yamakawa. *Helical Wormlike Chains in Polymer Solutions*. Springer, Berlin, 1997. [5](#), [104](#), [108](#), [109](#), [113](#), [123](#), [125](#), [137](#), [146](#), [160](#), [164](#), [192](#), [199](#), [202](#)
- [23] C. Bustamante, J. F. Marko, E. D. Siggia, and S. Smith. Entropic elasticity of lambda phage DNA. *Science*, 265:1599–1600, 1994. [5](#), [96](#), [195](#)

- [24] T. R. Strick, V. Croquette, and D. Bensimon. Homologous pairing in stretched supercoiled DNA. *Proc. Natl. Acad. Sci. USA*, 95:10579–10583, 1998. [195](#), [197](#)
- [25] D. Shore and R. L. Baldwin. Energetics of DNA twisting 1. Relation between twist and cyclization probability. *Journal of Molecular Biology*, 170(4):957–981, 1983. [110](#), [113](#), [117](#), [148](#), [173](#), [198](#), [199](#)
- [26] M. Vologodskaja and A. Vologodskii. Contribution of the intrinsic curvature to measured DNA persistence length. *J. Mol. Biol.*, 317(2):205–213, 2002. [117](#), [118](#), [148](#), [199](#)
- [27] T. E. Cloutier and Jonathan Widom. DNA twisting flexibility and the formation of sharply looped protein–DNA complexes. *Proc. Natl. Acad. Sci. USA*, 102:3634–3650, 2005. [173](#), [198](#), [199](#), [202](#)
- [28] H. Jacobson and W. H. Stockmayer. Intramolecular reaction in polycondensations 1. The theory of linear systems. *J. Chem. Phys.*, 18(12):1600–1606, 1950. [110](#), [111](#), [146](#), [198](#), [199](#)
- [29] J. Shimada and H. Yamakawa. Ring-closure probabilities for twisted wormlike chains – applications to DNA. *Macromolecules*, 17:689–698, 1984. [113](#), [123](#), [149](#), [198](#), [199](#)
- [30] P. J. Hagerman. Flexibility of DNA. *Annu Rev Biophys Biophys Chem*, 17(0883-9182):265–86, 1988. [198](#)
- [31] Timothy J. Richmond and Curt A. Davey. The structure of DNA in the nucleosome core. *Nature*, 423:145–150, 2003. [165](#), [201](#)
- [32] J. Muller, S. Oehler, and B Muller-Hill. Repression of lac promoter as a function of distance, phase and quality of an auxiliary lac operator. *J. Mol. Biol.*, 257:21–29, 1996. [2](#), [102](#), [103](#), [118](#), [124](#), [152](#), [202](#)
- [33] Zev Bryant, Michael D. Stone, Jeff Gore, Steven B. Smith, Nicholas R. Cozzarelli, and Carlos Bustamante. Structural transitions and elasticity from torque measurements on DNA. *Nature*, 424:338–341, 2003. [202](#)

## 8.6 Appendix

### 8.6.1 Explicit expressions for $g_l$

It is straightforward to determine the  $g_l$  eigenvalues of any propagator using the orthonormal eigenbasis of the angular momentum representation. In two dimensions, the  $g_l$  are

$$g_l = \int_{-\pi}^{\pi} d\theta g(\vec{t}(\theta); \vec{e}_z) \exp i l \theta, \quad (8.51)$$

where  $\theta$  is defined as the angle away from the  $z$  axis:  $\vec{t}(0) = \vec{e}_z$ . In three dimensions, the  $g_l$  are

$$g_l = \int d^2\vec{t} g(\vec{t}(\theta); \vec{e}_z) P_l(\vec{t} \cdot \vec{e}_z), \quad (8.52)$$

where the  $P_l$  are the Legendre Polynomials and  $\cos \theta = \vec{t} \cdot \vec{e}_z$ .

### 8.6.2 Stiff polymer limit

In this section, we show that a narrowly distributed fundamental tangent distribution function generically implies WLC statics at long contour length. In dimension  $D$ , this calculation, though straight forward, requires some technical mathematics, but these technical details are not important for the interpretation of the result.

We begin the derivation with the definition of the  $l$ th moment of the tangent distribution function expressed in terms of the propagator Eq. 8.18

$$g_l = \langle l\mathbf{m} | \mathcal{G} | l\mathbf{m} \rangle, \quad (8.53)$$

where rigid-body-rotational invariance implies that  $g_l$  is independent of  $\mathbf{m}$ . We insert two complete sets of states into the tangent representation

$$g_l = \int d\vec{t} d\vec{t}' \langle l\mathbf{m} | \vec{t} \rangle \langle \vec{t} | \mathcal{G} | \vec{t}' \rangle \langle \vec{t}' | l\mathbf{m} \rangle, \quad (8.54)$$

where we can now replace the matrix element of the propagator with the fundamental tangent distribution function  $g(\vec{t}; \vec{t}')$  (Eq. 8.12).

Remember that this function depends only on the relative deflection angle of the tangents. We therefore replace the integral over the second tangent with an integral over rotation matrices,  $\mathcal{R}$ , and make the substitution  $\vec{t}' \equiv \mathcal{R}\vec{t}$ :

$$g_l = \int d\vec{t} d\mathcal{R} \left| \frac{d\vec{t}'}{d\mathcal{R}} \right| \langle l\mathbf{m} | \vec{t} \rangle g(\vec{t}; \mathcal{R}\vec{t}) \langle \vec{t} | \mathcal{D}_{\mathcal{R}}^\dagger | l\mathbf{m} \rangle, \quad (8.55)$$

where we represent the change in measure symbolically and we have introduced the rotation operator [20]

$$\mathcal{D}_{\mathcal{R}} | \vec{t} \rangle \equiv | \mathcal{R}\vec{t} \rangle. \quad (8.56)$$

Our interest is in the case where the tangent distribution function is narrowly distributed. We shall therefore expand the rotation operator,  $\mathcal{D}$ , with respect to the rotation angles which we shall assume are small. The rotation operator can be expanded in terms of these angles and the rotation

generators [20]

$$\mathcal{D}_{\mathcal{R}} = \exp -i\theta_{ij}\mathcal{L}_{ij} \quad (8.57)$$

$$= 1 - i\theta_{ij}\mathcal{L}_{ij} - \frac{1}{2}\theta_{ij}\mathcal{L}_{ij}\theta_{mn}\mathcal{L}_{mn} + \dots, \quad (8.58)$$

where the  $\theta_{ij} = -\theta_{ji}$  are the components of the rotation angle which multiply the generators of rotations in the  $ij$  plane.

To evaluate the integral over the rotation matrices, we must now choose a set of  $\theta$ 's which give a single cover of the tangent space. Since  $g(\vec{t}; \mathcal{R}\vec{t})$  is independent of  $\vec{t}$ , it is convenient to temporally assume a coordinate system in which  $\vec{t}$  is in the direction of the  $D$  axis. (We shall return to the unrotated frame before performing the integral over  $\vec{t}$ .) In this new coordinate system, it is convenient to use the cover generated by the coordinates  $\{\theta_{Di}\}_{1..D-1}$  while setting all other  $\theta$ 's to zero.

We shall denote the average taken with respect to the distribution function  $\langle \rangle$ . Due to rigid-body-rotational invariance around the  $D$  axis,

$$\langle \theta_{iD} \rangle = 0, \quad (8.59)$$

$$\langle \theta_{iD}\theta_{nD} \rangle = \langle \theta^2 \rangle \delta_{in}/(D-1), \quad (8.60)$$

where  $\theta^2 \equiv \theta_{iD}^2$  is the total deflection angle.

The remaining matrix elements can be put in a coordinate invariant form

$$\langle lm | \vec{e}_D \rangle \langle \vec{e}_D | \mathcal{L}_{Di}\mathcal{L}_{Di} | lm \rangle = \langle lm | \vec{e}_D \rangle \langle \vec{e}_D | \mathcal{L}^2 | lm \rangle \quad (8.61)$$

since the added terms in the Casimir operator,  $\mathcal{L}^2$ , are zero on  $|\vec{e}_D\rangle$ . We can now reassume the unrotated coordinate system by setting  $\vec{e}_D = \vec{t}$ .

After integrating over the complete set of tangent vectors, the resulting moment is

$$g_l = 1 - \frac{1}{2}(D-1)^{-1} \langle \theta^2 \rangle \langle l\mathbf{m} | \mathcal{L}^2 | l\mathbf{m} \rangle + \mathcal{O}(\mathcal{L}^4 \langle \theta^4 \rangle). \quad (8.62)$$

Since this expression is only correct to  $\mathcal{O}(\theta^4)$ , it is convenient to replace  $\frac{1}{2}\theta^2$  with  $1 - \cos\theta$ . We can now use the definition of the persistence length given in Eq. 8.25 to eliminate the dependence on  $\langle \cos\theta \rangle$ :

$$g_l = 1 - \frac{\ell}{2\xi} \langle l\mathbf{m} | \mathcal{L}^2 | l\mathbf{m} \rangle + \mathcal{O}(\mathcal{L}^4 \ell^2 / \xi^2). \quad (8.63)$$

Finally, we reconstruct the propagator from its moments

$$\mathcal{G} = \sum_{l, \mathbf{m}} g_l |l \mathbf{m}\rangle \langle l \mathbf{m}| = 1 - \frac{\ell}{2\xi} \mathcal{L}^2 + \mathcal{O}(\mathcal{L}^4 \ell^2 / \xi^2), \quad (8.64)$$

which completes the derivation. This result is discussed in Sect. 8.2.7.

### 8.6.3 The transformed spatial propagator

To derive closed form expressions for the spatial propagator, we Fourier Transform the spatial propagator over the relative displacement,  $\vec{X}$ . In particular, we consider the Fourier Transform of Eq. 8.34 since in Fourier space, the spatial convolutions are simply products:

$$\tilde{\mathcal{G}}(\vec{k}; L + L') = \tilde{\mathcal{G}}(\vec{k}; L) \tilde{\mathcal{G}}(\vec{k}; L'). \quad (8.65)$$

We shall choose the coordinate system so  $\vec{k}$  is in the z direction.

We now wish to use this composition property of the spatial propagator to write a differential equation for  $\mathcal{G}$ . We will therefore consider  $\mathcal{G}$  for a differential arc length  $dL$  and then expand the Fourier Transform of Eq. 8.32 for arc length  $dL$ :

$$\tilde{\mathcal{G}}(\vec{k}; dL) = \mathcal{I} - \mathcal{A}dL, \quad (8.66)$$

where  $\mathcal{I}$  is the identity operator and  $\mathcal{A} \equiv \mathcal{H} + ik \cos \Theta$  where  $\Theta$  takes its canonical meaning in spherical coordinates:  $\cos \Theta = \vec{t} \cdot \hat{z}$ . Substituting this expression into Eq. 8.65, we can write a differential equation for  $\tilde{\mathcal{G}}$ :

$$\frac{d}{dL} \tilde{\mathcal{G}}(k; L) = -\mathcal{A} \tilde{\mathcal{G}}(k; L). \quad (8.67)$$

It is now convenient to make a Laplace transform over the arc length where  $p$  is the arc length Laplace conjugate. After solving for the propagation operator, we have an operator equation for the Laplace-Fourier Transform of the spatial propagator:

$$\tilde{\mathcal{G}}(k; p) = \{p\mathcal{I} + \mathcal{A}(k)\}^{-1} = \{p\mathcal{I} + \mathcal{H} + ik \cos \theta\}^{-1}, \quad (8.68)$$

but this expression is not explicit since it is written in terms of the inverse of an infinite dimensional operator.

We can express  $\cos \Theta$  in the angular momentum basis. It is most convenient to define a set of ladder operators:

$$\cos \theta = a_+ + a_-, \quad (8.69)$$

$$\begin{aligned}
l \text{---} &= p + h_l \\
\begin{array}{c} l+1m \\ \vdots \\ lm \end{array} \text{---} &= ikA_{ll+1m} \\
\begin{array}{c} \vdots \\ l \end{array} \text{---} &= \tilde{G}_{lm}^+ \\
\begin{array}{c} \vdots \\ lm \end{array} \text{---} &= \begin{array}{c} lm \text{---} \\ + \begin{array}{c} l+1m \\ \vdots \\ lm \end{array} \text{---} \\ + \begin{array}{c} l+1m \\ \vdots \\ lm \end{array} \text{---} \\ + \dots \end{array}
\end{aligned}$$

Figure 8.9: Diagrammatic rules for the propagator: diagrams and their algebraic representations. Connected diagrams represent the products of their algebraic representation. The matrix element of the spatial propagator  $\tilde{G}_{l+1m}^+$  is the sum of all diagrams which begin at state  $lm$  and end at state  $l'm$  with an arbitrary number of intermediate transitions. Horizontal lines represent propagation. Vertical lines represent transitions induced by the wave number.  $\tilde{G}_{lm}^+$  is the matrix element of the spatial propagator where transitions to states with total angular momentum  $l-1$  or smaller are forbidden. This matrix element is represented by the line with ellipses, representing all transitions to states with higher  $l$ , and can be defined recursively in terms of  $\tilde{G}_{l+1m}^+$  as illustrated above. The definition of  $\tilde{G}_{lm}^-$  is analogous, but it is the sum of all diagrams with transitions to states with total angular quantum number  $l$  and smaller.

where the ladder operators are defined

$$a_+ \equiv \sum_{l=0}^{\infty} \sum_{m=-l}^l A_{l+1,l,m} |l+1, m\rangle \langle l, m|, \quad (8.70)$$

$$a_- \equiv \sum_{l=0}^{\infty} \sum_{m=-l}^l A_{l,l+1,m} |l, m\rangle \langle l+1, m|, \quad (8.71)$$

and where the  $A_{l,l+1,m}$  are:

$$A_{l,l+1,m} = A_{l+1,l,m} = \sqrt{\frac{(l-m+1)(l+m+1)}{(2l+1)(2l+3)}}. \quad (8.72)$$

The ladder operators have the property that they increase (decrease) the total momentum quantum number of a state by plus (minus) one.

#### 8.6.4 Matrix elements of the spatial propagator

In this section, we will give explicit expressions for the matrix elements of the transformed spatial propagator. The Hamiltonian is diagonal in the angular representation, so it is convenient to factor the spatial propagator into diagonal and nondiagonal factors:

$$\tilde{\mathcal{G}}(k; p) = [\mathcal{I} + \{p\mathcal{I} + \mathcal{H}\}^{-1} ik(a_+ + a_-)]^{-1} \{p\mathcal{I} + \mathcal{H}\}^{-1}, \quad (8.73)$$

and expand it in a power series

$$\tilde{\mathcal{G}}(k; p) = \sum_{n=0}^{\infty} [-ik\{p\mathcal{I} + \mathcal{H}\}^{-1}(a_+ + a_-)]^n \{p\mathcal{I} + \mathcal{H}\}^{-1}. \quad (8.74)$$

As a first step, we will compute a diagonal matrix element:

$$\tilde{G}_{lmlm} = \langle l \ m | \tilde{\mathcal{G}}(k; p) | l \ m \rangle. \quad (8.75)$$

Computing these matrix elements is achieved by grouping the infinite set of terms in Eq. 8.74 into sub sets which can be summed exactly [10].

We introduce  $\tilde{G}_{l'm'l'm}^+$  which is the matrix element of the spatial propagator, a subset of the terms in Eq. 8.74, in which there are only transitions to states with total momentum  $l = l'$  or greater [10]. This matrix element can be defined recursively since only transitions to adjacent states are defined. The matrix element is the sum over  $n$  of the matrix elements with  $n$  transition to and from the  $l \geq l' + 1$  states, which can be written in terms of  $\tilde{G}_{l'+1ml'+1m}^+$ . The terms of this matrix element, a geometric series, can be summed exactly [11]:

$$\tilde{G}_{lmlm}^+ = \frac{1}{p + h_l} \sum_{n=0}^{\infty} \left[ \frac{-k^2 A_{l,l+1,m}^2 \tilde{G}_{l+1ml+1m}^+}{p + h_l} \right]^n = \left[ p + h_l + k^2 A_{l,l+1,m}^2 \tilde{G}_{l+1ml+1m}^+ \right]^{-1}, \quad (8.76)$$

This sum is pictured schematically in Fig. 8.6.4.

Similarly, we can define  $\tilde{G}_{l'm'l'm}^-$  which is the matrix element of the propagation operator which allows transitions to states with total momentum  $l = l'$  or less:

$$\tilde{G}_{lmlm}^- = \left[ p + h_l + k^2 A_{l,l-1,m}^2 \tilde{G}_{l-1ml-1m}^- \right]^{-1}. \quad (8.77)$$

In terms of  $G^\pm$  we can now define the matrix element without transition restrictions by grouping the transitions into sets that do not cross  $l = l'$ . These sets can be written in terms of the matrix elements of  $\mathcal{G}^\pm$  and then summed in a geometric series [11]:

$$\tilde{G}_{lmlm} = \left[ p + h_l + k^2 A_{l,l+1,m}^2 \tilde{G}_{l+1ml+1m}^+ + k^2 A_{l,l-1,m}^2 \tilde{G}_{l-1ml-1m}^- \right]^{-1}. \quad (8.78)$$

The diagonal matrix element computed above is sufficient for describing many observables of phenomenological interest. Note that the only difference between this expression and the WLC expression is that the eigenvalues of the Hamiltonian operator have changed.

For some applications we will want completely general matrix elements  $\tilde{G}_{lml'm'}$ . We can again define these general matrix elements in terms of the recursive definitions of  $G^\pm$ . Again, the trick to summing the terms is grouping them. In this general case, there are many equivalent ways of

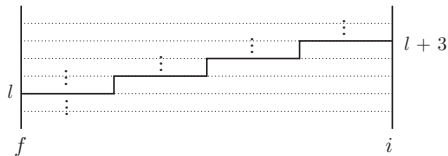


Figure 8.10: General matrix elements. A diagram of the sum for the matrix element  $\tilde{G}_{lm+l+nm} = \tilde{G}_{l+nmlm}$ . To compute the matrix element, we group the terms by the location of the first steps from  $l+n$  to  $l+n-1$  and from  $l+n-1$  to  $l+n-2$  etc. In the diagram, these steps are represented by the vertical lines. We use the  $\mathcal{G}^+$  operator to sum over all possible diagrams with upward transitions between these steps. These upward transitions are represented by the ellipses. We multiply by the transition matrix element for each of the vertical lines. After we reach  $l$  for the first time we allow all transitions up or down. This enumeration counts each contributing diagram once but this recipe is not unique.

achieving this grouping. See the figure for an explanation of the set grouping. The matrix element can be written [11]

$$\tilde{G}_{l+nmlm'} = \tilde{G}_{lm+l+nm'} = \delta_{m-m'} \tilde{G}_{lm} \prod_{q=1}^n -ik A_{l+q-1, l+q, m} \tilde{G}_{l+qml+qm}^+ \quad (8.79)$$

We have now explicitly solved for spatial propagator having written expressions for all the matrix elements.

### 8.6.5 The computation of spatial distributions

In the last section, we have discussed near-exact expressions for the Fourier-Laplace transformed spatial and tangent-spatial distribution functions. Exact closed-form expressions for these functions are unknown and we must invert the transforms numerically to compute the distribution functions.

For contour lengths of about two persistence lengths and above, it is convenient to directly invert the transforms numerically. Typically, we cut off the continued fraction at  $l = 15$  and then use the `InverseLaplaceTransform` function in *Mathematica*. We then integrate numerically to invert the Fourier transform.

For contour lengths on order a persistence length and shorter inverting the transformed expressions is of very little practical convenience. The continued fraction in increasing momentum is essentially an expansion around weak end-tangent correlation. For contour lengths shorter than a persistence length, a larger  $l$  cutoff is required, significantly slowing the numerical inversions. In addition, the numerical integration over the wave number becomes impractical since the numerical integrations must be extended to very a large cutoff momentum. These convergence issues are not unique to the continued fraction approach. For example, the transfer matrix approach is plagued by similar shortcomings, requiring a considerable amount of numerical heroics at short contour length [15].

We dispense with such heroics here for another much simpler although less elegant solution in the form of direct Monte Carlo integrations. Monte Carlo integration in the short-contour-length regime is (i) numerically more efficient than direct inversion, (ii) requires very minimal implementation, and (iii) serves as a useful check of our theoretical results. These checks appear few places explicitly in the paper since the agreement between these two methods is excellent and the focus of this paper is physics rather than numerical computations. The theoretical curves for the looping  $J$  factor and cyclization  $J$  factor contain both inversion and Monte Carlo computations.

## Appendix A

# Appendix

### A.1 AFM Tracing Code

```

%%%%%%%%%%%%%%%%%%%%%%%%%%%%%%%%%%%%%%%%%%%%%%%%%%%%%%%%%%%%%%%%%%%%%%%%
%
%           Function TracerPicker
%           (Matlab)
%
% TracerPicker is an automated code for tracing polymer molecules
% from
% AFM traces. The user clicks on the start of the molecule and the
% a second time to give the initial guess for the direction of the
% polymer. Finally the user picks and end point at which to stop
% the trace. The program then traces the polymer based on fitting
% the height. The details are explained in more detail below. The
% return value is an array of traced points seperated by a user
% defined spacing.
%
% 3/16/2005
% Cees Dekker (Delft) and Rob Phillips (Caltech) Groups
%
% written by:
% -----
% Paul Wiggins
% Thijn van der Heijden
% Fernando Moreno
%
%%%%%%%%%%%%%%%%%%%%%%%%%%%%%%%%%%%%%%%%%%%%%%%%%%%%%%%%%%%%%%%%%%%%%%%%

function [ r, t, theta ] = tracer6( rawdata );

% choose the step size in nm and then convert to pixels by
% multiplying by 512/1000 to give the step size in pixels

stepsize = 2.5/(1000/512);

%stepsize = 5/(1000/512);

```

```

% choose the radius (in pixels) of the region explored normal
% to the tangent in order to compute the the center of mass.
scansize = 3;

% the number of divisions of the region defined above. The data
% is interpolated at scannum points on each side of the guess to
% total distance scansize pixels.
scannum = 10;

% The code ends when the trace comes within endradius pixels of
% the end point input by the user.
endradius = 1.5*stepsize;

% max number of point traced
maxiter = 1000;

% open a figure inwhich to plot the density plot to be tracked by
% tracer5 then clear it and set the hold
figure(1);
clf;
hold on;

% we want to plot the density plot so that the pixels are draw
% centered around integer values... This command makes a mesh on which
% to plot the x height
junk = (1:512)-.5;
[Xb Yb] = meshgrid(junk,junk);

% density plot of heights
pcolor(Xb,Yb,rawdata);

% set the shading to avoid facets which are default. Facets make the
% image black since there are so many data points
shading flat;

% set the dynamic range of the data... in nm to be colored by p color
caxis([0,0.9]);

% make an array in which to store the traced data points
r = zeros(maxiter,2);

% prompt the user to define the start of the molecule
'find start of molecule'
junk = input('hit enter when ready');

% ginput gets the mouse clicks until enter is pressed
[x,y] = ginput;
'got points'
% load these coords into the first r value
r(1,:) = [x(1), y(1)];

% plot this point on the graph
plot(r(1,1),r(1,2),'wx');

```

```

% ask the user to input another point with the mouse to
% compute a guess for the initial tangent... again it
% waits for enter to begin...
'direction'
junk = input('hit enter when ready');

% ginput gets the positions of mouse clicks
[x,y] = ginput;

% and puts them into r2
r2 = [x(1),y(1)]
% and plots this point
plot(r2(1),r2(2),'wx');

% prompts the user to give the end point of the molecule
% again wait for an enter before starting
'end point of molecule'
junk = input('hit enter when ready');

% the end position is stored in rend
[x,y] = ginput;
rend = [x(1),y(1)]
% plot it on the density plot
plot(rend(1),rend(2),'wx');

% prompt the user to begin the calculation
'ready to go?'
junk = input('hit enter when ready');

% init tangent
t = r2-r(1,:);
t = t/norm(t);

% start the main tracing loop... the loop can end in two ways
% either the max iteration is reached set by maxiter or the end
% of the chain is found and the loop is stopped by a break command.
% ugly but effective

for c = 1:maxiter;

    % plot current position and attempt to refresh the
    % display to show the user where the code has gotten to
    % this feature doesn't yet work... I think.
    plot(r(c,1),r(c,2),'k. ');
    refresh;

    % here is the break command that is used to end the loop when
    % the end is found. If the distance between the current position
    % and the end point is less than the end radius, the main
    % loop breaks.
    if( norm(r(c,:)-rend)<endradius)
        break;

```

```

end;

% Now I will explain the algorithm
% use the last tangent to guess the position
% of the next point distance stepsize away. We
% will find the true point iteratively...
for a=1:2;

    % use the last tangent to guess the position
    % of the next point distance stepsize away.
    rn = r(c,:)+t*stepsize;
    %plot(rn(1)+.5,rn(2)+.5,'w.');
```

% compute a normal to the tangent
 normal = [t(2),-t(1)];

% and project the data onto a segment defined
 % by scanvec. scanvec is a vector with the
 % distance at which the the data will be interpolated
 % on the normal...
 scanvec = ((-scannum):scannum)/scannum\*scansize;

% get the length of this vector
 sizescan = max(size(scanvec));

% now make the point at which we wish to interp
 % the data. They are at the guessed position normal
 % to the curve with the spacing given by scanvec.
 rscanvec = zeros(sizescan,2);
 rscanvec = scanvec'\*normal + ones(sizescan,1)\*rn;

% now we do the interpolation onto these point producing
 % a vector of z values
 z = interpolate\_im3(rawdata',rscanvec);

% Now we compute the center of mass by multiplying these
 % z values (the mass) by their spacial positions
 rnn = z'\*rscanvec;

% and dividing by the sum of the z's or the total mass
 rn = rnn/sum(z);

% to give a new guess for the position of the curve...
 % but this new point does not lie at the right distance
 % so we will compute the tangent only... which in turn
 % will update the the r guess... then we iterate to improve
 % the guess
 t = (rn-r(c,:))/norm(rn-r(c,:));
 rn = r(c,:)+t\*stepsize;
end;
% make the next point equal to the guess... which is now pretty
% good since we interated it...
r(c+1,:)=rn;

```
end;

% end of the main loop... now we keep only the r values which we
% have traced. these will be returned since the function is array
% valued
r = r(1:c,:);

% plot the trace on the density plot
plot( r(:,1), r(:,2),'k');

% and compute the tangents
t = (r(2:c,:)-r(1:c-1,:));
t = [t(:,1)./sqrt(t(:,1).^2+t(:,2).^2),t(:,2)./sqrt(t(:,1).^2+t(:,2).^2)];

% and the angles
theta = compute_theta(t);
figure(3);
clf;

% which are then plotted in a histogram
hist(theta,20)
```